

AMERICAN UNIVERSITY OF BEIRUT

CONDITION ASSESSMENT OF DISSIMILAR FRICTION-
STIR-WELDED JOINTS USING ULTRASONIC LAMB
WAVES

by
MOHAMMAD ALI HASSAN FAKIH

A dissertation
submitted in partial fulfillment of the requirements
for the degree of Doctor of Philosophy
to the Department of Mechanical Engineering
of the Maroun Semaan Faculty of Engineering and Architecture
at the American University of Beirut

Beirut, Lebanon
April 2021

AMERICAN UNIVERSITY OF BEIRUT

CONDITION ASSESSMENT OF DISSIMILAR FRICTION-
STIR-WELDED JOINTS USING ULTRASONIC LAMB
WAVES

by
MOHAMMAD ALI HASSAN FAKIH

Approved by:

Dr. Samir Mustapha, Associate Professor
Department of Mechanical Engineering
American University of Beirut, Lebanon



Advisor

Dr. Kamel Aboughali, Professor
Department of Mechanical Engineering
American University of Beirut, Lebanon



Chair of Committee

Dr. Mohammad S. Harb, Assistant Professor
Department of Mechanical Engineering
American University of Beirut, Lebanon



Member of Committee

Dr. Manuel Chiachío Ruano, Associate Professor
Department of Structural Mechanics and Hydraulics Engineering
University of Granada, Spain



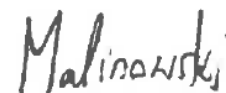
Member of Committee

Dr. Ching-Tai (Alex) Ng, Associate Professor
School of Civil, Environmental and Mining Engineering
The University of Adelaide, Australia



Member of Committee

Dr. Paweł Malinowski, Associate Professor
Institute of Fluid-Flow Machinery
Polish Academy of Sciences, Poland



Member of Committee

Date of dissertation defense: April 27, 2021

AMERICAN UNIVERSITY OF BEIRUT

DISSERTATION RELEASE FORM

Student Name: Fakih Mohammad Ali Hassan
Last First Middle

I authorize the American University of Beirut, to: (a) reproduce hard or electronic copies of my dissertation; (b) include such copies in the archives and digital repositories of the University; and (c) make freely available such copies to third parties for research or educational purposes:

- As of the date of submission
- One year from the date of submission of my dissertation.
- Two years from the date of submission of my dissertation.
- Three years from the date of submission of my dissertation.

Mohammad Ali Hassan Fakih May 10, 2021

Signature

Date

ACKNOWLEDGMENTS

Thank You, my Lord, Allah, for giving me the strength, patience, persistence, ambition, and capability to achieve what I have achieved throughout my life. Without Your guidance and divine care, I would have reached nowhere! My God, I've been always delinquent in expressing my thanks, and whatever I do, I will not be able to thank even one of Your uncountable boons and blessings! Please help me to be always thankful, to always remember Your blessings, and to use them for the good of humanity and the rest of Your creations. Help me to be always humble about what I have accomplished, and know it will be nothing, but a curse, if not used in what You love and if not accompanied with benefit to the human race. Remind me, my God, to be always grateful to those surrounding me without whom I wouldn't have been who I am or have attained this beautiful grace, as everything You give, my Lord!

I will always be grateful from deep inside to my advisor and mentor Dr. Samir Mustapha. You were the best advisor that anyone can imagine, and I could have never asked for better than you to guide me and take care of me during this critical stage of my life. You were, and I know that you will stay, always there to give me all kinds of support and advice. You have backed me up by all means of mental, emotional, and even financial support. You gave me lessons and advice in all sorts of smart ways on the professional and personal life levels. You have always been as close as family, as understanding as an elder brother, and as strict and tolerant as a parent who always aimed to put me on the right path. The most important is how much you believed in me, and, thus, how much self-confidence you provided me with. There is too much to say, but it would never be enough to say thank you! Dr. Samir, I will honestly never be able to express my gratefulness! If I weren't sure the world still has nice people like you, I would have said: "May God help me bear working with any other manager after all the kindness and respect I have seen from you"!

I would like to sincerely thank all the committee members for accepting to be on my thesis committee and for their thorough reviews, valuable comments, and constructive suggestions. Without your expert revision and recommendations, my thesis would have lost too much of its value.

Dr. Mohammad Harb, you were always there to help when I asked. You were always there when I needed advice. You even were always there to provide me with the support of a real brother. You even offered me to stay at your place when I'm overloaded and need to spend some nights at campus to avoid commuting and complete my work! What could I expect more than that! We played football together along with Dr. Samir, and I am still willing to benefit from your offer to have free diving lessons and trips with you. You traveled to the US to do some experiments for my research and much more to mention. You were a friend and an elder brother rather than just a professor!

Dr. Kamel Aboughali, you have always supported me during my entire journey at the American University of Beirut (AUB), including my Master's and Ph.D. studies, as the former Chairman of the Department of Mechanical Engineering. Without your kind

help and funding support, I wouldn't have been here, I couldn't have finished my work, and I probably couldn't have traveled to do my research!

I've honestly spent some of the best days of my life working under the supervision of Drs Manuel and Juan Chiachío Ruano in Granada, Spain. The twin brothers made me feel I'm a third brother and a very close friend! We hanged around together and made family visits, and they backed me up when I asked for any kind of personal or professional help. Drs Chiachío, you never made me feel the difference as you being my supervisors, as you were just family far away from home! Dr. Manuel, you started taking care of me even before my arrival in Granada; you planned a research topic and helped me get the scholarship, checked the house for me, got me the keys, welcomed me in the train station, and helped me with the bags all the way home! And both of you are still taking care of me until now! I really know how lucky I am and feel the divine care when thinking about such people I was destined to work with and build such nice professional and personal relations during my Ph.D. Your creative ideas helped me accomplish an important part of my thesis work, and your lessons about life, work, and life-work balance shall never be forgotten! I shall never forget, as well, how difficult was the goodbye between us, and I am always thinking about the day I will arrive again in Granada and meet with you again. Recognition is extended to the European Commission, AUB's Office of International Programs (OIP), and the University of Granada (UGR) for providing me this amazing opportunity and granting me an Erasmus+ mobility scholarship to spend a semester at UGR.

I would like also to express my special thanks to Dr. Guillermo Rus for helping me to get the Erasmus+ scholarship and for welcoming me at his lab during my stay. You offered me all kinds of support and allowed me to ask and learn from your research group and to benefit from the available facilities. I would never forget my days at the lab and the very nice times you have all created, starting from our daily breakfasts with the whole group, our seminars, going out and partying together, watching movies, and reaching the goodbye lunch invitation that you made for me! I have discovered at your lab how work and research could be fun and happiness due to your wonderful mindset! Having a supervisor so close and kind, as you are to your students, would always be the gear to hard work and magnificent achievements, as you and your group are providing a practical model. My sincere and deep thanks are extended to all my friends in the END lab who were all so close, nice, helpful, and supportive, and who will always be my amazing brothers and sisters!

Dr. Ching-Tai (Alex) Ng, I know we were both so busy during my short visit to your lab at The University of Adelaide, but I would never forget your help before, during, and after my stay! You helped me do all the necessary paperwork, find proper accommodation, and have nice welcome, lab induction, workplace, and technical support. I will never forget your lunch invitation upon my arrival and taking me to one of the peaks to have a nice talk with an amazing night view of the city before I leave. You were extremely supportive providing me with all means of help, guidance, advice, follow-up meetings, and logistics to make sure I would satisfy the objectives of my visit and get the best experience and exposure that I need. You even took responsibility to make me special permissions to stay at the lab overnights to finish my work! You have helped me in person and assigned your Ph.D. student for help during my stay and for

continuing the needed experiments after I leave! I am deeply grateful and I hope we will meet again and will keep this nice and beneficial collaboration. Great thanks and appreciation are also due to Ms. Carman Yeung who has kindly helped in using the 3D laser scanner and assisted in running some experiments. I am also grateful to many lab assistants at The University of Adelaide for their kind help, training, advice, and support to successfully perform the experiments and get answers to many technical questions. I would like to particularly mention here Mr. Adam Ryntjes who did a great job taking good care of me and all my needs, and Mr. Aubrey Slater who gave me the idea of using the retroreflective spray, taught me how to use it, and provided me with the needed material!

Dr. Paweł Malinowski, thank you for being part of the committee and for your thorough review of my dissertation. We have first met in Hong Kong, where you have attended my presentation at the APWSHM conference and asked some important questions about part of my thesis work. I can still remember my nice chat in the opening ceremony, with a very gentle, kind, and humble person, who happened to know my advisor, Dr. Samir Mustapha. I hope we will meet again soon and will have further collaborations together.

Prof. Hazem Chahine, you were always taking care of me and pushing from the back. You supported me whenever I needed and probably without asking. You always followed my progress and empowered me with your priceless advice and encouraging words. With your invaluable experience and warm feelings, you always knew how to guide me in the best way! Without your continuous support, I wouldn't have been here today!

Recognition and gratitude are addressed to the National Council for Scientific Research of Lebanon (CNRS-L) for granting me a 3-year doctoral scholarship. I would like also to use this opportunity to thank the faculty, technical and academic staff, and my dear friends and officemates at AUB, The University of Adelaide, Kathleen Lumley College in Adelaide, and University of Granada, and everyone who had any small contribution to my knowledge, my research, my sense of comfort, and to my success. Special thanks are due to Dr. Nayla Cortas and Ms. Salam Al Hamra at the American University of Beirut – Medical Center (AUBMC) for their help in performing the CT scans for the testing specimens. Special acknowledgments are also due to all the staff at the Department of Mechanical Engineering and the Dean's Office of Maroun Semaan Faculty of Engineering and Architecture at AUB, to the Chairman, Dr. Issam Lakkis, and the Dean, Dr. Alan Shehadeh. You have all facilitated and provided academic, technical, and financial support to allow me to smoothly pass this journey with the best possible local and international training and expertise.

I would like also to thank all my beloved friends here and abroad who were always there to listen, encourage, and help in all possible ways! I will never forget the amazing, beautiful, and tough times we have spent together, how we shared our feelings, and how we stood together against difficulties. Without you in my life, especially the close ones, things would have been so much different and so much difficult! Having such great, loving, honest, loyal, and encouraging friends is a divine blessing that I should forever be thankful for.

My deepest and greatest thanks are reserved for my dear family (my grandparents, my parents, my parents-in-law, my wife Areej, my son Mahdi, my siblings and their families, my siblings-in-law and their families, my uncles and aunts, my cousins, and everyone). Without your unconditional love and support, none of this would have been possible! For my closest circle, forgive me for all the hard time I have caused you and for the precious time that I wasn't always able to spend with you, especially my parents, Areej, and my dear son Mahdi! I'm really sorry, and I hope, and I promise that I will try to compensate for all of this since all I want is your happiness!

They say a sister is a haven, and I thankfully have two beautiful havens! They also say a brother is a backbone, and I know I have the best two backbones ever! You have always helped me and took good care of me. Examples and memories that I have in mind for each one of you, Fatima, Sara, Abbas, and Haydar are numerous! You provided me with all what you can to make sure I am happy, relaxed, and efficient. You even deprived yourselves and your families to give me what I need! With my parents and parents-in-law, you took care of my family when I wasn't able to do my job! You are my dearest, even if I didn't tell! I love you so much and I'm deeply grateful for all your love, care, kindness, support, and encouragement. I will always be indebted to you, and may God help me to be always the best brother that you could have!

To my wife's family, especially my parents-in-law, I have observed the love and tears in your eyes exactly as I have seen in the eyes of my parents! I have seen the unconditional care and backup the same that I would expect from great loving parents. You have always followed up on my progress with the utmost care and the greatest support and encouragement. You continuously took care of all of us and looked after my family when I traveled. You always treated me like a son and perhaps even better! Without your love, support, and guidance for me and my wife, this success would have been impossible. I am truly blessed to have such a wonderful family!

Mom and dad, you are my most precious treasure, and everything I have is because of you! You are the greatest parents ever, even though I wasn't always the best son! You gave me everything, since my childhood, and encouraged me, by all means, to be successful and to strive to be the best! If I were to write down your favors, I would probably need to write another dissertation! However, I know that whatever I say or whatever I do, I will not be able to pay even a small portion of your eternal debt! There is no better act than drawing a smile on your faces and no better feeling than observing the tears of happiness and pride in your eyes! I hope I will always be able to draw these smiles and preserve your pride! May God forever bless you as you are my cause to exist and the reason I would like to stay!

Areej and Mahdi, I can only thank God for having you in my life and thank you for standing next to me during all circumstances. Crossing difficult paths full of obstacles definitely requires having a wonderful, strong, patient, and loving wife and a lovely, clever, understanding, and solid little man, like you both are! The fulfillment of my thesis and many other accomplishments would have been impossible without you. Areej, you have borne with me all the difficult circumstances, shared with me all the stress, even helped me when overloaded, and, most importantly, provided me with all the love and care that I need. You are my best love, my best friend, and the best partner

that I would ever ask for! Dear Mahdi, from you, I have learned how life can be all narrowed down to be seen from your eyes, and how a son turns out to be the only center around which everything will revolve and for which everything is devoted! From your innocence and infinite love, I have learned what true love is and what real pleasure is all about. I can see a great future ahead of you, by God's will. I would also like to thank our upcoming baby (probably Hadi) for planting another hope and more joy and happiness into our lives in the last few months. We are all waiting for you and expecting more blessings with your arrival! You all give my life its meaning, and without you and my parents, there's nothing in this worldly life that is worth my hard work! You are the best thing that ever and will ever happen to me!

Thank you all! I'm faithfully and forever thankful for having such special people in my life!

ABSTRACT OF THE DISSERTATION OF

Mohammad Ali Hassan Fakh

for

Doctor of Philosophy

Major: Mechanical Engineering

Title: Condition Assessment of Dissimilar Friction-Stir-Welded Joints Using Ultrasonic Lamb Waves

Condition monitoring is increasingly being considered a necessity to ensure the safe use of our structures and to extend their lifetime. Lamb waves (LWs) are ultrasonic guided waves (GWs) that are widely used for damage detection, towards integration in structural health monitoring of mechanical, aerospace, and civil structures.

The growing mechanical and economical demands in modern systems and structures are forcing an inevitable need for joining dissimilar materials, thus creating the challenge of establishing a process to inspect and monitor dissimilar joints. Friction stir welding (FSW) has emerged as one of the most promising and successful methods for producing sound dissimilar-metallic joints. This work is an extensive investigation of LWs' potential for the nondestructive evaluation of dissimilar FSW.

As a prior step, the propagation behavior of the fundamental symmetric (S_0) and anti-symmetric (A_0) LW modes, upon interaction with welded joints of dissimilar materials, was investigated. A plate with an intact AA6061-T6/AZ31B dissimilar joint was employed, and the interaction of the propagating wave with the material interface was scrutinized numerically and validated experimentally. Plane-wave approximation (PWA) analytical solution was also adopted to investigate the behavior of the symmetric modes, and its performance was compared to the numerical and experimental results. The effect of the angle of incidence on the reflection, transmission, and mode conversion of the incident modes was analyzed. The transmission coefficients of the S_0 and A_0 modes were found to be almost constant until reaching very steep incidence angles ($\hat{i} > 78^\circ$). Further, the fundamental shear-horizontal (SH_0) GW mode has evolved upon the interaction of the obliquely-incident S_0 mode with the interface. The experimental results from an intact AA6061-T6/AZ31B FSW joint showed very good agreement with both the analytical and numerical ones. PWA was shown to be a very good approximation to determine the transmission and reflection coefficients of the in-plane symmetric modes for a certain frequency range. The importance of the obtained findings for the implementation of LW sensor networks in structures containing dissimilar-material joints was finally explained.

In the next step, a novel Bayesian-based framework for full damage identification was proposed. Simulated damage within a dissimilar-material joint was identified, in six parameters of damage extent and location (length, width, thickness, and x -, y -, and z -positions), using only one actuator and one sensor. Surrogate models that can predict LW sensor measurements, given the damage size and position, were developed. The surrogate models were based on artificial neural networks (ANNs) trained using finite element (FE) simulations of the monitored plate, with a pre-allocated sensor network. The ANNs were utilized to perform a statistical damage inference based on Approximate Bayesian Computation by Subset Simulation (ABC-SubSim). Data fusion for ABC-SubSim inference using multiple sensor measurements was successfully employed. The results showed that damages of different sizes and locations were identified with a high level of resolution and with quantified uncertainty. A precise and robust damage inference was achieved using a minimal sensing set-up based on one PZT actuator and two sensors. These findings are very promising for damage detection and assessment and form a step forward towards online/onboard monitoring applications.

Furthermore, the potential of LWs for the detection and evaluation of micro-scaled intermetallic compounds (IMCs) at the weld interface was examined. Intermetallic regions are common in welded joints of dissimilar materials, and their presence leads to weakness of the joint (due to their brittle behavior). FSW lap joints, between AA5052-H32 aluminum and ASTM 516-70 steel, with various intermetallic conditions, were simulated using the Murnaghan nonlinear-elastic model. The synchronism and non-zero power flux conditions between higher-order symmetric LW modes (S_1 and S_2) were used to determine the needed LW excitation frequency. Symmetric LWs were selectively generated and the collected signals were analyzed in the time, frequency, and time-frequency domains. It was found that the relative acoustic nonlinearity parameter varies linearly with the thickness of the IMC layer, where variations down to $2 \mu\text{m}$ are easily differentiated. The attained results prove the sensitivity of LW nonlinear features to microstructural variations, within dissimilar FSW joints, and demonstrates the capability of LWs in accurately scrutinizing their strength. Such novel findings would open the way towards the quantitative nondestructive assessment of intermetallic compounds using LW-based techniques.

TABLE OF CONTENTS

ACKNOWLEDGMENTS	1
ABSTRACT	6
ILLUSTRATIONS	11
TABLES	16
NOMENCLATURE	18
ABBREVIATIONS	26
1. INTRODUCTION	29
1.1 Dissimilar Friction Stir Welding.....	29
1.2 Structural Health Monitoring of Friction Stir Welding	33
1.3 Thesis Overview	35
1.3.1 Research Objectives	35
1.3.2 Chapter Summaries	38
2. THE INTERACTION OF THE FUNDAMENTAL LAMB- WAVE MODES WITH MATERIAL DISCONTINUITY	41
2.1 Introduction.....	41
2.2 Theoretical Background and Analytical Approximation.....	45
2.2.1 Fundamentals of Lamb Waves	45
2.2.2 Wave Modes Identification	48
2.2.3 Wave-Joint Interactions.....	54
2.2.3.1 Mode Conversion	55
2.2.3.2 Critical Angles.....	57
2.2.4 Plane-Wave Approximation of In-Plane Modes	61
2.3 Finite Element Modeling	71
2.3.1 Finite Element Method for Wave Propagation.....	71
2.3.2 Problem Modeling	73
2.4 Experimental Validation	76

2.4.1 Sample Preparations	76
2.4.2 Experiment Setup	79
2.5 Results and Discussion	82
2.5.1 Mode Extraction	82
2.5.2 Reflection Separation	89
2.5.3 S_0 - SH_0 Transmission Separation	94
2.5.4 Attenuation Curves	97
2.5.5 Transmission and Reflection Coefficients.....	105
2.6 Summary	113
3. A BAYESIAN DAMAGE IDENTIFICATION FRAMEWORK	114
3.1 Introduction.....	114
3.2 Finite Element Modeling	119
3.3 ANN-Based Lamb-Wave Surrogate Modeling.....	125
3.3.1 Data Preparation	126
3.3.1.1 Exploiting the Entire Ultrasonic Signal.....	126
3.3.1.2 Data Preprocessing	128
3.3.2 ANN Design and Performance	129
3.3.2.1 Training and Testing Datasets	129
3.3.2.2 ANN Architecture and Training	133
3.4 Damage Inference by Approximate Bayesian Computation	136
3.4.1 Standard ABC for Damage Inference using One Sensor Measurement	137
3.4.2 ABC-SubSim for Damage Inference using One Sensor Measurement	139
3.4.3 Data Fusion: Applying ABC-SubSim to Multiple Sensor Measurements	143
3.5 Results and Discussion	145
3.5.1 Damage Detection	145
3.5.2 Damage Identification and Inference Evaluation	148
3.5.3 ABC-SubSim based on One Sensor Measurement.....	152
3.5.4 ABC-SubSim based on Multiple Sensor Measurements.....	162
3.5.5 Effect of Sensing Noise	164
3.5.6 Discussion.....	169
3.6 Summary	174

4. ASSESSMENT OF INTERMETALLIC COMPOUNDS WITHIN DISSIMILAR JOINTS USING LAMB-WAVE NONLINEARITY.....	176
4.1 Introduction.....	176
4.2 Theoretical Background.....	180
4.3 Finite Element Modeling	183
4.3.1 Available Specimens	183
4.3.2 Single-Material Model.....	186
4.3.3 Dissimilar Lap-Weld Model with Variable IMCs.....	188
4.4 Results and Discussion	191
4.4.1 Time-Domain Mode Identification.....	191
4.4.2 Spectral and Nonlinearity Analysis	194
4.4.2.1 Fast Fourier Transform	194
4.4.2.2 Short-Time Fourier Transform	198
4.4.2.3 Cumulative Second-Harmonic Generation.....	202
4.4.3 Assessment of Intermetallic Compounds	207
4.5 Summary	210
5. CONCLUSIONS AND RECOMMENDATIONS.....	212
5.1 Introduction.....	212
5.2 Concluding Remarks.....	212
5.3 Recommendations for Future Work	216
APPENDIX. LIST OF PUBLICATIONS.....	220
BIBLIOGRAPHY	222

ILLUSTRATIONS

Figure

1.1. A Schematic of the friction stir welding process [17].	31
1.2. FSW defects, from the left to the right, top then bottom row: worm hole, scalloping, ribbon flash, surface lack of fill, nugget collapse, and surface galling [18].	32
2.1. Particle motions for the symmetric and anti-symmetric LW modes [26].	48
2.2. Illustrations of the predominant oscillation directions of the fundamental guided-wave modes.	49
2.3. Group-velocity dispersion curves for a plate of 3- <i>mm</i> thickness: (a) AA6061-T6 and (b) AZ31B.	51
2.4. Simulated signals at two different sensing positions to illustrate mode identification.	54
2.5. Mode conversion at the interface assuming no reflection; L: longitudinal wave and S: shear wave.	56
2.6. General case of a longitudinal incident wave and illustrations of the 1 st and 2 nd critical angles for a solid-solid material interface; L: longitudinal wave and S: shear wave.	60
2.7. Transmission and reflection coefficients at 200 <i>kHz</i> of the S_0 and S_0 - SH_0 modes using PWA.	67
2.8. Through-thickness normalized amplitude of the refracted S_0 mode for a wave propagating in the forward direction at $\hat{i} = 20^\circ$ (sensor position = 80 <i>mm</i>).	68
2.9. Transmission and reflection coefficients of the S_0 and S_0 - SH_0 modes at different excitation frequencies using PWA and FE simulations for a wave propagating in the forward direction at $\hat{i} = 20^\circ$.	69
2.10. S_0 mode shape across the thickness for different excitation frequencies.	71
2.11. Details and mesh of the FE model.	75
2.12. Photographs of the specimens used in this study and a drawing of the template used for PZT placement.	78
2.13. A through-thickness cross-sectional view of the welded test specimen, from a CT scan, showing its intact weld condition. Dimensions are in <i>mm</i> .	78

2.14. A photo of the experimental setup showing the Polytec PSV-400 3D SLV and its control box, the signal generator, the amplifier, and a testing specimen. The specimen shown in the figure is before using gummy tapes on its edges.....	79
2.15. The Polytec PSV-3D SLV with one of the testing specimens – the laser and the specimen were totally covered with the shown black cloth when performing the measurements.....	81
2.16. Spatial-time plots of the in-plane normalized velocity field (along the wave propagation direction) measured from the FSW plate, for a wave propagating from AA6061-T6 to AZ31B at $\hat{i} = 0^\circ$	82
2.17. (a) Sample out-of-plane displacements on the surface of the plate for a wave propagating in the forward direction at $\hat{i} = 40^\circ$. (b) and (c) two illustrating examples of S_0 and SH_0 wavefield calculations.....	85
2.18. Spatial-time plots of the simulated and experimental wavefields, along the incidence and transmission directions of different modes, for a wave propagating in the forward direction at $\hat{i} = 20^\circ$	87
2.19. Typical normalized experimental raw signals for U_{A_0} at two different sensing positions.....	89
2.20. Separation of the S_0 reflection – FE simulation measurements along S_0 reflection direction, for a wave propagating in the forward direction at $\hat{i} = 20^\circ$	92
2.21. Separated A_0 and S_0 - SH_0 reflection fields – FE simulation measurements along their respective reflection directions, for a wave propagating in the forward direction at $\hat{i} = 20^\circ$	93
2.22. Separation of the S_0 reflection – experimental measurements along S_0 reflection direction, for a wave propagating in the forward direction at $\hat{i} = 20^\circ$	94
2.23. Separation of the S_0 - SH_0 transmission – FE measurements along S_0 - SH_0 transmission direction, for a wave propagating in the forward direction at $\hat{i} = 20^\circ$	97
2.24. Experimental S_0 -mode attenuation curves in both the AA6061-T6 plate (averaged from all incidence angles) and the AA6061-T6/AZ31B plate (forward direction; $\hat{i} = 0^\circ$).	102
2.25. Experimental S_0 -mode spatial-time plots in both the AA6061-T6 plate and the AA6061-T6/AZ31B plate (forward direction; $\hat{i} = 0^\circ$).	102
2.26. FE S_0 -mode attenuation curves in both the AA6061-T6 plate ($\hat{i} = 0^\circ$) and the AA6061-T6/AZ31B plate (forward direction; $\hat{i} = 0^\circ$).	104
2.27. S_0 -mode attenuation curves in both the AZ31B plate (FE result; $\hat{i} = 0^\circ$; 3 rd peak) and the AA6061-T6/AZ31B plate (FE and experimental results; backward direction; $\hat{i} = 0^\circ$; 3 rd peak).....	104

2.28. Transmission and reflection coefficients of the studied symmetric modes.	112
2.29. Transmission and reflection coefficients of the A_0 mode.....	112
3.1. A schematic illustrating the main steps of the damage identification framework proposed in this chapter.	119
3.2. A view of the FE model showing the actuator model (inset) and the sensing point S1 (in red) on the other side of the weld line. Dimensions are expressed in <i>mm</i>	121
3.3. An illustration showing the welded plate containing a damage example (in red) and the six damage parameters. Position parameters are measured with respect to the center of the damage.....	123
3.4. FE U_2 displacements for the intact weld and a sample damage case D1; D1: $L = 50, W = 2, th = 1.5, x = 0, y = 0,$ and $z = 0.25$	125
3.5. Raw signals of U_{2S1} for the intact weld and two sample damage cases. Damage D1 lies within the coverage of the sensing path, while damage D2 lies outside the coverage of the sensing path; D1: $L = 50, W = 2, th = 1.5, x = 0, y = 0,$ and $z = 0.25$; D2: $L = 50, W = 2, th = 1.5, x = -75, y = 0,$ and $z = 0.25$; all parameters are in <i>mm</i>	128
3.6. An illustration showing a well-balanced and well-distributed training dataset which should be convenient for training down to extremely-low performance errors, without generalization concerns when seeing a real damage case.....	131
3.7. Scatter plots of the damage parameters of the training and testing datasets, chosen from the FE simulations.....	133
3.8. The architecture of the used ANNs for Lamb-wave surrogate modeling, determined using a trial and error process.	135
3.9. Two sample results of the ANN prediction of LW sensor measurement, when given specific damage parameters, compared to the signals obtained using FE simulation; D3: $L = 25, W = 1, th = 1, x = -75, y = -1,$ and $z = -1$; D4: $L = 100, W = 3, th = 1, x = 50, y = 1,$ and $z = 0$; all parameters are in <i>mm</i>	136
3.10. A flowchart explaining ABC damage inference from one sensor measurement using an ANN Lamb-wave surrogate model.	139
3.11. A flowchart explaining ABC-SubSim damage inference from one sensor measurement using an ANN Lamb-wave surrogate model.	143
3.12. ABC-SubSim damage-inference results of the intact weld using U_{2S1} : (a) without and (b) with adding sensing noise.....	147

3.13. ABC-SubSim damage-inference results of test case 15 (refer to Table 3.5) using $U_{3S1} - m = 13$ simulation levels and $R_{acc} = 22.9\%$	150
3.14. ABC-SubSim damage-inference results of test case 5 (refer to Table 3.5) using $U_{3S1} - m = 12$ simulation levels and $R_{acc} = 17.9\%$. The real damage parameters are marked and labeled in red color.....	151
3.15. ABC-SubSim damage-inference results of test case 12 (refer to Table 3.5) using $U_{2S1} - m = 13$ simulation levels and $R_{acc} = 22.2\%$. The real damage parameters are marked and labeled in red color. The x -position, marked in black, is the symmetric value of the actual x -position.....	157
3.16. (a) An illustration demonstrating the need for using the whole signal, including the wave's boundary reflections, to perceive damages lying outside the coverage of the sensing path. The illustration also shows how two symmetric damage cases would yield the same LW measurement at a sensor located along the Y -axis. The damages are drawn in red color. (b) FE results of symmetric sample damage cases; D2: $L = 50, W = 2, th = 1.5, x = -75, y = 0,$ and $z = 0.25$; D2-sym: $L = 50, W = 2, th = 1.5, x = 75, y = 0,$ and $z = 0.25$; all parameters are in mm	158
3.17. The FE model showing the two added sensing points S2 and S3 (in red).....	160
3.18. Boxplots summarizing the precision and uncertainty of ABC-SubSim damage inference for the whole testing dataset (594 cases) using U_{2S2} . Results of different damage lengths are shown separately.	161
4.1. Dispersion curves of LW modes in a 2- mm thick AA5052-H32 aluminum plate.	183
4.2. Two photographs of the top and cross-sectional views of a cut FSDC specimen with two cladding passes [159].....	184
4.3. Top and side photos of one of the available FSDC samples.	185
4.4. The interface-layer thickness (in μm) of different specimens [159].	185
4.5. Geometry and mesh of the single-material (AA5052-H32) 2D plane-strain FE model.	187
4.6. Geometry and mesh of the AA5052-H32/ASTM 516-70 lap-weld 2D plane-strain FE model.....	190
4.7. EDS line scan analyzing the interface layer of a selected A50 sample [159].	190
4.8. Time-domain signals from the single-material AA5052-H32 model, measured at sensor positions = 50 and 160 mm	193
4.9. Time-domain signals from the dissimilar lap-weld model with no IMCs, measured at sensor positions = 9 and 24 mm	193

4.10. A sample raw signal and its FFT, measured at sensor position = 100 mm in the single-material AA5052-H32 model.	196
4.11. A sample raw signal and its FFT, measured at sensor position = 54 mm in the dissimilar lap-weld model with no IMCs.	197
4.12. Sample raw signals, their STFT spectrograms, and their reconstructed time-domain signals at the fundamental (1,785 kHz) and second-harmonic (3,570 kHz) frequencies – measured at different sensor positions in the single-material AA5052-H32 model.	200
4.13. Sample raw signals, their STFT spectrograms, and their reconstructed time-domain signals at the fundamental (1,785 kHz) and second-harmonic (3,570 kHz) frequencies – measured at different sensor positions in the dissimilar lap-weld model with no IMCs.	202
4.14. β' versus the sensor positions in the single-material model.	205
4.15. β' versus the sensor positions in the dissimilar lap-weld model with no IMCs. .	207
4.16. The linear trend between β' and the IMC-layer thickness – shown for four different sensor positions on the aluminum and steel sub-plates, based on both FFT (left) and STFT (right).	210

TABLES

Table

1.1. Advantages of friction stir welding over conventional welding techniques [7, 15].	31
2.1. Physical and mechanical properties of the used materials.....	50
2.2. Theoretical group velocities of the existing guided-wave modes at 200 kHz.....	52
2.3. Theoretical phase velocities and critical angles of the existing guided-wave modes at 200 kHz.	59
2.4. FE and experimentally obtained group velocities of the LW modes for a wave propagating in the forward direction at $\hat{\iota} = 20^\circ$	86
3.1. Ranges of the damage parameters used for the simulated damage cases. The third row shows the incremental step per damage parameter.	122
3.2. Range of virtual damage positions of the healthy signals added to the training dataset (for data balance). 1,859 healthy signals with different virtual damage positions were finally added.....	132
3.3. Range of definition of the damage parameters when randomly generating damage cases (θ_r) for the application of ABC or ABC-SubSim.	139
3.4. ABC-SubSim control parameters used in this study.	145
3.5. Damage parameters of the selected damage cases.....	149
3.6. A summary of the ABC-SubSim inference results using U_{2S1} sensor measurement, for the selected damage cases.	154
3.7. A summary of the ABC-SubSim inference results using U_{3S1} sensor measurement, for the selected damage cases.	155
3.8. A summary of the ABC-SubSim inference results using U_{2S1} and U_{2S2} sensor measurements, for the testing damage cases 1 to 6.	163
3.9. A summary of the ABC-SubSim inference results using U_{2S2} and U_{2S3} sensor measurements, for the testing damage cases 1 to 6.	163
3.10. A summary of the ABC-SubSim inference results using the three sensor measurements (U_{2S1} , U_{2S2} , and U_{2S3}), for the testing damage cases 1 to 6.	164
3.11. A summary of the ABC-SubSim inference results using U_{2S2} sensor measurement with variable sensing-noise levels, for the selected damage cases of $L = 25 \text{ mm}$	166

3.12. A summary of the ABC-SubSim inference results using U_{2S2} sensor measurement with variable sensing-noise levels, for the selected damage cases of $L = 100 \text{ mm}$	167
3.13. A summary of the ABC-SubSim inference results using U_{2S2} sensor measurement with variable sensing-noise levels, for the selected damage cases of $L = 200 \text{ mm}$	168
3.14. A summary of the ABC-SubSim inference results using U_{2S1} and U_{2S2} sensor measurements with variable sensing-noise levels, for the healthy-weld case.	169
4.1. Geometry and variable welding parameters of the available FSDC specimens....	185
4.2. Physical and mechanical properties of the used sub-plate materials.	187
4.3. Physical and mechanical properties of the $6\text{-}\mu\text{m}$ IMC layer, divided into three sub-layers whose properties were determined via linear interpolation between the material properties of AA5052-H32 and ASTM 516-70.	191

NOMENCLATURE

$[C]$	Damping matrix
$\{\ddot{\mathbf{d}}\}$	Nodal-acceleration vector
$\{\dot{\mathbf{d}}\}$	Nodal-velocity vector
$\{\mathbf{d}\}$	Nodal-displacement vector
$\{\mathbf{F}\}$	Nodal-load vector
$[K]$	Global stiffness matrix
$[M]$	Mass matrix
$\theta_{\tilde{m}}$	The acute angle between the propagation direction of the mode “ \tilde{m} ” and the normal to the material interface
θ_1	The acute angle between the incident mode’s propagation direction and the normal to the material interface
θ_{1L}	Incidence angle of the longitudinal wave mode
θ_2	The acute angle between the reflected/transmitted mode’s propagation direction and the normal to the material interface
θ_{2L}	Transmission/refraction angle of the longitudinal wave mode
θ_{2S}	Transmission/refraction angle of the shear-horizontal wave mode
θ_c	Critical angle
θ_{cL}	Critical angle of the longitudinal wave mode
θ_{cS}	Critical angle of the shear wave mode
θ'_{MAP}	Set of predicted damage parameters based on <i>maximum a posteriori</i>
θ_{max}	Set of maximum allowed values of the damage parameters, imposed by the geometrical constraints

θ_{min}	Set of minimum allowed values of the damage parameters, imposed by the geometrical constraints
θ_r	Randomly-generated damage parameters
θ_σ	Standard deviation of the <i>approximated posterior</i>
Θ_r	Set of N random samples θ_r
ϵ_f	Final tolerance parameter
$\phi_{\tilde{m}}$	The angle between the x -axis and the mode's propagation direction
α	Damage-detection threshold of the damage-length parameter L
β	Damage-detection threshold of the damage-width parameter W
γ	Damage-detection threshold of the damage-thickness parameter th
β	Acoustic nonlinearity parameter
β'	Relative acoustic nonlinearity parameter
δ	A scaling function for Lamb waves
θ	Set of real damage parameters
λ	Material's Lamé second-order elastic constant
μ	Material's Lamé second-order elastic constant
ν	Poisson's ratio
ξ	Damage-inference uncertainty
ρ	Distance metric that compares between two signals
$\rho_s(n)$	ρ of the n^{th} θ_r , within the set Θ_r , based on the s^{th} sensor measurement
ω	Angular frequency
ϵ	Tolerance parameter
A_1	Amplitude of the fundamental probing wave mode

A_2	Amplitude of the second-harmonic wave mode paired to the fundamental probing mode
A_L^{inc}	Amplitude of the incident longitudinal wave
A_L^{refl}	Amplitude of the reflected longitudinal wave
A_L^{tr}	Amplitude of the transmitted (refracted) longitudinal wave
A_S^{refl}	Amplitude of the reflected shear (transverse) wave
A_S^{tr}	Amplitude of the transmitted (refracted) shear (transverse) wave
$A_{refl}^i(\tilde{m})$	Amplitude of the reflected mode “ \tilde{m} ” after traveling a distance r in material X; incident wave propagating from material X to material Y at an angle of incidence \hat{i}
$A_{tr}^i(\tilde{m})$	Amplitude of the transmitted mode “ \tilde{m} ” after traveling a distance r from material X to material Y; incident wave propagating from material X to material Y at an angle of incidence \hat{i}
$A_{tr-s}(\tilde{m})$	Amplitude of the transmitted mode “ \tilde{m} ” after traveling a distance r in a single material X
$R_{(\tilde{m})}^i$	Reflection coefficient of mode “ \tilde{m} ” at an incidence angle \hat{i}
R_{acc}	Acceptance rate of the newly-generated samples
STD_{prop}	Proposed standard deviation within which a new sample is generated around a parent sample
$T_{(\tilde{m})}^i$	Transmission coefficient of mode “ \tilde{m} ” at an incidence angle \hat{i}
$U_{S_0-SH_0(X/Y)}$	The refracted S_0 - SH_0 wavefield, converted from the S_0 mode of an incident wave propagating from material X to material Y at an angle of incidence \hat{i}

$U_{\tilde{m}}$	Displacement/velocity field of the mode “ \tilde{m} ”
U_1	Displacements/velocities along the X -axis
U_2	Displacements/velocities along the Y -axis
U_3	Displacements/velocities along the Z -axis
$U_{R(X/Y)}$	The wavefield, reflected from the material interface, from an incident wave propagating from material X to material Y at an angle of incidence \hat{i}
$U_{RD(X/X)}$	The wavefield, measured along the reflection direction, from an incident wave propagating from material X to material X at an angle of incidence \hat{i}
$U_{RD(X/Y)}$	The wavefield, measured along the reflection direction, from an incident wave propagating from material X to material Y at an angle of incidence \hat{i}
$U_{SH_0D(X/X)}$	The SH_0 wavefield, measured in the same direction as $U_{SH_0D(X/Y)}$, from an incident wave propagating from material X to material X at an angle of incidence \hat{i}
$U_{SH_0D(X/Y)}$	The SH_0 wavefield, measured along the S_0 - SH_0 transmission direction, from an incident wave propagating from material X to material Y at an angle of incidence \hat{i}
U_{iSj}	U_i displacements measured at sensing position Sj ; $i, j \in \{1, 2, 3\}$
c_L	Velocity of the longitudinal wave
c_S	Velocity of the shear (transverse) wave
c_L	Longitudinal bulk-wave velocity
c_T	Shear bulk-wave velocity

c_g	Group velocity
c_p	Phase velocity
c_{p1}	Phase velocity of the incident mode
c_{p2}	Phase velocity of the reflected/transmitted mode
f_E	Fundamental excitation frequency
$f_{n(FFT)}$	Fundamental frequency captured by FFT
\hat{i}	Incidence angle
k_1	Wavenumber of the incident mode
k_2	Wavenumber of the reflected/transmitted mode
p_0	Conditional-probability value
\hat{r}	Reflection angle
\hat{t}	Transmission (refraction) angle
A_0	The fundamental anti-symmetric Lamb-wave mode
AA5052-H32	Aluminum alloy
AA6061-T6	Aluminum alloy
A_j	The j^{th} anti-symmetric Lamb-wave mode
ASTM 516-70	Steel alloy
AZ31B	Magnesium alloy
h	Half the plate's thickness
L	Longitudinal ultrasonic wave
l	Material's Murnaghan third-order elastic constant
L_1	Incident in-plane longitudinal wave mode
L_2	Transmitted (refracted) in-plane longitudinal wave mode

L_{int}	In-plane longitudinal mode transmitted (refracted) along the material interface
m	Material's Murnaghan third-order elastic constant
n	Material's Murnaghan third-order elastic constant
S	Shear ultrasonic wave
S_0	The fundamental symmetric Lamb-wave mode
SH_0	The fundamental shear-horizontal guided-wave mode
S_{int}	In-plane shear mode transmitted (refracted) along the material interface
S_j	The j^{th} symmetric Lamb-wave mode
D	Density
E	Young's modulus
L	Damage length
L'	Predicted damage length
N	Number of samples
P	Set of N distances ρ
$P(n)$	P of the n^{th} θ_r within the set Θ_r
Pr	Damage-inference precision
R	Reflection coefficient
T	Transmission (refraction) coefficient
V	Set of N ultrasonic waves predicted by the ANN, based on the set of all random samples Θ_r
V_s	V based on the s^{th} used sensor measurement
W	Damage width

W'	Predicted damage width
a	The coefficient that normalizes the amplitudes of $U_{SH_0D(X/X)}$ to those of $U_{SH_0D(X/Y)}$, determined from a chosen peak of the 1 st wave-pack and at a chosen sensor position
d	Plate's thickness
f	Frequency
k	Wavenumber
m	Maximum number of simulation levels
r	Wave's propagation distance
$rand$	Standard normally-distributed random number; $rand \in [0, 1]$
t	Time
th	Damage thickness
th'	Predicted damage thickness
u	Real sensor measurement or noise-corrupted FE measurement
u_s	s^{th} real sensor measurement or noise-corrupted FE measurement
u'	Transpose of u
v	Ultrasonic wave predicted by the ANN, based on the randomly-generated damage parameters θ_r
v'	Transpose of v
x	Damage x -position
x'	Predicted damage x -position
y	Damage y -position
y'	Predicted damage y -position
z	Damage z -position

z' Predicted damage z-position

S Number of used sensor measurements

ABBREVIATIONS

2D	Two dimensional
3D	Three dimensional
ABC	Approximate Bayesian Computation
ABC-SubSim	Approximate Bayesian Computation by Subset Simulation
AI	Artificial intelligence
ANN	Artificial neural network
CMEP	Complex modes expansion with vector projection
CPU	Central processing unit
CT	Computed tomography
DI	Damage index
DLPT	Double-layered piezoelectric transducers
EDS	Energy dispersive spectroscopy
FE	Finite element
FEA	Finite element analysis
FEM	Finite element method
FFT	Fast Fourier transform
FRP	Fiber-reinforced polymer
FSDC	Friction stir diffusion cladding
FSW	Friction stir welding
GW	Guided wave
IMCs	Intermetallic compounds
IQR	Interquartile range
LDV	Laser Doppler vibrometer

LW	Lamb wave
MAP	<i>Maximum a posteriori</i>
MMA	Modified Metropolis algorithm
MSE	Mean square error
NDE	Non-destructive evaluation
NL	Noise level
PDF	Probability density function
PWA	Plane-wave approximation
PZT	Lead Zirconate Titanate
RANP	Relative acoustic nonlinearity parameter
SAFE	Semi-analytical finite element
SHG	Second-harmonic generation
SHM	Structural health monitoring
SLV	Scanning laser vibrometer
SNR	Signal-to-noise ratio
SoE	Second-order elastic
STFT	Short-time Fourier transform
ToE	Third-order elastic
TWI	The Welding Institute
WDICs	Wave-damage interaction coefficients
<i>RPM</i>	Rounds per minute

To my most loving and most lovely family...

CHAPTER 1

INTRODUCTION

1.1 Dissimilar Friction Stir Welding

The increased demand for higher fuel efficiency in all kinds of mobile vehicles has led to a greater interest in using lightweight materials in their structures [1, 2]. Variants of aluminum and magnesium alloys are being widely used in transportation and aerospace industries due to their light weight and attractive properties, including high specific strength, corrosion resistance, and good formability [1, 3]. Different materials, and due to their specific properties (mechanical, thermal, physical, chemical, etc.), may be more advantageous than others for specific applications or locations within the structure [4]. For this reason, combinations of dissimilar materials are being inevitably used together to optimize the design from both mechanical and economical perspectives [2, 4]. While fasteners are widely utilized for dissimilar-material joining, welding is still preferred, in the case of metals, to achieve higher productivity and lower costs [4]. Further, due to the low ductility of magnesium alloys, riveting may induce cracks in the material [1].

Attempts to joining alloys of dissimilar materials using conventional welding techniques were not very successful [5]. This is mainly due to the difference in the mechanical, physical, and chemical properties between the two alloy families [1]. Using conventional fusion welding techniques leads to the formation of a thick layer of intermetallic compounds between the two joined materials. This layer is usually brittle, thus leading to considerable weakness in the weld [2, 5].

However, friction stir welding (FSW) has proven to be very efficient in joining dissimilar metals [4, 6]. FSW is a modern environment-friendly solid-state welding technique [7]. It was invented and validated by W. Thomas and his colleagues at The Welding Institute (TWI) in the UK in 1991 [8, 9]. FSW is performed at a temperature below the melting points of the joined metals [10, 11] and does not involve bulk material melting, thus exposing the joined metals to less heat. This improves the mechanical microstructure and properties of the weld and provides several advantages over other welding techniques [12, 13]. FSW has made a large impact on the welding community for the past three decades and has attracted the attention of many people in research and industry. It is heavily used in many applications including automotive, marine, railway, and aerospace industries [14]. Some advantages of FSW over other conventional welding techniques are summarized in Table 1.1 [7, 15]. FSW has found its way into high production since 1996, however, this does not eliminate some of the disadvantages of the process. Disadvantages include leaving a hole behind when the tool is withdrawn, requiring a large downforce, and being less flexible than manual and arc welding processes [16].

FSW is performed using a non-consumable cylindrical tool including a pin and a shoulder. In the case of a butt weld, the rotating tool's pin is plunged into the adjacent edges of the sheets/plates to be joined (or into the surface of the top plate in the case of a lap joint) and then traversed along the line of the joint (Figure 1.1). The pin is slightly shorter than the required weld depth, and the shoulder is pushed down on the plates' surfaces causing a high frictional force while rotating. In this way, the tool provides the heating to the workpiece, and at the same time, ensures the flow of the material to produce the joint.

Table 1.1. Advantages of friction stir welding over conventional welding techniques [7, 15].

Advantages of friction stir welding	
Metallurgical advantages	<ul style="list-style-type: none"> • Good steadiness in dimensions; • Potential for being repeatable; • No need for filling materials; • Exceptional mechanical properties in the weld region; • Avoiding some welding imperfections as porosity and solidification cracking.
Environmental advantages	<ul style="list-style-type: none"> • No grinding wastes; • No harmful emissions; • Minimum need for surface cleaning.

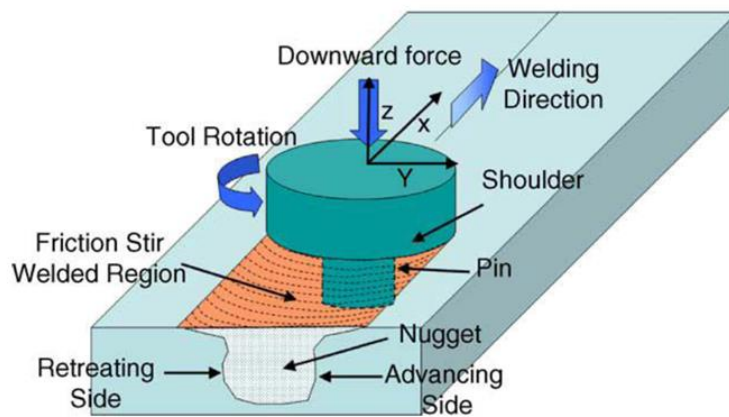


Figure 1.1. A Schematic of the friction stir welding process [17].

Defects, that FSW is susceptible to, differ from those of fusion welding. Different factors, including welding parameters, tool geometry, working piece temperature, and thermal conductivities of the involved metals, may all affect the quality of the weld. The wrong selection of process parameters may cause one or more

types of defects such as wormhole, scalloping, ribbon flash, surface lack of fill, nugget collapse, and surface galling [18]. Figure 1.2 shows surface and cross-sectional images of different friction stir welds showing examples of the aforementioned defects.

Welding parameters include the tool's rotational and feed speeds, its tilt angle, its pin's insertion depth into the workpiece [17], and the shift in the tool's insertion location towards one of the sub-plates being joined together (in the case of a butt weld) [19].

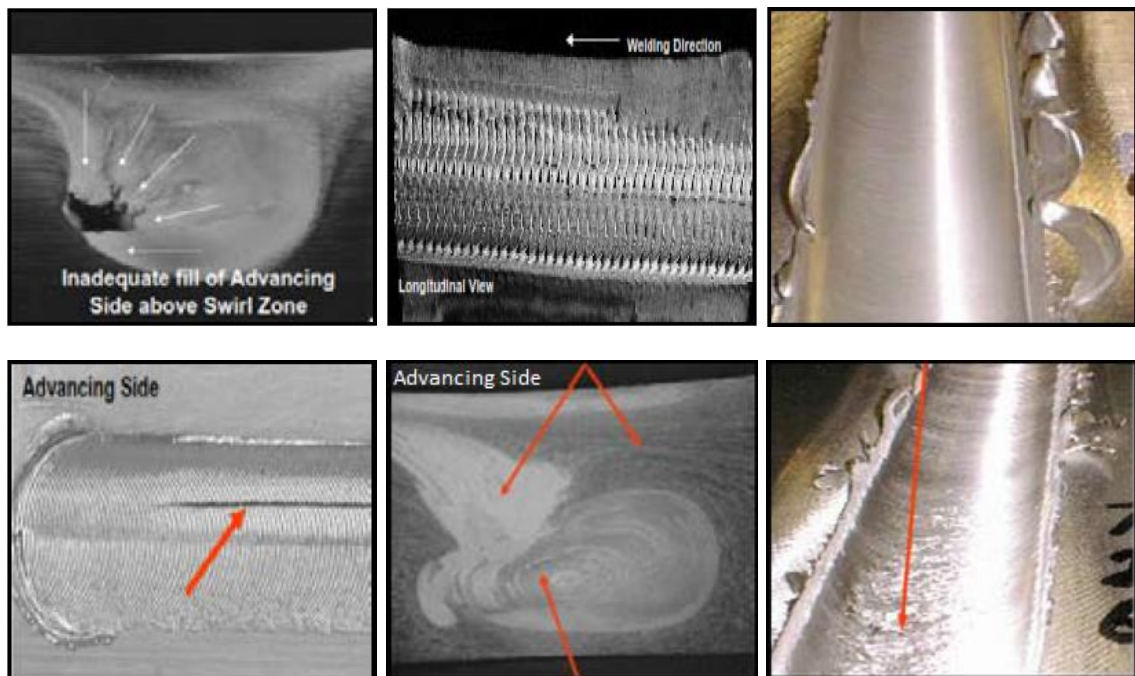


Figure 1.2. FSW defects, from the left to the right, top then bottom row: worm hole, scalloping, ribbon flash, surface lack of fill, nugget collapse, and surface galling [18].

Invisible or buried defects within welded regions, if remained undetected, may develop into bigger cracks, compromising the safety of the whole structure, and leading to catastrophic failures [20]. Several common nondestructive evaluation (NDE) methods are available for quality control of welds, including visual inspection, acoustic

emission, Eddy current, and traditional ultrasonics. As visual inspection cannot detect possible buried defects of FSW, the other techniques are capable of providing only local inspections. A wide range of ultrasonic NDE techniques has been developed in the last few decades [21, 22], and they have proven to provide precise and reliable results, ranging from local and simple contact A-, B-, and C-scan techniques to global and non-contact air-coupled and laser ultrasound [23, 24]. Local techniques can be very time-consuming and labor-intensive, and may not even be feasible in the case of complicated structures. Consequently, a more effective solution is needed for the condition assessment of structures containing FSW joints to improve their integrity and extend their life span.

1.2 Structural Health Monitoring of Friction Stir Welding

Structural health monitoring (SHM) is the act of monitoring a structure periodically or continuously for assessing its technical condition. It aims for the early detection of any damage that may appear in the structure to prevent sudden failure. SHM of critical structures, such as aerospace vehicles, is of high importance to provide continuous evaluation and ensure their integrity. This topic has attracted the attention of many researchers for more than three decades, where the use of ultrasonic guided waves (GWs) has emerged as a promising solution, for both composite and metallic structures [12, 25, 26].

GWs are capable of propagating for long distances in simple and complex curvatures [27-29]. In particular, Lamb waves (LWs) are GWs that propagate in plate-like structures. LWs can be employed to monitor large sections of structures using distributed transducer networks, without the need for tiresome local examinations [26].

This provides a time and cost-effective inspection solution when dealing with components that are difficult to disassemble for conventional NDE or in-situ inspection of inaccessible regions of the structures [26, 30]. The fundamental symmetric (S_0) and anti-symmetric (A_0) LW modes were proved to be highly sensitive to surface and internal cracking in plates [31-33]. They have been widely used to develop damage identification algorithms for assessing fatigue cracking [34, 35], delamination [36, 37], fiber breakage [38, 39], debonding [40, 41], cracks/notches [42-44], and corrosion [45]. As a result, LWs have been considered as an essential tool to be implemented in SHM systems towards continuous monitoring of structures.

Santos et al. [46] have investigated the ability of LWs to assess FSW in aluminum plates in comparison to x-ray and C-scan inspection methods. The authors have used a pitch-catch setup accompanied by mechanical scanning along the line of the weld, in an aqueous medium. They have found that the LW technique was more efficient than x-ray and C-scan, in the qualitative classification of FSW, in terms of simplicity, time, and expenses. The authors have noticed, however, that this technique still gives uncertain discrimination for very small weld flaws. Delrue et al. [47] have also used an immersion setup and a pitch-catch technique to capture the nonlinear features, that occur in the reflected signals, due to FSW kissing bond defects. The authors have used Fermat design transducers to focus and receive ultrasonic shear waves in aluminum welded plates. The signals were then analyzed by means of pulse inversion, and the results were numerically and experimentally validated. In another work [48], and employing an immersion setup as well, the same authors have used an angle-beam technique for ultrasonic inspection of FSW aluminum butt-joints. After scanning the whole weld in the cross-sectional and longitudinal directions, the authors

could detect and qualitatively identify the kind and severity of root flaws by looking at the backscattered energy from the bottom of the weld.

LWs' potential for assessing defects in FSW has been examined by Fakhri et al. [12, 33, 49]. The assessment of flaws in similar AZ31B FSW magnesium plates was scrutinized both experimentally and numerically [12, 49]. LWs were excited and received using Lead Zirconate Titanate (PZT) transducers placed on both sides of the weld line. After separating the S_0 mode from the complex signals, it was successfully employed to classify wormholes of various severities using an attenuation-based damage index. In [33], LWs were excited using PZT wafers and received using a scanning laser Doppler vibrometer (LDV). The frequency-wavenumber filtering technique was implemented to separate the wave reflected from the welded joint. The reflection of the A_0 mode from the material interface in an intact dissimilar AA6061-T6/AZ31B FSW was found to be minimal, while this reflection has become significant in the presence of a wormhole within the welded joint.

The objectives of this dissertation and chapter summaries are presented in Section 1.3.

1.3 Thesis Overview

1.3.1 Research Objectives

This work explores key aspects of Lamb-wave propagation behavior in dissimilar friction-stir-welded joints and their interaction with material discontinuity, damage, and intermetallic compounds within the welded region. Such understanding, along with the proof of LWs' potential for the precise assessment of macro-sized damage and micro-scale intermetallic layers, ultimately aims to the development of a

reliable framework for the condition assessment of structures including dissimilar FSW joints.

The main research objectives are to:

1. Understand the interaction of the fundamental LW modes with material discontinuity defined by the change in the material of the propagation medium, namely in an AA6061-T6/AZ31B dissimilar welded plate.

i. Theoretically explore the available GW modes and their propagation directions based on the governing propagation phenomena (transmission, reflection, and mode conversion), at different incidence angles between the excited LW and the joint.

ii. Analytically calculate the transmission and reflection coefficients of the fundamental symmetric GW modes using plane-wave approximation.

iii. Develop and/or employ signal processing techniques to extract the fundamental wave modes and separate reflection and transmission wavefields from numerical and experimental three-dimensional (3D) measurements.

iv. Determine the transmission and reflection coefficients of the propagating wave modes, at different incidence angles, across the material discontinuity (numerically and experimentally).

v. Compare analytical and numerical results with experiments for validation.

vi. Analyze the obtained results and recommend efficient practices for LW data analysis and sensor placement on structures including dissimilar-material joints.

2. Develop a novel and robust Bayesian-based damage identification framework using LWs, with application on wormhole defects in dissimilar FSW joints.

i. Achieve the three damage identification objectives (detection, localization, and assessment) using a minimal sensing configuration.

ii. Develop a surrogate model for the prediction of LW propagation using artificial intelligence (AI) techniques, trained using data from finite element (FE) simulations.

iii. Use the surrogate model to perform probabilistic damage inference using an Approximate Bayesian Computation (ABC) algorithm, in particular, ABC by Subset Simulation (ABC-SubSim).

iv. Apply data fusion for damage inference using multiple sensor measurements.

v. Evaluate the performance of the proposed damage identification framework on a big enough testing dataset for validation and analysis.

3. Prove the capability of nonlinear LW feature(s) to assess micro-scaled brittle intermetallic layers formed in dissimilar-material joints.

i. Numerically simulate 2nd harmonic generation and the accumulation of the relative acoustic nonlinearity parameter (RANP) in the targeted material using a nonlinear-elastic material model.

ii. Examine the 2nd harmonic generation and the accumulation of RANP when the aforementioned material is welded to a different material.

iii. Introduce micro-scaled intermetallic layers within the welded region with a variable thickness and scrutinize the sensitivity of RANP to their existence.

iv. Analyze the potential of LWs for the detection and quantitative assessment of intermetallics in dissimilar FSW joints.

1.3.2 Chapter Summaries

This dissertation includes five chapters, where the rest of the text is organized as follows:

Chapter 2 focuses on understanding LW propagation through material discontinuity. A comprehensive analysis of the interaction of the fundamental LW modes (S_0 and A_0) with a dissimilar welded joint is performed. An intact AA6061-T6/AZ31B joint is considered, and a theoretical, numerical, and experimental investigation is presented. Mode conversion, transmission, and reflection are all quantified versus the angle of incidence of the excited LW. The study is conducted as the excited wave propagates from AA6061-T6 to AZ31B, and when the propagation direction is reversed. Different techniques are developed to identify the in-plane and out-of-plane modes from the 3D measurements and to separate wave-joint reflections and transmissions. Finally, analytical, numerical, and experimental results are compared and analyzed.

Chapter 3 proposes a novel approach for damage detection, localization, and assessment through Bayesian inference using LW surrogate models. More specifically, the proposed framework provides a full identification of damage, within a dissimilar-material joint, by inferring six parameters of damage extent and location, namely the

length, width, thickness, and x -, y -, and z -positions. Surrogate models that can predict LW propagation in presence of damage are developed based on Artificial Neural Networks (ANNs). Finite element simulations are performed to simulate the measured LWs and generate the data required to train the ANNs. Each ANN serves as a surrogate model that can predict the signal at a certain measurement point, with reduced computational cost, given the damage size and position. Probabilistic inference of damage is further performed using the surrogate models, based on Approximate Bayesian Computation. Data are fused from multiple sensor measurements to provide a more reliable damage inference. High inference precision and low uncertainty are attained using only one PZT actuator and two sensors, thus providing a promising solution for condition evaluation and online monitoring applications.

In Chapter 4, the capability of LWs in the evaluation of micro-scaled intermetallic compounds (IMCs) is demonstrated. The appearance of brittle intermetallics in the microstructure of dissimilar welds is correlated to their weakness. A dissimilar FSW lap joint, between AA5052-H32 aluminum and ASTM 516-70 steel, is numerically modeled using nonlinear-elastic material properties, and IMC layers of various thicknesses are introduced. A proper excitation frequency is chosen based on the synchronism and zero-flux conditions between the symmetric S_1 and S_2 LW modes. Symmetric LWs are selectively excited in the aluminum plate, and measurements from several sensing positions are analyzed in the time, frequency, and time-frequency domains. The relative acoustic nonlinearity parameter is determined at multiple sensing locations and for different IMC conditions. A linear relation between RANP and the thickness of the IMC layer is observed. Variations in the order of two micrometers are

clearly detected and distinguished, proving the potential of nonlinear LW features for strength inspection of dissimilar FSW joints.

The closing chapter, Chapter 5, concludes the dissertation with a final summary and recommendations for future work.

CHAPTER 2

THE INTERACTION OF THE FUNDAMENTAL LAMB-WAVE MODES WITH MATERIAL DISCONTINUITY

2.1 Introduction

The increasing availability of structures containing dissimilar joints between different metallic alloys necessitates finding effective technological solutions to guarantee their structural integrity. However, the interaction of GWs with a material discontinuity is not yet well understood.

Previous work by Fakih et al. [50, 51] aimed at understanding LWs' propagation through similar and dissimilar welds. Results have indicated that the wave behavior is only affected by the change in elastic properties between the two joined metals, irrespective of the thermo-mechanical changes. Different similar and dissimilar intact FSW plates were used for the study, namely AA7020-T651/AA7020-T651, AA6060/AA7020-T651, and AA6061-T6/AZ31B welded plates. LWs were actuated and received in the normal incidence direction (perpendicular to the weld interface). No reflections were noticed in both the similar and dissimilar aluminum/aluminum welded plates, while clear reflections were observed in the case of the aluminum/magnesium (AA6061-T6/AZ31B) welded plate. At 200 *kHz*, the average reflection was calculated to be around 27% of the incident wave, when the wave propagated from AA6061-T6 to AZ31B, and about 35% for the opposite propagation direction. The results were correlated with the measurements obtained from a nano-indentation experiment, where a sharp change in the elastic properties of the base metals was detected in the AA6061-T6/AZ31B welded joint, unlike the other two plates that showed constant elastic properties across the weld zones.

The assessment of FSW joints using LWs requires a thorough understanding of the interaction of the wave modes with the material discontinuity at different incidence directions. This includes reflection, scattering, refraction, and mode conversion. As an example, the amplitude of a transmitted LW through features, such as welds, stiffeners, and bends, can be used to indicate its sensitivity to defects beyond or within those features [52]. This clear understanding would allow the integration of LW-based techniques in SHM systems and sensor-network designs in structures containing combinations of dissimilar materials.

Intensive work has been done over the years to understand the propagation behavior of bulk waves [53-59]. Analytical solutions providing the reflection and transmission coefficients of bulk waves, at normal and oblique incidence and between different types of materials, can be readily found in textbooks [30, 60]. The problem becomes more complex when dealing with GWs due to the need for numerical methods for solving the governing equations [52]. Gregory and Gladwell [61] have developed an analytical solution to determine the reflection of a normally-incident symmetric Rayleigh-Lamb wave from a fixed or free edge of a semi-infinite plate. The energy distribution between the various reflected wave modes was then numerically determined, for a fixed Poisson ratio, and was analyzed for a range of wavenumbers. Scandrett and Vasudevan [62] have addressed an in-depth theoretical study on the propagation behavior of normally-incident Rayleigh-Lamb waves in perfectly bonded dissimilar materials. Using a similar approach as in [61], the authors have presented and analyzed the energy distributions of the reflected and transmitted wave modes over a range of excitation frequencies. Symmetric and anti-symmetric incident fields were studied for different material combinations.

Unlike normal incidence problems, Lamb waves and shear-horizontal waves cannot be separately analyzed in oblique incidence problems due to the existence of mode conversions between them [63]. Gunawan and Hirose [63] analyzed the edge-reflection problem of obliquely-incident GWs in a plate using the mode decomposition semi-analytical method. Reflection coefficients of different wave modes were plotted against non-dimensional frequency for various cases of symmetric and anti-symmetric incident Lamb modes. Experimental validation was performed on a steel plate with different incidence angles showing very good agreement with the numerical results. Wilcox et al. [52] have used a semi-analytical finite element (SAFE) method to model the scattering of obliquely-incident GWs from an infinitely-long feature in a waveguide. Transmission and reflection coefficients were calculated for different incidence angles and frequencies. The authors compared their simulation solutions to the experimental data for an adhesively-bonded stiffener. Santhanam and Demirli [64] have also addressed the reflection of obliquely-incident LWs from the free edge of a plate. Symmetric and anti-symmetric LW incident modes were considered, and the problem was analyzed by orthogonal mode decomposition and by enforcement of traction-free boundary conditions using the collocation method. Energy-based reflection coefficients were determined for different frequency-thickness values. A qualitative experimental validation was performed using PZT transducers, while the authors have commented that only order-of-magnitude estimates of the energy coefficients can be determined using such transducers.

On the other hand, several researchers have tackled the problem of LW scattering and mode conversion from damage and geometric discontinuities. Shen and Giurgiutiu [65] have developed an analytical predictive tool for GW propagation and

damage interaction. A framework for an exact two-dimensional (2D) LW solution in the frequency domain was proposed. Wave-damage interaction coefficients (WDICs), determined from a local FE model with non-reflective boundaries, are used to describe scattering and mode conversion from the existing damage. Those WDICs are then coupled with the analytical solution to solve for the total wavefield at the needed sensor location. The solution is finally transformed back into the time domain to provide the predicted sensor measurement. Limiting the needed FE calculations to the local region of the damage bypasses the computational and time demands of a full FE model, for large-scale problems, while still benefitting from FE capabilities for modeling complex damage geometries. Poddar and Giurgiutiu [66] suggested a new analytical method to compute the scattering of straight-crested LWs from geometric discontinuities, which they called complex modes expansion with vector projection (CMEP). The authors applied CMEP to the problem of a step-like change in the plate's thickness. They verified their results by comparison to the axial-flexural model at low frequencies and to 2D FE analysis at higher frequencies. CMEP achieved a perfect agreement with FE results up to 1.5 MHz.mm with 200-times less computational time. Finally, the authors have suggested techniques for the application of CMEP to damages such as notches, cracks, and delamination. As a continuation of the work, Haider et al. [67] used CMEP in a global-local analytical method to analyze the scattering of A_0 incident waves from an intact and a damaged stiffener within the plate. By comparing the resultant waveforms between the two cases, the crack within the stiffener could be detected. Experiments with selective excitation of straight-crested anti-symmetric LWs were conducted for validation, and good agreement in results was attained.

A lot of work, available in the literature, tackles the scattering and interaction of LWs with geometric or structural discontinuity, but there exists very little work tackling their interaction with dissimilar welds.

This chapter presents an in-depth analysis of the behavior of the S_0 and A_0 LWs, upon the normal and oblique interaction with a dissimilar solid joint. An intact AA6061-T6/AZ31B joint is considered, and different wave-joint interactions are investigated numerically and experimentally. Transmission, reflection, and mode conversion are determined for different incidence angles at which the excited LW interacts with the dissimilar-material joint. The results of the in-plane symmetric modes are also compared to PWA analytical solution.

Section 2.2 introduces a general theoretical background about the problem. Identification of the involved GW modes, namely S_0 , A_0 , and SH_0 modes, based on their oscillation directions and group velocities is explained. Wave-joint interactions including mode conversion, reflection and transmission directions, and critical-angle calculations are investigated. An analytical solution of the in-plane modes based on plane-wave approximation is introduced. Section 2.3 describes the FE model and measurement details. Section 2.4 describes the samples used for experimental validation, the experimental setup, and data acquisition. Section 2.5 presents the results and discussion. Finally, concluding remarks are presented in Section 2.6.

2.2 Theoretical Background and Analytical Approximation

2.2.1 Fundamentals of Lamb Waves

Lamb waves are elastic waves guided by the free top and bottom surfaces of thin plates [26]. They were discovered by Horace Lamb and published in one of his

publications in 1917 [68]. In thin plates, the in-plane dimensions are much larger than the thickness and the wavelength is in the order of the thickness, which provides upper and lower boundaries to guide continuous propagation of the waves [30]. The general description of LWs in a homogeneous plate is given as follows [30]:

$$\frac{\tan(qh)}{\tan(ph)} = \frac{4k^2qp\mu}{(\lambda k^2 + \lambda p^2 + 2\mu p^2)(k^2 - q^2)} \quad (2.1)$$

$$q^2 = \frac{\omega^2}{c_T^2} - k^2$$

$$p^2 = \frac{\omega^2}{c_L^2} - k^2$$

$$\omega = 2\pi f$$

where:

- h : is half the plate's thickness = $d/2$;
- k : is the wavenumber;
- λ and μ : are the material's Lamé elastic constants;
- ω : is the angular frequency;
- c_T : is the shear bulk-wave velocity;
- c_L : is the longitudinal bulk-wave velocity;
- f : is the frequency.

After simplification, equation (2.1) can be split into two parts with solely symmetric and anti-symmetric properties, implying that LWs in a plate consist of symmetric and anti-symmetric modes [30]:

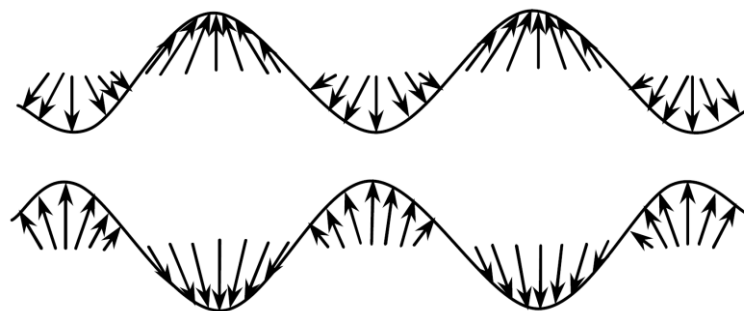
$$\frac{\tan(qh)}{\tan(ph)} = -\frac{4k^2qp}{(k^2 - q^2)^2} \quad (2.2)$$

for symmetric modes, and

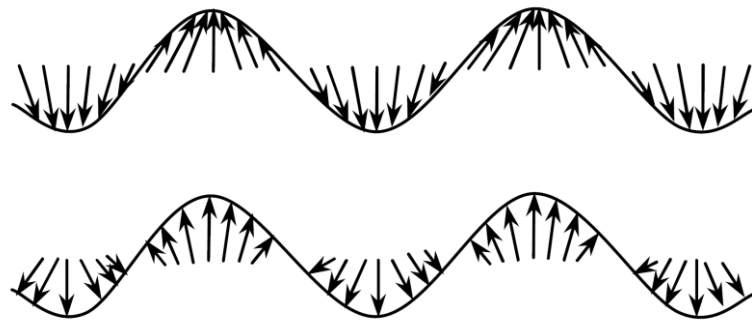
$$\frac{\tan(qh)}{\tan(ph)} = -\frac{(k^2 - q^2)^2}{4k^2qp} \quad (2.3)$$

for anti-symmetric modes.

Equations (2.2) and (2.3) are known as the Rayleigh-Lamb equations and can be used to compute the velocity/velocities at which a wave of a certain frequency ($f \cdot h$ or $f \cdot d$ product) propagates within the plate. Such equations are known as dispersion relations and can only be solved using numerical methods [30]. S_j and A_j ($j = 0, 1, 2, \dots$) are used to denote the symmetric and anti-symmetric Lamb modes, respectively. The schematics of particle motions in the symmetric and anti-symmetric LW modes are plotted in Figure 2.1 (exaggerated thickness cross-section). A symmetric wave mode is usually known as “compressional”, presenting a bulging and contracting thickness, and an anti-symmetric wave mode is described as “flexural”, showing a flexing but constant thickness, with more complex through-thickness displacements for higher-order anti-symmetric modes. For the same excitation condition, the magnitude of the symmetric modes is usually smaller than that of the anti-symmetric modes [26].



(a) Symmetric modes



(b) Anti-symmetric modes

Figure 2.1. Particle motions for the symmetric and anti-symmetric LW modes [26].

2.2.2 Wave Modes Identification

The fundamental LW modes are distinguished by their predominant longitudinal and shear-vertical vibrations of particles. A longitudinal wave oscillates the plate particles back and forth in the direction of wave propagation, while a shear-vertical wave oscillates the particles vertically (normal to the plate surface) and perpendicular to the direction of wave propagation. Based on its predominant in-plane longitudinal particle displacement, the fundamental symmetric mode (S_0) can be referred to as the fundamental longitudinal LW mode. Similarly, the fundamental anti-symmetric mode (A_0) can be referred to as the fundamental shear-vertical LW mode. On the other hand, the fundamental shear-horizontal mode (SH_0) is a guided-wave mode that also propagates in thin plates, with the particles purely vibrating in the horizontal plane (parallel to the plate's surface) and perpendicular to the wave propagation direction. While in-depth analyses of guided-wave modes' displacements and shapes can be found in comprehensive textbooks [26, 30, 69], Figure 2.2 illustrates the predominant vibration directions of the S_0 , A_0 , and SH_0 modes with respect to their propagation direction. In addition to their particle-oscillation directions, different

guided-wave modes can be also identified in the measured wavefields based on their group velocities (c_g).

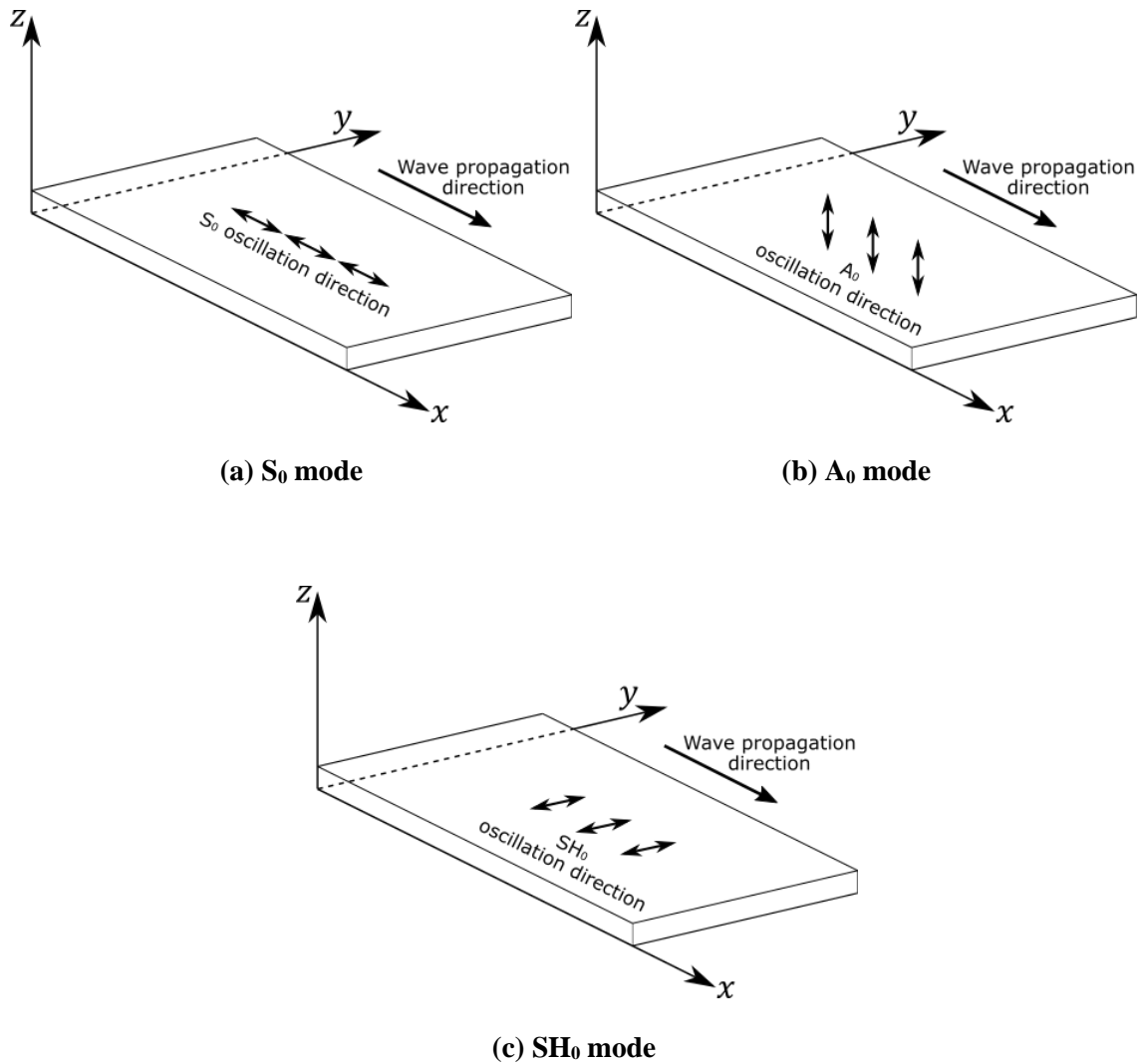


Figure 2.2. Illustrations of the predominant oscillation directions of the fundamental guided-wave modes.

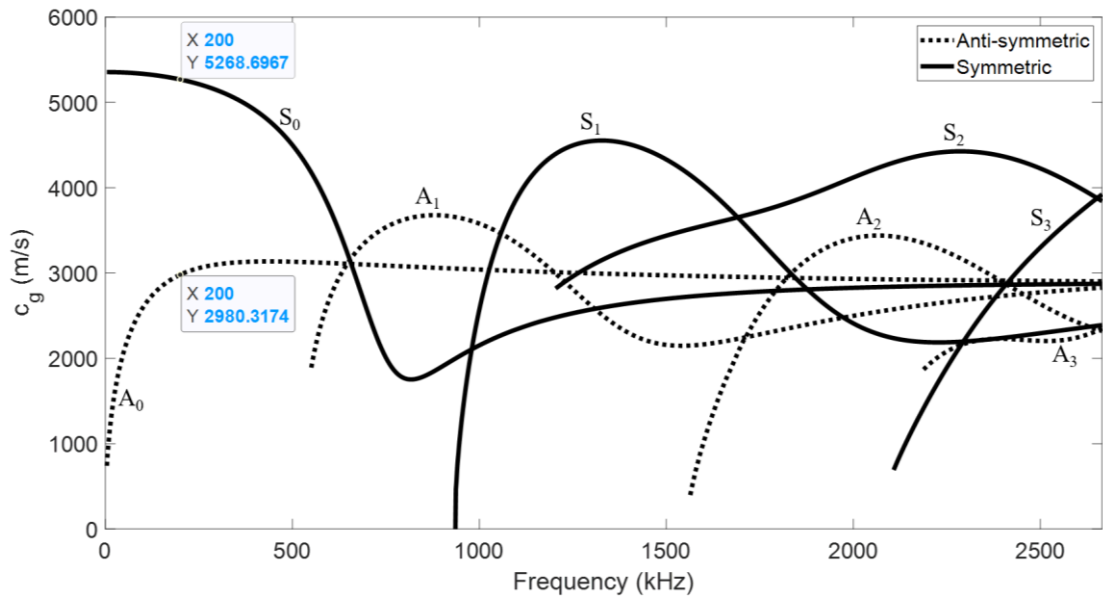
Considering two aluminum-alloy (AA6061-T6) and magnesium-alloy (AZ31B) plates of 3-*mm* thickness joined together, the theoretical group and phase-velocity dispersion curves of the propagating LW modes (mainly A_0 and S_0) were determined

using *Wavescope* [70]. Since SH_0 is a non-dispersive mode and based on its theoretical formulation [71], both the group and phase velocities of the SH_0 mode were found to be equal to the shear bulk-wave velocity (c_T). The material properties of the joined materials are summarized in Table 2.1 [72]. The velocities should be determined for each of the joined materials separately, as the wave modes will be expected to propagate at their corresponding group velocities in each of the materials either before or after interaction with the joint.

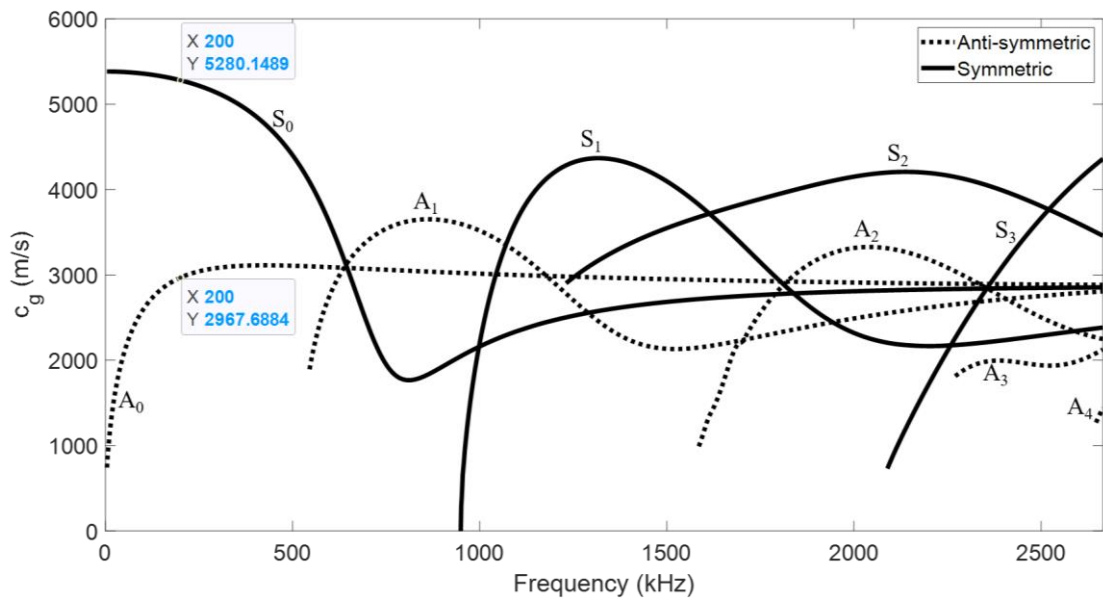
The obtained group-velocity dispersion curves of the LW modes are shown in Figure 2.3. A typical central frequency of 200 *kHz* was chosen for LW excitation. The frequency was chosen so that only the fundamental modes (A_0 and S_0) are excited in the plate. Table 2.2 shows the theoretical group velocities of the modes of interest at 200 *kHz*. The group velocities of the A_0 and S_0 modes are very different, which assures well-separated modes after propagating for some distance. The phase velocities of the fundamental modes at 200 *kHz* are listed in Table 2.3.

Table 2.1. Physical and mechanical properties of the used materials.

Material	Density (D) in kg/m^3	Young's modulus (E) in GPa	Poisson's ratio (ν)
AA6061-T6	2700	69	0.33
AZ31B	1770	45	0.35



(a)



(b)

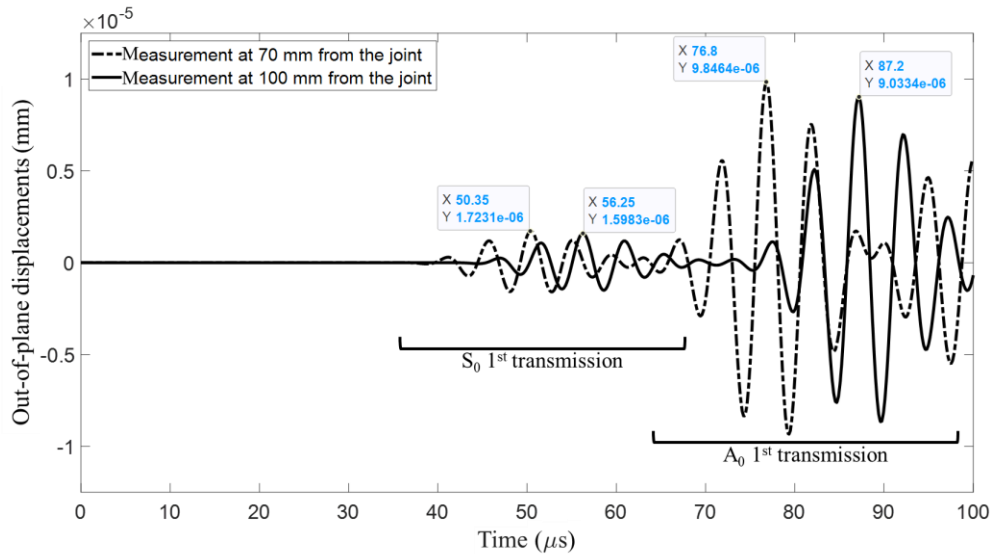
Figure 2.3. Group-velocity dispersion curves for a plate of 3-mm thickness: (a) AA6061-T6 and (b) AZ31B.

Table 2.2. Theoretical group velocities of the existing guided-wave modes at 200 kHz.

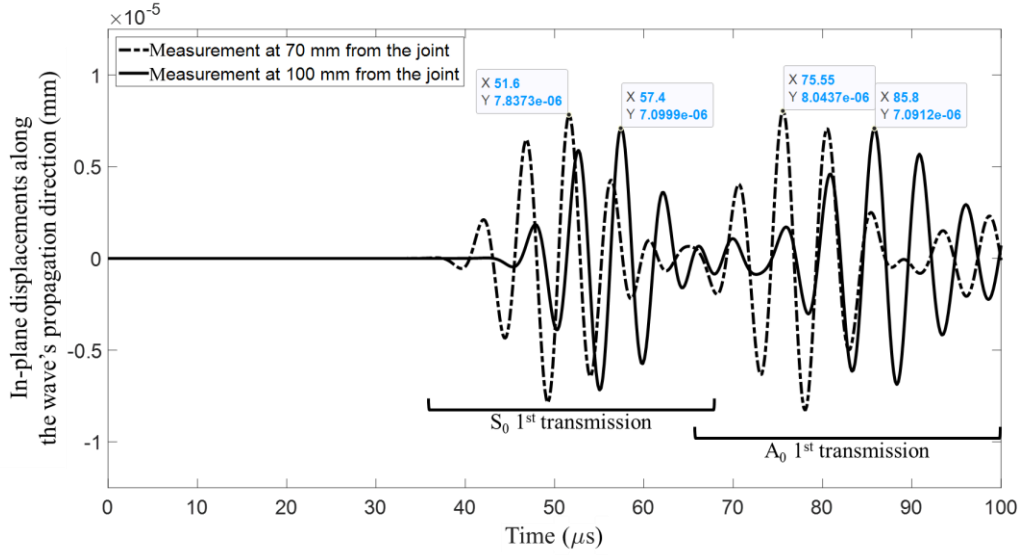
Wave mode	c_g (m/s) in AA6061-T6	c_g (m/s) in AZ31B
S_0	5268.7	5280.15
A_0	2980.32	2967.69
SH_0	3099.6	3068.6

Figure 2.4 shows examples of simulated measurements for a 200-kHz guided wave propagating in the plate (details of the FE simulations are explained in Section 2.3). The wave was excited using a PZT wafer placed on the AA6061-T6 sub-plate. The wave propagated through the intact dissimilar joint and then was captured in the AZ31B sub-plate (check Figure 2.11 for the detailed FE model). Two measurements, taken at two different sensing positions, are shown in Figure 2.4. The distance between the two sensing positions is 30 mm, which was used for group-velocity calculations. As the propagating modes have the same shape as the five-cycle Hann-windowed sinusoidal excitation signal, the first two wave packets in the signals were identified as the first transmission of the S_0 and A_0 LW modes, respectively. The group velocities of these two modes were calculated using the time-of-arrival of the wave packets, based on the highest peaks (marked in Figure 2.4). The calculated velocities of the S_0 and A_0 modes in the out-of-plane displacements (Figure 2.4(a)) were 5084.75 m/s and 2884.62 m/s, respectively, and in the in-plane displacements (Figure 2.4(b)) were 5172.41 m/s and 2926.83 m/s, respectively. The results are in good agreement with the theoretical velocities listed in Table 2.2 (the values are compared to velocities in AZ31B since the two sensing positions lie within the AZ31B sub-plate).

Although A_0 is the predominant mode in the out-of-plane displacements, the S_0 mode can still be captured, as shown in Figure 2.4(a), due to bending and mode-shape effects. However, this wave mode is more pronounced in the in-plane measurement (Figure 2.4(b)), which is the predominant oscillation direction of the S_0 mode. Similarly, the A_0 mode is more pronounced in the out-of-plane measurement (Figure 2.4(a)) than it is in the in-plane measurement (Figure 2.4(b)).



(a) Out-of-plane displacements



(b) In-plane displacements along the wave's propagation direction

Figure 2.4. Simulated signals at two different sensing positions to illustrate mode identification.

2.2.3 Wave-Joint Interactions

Assuming a perfect joint between dissimilar material, ideal transmissions and reflections are expected with no scattering. Upon interaction with the material interface, the energy of the incident modes is distributed among the reflected and transmitted (or so-called refracted) wave modes. Mode conversion is also expected to occur upon the wave interaction with the interface (i.e., the welded joint), thus producing additional modes in the reflected and transmitted portions of the incident wave [30]. The relation between the angles of the incident modes and their corresponding reflected or transmitted modes is defined by Snell's law [60] (traction-free boundary condition at the material interface):

$$k_1 \sin(\theta_1) = k_2 \sin(\theta_2) \quad (\text{Snell's law})$$

$$\Leftrightarrow \frac{\omega}{c_{p1}} \sin(\theta_1) = \frac{\omega}{c_{p2}} \sin(\theta_2)$$

$$\begin{aligned} \Rightarrow \sin(\theta_2) &= \frac{c_{p2}}{c_{p1}} \sin(\theta_1) \\ \Rightarrow \frac{c_{p1}}{\sin(\theta_1)} &= \frac{c_{p2}}{\sin(\theta_2)} \end{aligned} \quad (2.4)$$

where:

- k_1 and k_2 : are the wavenumbers of the incident and reflected/transmitted modes, respectively;
- θ_1 and θ_2 : are, respectively, the acute angles between the incident or reflected/transmitted modes' propagation direction and the normal to the material interface;
- c_{p1} and c_{p2} : are the phase velocities of the incident and reflected/transmitted modes, respectively.

To differentiate between different angles that will be used throughout the chapter, incidence angles will be defined as \hat{i} instead of θ_1 , while reflection and transmission angles will be respectively named \hat{r} and \hat{t} instead of θ_2 .

2.2.3.1 Mode Conversion

In the case of oblique incidence, incident wave modes may convert into other wave modes, at the level of the joint, while being transmitted to the other material or reflected into the same material. Figure 2.5 illustrates the concept of the mode conversion phenomenon in the case of an obliquely-incident longitudinal wave, presuming no reflection occurs. The in-plane longitudinal incident wave is expressed as a force acting at the interface between the two materials at an angle equal to the angle of incidence θ_{1L} . The incident force causes a complex wave propagation in the structure. This complex wave propagation can be considered as a superposition of two

propagating waves [30], a longitudinal wave, that is associated with the force along the transmission direction of the longitudinal mode (θ_{2L} upon deviation according to Snell's law), and an in-plane shear wave, which is associated with the shear force perpendicular to the transmission direction of the shear-horizontal mode (θ_{2S}). The summation of the three forces should satisfy the force-equilibrium condition at the interface. A complete breakdown of the problem would also consider two other forces associated with the reflected longitudinal and in-plane shear modes. In such a case, both longitudinal and shear waves may be generated in both solid materials. The superposition of the side lobes of those waves may produce an interface wave, which propagates along the material interface [30].

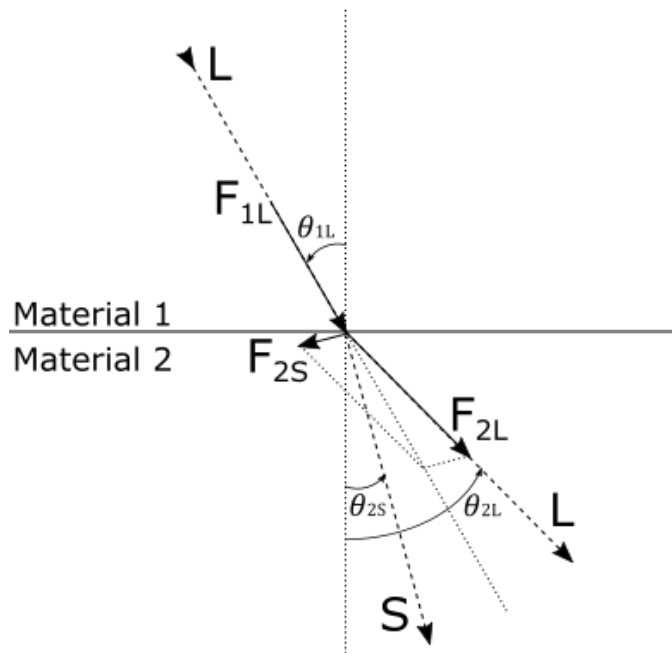


Figure 2.5. Mode conversion at the interface assuming no reflection; L: longitudinal wave and S: shear wave.

Based on the above discussions, a portion of the incident S_0 wave mode will be converted into the symmetric SH_0 mode when obliquely interacting with the joint [71].

SH₀ mode would also be generated upon the interaction of the S₀ mode with the plate's boundaries. This study will focus on the interaction of incident LW modes with dissimilar-material joints; thus, the studied SH₀ mode will be only the mode converted from the incident S₀ wave mode upon its interaction with the joint. This mode will be referred to as S₀-SH₀ mode in the rest of the chapter.

On the other hand, since the predominant displacement of the A₀ mode is parallel to the material interface (at both normal and oblique incidence), no other displacement component would be generated upon its interaction with the weld. Thus, the A₀ mode should not undergo any mode conversion under the assumption of a perfect joint.

2.2.3.2 Critical Angles

The critical angle (θ_c) of a wave mode is defined as the largest incidence angle which still results in the refraction of this mode. Beyond this angle ($\theta_1 > \theta_c$), the mode would undergo total internal reflection after interacting with the interface [30]. If the wave mode is excited at its critical incidence angle ($\theta_1 = \theta_c$), it would refract along the material interface, i.e., with an angle of refraction $\theta_2 = 90^\circ$. Thus, the critical angle of each mode can be calculated using Snell's law by replacing θ_2 by 90° :

$$\frac{c_{p1}}{\sin(\theta_c)} = \frac{c_{p2}}{\sin(90^\circ)}$$

$$\Rightarrow \theta_c = \arcsin \left[\frac{c_{p1}}{c_{p2}} \right] \quad \forall c_{p1} < c_{p2} \quad (2.5)$$

If the incident wave mode undergoes conversion at the interface, two critical angles may exist [30]. Figure 2.6(a) illustrates the general case of an in-plane longitudinal mode (L₁) incident at a solid-solid material interface. A portion of the

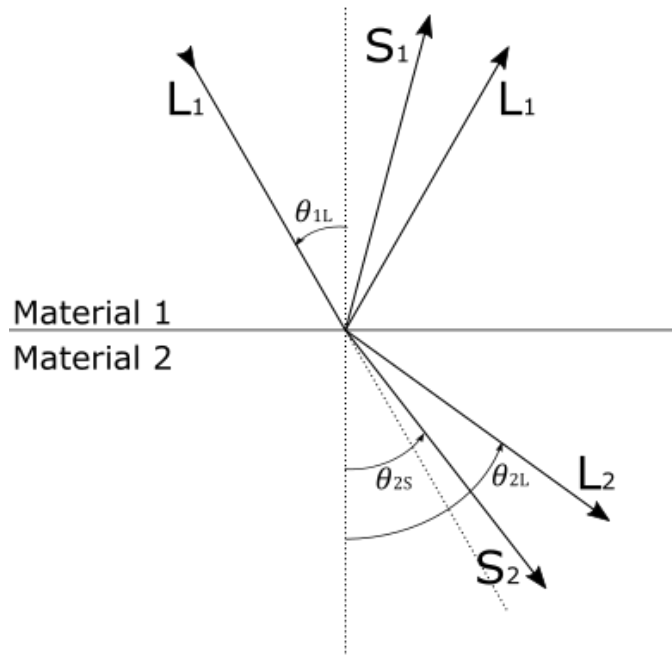
incident L_1 converts into an in-plane shear mode (S) after interacting with the interface. This yields two in-plane modes (L_1 and S_1) reflecting into Material 1, and two other in-plane modes (L_2 and S_2) transmitted into Material 2. Upon exciting at the first critical angle (θ_{cL}), L_2 will be refracted along the material interface (L_{int} in Figure 2.6(b)). Beyond θ_{cL} , the unconverted portion of the incident L_1 would undergo total internal reflection within Material 1, while S_2 keeps refracting into Material 2. If the incidence angle was increased up to the second critical angle (θ_{cS}), if exists, S_2 will be refracted along the material interface (S_{int} in Figure 2.6(c)), which means no wave will be transmitted into Material 2 anymore. Beyond θ_{cS} , the whole incident mode will undergo total internal reflection in Material 1.

In particular, because the incident S_0 mode within the current study may convert into the SH_0 mode, two critical angles may exist. The first critical angle is for the transmitted S_0 mode, while the second critical angle is for the transmitted S_0 - SH_0 mode. According to equation (2.5), the critical angle exists only if the phase velocity of the transmitted wave mode in Material 2 is greater than that of the incident mode in Material 1 (i.e., when propagating from a slower to a faster medium in terms of the phase velocities of the involved modes).

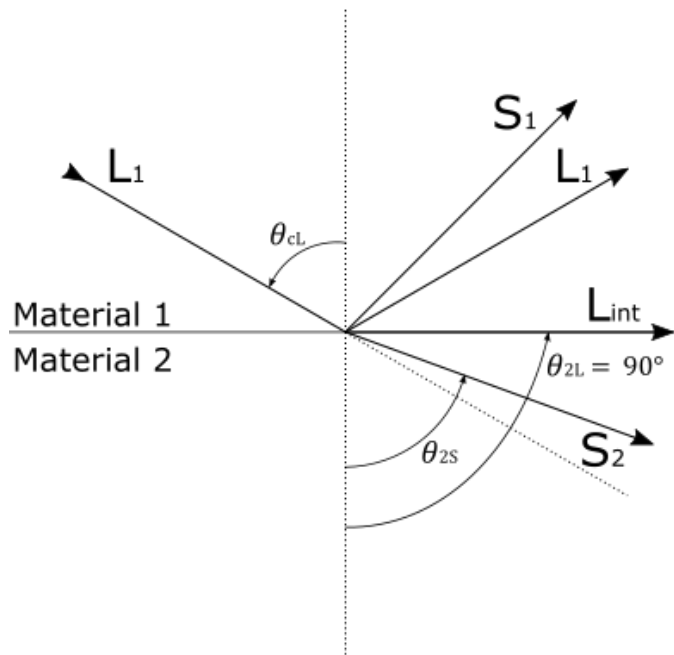
Table 2.3 summarizes the theoretical phase velocities and critical angles of the modes considered in this study. The second critical angle does not exist for the S_0 - SH_0 mode since the phase velocity of the incident mode (S_0) is always greater than that of the refracted mode (SH_0). Similarly, no critical angle exists for the S_0 mode when the wave propagates from AZ31B to AA6061-T6, as well as for the A_0 mode when the wave propagates from AA6061-T6 to AZ31B.

Table 2.3. Theoretical phase velocities and critical angles of the existing guided-wave modes at 200 kHz.

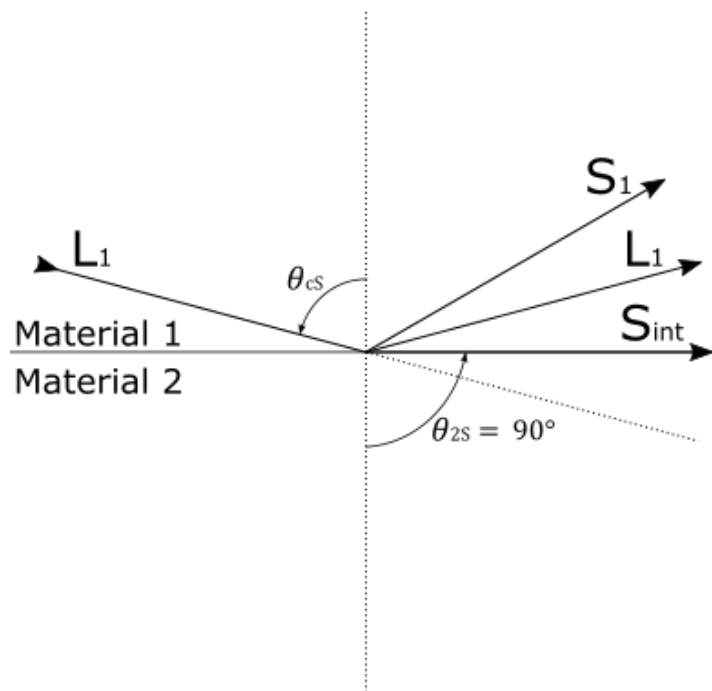
Wave mode	c_p (m/s) in AA6061-T6	c_p (m/s) in AZ31B	θ_c AA6061-T6 to AZ31B	θ_c AZ31B to AA6061-T6
S_0	5327.06	5349.19	84.79°	-
A_0	1990.08	1989.21	-	88.31°
S_0 - SH_0	$c_{p1(S_0)} = 5327.06$	$c_{p2(SH_0)} = 3068.6$	-	
	$c_{p2(SH_0)} = 3099.6$	$c_{p1(S_0)} = 5349.19$		-



(a) General case of a longitudinal wave incident at a solid-solid material interface



(b) 1st critical angle ($\theta_{1L} = \theta_{cL}$)



(c) 2nd critical angle ($\theta_{1L} = \theta_{cs}$)

Figure 2.6. General case of a longitudinal incident wave and illustrations of the 1st and 2nd critical angles for a solid-solid material interface; L: longitudinal wave and S: shear wave.

2.2.4 Plane-Wave Approximation of In-Plane Modes

According to Gunawan and Hirose [63], when $\omega h/c_T \rightarrow 0$, the S_0 mode behaves as the longitudinal bulk wave with a constant through-thickness value and a zero out-of-plane value. Under the same condition, the SH_0 mode is reduced to the shear bulk wave which is also constant through-thickness and null in the out-of-plane direction. In other words, when $\omega h/c_T \rightarrow 0$, the amplitudes of the fundamental symmetric modes (S_0 and SH_0 modes) can be determined under the assumption that the plate is in a 2D plane-stress state. This means that the transmission and reflection coefficients of the S_0 and SH_0 modes can be approximated by those of the longitudinal and shear bulk waves, respectively. The authors of [63] have studied the reflection of obliquely-incident guided waves from the free edge of a plate, where they have compared their semi-analytical results to the bulk-wave approximation results. This approximation was found to be accurate at a value of $\omega h/c_T = 1.96$.

Wilcox et al. [52] have also confirmed this concept justifying that the mode shapes of the symmetric S_0 and SH_0 modes are almost constant through the plate's thickness at low frequency \times thickness ($f \cdot d$) values, which makes their solutions analogous to longitudinal and transverse bulk waves. The authors have used this analogy as one of the validations of their SAFE approach. Similarly, they compared the results of their SAFE model, for the S_0 and S_0 - SH_0 reflections from the free edge of a 1- mm aluminum plate in the case of an incident S_0 mode, to explicit analytical solutions of bulk waves [73]. The comparison was conducted both at different incidence angles and using a constant incidence angle with a variable excitation frequency. Very good agreement of the results was attained up to a $f \cdot d$ value of 1.5 $MHz \cdot mm$. The authors have commented that such an agreement up to 1.5 $MHz \cdot mm$ cannot be attributed to the

plane-stress analogy because the mode shape of the S_0 mode, at such frequencies, contains significant out-of-plane stress. On the other hand, the disagreement of the results at $f \cdot d$ values lower than $0.2 \text{ MHz} \cdot \text{mm}$ was justified by the deterioration of a part of their model's performance (absorbing region) at low frequencies.

In the current work, and for ease of statement throughout the text, this analogy will be named as plane-wave approximation (PWA) since the S_0 and $S_0\text{-SH}_0$ modes are approximated as plane waves propagating in a certain direction with constant mode shapes through the plate's thickness. Based on the mentioned literature results [52, 63], PWA is expected to be valid for the used $f \cdot d$ value ($f \cdot d = 200 \text{ kHz} \times 3 \text{ mm} = 0.6 \text{ MHz} \cdot \text{mm}$) and for both examined materials ($\omega h/c_T \approx 0.61$ for both AA6061-T6 and AZ31B). It should be noted here that PWA can only be applied to the in-plane modes (assumed constant through-thickness, i.e., assumed in a 2D plane-stress condition) and cannot be applied to the case of an incident A_0 mode.

Joseph Rose, in his book "Ultrasonic Guided Waves in Solid Media" [30], provides a matrix formulation for the analytical calculation of transmission and reflection coefficients (vector $\{X\}$), of a harmonic plane wave incident at a perfect solid-solid interface, as follows:

$$[M]\{X\} = \{a\} \quad (2.6)$$

$$[M] = \begin{bmatrix} -\cos \hat{r}_L & \sin \hat{r}_S & -\cos \hat{t}_L & \sin \hat{t}_S \\ -\sin \hat{r}_L & -\cos \hat{r}_S & \sin \hat{t}_L & \cos \hat{t}_S \\ -k_{1L}(\lambda_1 + 2\mu_1) \cos 2\hat{r}_S & k_{1S}\mu_1 \sin 2\hat{r}_S & k_{2L}(\lambda_2 + 2\mu_2) \cos 2\hat{t}_S & -k_{2S}\mu_2 \sin 2\hat{t}_S \\ -k_{1L}\mu_1 \sin 2\hat{r}_L & -k_{1S}\mu_1 \cos 2\hat{r}_S & -k_{2L}\mu_2 \sin 2\hat{t}_L & -k_{2S}\mu_2 \cos 2\hat{t}_S \end{bmatrix}$$

$$\{X\} = \begin{bmatrix} R_L \\ R_S \\ T_L \\ T_S \end{bmatrix}, \quad \{a_L\} = \begin{bmatrix} -\cos \hat{r}_L \\ \sin \hat{r}_L \\ k_{1L}(\lambda_1 + 2\mu_1) \cos 2\hat{r}_S \\ -k_{1L}\mu_1 \sin 2\hat{r}_L \end{bmatrix}, \quad \text{and} \quad \{a_S\} = \begin{bmatrix} \sin \hat{r}_S \\ \cos \hat{r}_S \\ -k_{1S}\mu_1 \sin 2\hat{r}_S \\ -k_{1S}\mu_1 \cos 2\hat{r}_S \end{bmatrix}$$

where:

- 1 and 2: are the indices of Material 1 and Material 2, respectively;
- R and T : are the reflection and transmission (refraction) coefficients, respectively;
- L and S: are the indices for longitudinal and shear (transverse) waves, respectively;
- \hat{r} and \hat{t} : are the reflection and transmission (refraction) angles, respectively;
- $\{a_L\}$ or $\{a_S\}$: are used if the incident wave is a longitudinal wave or a shear (transverse) wave, respectively;
- c_L and c_S : are the velocities of the longitudinal and shear (transverse) waves, respectively.

The relations between the material elastic constants and the bulk-wave velocities are given as follows [30]:

$$Dc_L^2 = \lambda + 2\mu \quad \text{and} \quad Dc_S^2 = \mu \quad (2.7)$$

Thus, the terms containing these constants in (2.6) can be replaced as such:

$$\left\{ \begin{array}{l} k_L(\lambda + 2\mu) = \frac{\omega}{c_L} (Dc_L^2) = \omega Dc_L = 2\pi f Dc_L \\ k_S\mu = \frac{\omega}{c_S} (Dc_S^2) = \omega Dc_S = 2\pi f Dc_S \\ k_L\mu = \frac{\omega}{c_L} (Dc_S^2) = 2\pi f Dc_S^2/c_L \end{array} \right. \quad (2.8)$$

where:

- D : is the material's density.

For an incident longitudinal wave, the 1st equation in (2.6) is derived from the 1st boundary condition of particle displacements/velocities, at the interface, in the normal direction as follows [30]:

$$\begin{aligned}
& -A_L^{refl} \cos \hat{r}_L + A_S^{refl} \sin \hat{r}_S - A_L^{tr} \cos \hat{t}_L + A_S^{tr} \sin \hat{t}_S = -A_L^{inc} \cos \hat{r}_L \\
\Rightarrow & -\frac{A_L^{refl}}{A_L^{inc}} \cos \hat{r}_L + \frac{A_S^{refl}}{A_L^{inc}} \sin \hat{r}_S - \frac{A_L^{tr}}{A_L^{inc}} \cos \hat{t}_L + \frac{A_S^{tr}}{A_L^{inc}} \sin \hat{t}_S = -\cos \hat{r}_L \\
\Rightarrow & -R_L \cos \hat{r}_L + R_S \sin \hat{r}_S - T_L \cos \hat{t}_L + T_S \sin \hat{t}_S = -\cos \hat{r}_L \\
\Rightarrow & \frac{R_L \cos \hat{r}_L}{\cos \hat{r}_L} - \frac{R_S \sin \hat{r}_S}{\cos \hat{r}_L} + \frac{T_L \cos \hat{t}_L}{\cos \hat{r}_L} - \frac{T_S \sin \hat{t}_S}{\cos \hat{r}_L} = 1 \tag{2.9}
\end{aligned}$$

where:

- A_L^{refl} : is the amplitude of the reflected longitudinal wave;
- A_S^{refl} : is the amplitude of the reflected shear (transverse) wave;
- A_L^{tr} : is the amplitude of the transmitted (refracted) longitudinal wave;
- A_S^{tr} : is the amplitude of the transmitted (refracted) shear (transverse) wave;
- A_L^{inc} : is the amplitude of the incident longitudinal wave.

To apply these formulations for the case of the incident longitudinal S_0 mode, c_L will be replaced by the phase velocity of the S_0 mode ($c_{p(S_0)}$), and c_S will be replaced by the phase velocity of the converted S_0 - SH_0 mode ($c_{p(SH_0)}$).

Figure 2.7(a) shows the results for the S_0 incident wave propagating from AA6061-T6 to AZ31B, while Figure 2.7(b) shows the same results in the opposite propagation direction. The negative sign of the reflection coefficient indicates that the reflected mode is out-of-phase with respect to the incident mode (180°-phase

difference). The sum along the normal to the material interface is shown in the figures for verification; this sum should be equal to unity according to equation (2.9).

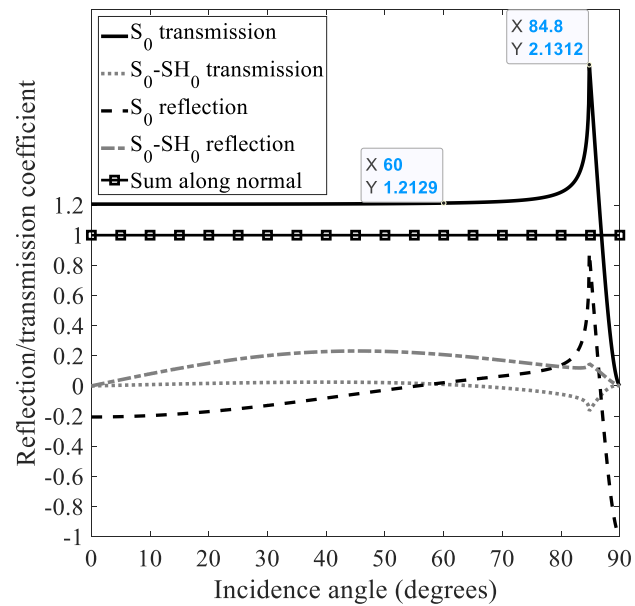
Figure 2.7 can be obtained using equation (2.6) by calculating X . Each row gives one of the transmission and reflection coefficients, knowing the material properties and the angles. The angles, in turn, can be calculated using Snell's law explained in equation (2.4).

The transmission coefficient of the S_0 mode stays almost constant from normal incidence ($\hat{i} = 0^\circ$) until reaching a steep angle (changes by less than 5% up to $\hat{i} = 78^\circ$). The constant value when the wave propagates from AA6061-T6 to AZ31B is about 1.2, while it is about 0.8 in the other propagation direction. Both S_0 transmission and mode conversion drop down to zero at $\hat{i} = 90^\circ$ (excitation along the interface), while the S_0 mode's reflection coefficient gives a value of -1. This indicates that the waves will not be transmitted into the second material in this case.

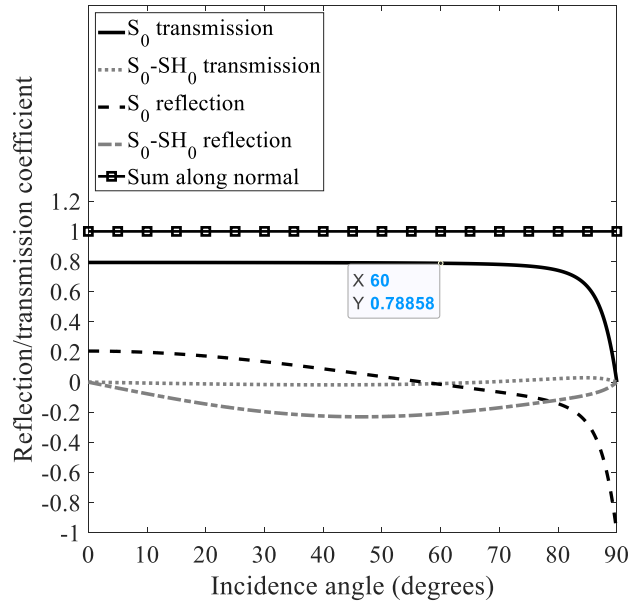
The abrupt changes in the reflection and transmission coefficients, in the AA6061-T6 to AZ31B propagation (Figure 2.7(a)), are because the incidence angle is close to the critical angle. The value of the critical angle in the figure is in good agreement with the value that was calculated in Section 2.2.3.2 (Table 2.3). The transmission coefficient of the S_0 mode sharply drops to zero after the critical angle since no S_0 mode will be refracted. Since the 2nd critical angle does not exist for the S_0 - SH_0 mode (Table 2.3), the total reflection of the incident wave does not occur. Smooth curves appear in Figure 2.7(b) since no critical angles exist when the S_0 mode propagates from AZ31B to AA6061-T6.

The highest S_0 - SH_0 mode conversion occurs around $\hat{i} \approx 45^\circ$ in both propagation directions. While the transmitted S_0 - SH_0 mode is extremely weak, its reflection reaches significant values of above 20% of the incident S_0 amplitude.

The results of the reflection and transmission coefficients, presented in Figure 2.7, will be discussed in more detail and compared to the numerical and experimental results in Section 2.5.5.



(a) AA6061-T6 to AZ31B



(b) AZ31B to AA6061-T6

Figure 2.7. Transmission and reflection coefficients at 200 kHz of the S_0 and S_0 - SH_0 modes using PWA.

FE analysis was conducted to extend on the application of PWA. The details of the FE model will be explained later (Section 2.3). For an excitation frequency of 200 kHz and an incidence angle of $\hat{i} = 20^\circ$, the amplitude of the 2nd peak of the refracted S_0 mode, after propagating from AA6061-T6 to AZ31B, was plotted versus the plate's thickness in Figure 2.8. A measurement was taken at every 0.5 mm in the through-thickness direction after S_0 has propagated for a distance of 85 mm in AA6061-T6 and 80 mm in AZ31B. The amplitudes were normalized based on their highest value for easier analysis. It can be noticed that the maximum amplitude variation through the plate's thickness is around 4%. This confirms the validity of the S_0 mode's approximation as a plane wave in both materials (AA6061-T6 and AZ31B) at the used $f \cdot d$ value.

FE simulations were also conducted at different excitation frequencies (50 kHz to 400 kHz) for a Lamb wave propagating from AA6061-T6 to AZ31B at a constant incidence angle ($\hat{i} = 20^\circ$). The transmission and reflection coefficients of the S_0 and S_0 - SH_0 modes were determined and compared to those calculated using PWA (Figure 2.9). A good agreement between the FE results and PWA is observed over the studied range of $f \cdot d$ values (0.15 MHz.mm to 1.2 MHz.mm). Hence, the use of PWA to approximate the symmetric modes is valid within the excited frequency range.

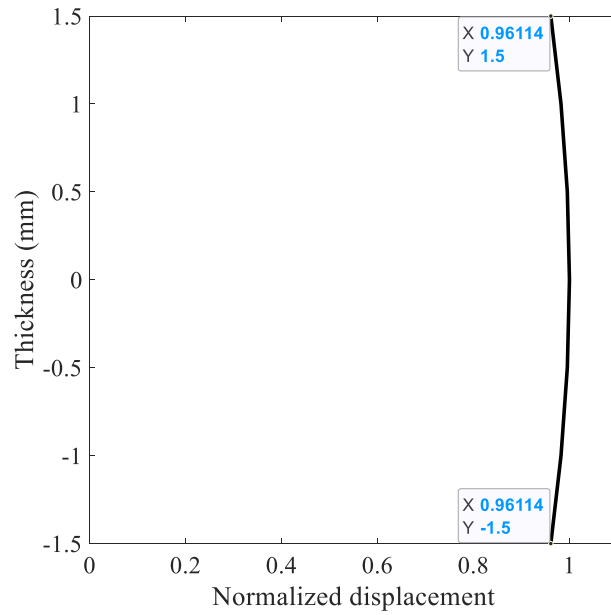


Figure 2.8. Through-thickness normalized amplitude of the refracted S_0 mode for a wave propagating in the forward direction at $\hat{i} = 20^\circ$ (sensor position = 80 mm).

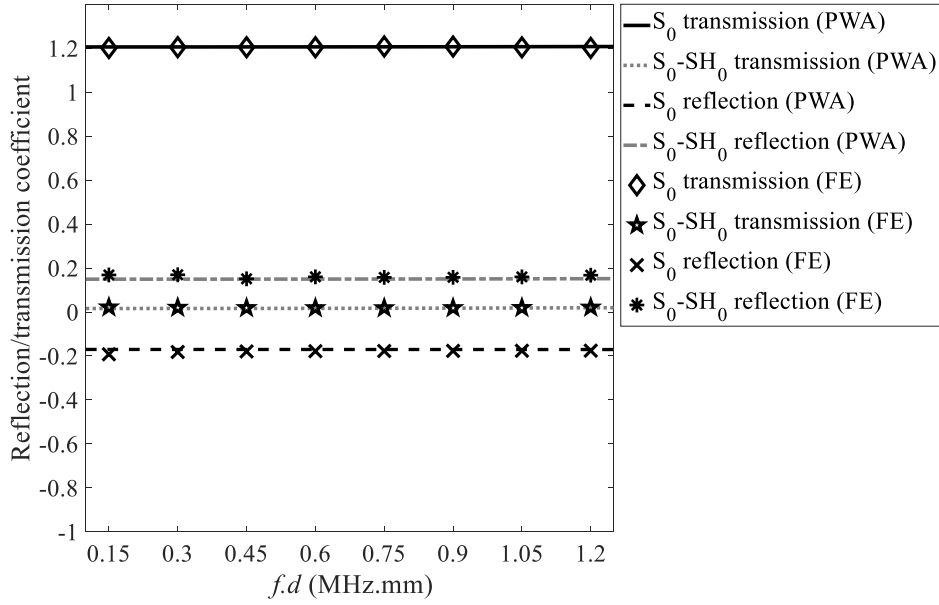
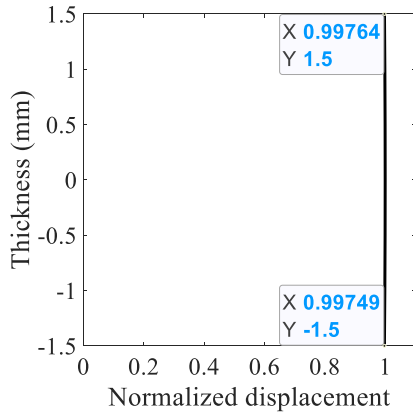


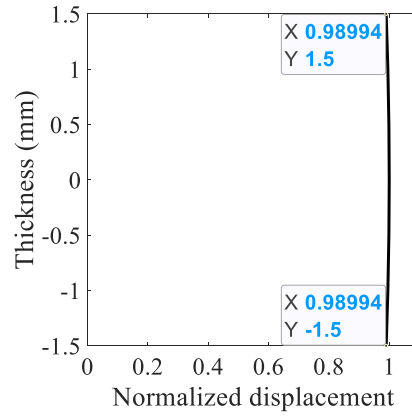
Figure 2.9. Transmission and reflection coefficients of the S_0 and S_0 - SH_0 modes at different excitation frequencies using PWA and FE simulations for a wave propagating in the forward direction at $\hat{i} = 20^\circ$.

The S_0 mode shape through the plate's thickness was also checked over the aforementioned excitation frequencies to ensure that the approximation of this mode as a plane-wave is still valid. Plots similar to that in Figure 2.8 are shown in Figure 2.10(a-h) for all the used excitation frequencies. The variation in the S_0 amplitude through-thickness increases with the excitation frequency as can be observed from the comparison between different plots. While the maximum amplitude variation through the plate's thickness was less than 0.3% at 50 kHz ($f.d = 0.15$ MHz.mm), it reached a value of around 12% at 400 kHz ($f.d = 1.2$ MHz.mm; $\omega h/c_T \approx 1.22$ & 1.23 for AA6061-T6 & AZ31B, respectively). Further increase in the $f.d$ value is expected to yield a deviation from the PWA solution until it becomes an invalid approximation at higher $f.d$ values. More analysis of Lamb-wave mode shapes through the plate's

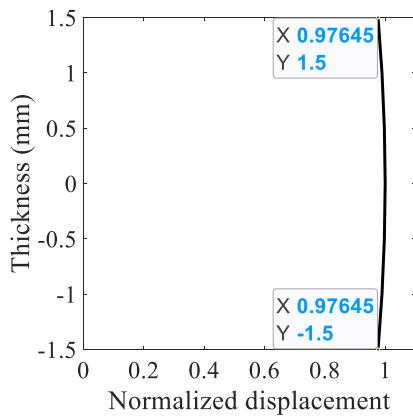
thickness both in the in-plane and out-of-plane directions can be found in comprehensive textbooks [30, 69].



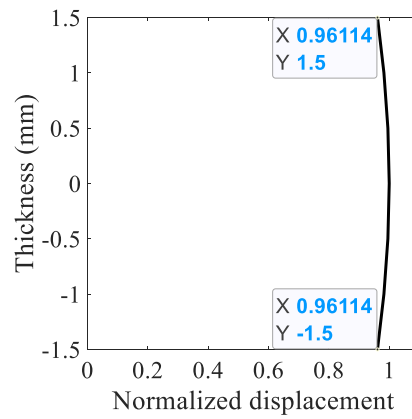
(a) 50 kHz



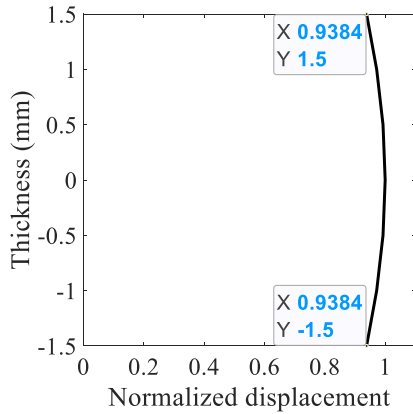
(b) 100 kHz



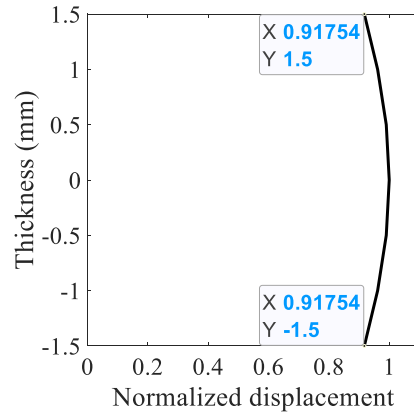
(c) 150 kHz



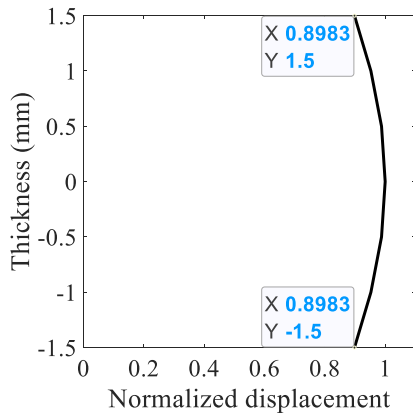
(d) 200 kHz



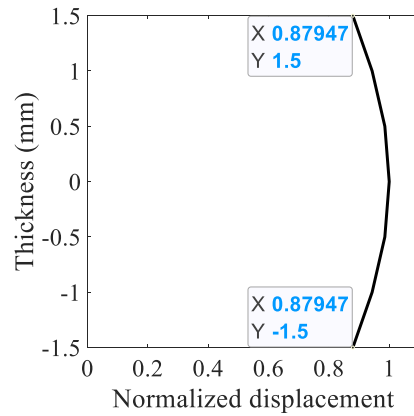
(e) 250 kHz



(f) 300 kHz



(g) 350 kHz



(h) 400 kHz

Figure 2.10. S_0 mode shape across the thickness for different excitation frequencies.

2.3 Finite Element Modeling

2.3.1 Finite Element Method for Wave Propagation

The finite element method (FEM) or finite element analysis (FEA) is a numerical approach that is widely used for solving wave propagation and vibration problems. If the physical problem is correctly modeled and an appropriate mathematical model is chosen, FEM can give accurate and computationally-efficient solutions for complex differential or integral equations [30, 74]. Since wave propagation is a

dynamic problem, the governing dynamic equation of FEM, representing a generalized Newton's second law, is given as follows:

$$[M]\{\ddot{d}\} + [C]\{\dot{d}\} + [K]\{d\} = \{F\} \quad (2.10)$$

where:

- $[M]$: is the mass matrix;
- $[C]$: is the damping matrix;
- $[K]$: is the global stiffness matrix;
- $\{d\}$: is the nodal-displacement vector;
- $\{\dot{d}\}$: is the nodal-velocity vector;
- $\{\ddot{d}\}$: is the nodal-acceleration vector;
- $\{F\}$: is the nodal-load vector.

Equation (2.10) can be simplified, for a harmonic wave with an angular frequency ω in an undamped material, to be:

$$([K] - \omega^2[M])\{d\} = \{F\} \quad (2.11)$$

where:

- $[K] - \omega^2[M]$: represents the dynamic stiffness matrix.

The dynamic problem can then be solved in both the time or frequency domains, where a numerical calculation method is needed to solve it in the time domain. The governing equation is solved while satisfying the loading and boundary conditions [75]. Direct integration methods can be used including the center difference, Newmark, and Wilson Theta methods, among others [30]. Several commercial FEM packages are usually utilized to simulate wave propagations, in both isotropic and composite

materials, from which *Abaqus*[®] and *COMSOL*[®] *Multiphysics* were used in the work presented in this dissertation.

2.3.2 Problem Modeling

COMSOL[®] *Multiphysics* FE software was used to create two adjoining metallic plates of 3-*mm* thickness and the same size along the common interface (Figure 2.11). The two plates were joined together to represent a dissimilar-material welded plate assuming a perfect joint. The material properties assigned to each of the sub-plates are listed in Table 2.1. Homogeneous isotropic linearly-elastic materials were assumed.

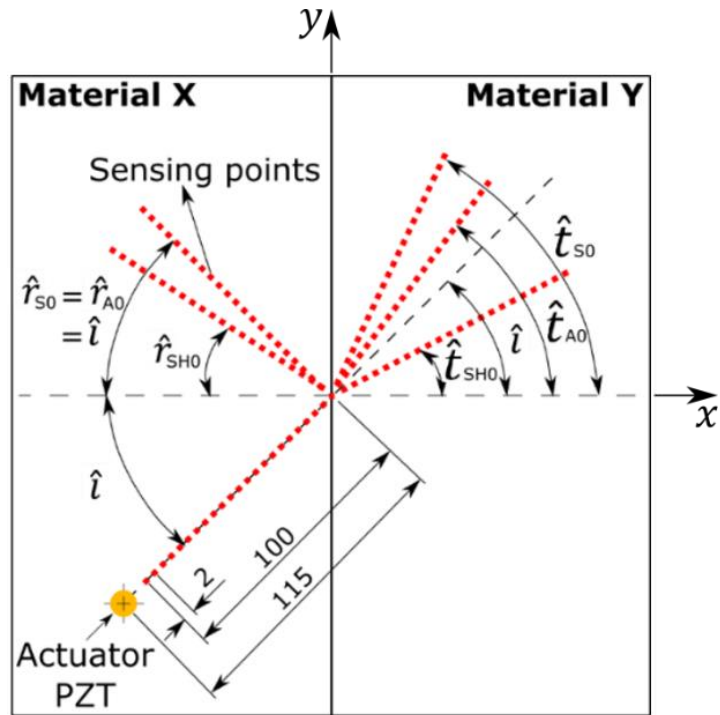
Circular piezoelectric (PZT-5H) transducers, 10 *mm* in diameter and 1 *mm* in thickness, were modeled based on a solid-mechanics/electrostatics multi-physics solver and were used to excite the Lamb waves. The actuator was placed at 115 *mm* from the joint's center, and nine incidence directions were used for excitation, namely, 0°, 10°, 20°, 30°, 40°, 50°, 60°, 70°, and 80° with the normal to the material interface (as shown in Figure 2.11(a)). The width and length of the two sub-plates were changed, as convenient, based on the position of the transducer and the sensing points upon changing the angle of incidence and propagation direction. Five-cycle Hann-windowed sinusoidal signals, of 200-*kHz* central frequency and 240-*V* peak-to-peak voltage, were fed into the poles of the PZT wafer. Forward and backward directions were simulated (AA6061-T6 to AZ31B and reversed) for each incidence angle. A free tetrahedral mesh was used with a maximum element size of 2 *mm* (Figure 2.11(b)). The outer side edges of the plate were assigned low reflecting boundaries to minimize the boundary reflections. Similar analyses were also completed for single-material plates (non-welded AA6061-T6 plate and AZ31B plate) to be used for the separation of interface reflection

and transmission wavefields from other wave superposition. The separation techniques are explained in Section 2.5.2 and Section 2.5.3.

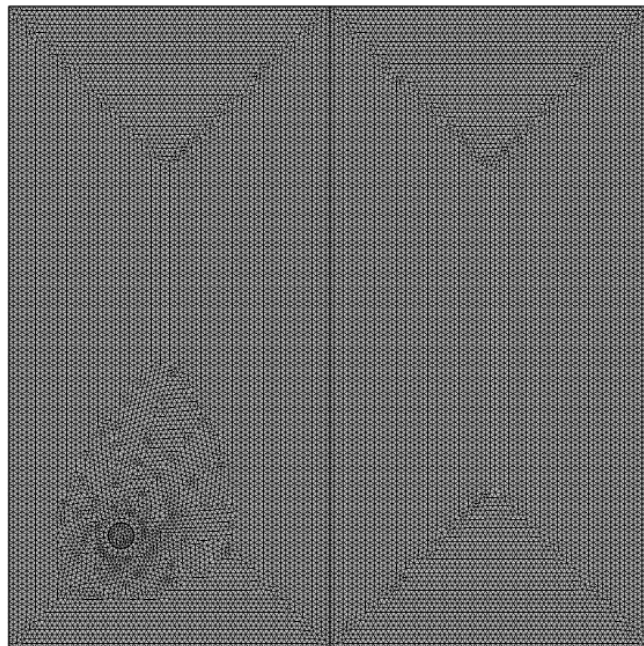
Measurements were taken on all transmission and reflection directions of each of the targeted wave modes. The angles defining those directions are denoted in Figure 2.11(a) as \hat{i} , \hat{r}_{mode} , and \hat{t}_{mode} for the incidence, reflection, and transmission angles, respectively. The angles were derived based on Snell's law as discussed in Section 2.2.3. Using equation (2.4), given that the phase velocity of the incident modes is constant when propagating in the same material, then their reflecting angles are the same as their incidence angles. The incident wave excited by the PZT wafer contains both S_0 and A_0 modes, therefore, $\hat{r}_{S_0} = \hat{r}_{A_0} = \hat{i}$ as designated on Figure 2.11(a).

Fifty sensing points were chosen along each of the propagation directions and an additional measurement was taken on the material interface (central point). This resulted in a total of 301 sensing points that are allocated on the surface of the plate based on the incidence angle and propagation directions across materials. All the sensing points were placed at 2-*mm* spacing (as seen in Figure 2.11(a)). They were distributed along a distance of 100 *mm* before and 100 *mm* after the interface and along the transmission and reflection directions of each mode. This will be indicated, later in this paper, as -100 *mm* to 100 *mm* in the spatial-time plots of the waves.

Displacements, at the sensing points, in the x-direction (U_1), y-direction (U_2), and z-direction/out-of-plane (U_3) were extracted at a sampling rate of 20 *MHz*. The collected data were then used to determine the wavefields related to each mode. The mode extraction, based on the FE and experimental measurements, is discussed in detail in Section 2.5.1.



(a) A schematic of the FE model (all dimensions are in *mm*)



(b) Top-view of the meshed FE model ($\hat{i} = 40^\circ$)

Figure 2.11. Details and mesh of the FE model.

2.4 Experimental Validation

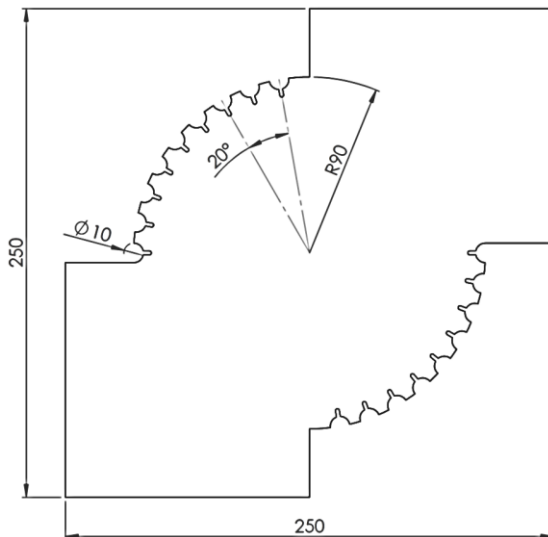
2.4.1 Sample Preparations

Two specimens were used for the experimental validation, one non-welded AA6061-T6 plate and another intact friction-stir-welded AA6061-T6/AZ31B plate. The two plates are of $250 \times 250 \times 3 \text{ mm}^3$ dimensions, as shown in Figure 2.12. The measurements from the non-welded AA6061-T6 plate were used for the separation of reflection and transmission wavefields, as will be explained later in Section 2.5.2 and Section 2.5.3.

Circular PZTs with wrapped electrodes, of 10-*mm* diameter and 1-*mm* thickness, were placed in a circular pattern on the surface of the specimens. This has allowed the wave actuation at different incidence angles while keeping a constant distance (along the propagation direction) from the welded joint or the middle line of the plate. The distance from the center of the PZT actuators to the center of the joint was 90 *mm*. A special template was cut using a laser cutting machine to be used for fixing the PZTs at a constant radius with a 20° -angular distribution (Figure 2.12(a)). The PZTs were placed at both sides of the joint to excite Lamb waves in both the forward and backward directions. The plate edges were covered by several layers of gummy tapes to dampen the boundary reflections of the excited waves (Figure 2.12(b) to (d)).

The scanning area was covered by a layer of retroreflective spray, as shown in Figure 2.12(b) and (d). The retroreflective effect reflects the laser beam back to the laser head with minimal scattering, which increases the laser focus and makes it more uniform among the scanned points. This would make the laser measurements less noisy and more reliable.

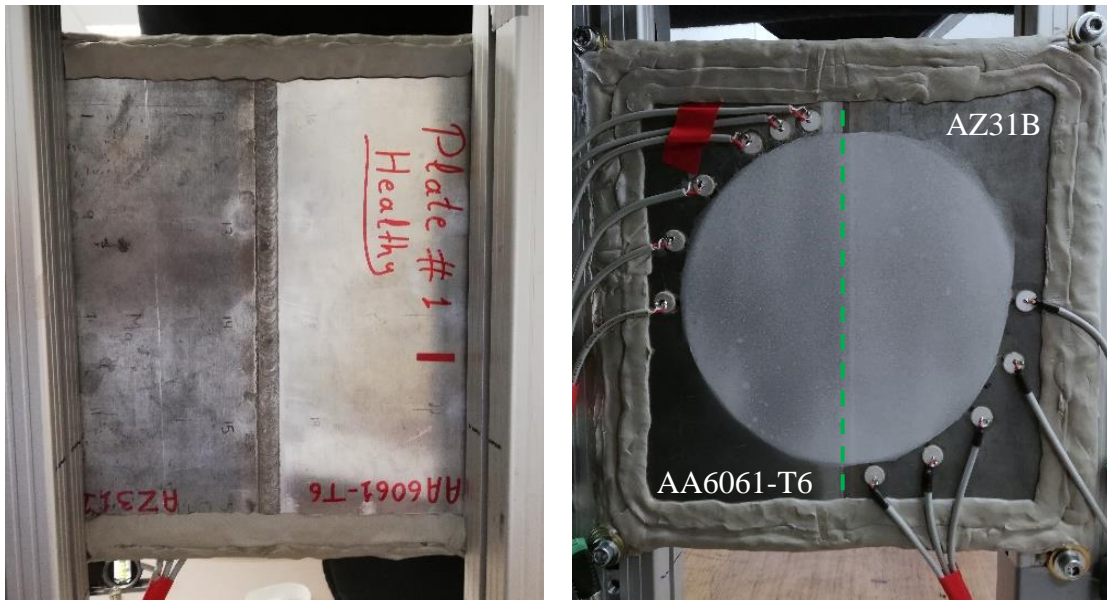
The healthy condition of the FSW plate was assured by performing a computed tomography (CT) scan of the plate and checking the weld for any damage. The CT scan was performed using a high-resolution CT scanner (Philips iCT 256). A through-thickness cross-sectional CT image of the welded plate is shown in Figure 2.13. No voids can be seen through the material interface, indicating the intact condition of the joint.



(a) The template used for proper PZT placement (dimensions are in *mm*)



(b) AA6061-T6 plate



(c) AA6061-T6/AZ31B plate's front-side (d) AA6061-T6/AZ31B plate's back-side

Figure 2.12. Photographs of the specimens used in this study and a drawing of the template used for PZT placement.

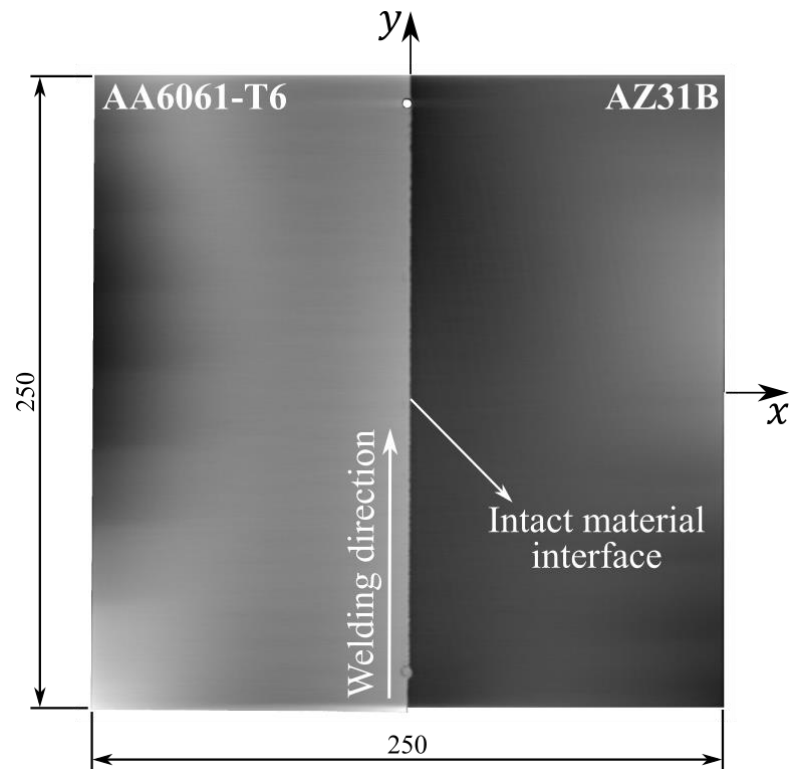


Figure 2.13. A through-thickness cross-sectional view of the welded test specimen, from a CT scan, showing its intact weld condition. Dimensions are in *mm*.

2.4.2 Experiment Setup

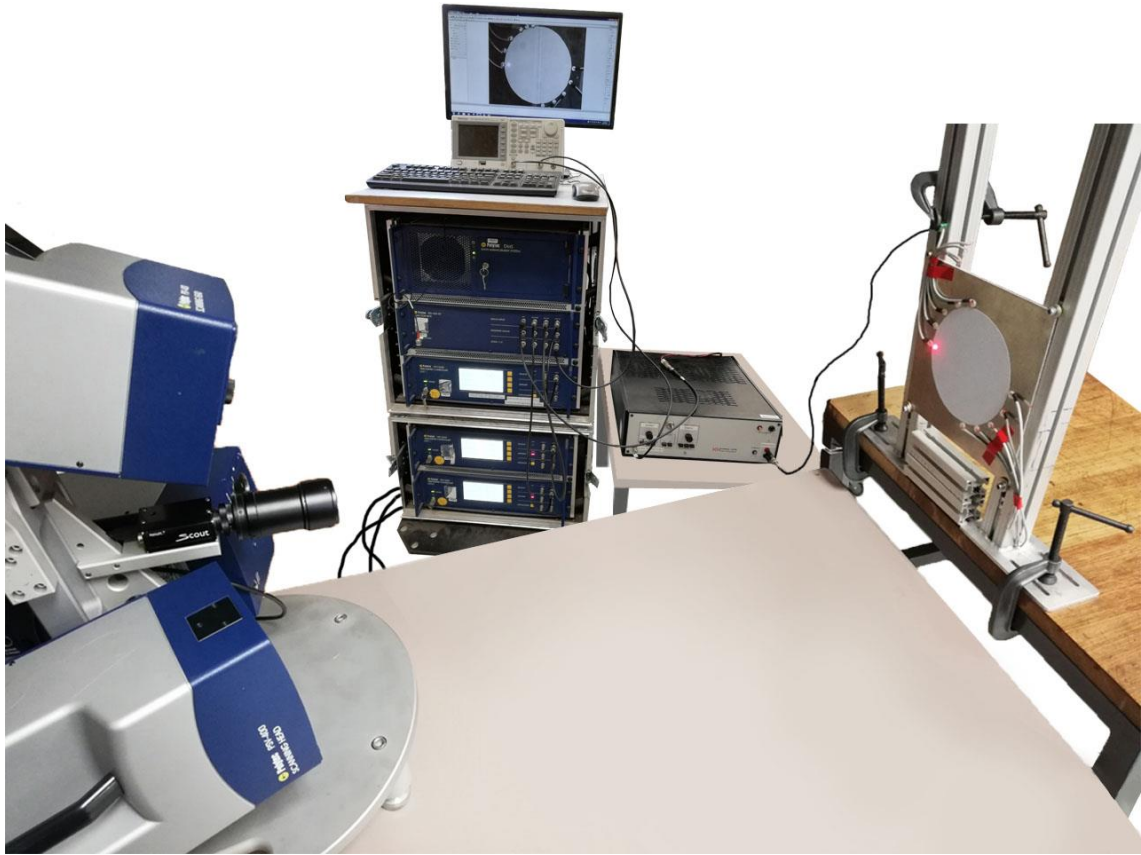


Figure 2.14. A photo of the experimental setup showing the Polytec PSV-400 3D SLV and its control box, the signal generator, the amplifier, and a testing specimen. The specimen shown in the figure is before using gummy tapes on its edges.

Figure 2.14 shows a photo of the system used to acquire the ultrasonic guided waves. A Polytec PSV-400 3D SLV (with three separate laser heads and a data acquisition system) was used to measure the GWs in the testing specimens. Five-cycle Hann-windowed tone burst signals, of 200-*kHz* central frequency, were used to excite the Lamb waves in the plates. The tone bursts were generated via a signal generator (Tektronix AFG 3021B), amplified up to 240-*V* peak-to-peak voltage using a power amplifier (Krohn-Hite model 7500), then fed into the piezoelectric transducers.

Different incidence angles, varying from 0° to 80° with a step of 20° , were used to excite the LWs. Waves were actuated in the forward and backward directions for every incidence angle, while measurements for each actuation were taken using the 3D scanning laser vibrometer (SLV).

The 3D velocity components were measured at all the reflection and transmission directions of the existing wave modes. Scanning points were defined along the propagation directions with a 2-mm resolution. This is to ensure a high-quality resolution image of the wave propagation. A scanning point was placed at the center of the material interface, while 40 other scanning points were distributed along each of the propagation directions, thus covering a scanning distance of 80 mm on either side of the weld. This is indicated as -80 mm to 80 mm in the spatial-time plots of the GWs.

The 3D laser and the specimen were totally covered by a black cloth (check Figure 2.15) to minimize measurement variations or noise due to the change in ambient light conditions. To increase the signal-to-noise ratio, 200 time-response measurements were averaged at each scanning point. A low-pass filter was applied to remove the high-frequency noise from the measurements. A sampling rate of 2.56 MHz was used in all experimental measurements.

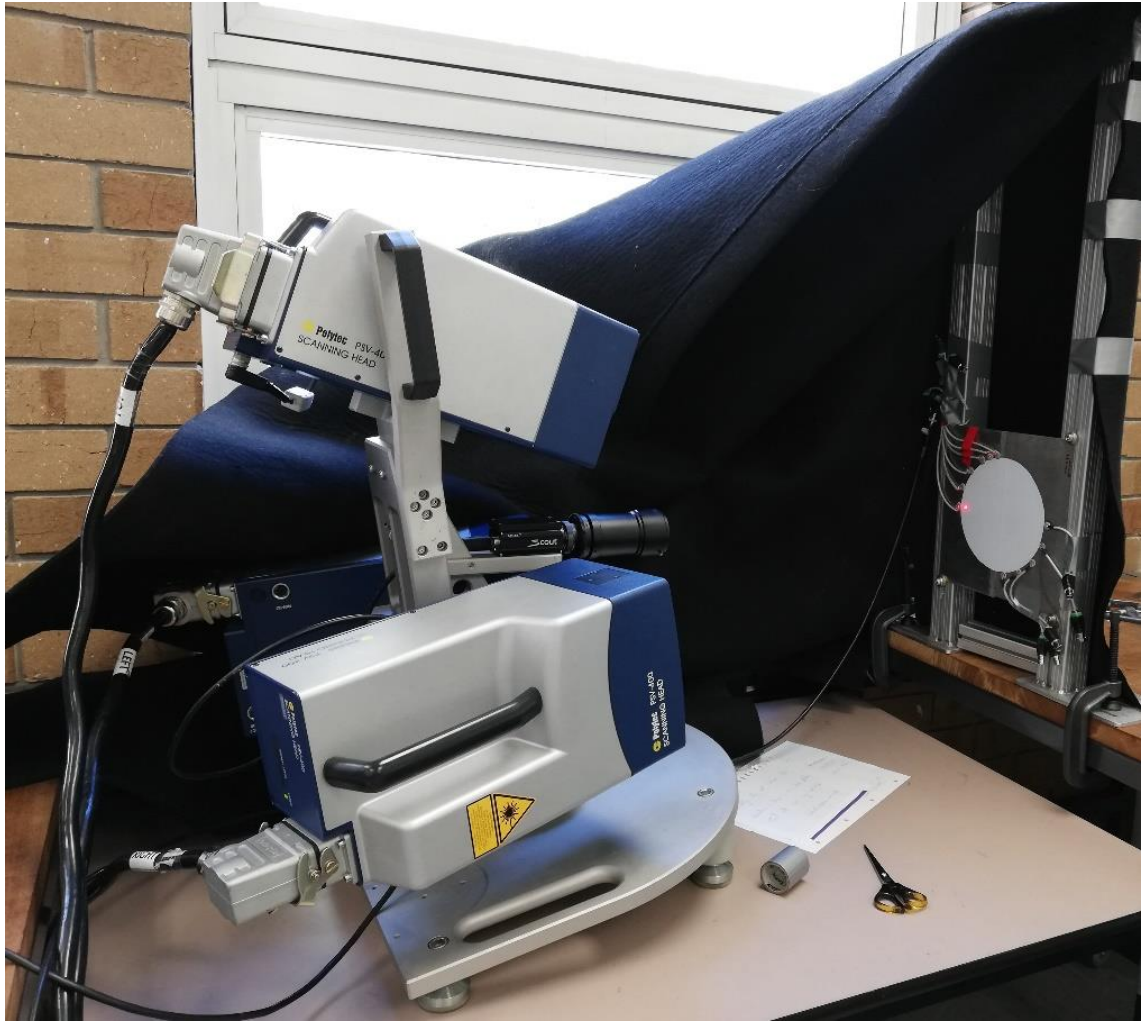


Figure 2.15. The Polytec PSV-3D SLV with one of the testing specimens – the laser and the specimen were totally covered with the shown black cloth when performing the measurements.

Figure 2.16 shows an example of the spatial-time plots of the in-plane normalized velocity fields (along the wave propagation direction) of a line scan from the AA6061-T6/AZ31B plate before and after using the gummy tapes and retroreflective spray. The line scan was made, along the central horizontal line while exciting the zero-incidence-angle PZT. A high percentage of the boundary reflections was absorbed by the gummy tapes, and focused measurements were obtained after using the retroreflective spray, as shown in Figure 2.16(b).

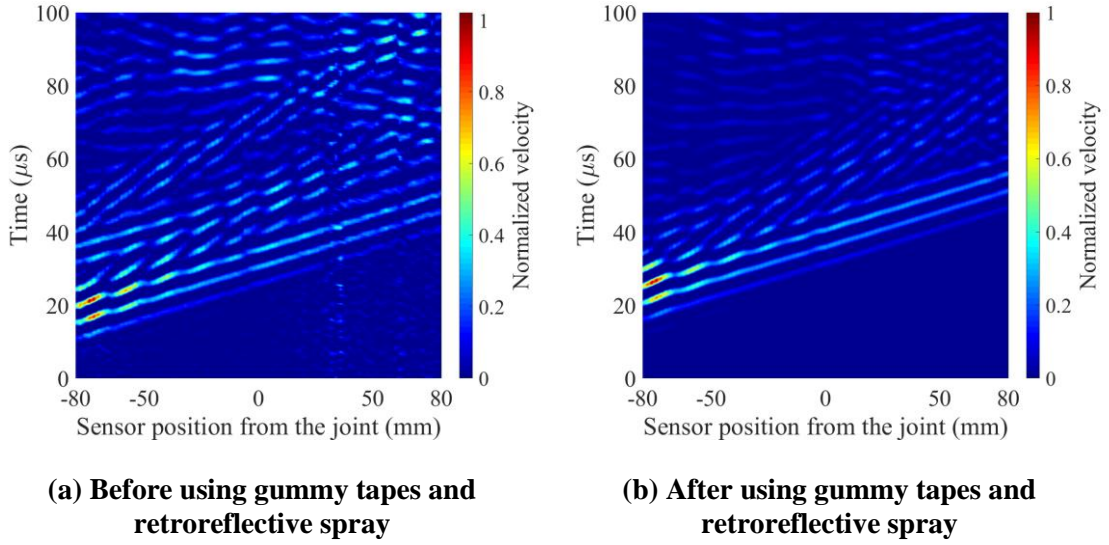


Figure 2.16. Spatial-time plots of the in-plane normalized velocity field (along the wave propagation direction) measured from the FSW plate, for a wave propagating from AA6061-T6 to AZ31B at $\hat{i} = 0^\circ$.

2.5 Results and Discussion

2.5.1 Mode Extraction

The in-plane displacements/velocities in the x - and y -directions (U_1 and U_2 respectively), as well as the out-of-plane displacements/velocities in the z -direction (U_3) were recorded at all the sensing points. The displacements/velocities (U_3) correspond mainly to the A_0 mode oscillations (Figure 2.17(a)). Referring to the schematic diagrams shown in Figure 2.17(b) and (c), the S_0 and SH_0 wavefields can be calculated according to equations (2.12) and (2.13) respectively:

$$U_{S_0} = U_1 \cos(\phi_{S_0}) + U_2 \sin(\phi_{S_0}) \quad (2.12)$$

$$U_{SH_0} = U_2 \cos(\phi_{SH_0}) - U_1 \sin(\phi_{SH_0}) \quad (2.13)$$

where:

- $U_{\tilde{m}}$: is the displacement/velocity field of the mode “ \tilde{m} ”;

- $\phi_{\tilde{m}}$: is the angle between the x -axis and the mode's propagation direction (\neq oscillation direction); based on the quadrant in which the sensing points are located and the wave's propagation direction, ϕ of a certain mode varies according to the following geometrical cases:

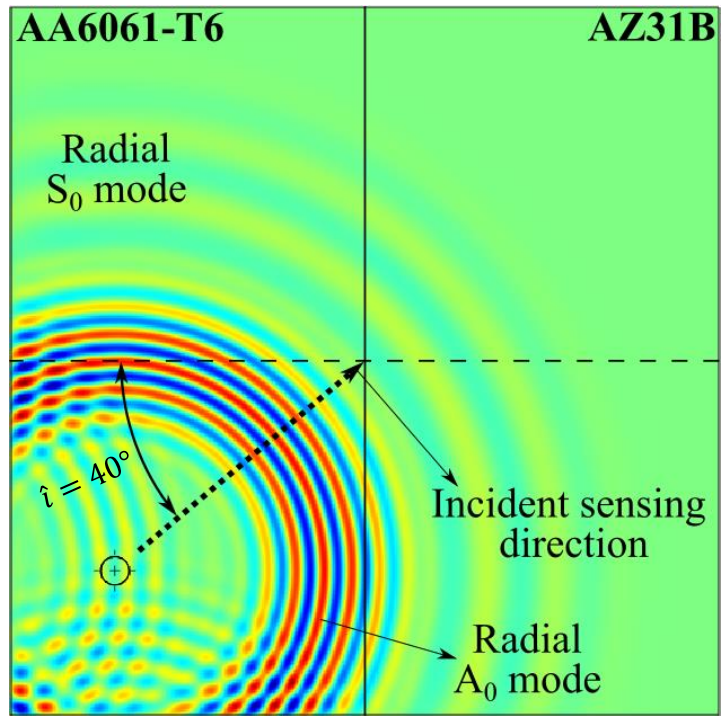
- Geometrical case 1: 1st or 3rd quadrant, a wave propagating from left to right: $\phi_{\tilde{m}} = \theta_{\tilde{m}}$;

- Geometrical case 2: 1st or 3rd quadrant, a wave propagating from right to left: $\phi_{\tilde{m}} = 180^\circ + \theta_{\tilde{m}}$;

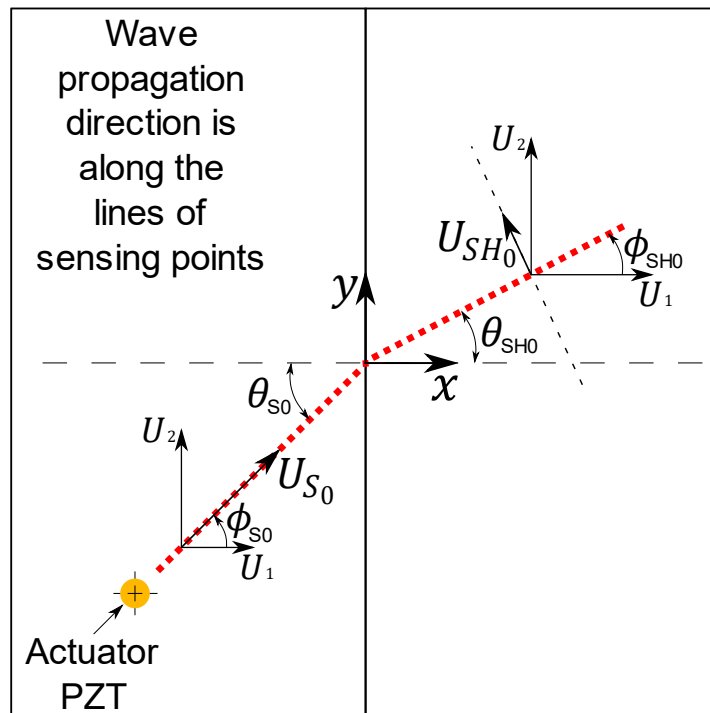
- Geometrical case 3: 2nd or 4th quadrant, a wave propagating from left to right: $\phi_{\tilde{m}} = -\theta_{\tilde{m}}$;

- Geometrical case 4: 2nd or 4th quadrant, a wave propagating from right to left: $\phi_{\tilde{m}} = 180^\circ - \theta_{\tilde{m}}$;

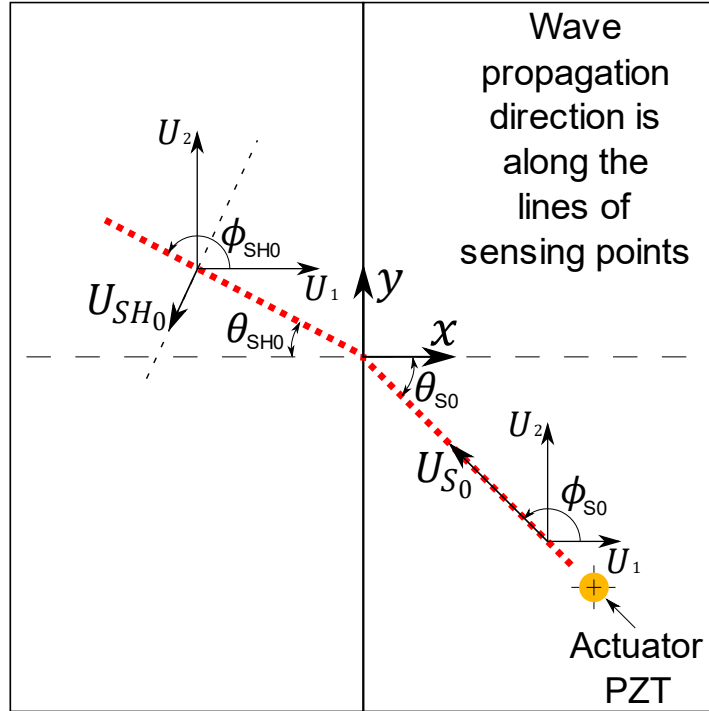
- $\theta_{\tilde{m}}$: is the acute angle between the propagation direction of the mode " \tilde{m} " and the normal to the material interface.



(a)



(b) Geometrical case 1 ($\phi_m = \theta_m$)



(c) Geometrical case 4 ($\phi_m = 180^\circ - \theta_m$)

Figure 2.17. (a) Sample out-of-plane displacements on the surface of the plate for a wave propagating in the forward direction at $\hat{i} = 40^\circ$. (b) and (c) two illustrating examples of S_0 and SH_0 wavefield calculations.

Although circular-crested waves are obtained by PZT actuation, determining the modes of interest along one propagation direction, as illustrated in Figure 2.17, proved to be an efficient simplification of the problem to be similar to an obliquely-incident straight-crested LW propagation.

Signals collected from all the sensing points along a given measurement direction can be plotted in the spatial-time domain. This can be achieved by accumulating all the vertical time plots of the signals side-by-side along the spatial axis (horizontal axis). Figure 2.18(a), (c), and (e) show the wavefields obtained using the FE simulations for the wave propagating in the forward direction, at $\hat{i} = 20^\circ$, for the S_0 , A_0 , and SH_0 modes, respectively. Different modes were identified based on their

measurement directions and velocities as discussed earlier. Further, Figure 2.18(b), (d), and (f) show similar results obtained from the experimental analysis. A good agreement was evident between the results of the FE simulations and the experiments. The obtained average group velocities of the S_0 and A_0 modes are summarized in Table 2.4.

Table 2.4. FE and experimentally obtained group velocities of the LW modes for a wave propagating in the forward direction at $\hat{i} = 20^\circ$.

Measurement	FE		Experimental	
Wave mode	c_g (m/s) in AA6061-T6	c_g (m/s) in AZ31B	c_g (m/s) in AA6061-T6	c_g (m/s) in AZ31B
S_0	5311.5	5335	5297.9	5311.5
A_0	2951.6	2975.9	3036.6	2829.8

It was observed that there were some weak boundary reflections in the experimental measurements; however, they are almost fully suppressed in the FE results due to the use of low reflecting boundaries.

The S_0 - SH_0 transmission did not appear clearly in Figure 2.18(e) due to its low amplitude when compared to the other wavefields propagating in the plate (less than one-tenth of S_0 amplitude). Experimentally, the S_0 - SH_0 transmission did not appear in Figure 2.18(f) since it is extremely weak. The separation of the S_0 - SH_0 transmission is discussed further in Section 2.5.3.

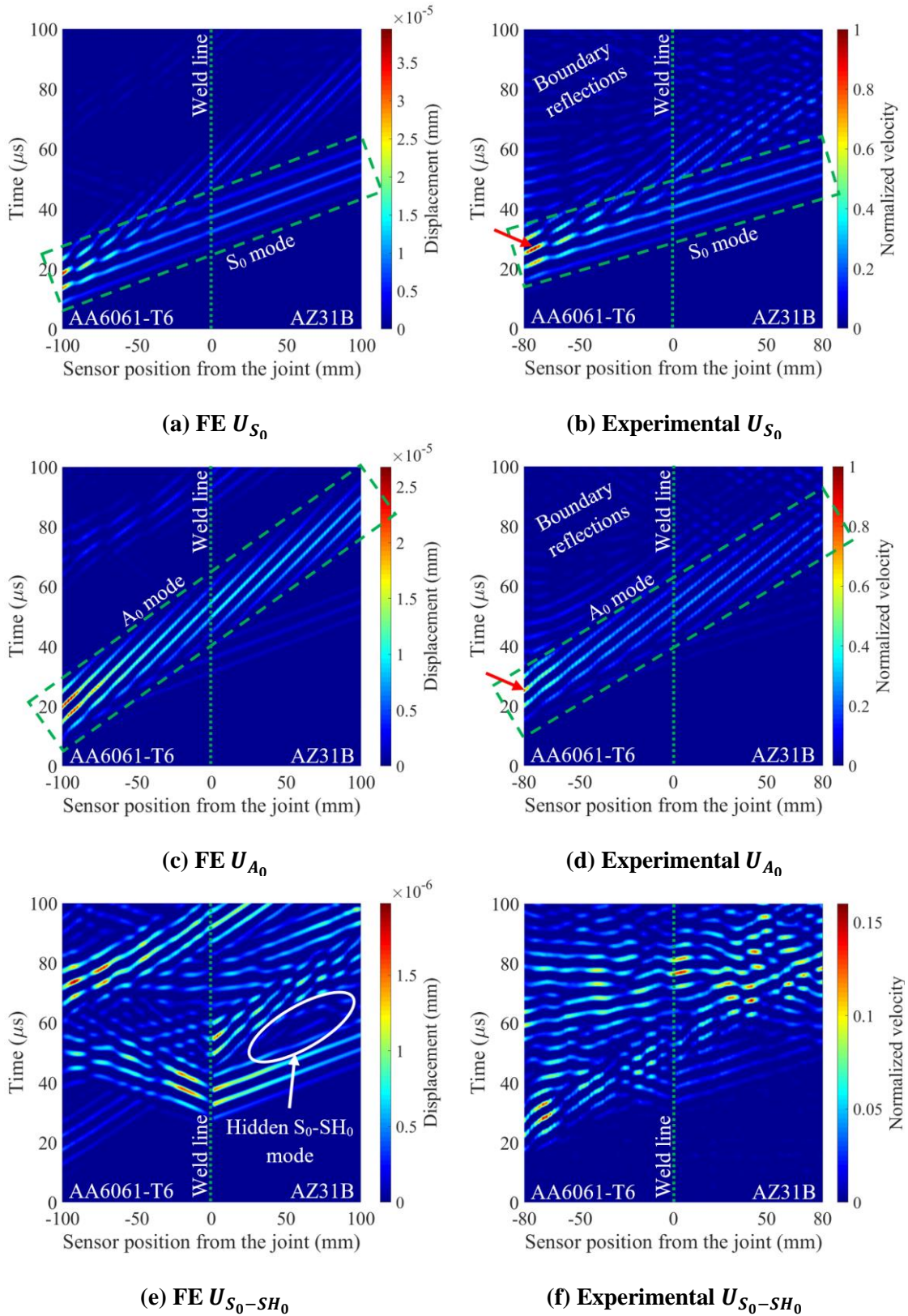


Figure 2.18. Spatial-time plots of the simulated and experimental wavefields, along the incidence and transmission directions of different modes, for a wave propagating in the forward direction at $\hat{i} = 20^\circ$.

The experimental measurements were collected using different actuators, therefore, experimental data were normalized. The A_0 wavefields (along the incidence, transmission, and reflection directions) were normalized to the peak value of the 1st transmission along the incidence direction (indicated by the red arrow in Figure 2.18(d)). The S_0 and the S_0 - SH_0 measurements were normalized using the peak value of the 1st transmission of the S_0 measurement along the incidence direction (indicated by the red arrow in Figure 2.18(b)). Figure 2.19 shows an example for the U_{A_0} signal (measured in the out-of-plane direction) at the 1st sensing point (sensor position = -80 mm) and at another sensing point (sensor position = 24 mm). Both signals are part of the wavefield shown in Figure 2.18(d). The red arrow indicates the peak value in the U_{A_0} wavefield, which was used to normalize all other signals of the wavefield of Figure 2.18(d).

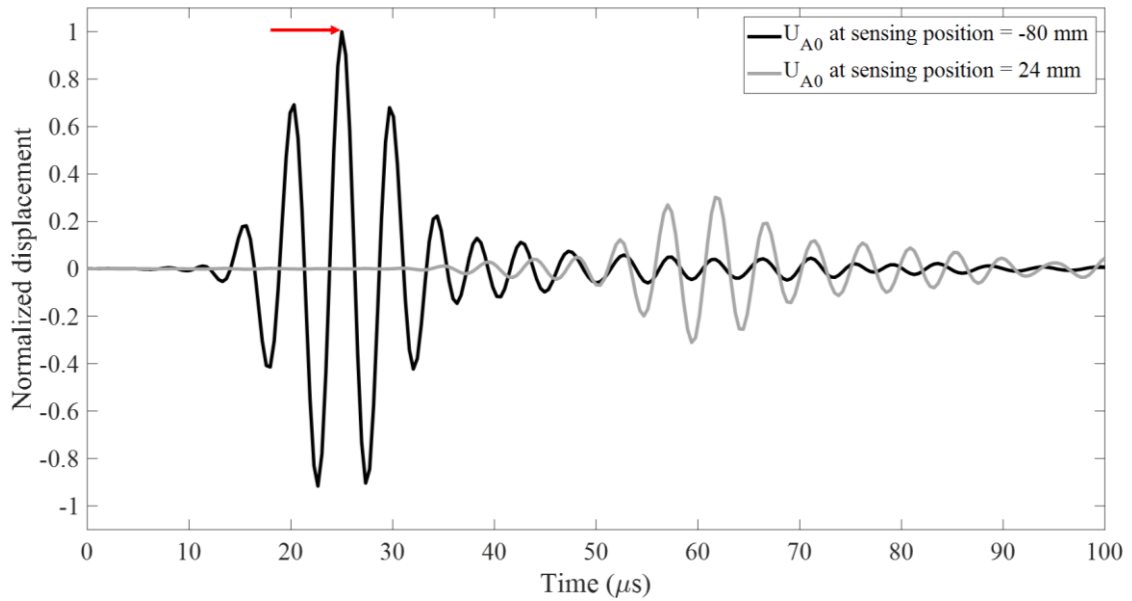


Figure 2.19. Typical normalized experimental raw signals for U_{A0} at two different sensing positions.

2.5.2 Reflection Separation

Figure 2.20(a) shows the FE simulation of the S_0 wavefield measured along the reflection direction, for a wave propagating in the forward direction at $\hat{t} = 20^\circ$. The waves measured at those sensing locations are the superposition of the direct transmissions from the actuator, boundary reflections, and reflections from the weld region. It is critical to separate the reflections caused by the presence of the material interface/discontinuity.

To separate interface reflections, measurements from the same actuator-sensor configurations were recorded in a single material for the same plate size. The wavefields measured at the reflection directions (e.g., Figure 2.20(b)) were then subtracted from the dissimilar-material reflection wavefields (e.g., Figure 2.20(a)). The obtained fields are those resulting from the waves' interactions with the dissimilar-

material interface (e.g., Figure 2.20(c)). To isolate the reflections in AA6061-T6 to AZ31B measurements, AA6061-T6 single-material measurements should be subtracted. Similarly, to isolate reflections in the opposite propagation direction, AZ31B single-material measurements are to be used. Equation (2.14) summarizes the followed reflection separation method for an incident wave propagating from Material X to Material Y:

$$U_{R(X/Y)} = U_{RD(X/Y)} - U_{RD(X/X)} \quad (2.14)$$

where:

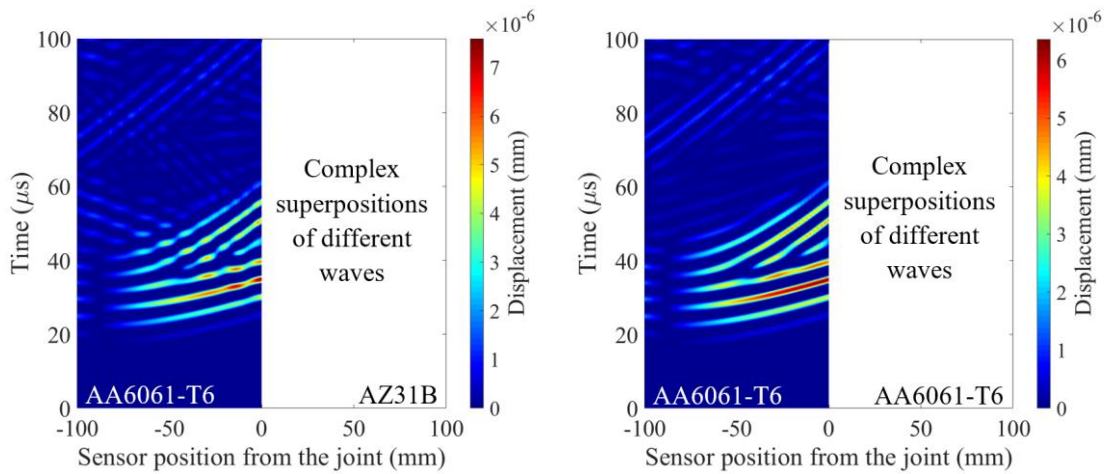
- $U_{R(X/Y)}$: is the wavefield, reflected from the material interface, from an incident wave propagating from material X to material Y at an angle of incidence \hat{i} ;
- $U_{RD(X/Y)}$: is the wavefield, measured along the reflection direction, from an incident wave propagating from material X to material Y at an angle of incidence \hat{i} ;
- $U_{RD(X/X)}$: is the wavefield, measured along the reflection direction, from an incident wave propagating from material X to material X at an angle of incidence \hat{i} .

Figure 2.20(c) shows a clear reflection field of the S_0 mode. This reflection has an average group velocity of 5333 m/s , which is in good agreement with the AA6061-T6 theoretical value presented in Table 2.2 (5268.7 m/s). The separated reflection fields of the other modes (A_0 and $S_0\text{-SH}_0$) of the same simulated wave are presented in Figure 2.21. As mentioned earlier, SH_0 was not significant before the wave interaction with the material interface; thus, its noticeable appearance in the reflection field is due to $S_0\text{-SH}_0$ conversion upon S_0 interaction with the joint [71]. This is also clear based on the amplitude of the SH_0 mode in the reflected field (Figure 2.21(b)), which is higher

than its amplitude in the incident field (Figure 2.18(e)). The average group velocities of the obtained A_0 and SH_0 reflections were determined to be 3062 m/s and 3094 m/s , respectively, and they are both close to the theoretical values shown in Table 2.2 (2980.32 m/s and 3099.6 m/s , respectively).

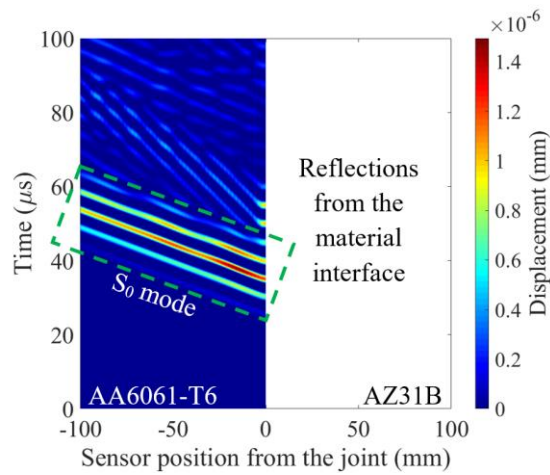
The same procedure was applied for the experimental measurements to separate interface reflections from other wave superposition. The separated reflection fields from experimental measurements were not as clear as those obtained from the FE simulations, which is expected. Figure 2.22 presents the experimental measurements of the S_0 mode along its reflection direction for an incident wave propagating in the forward direction at $\hat{i} = 20^\circ$ (Figure 2.22(a)), and similarly in the AA6061-T6 single-material plate (Figure 2.22(b)). After subtracting these two wavefields, the wavefield in Figure 2.22(c) was obtained. The reflection field of the S_0 mode can be identified as shown in the figure. It has an average group velocity of 5120 m/s , which has good agreement with the AA6061-T6 theoretical value presented in Table 2.2 (5268.7 m/s).

It should be noted here that several steps were taken during the experiments to minimize all possible differences between measurements from two different specimens including placement of PZTs, soldering, and connections. The retroreflective spray and gummy tapes were made as uniform and consistent as possible between the two plates. The two plates were placed at the same position and height with respect to the laser, and a precise and careful calibration of the 3D SLV was performed to have similar and accurate measurement positions. Data were normalized to account for differences between different actuator PZTs and bonding quality. Despite all this, errors still existed due to unavoidable operational and environmental variations.



(a) S_0 reflection wavefield measured in the AA6061-T6/AZ31B plate

(b) S_0 reflection wavefield measured in the AA6061-T6 plate



(c) S_0 reflection computed by subtracting the wavefield shown in (b) from the wavefield shown in (a)

Figure 2.20. Separation of the S_0 reflection – FE simulation measurements along S_0 reflection direction, for a wave propagating in the forward direction at $\hat{i} = 20^\circ$.

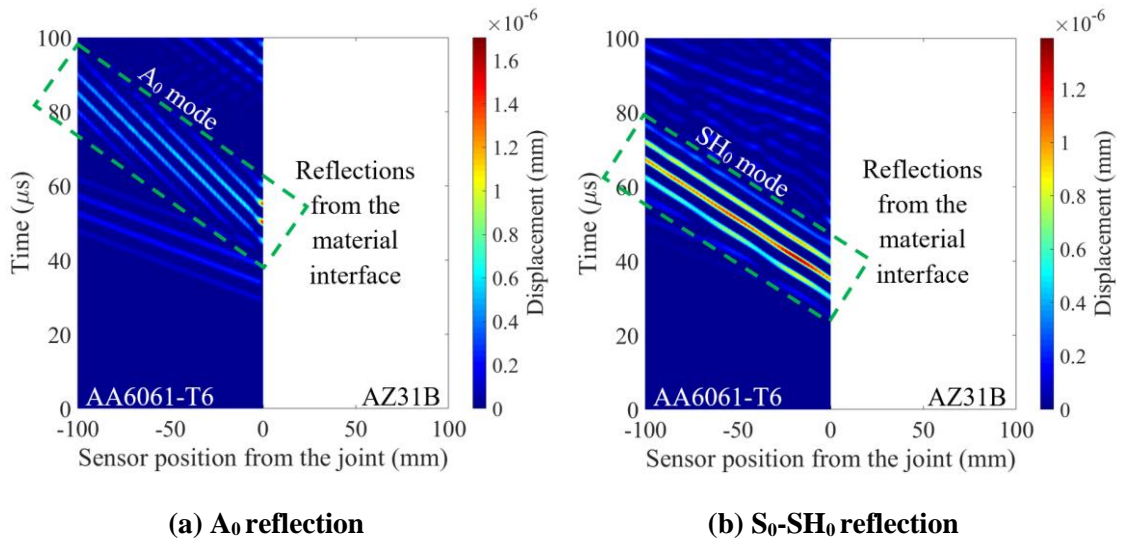
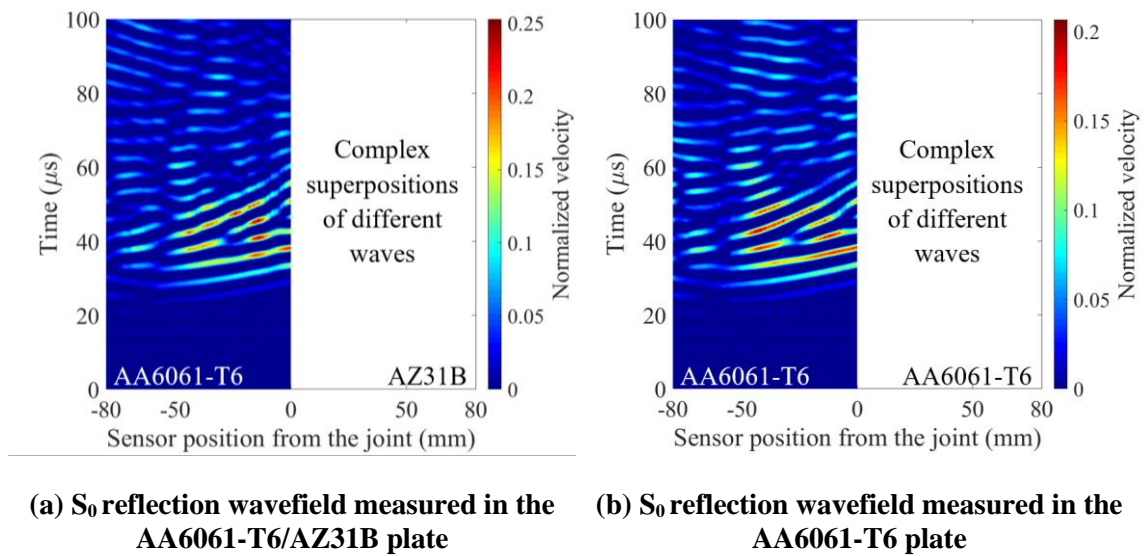
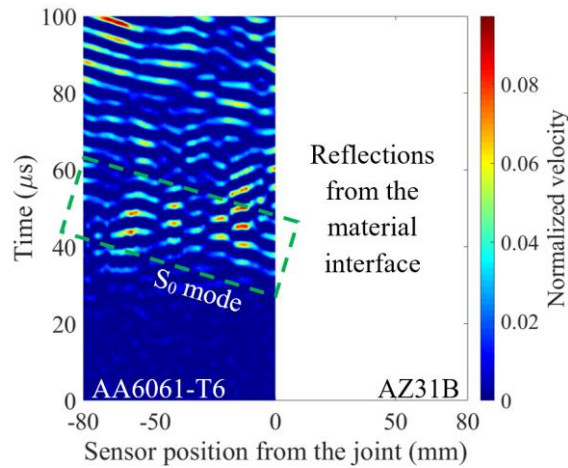


Figure 2.21. Separated A_0 and S_0 - SH_0 reflection fields – FE simulation measurements along their respective reflection directions, for a wave propagating in the forward direction at $\hat{t} = 20^\circ$.





(c) S_0 reflection computed by subtracting the wavefield shown in (b) from the wavefield shown in (a)

Figure 2.22. Separation of the S_0 reflection – experimental measurements along S_0 reflection direction, for a wave propagating in the forward direction at $\hat{i} = 20^\circ$.

2.5.3 S_0 - SH_0 Transmission Separation

The measured S_0 - SH_0 transmission along its expected propagation direction was noticed to have a low amplitude when compared to the other measured wavefields on the same plate. It was found that this mode is masked by other transmissions and reflections, as shown in Figure 2.18(e) and (f). Therefore, a separation procedure was established to extract the transmitted/refracted S_0 - SH_0 mode.

In the reflection separation (Section 2.5.2), the wavefields measured along the reflection directions would have both propagated only in material X, which makes their direct subtraction a reasonable solution. The wavefield measured along the S_0 - SH_0 transmission direction, across a dissimilar joint, would have passed from material X to material Y, while in a single-material plate, it would have propagated only in material X. To account for the amplitude variation between different materials, the single-material wavefield was normalized to that of dissimilar materials before subtraction.

Given that the first wave-pack was noticed to be common between the two subtracted wavefields (Figure 2.23(a) and (b)), the amplitude of the 3rd obvious peak in this wave-pack was used for amplitude normalization (other peaks can be used for normalization). This procedure is described as follows:

$$U_{S_0-SH_0(X/Y)} = U_{SH_0D(X/Y)} - a \times U_{SH_0D(X/X)} \quad (2.15)$$

where:

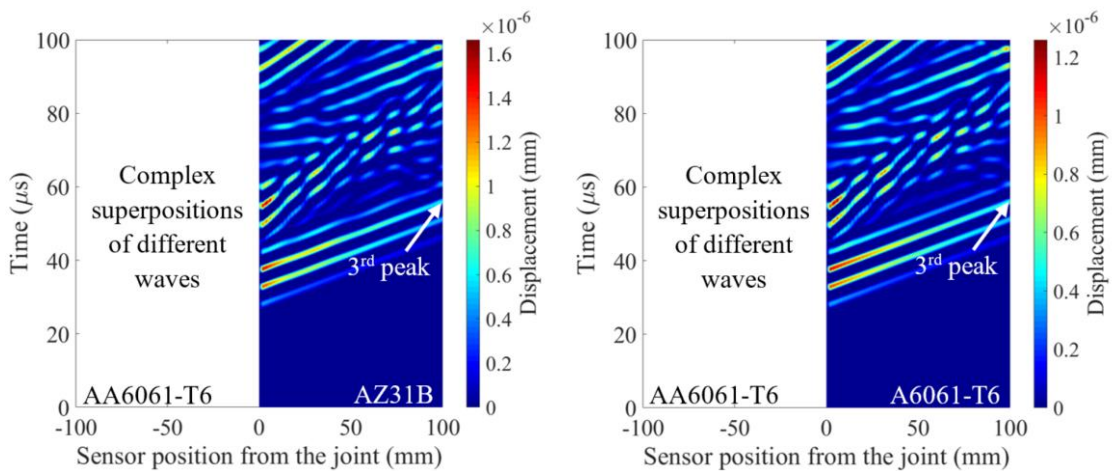
- $U_{S_0-SH_0(X/Y)}$: is the refracted S_0 - SH_0 wavefield, converted from the S_0 mode of an incident wave propagating from material X to material Y at an angle of incidence \hat{i} ;
- $U_{SH_0D(X/Y)}$: is the SH_0 wavefield, measured along the S_0 - SH_0 transmission direction, from an incident wave propagating from material X to material Y at an angle of incidence \hat{i} ;
- $U_{SH_0D(X/X)}$: is the SH_0 wavefield, measured in the same direction as $U_{SH_0D(X/Y)}$, from an incident wave propagating from material X to material X at an angle of incidence \hat{i} ;
- a : is the coefficient that normalizes the amplitudes of $U_{SH_0D(X/X)}$ to those of $U_{SH_0D(X/Y)}$, determined from a chosen peak of the 1st wave-pack (3rd peak in this case) and at a chosen sensor position.

Similarly, the time of arrival of the wave-pack, considered for normalization, is a bit different between the two wavefields due to propagation in different materials. This time-shift would have been more obvious if the group velocities of the studied materials were not close in values (refer to Table 2.2). The time-shift increases with the

propagation distance and, hence, differs from one sensor position to another. Therefore, time alignment should also be applied to $U_{SH_0D(X/X)}$, at each sensor position, before subtraction.

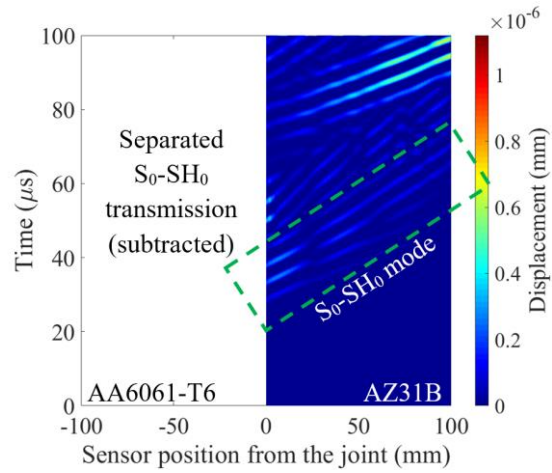
Figure 2.23 illustrates the separation of the S_0 - SH_0 transmission for the wave simulation of an incident wave propagating in the forward direction at $\hat{t} = 20^\circ$. The average group velocity of the obtained S_0 - SH_0 transmission is 3021 m/s , which is very close to the theoretical value presented in Table 2.2 (3068.6 m/s).

When applying the same separation method to the experimental measurements, the refracted S_0 - SH_0 mode was very weak to appear. This agrees with both the PWA results (Section 2.2.4) and the FE results.



(a) SH_0 transmission wavefield measured in the AA6061-T6/AZ31B plate

(b) SH_0 transmission wavefield measured in the AA6061-T6 plate



(c) S_0 - SH_0 transmission computed by subtracting the wavefield shown in (b) from the wavefield shown in (a), based on equation (2.15)

Figure 2.23. Separation of the S_0 - SH_0 transmission – FE measurements along S_0 - SH_0 transmission direction, for a wave propagating in the forward direction at $i = 20^\circ$.

2.5.4 Attenuation Curves

The attenuation curve provides information about the change in the amplitude of the propagating wave with distance. The naming “attenuation” comes from the fact that as a wave mode propagates in a single material, its amplitude is attenuated or reduced with distance. Attenuation of Lamb-wave modes occurs due to multiple possible mechanisms including dispersion, beam divergence, material damping, scattering, and leakage into a neighboring medium [76]. Attenuation by dispersion is interpreted as the diffusion of the energy along the propagation direction, while beam divergence is considered as the energy diffusion in the perpendicular direction. Further, as the wave propagates within the material, part of its energy is dissipated into heat due to material damping, thus causing amplitude reduction; this effect was considered by Wilcox et al. [76] as minimal in metallic plates. Scattering is the reflection or dissipation of the considered wave mode in directions other than the direction of

interest. It also includes possible mode conversions into other modes. Scattering may occur due to the wave interaction with impurities, flaws, material discontinuities, rough surfaces, or any other features or inhomogeneities in the plate's material. Finally, the 5th attenuation mechanism (leakage) is described as the possible radiation of the wave energy into a surrounding medium. This is usually significant if the metallic plate is immersed in water or embedded in another solid. However, this leakage is minimal for a metallic plate placed in the air because of the huge mismatch in the acoustic impedance between the metal and air [76]. Investigating the attenuation behavior across multiple media would allow for a better understanding of Lamb-wave propagation from one solid medium to another along with the underlying phenomena.

Attenuation in single-material plates (isotropic and non-welded) is not affected by the incidence angle since the material interface does not exist. Thus, the curves determined from multiple experimental measurements (at multiple incidence angles) in the AA6061-T6 plate were averaged to have one single reference and avoid experimental variations between different single-material recordings. Figure 2.24 shows the experimental S_0 attenuation curves when propagating in the AA6061-T6 plate and when propagating in the forward direction in the welded plate ($\hat{t} = 0^\circ$). The curves are presented for the 1st three positive peaks (check Figure 2.25(b)) to interpret the existing differences.

A sinusoidal variation in the S_0 amplitude is evident at the beginning of the attenuation curve of the 1st peak (Figure 2.24(a)), however, this variation increases significantly in the attenuation curves based on the 2nd and 3rd peaks (Figure 2.24(b) and (c)). This oscillation pattern indicates that the S_0 mode was not fully converged. This instability can be explained by two interrelated phenomena, namely, LW dispersion into

two different modes of different velocities (A_0 and S_0), and the superpositions between the two modes before their complete separation. To understand these two phenomena, the S_0 spatial-time plots, from which those attenuation curves were extracted, are shown in Figure 2.25. The two LW modes are identified on the figures, illustrating that the complete separation between the two modes did not occur before about 45 mm from the center of the plate (dashed-red line). The separation of the two modes (dispersion) and the superposition between them while separating, have both led to the sinusoidal shape that can be seen in the attenuation curves. It can be also noticed from Figure 2.25 how the A_0 mode separates from the 1st peak of the S_0 mode first (sensor position ≈ -50 mm), then it separates from the 2nd peak at a later stage (sensor position ≈ -25 mm), and finally from the 3rd peak approximately at the center of the plate. This explains why the sinusoidal variation lasts for different propagation distances between the attenuation curves of the three peaks (Figure 2.24).

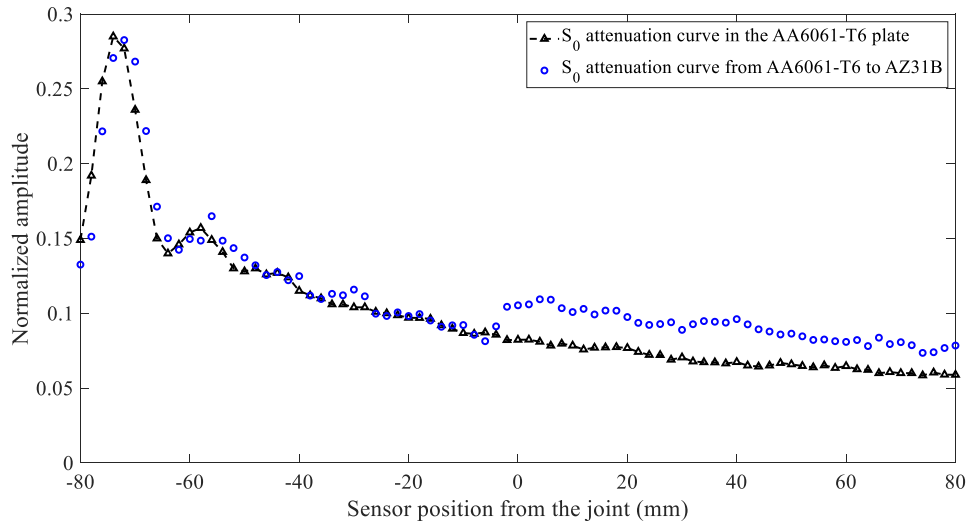
Upon crossing the material interface (around sensor position ≈ 0), the wave amplitude experiences a sudden jump before it continues in the normal attenuation behavior. This increase in amplitude may indicate that the wavefield is amplified when passing from a stiffer medium (AA6061-T6) to a softer medium (AZ31B). Figure 2.26 shows the FE results of the same case. Similar conclusions and observations can be drawn from Figure 2.26, while more data consistency is obvious, due to the absence of possible experimental errors and noise.

It is worth mentioning that waves reflecting from the boundaries of the plate can also overlap with the transmitted modes causing some disturbance. For example, the sudden drop in amplitude at the end of the attenuation curves, which is more evident for the 2nd and 3rd peaks (Figure 2.24(b) and (c)), is due to the superposition between the S_0

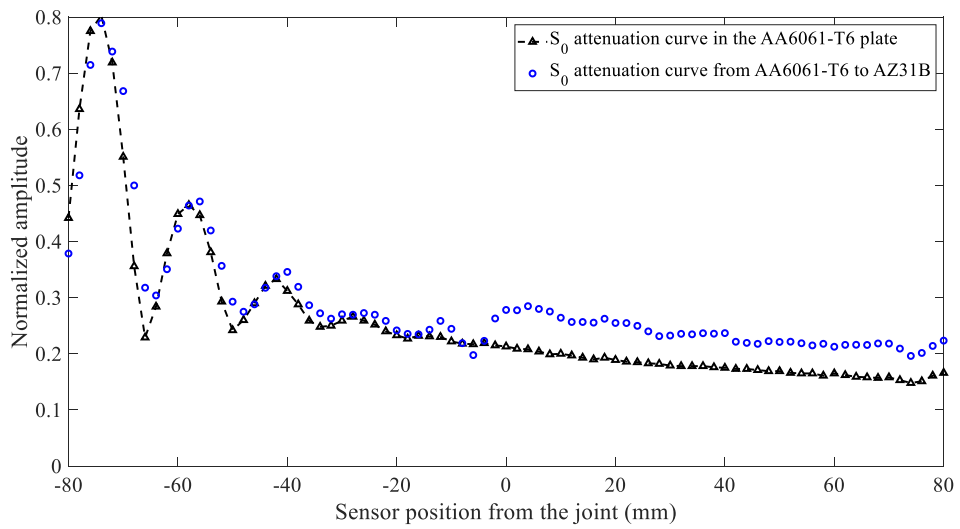
mode and its boundary reflection from the plate's far side. Since low reflection boundaries were assigned to the plates' edges in the FE simulations, the effect of boundary reflections on the attenuation curves is minimal in Figure 2.26.

Further, the disturbance in the attenuation curves, just before the material interface (sensor position $\approx 0 \text{ mm}$), is due to the superposition of the incident S_0 mode with its reflection from the material interface. This disturbance is more evident in the 2nd and 3rd peaks' attenuation curves in both experimental (Figure 2.24(b) and (c)) and FE results (Figure 2.26(b) and (c)).

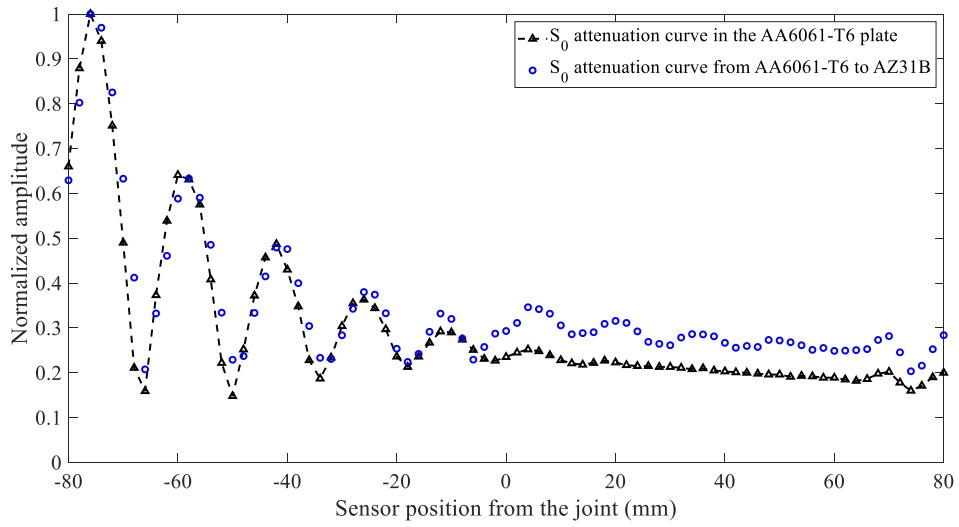
Figure 2.27 shows the experimental and FE attenuation curves of the backward propagation direction (3rd peak; $\hat{i} = 0^\circ$) as compared to that in the AZ31B single-material plate (non-welded). Unlike the amplitude amplification in the forward direction, the wavefield showed a sudden drop in amplitude upon passing from a softer medium (AZ31B) to a stiffer one (AA6061-T6). The variation between the experimental and FE attenuation curves at their start is because the sensing points in the FE model start at "sensor position = -100 mm ", while they start at "sensor position = -80 mm " in the experiments (in addition to the difference in the actuator position).



(a) 1st peak

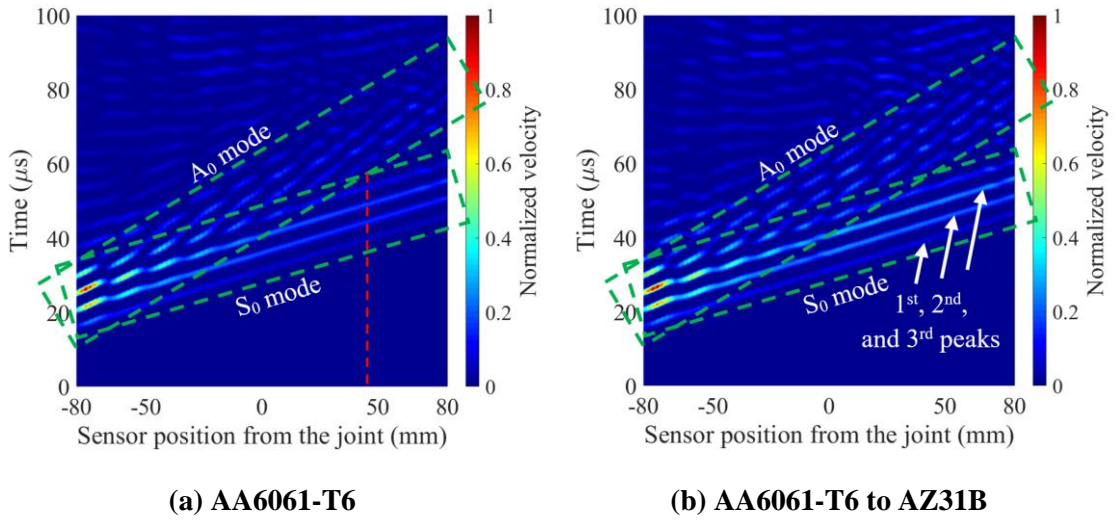


(b) 2nd peak



(c) 3rd peak

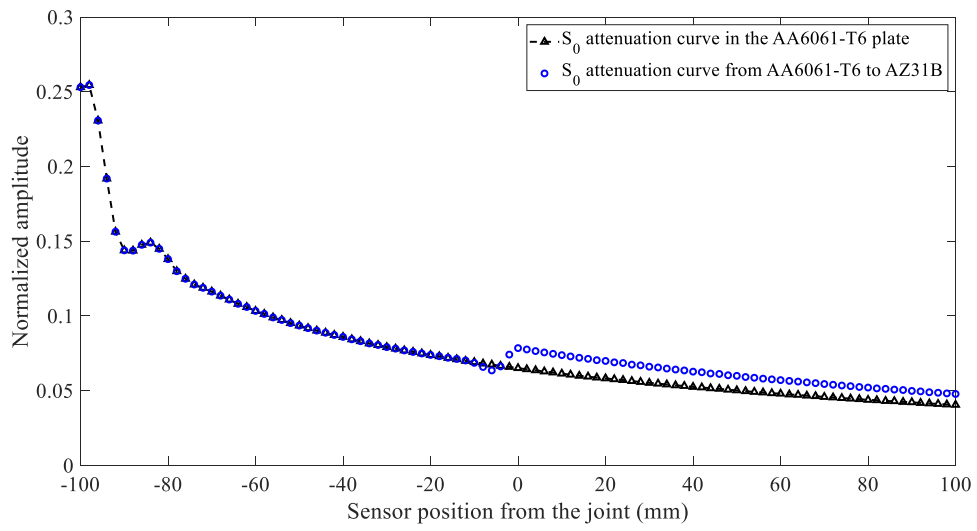
Figure 2.24. Experimental S_0 -mode attenuation curves in both the AA6061-T6 plate (averaged from all incidence angles) and the AA6061-T6/AZ31B plate (forward direction; $\hat{i} = 0^\circ$).



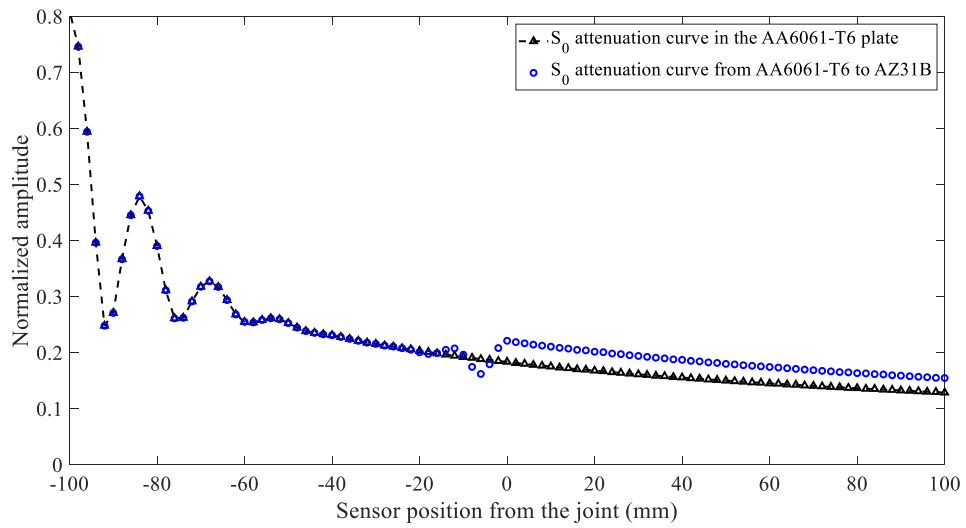
(a) AA6061-T6

(b) AA6061-T6 to AZ31B

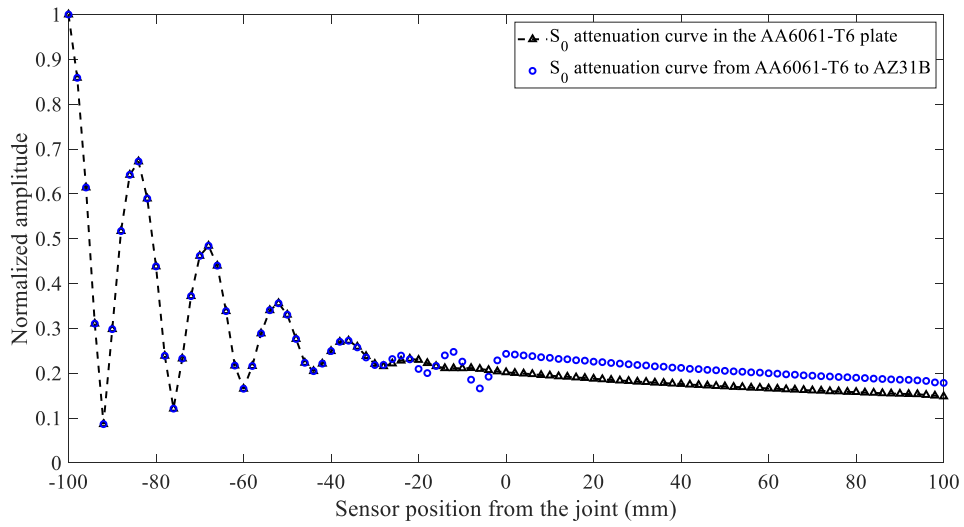
Figure 2.25. Experimental S_0 -mode spatial-time plots in both the AA6061-T6 plate and the AA6061-T6/AZ31B plate (forward direction; $\hat{i} = 0^\circ$).



(a) 1st peak



(b) 2nd peak



(c) 3rd peak

Figure 2.26. FE S_0 -mode attenuation curves in both the AA6061-T6 plate ($\hat{i} = 0^\circ$) and the AA6061-T6/AZ31B plate (forward direction; $\hat{i} = 0^\circ$).

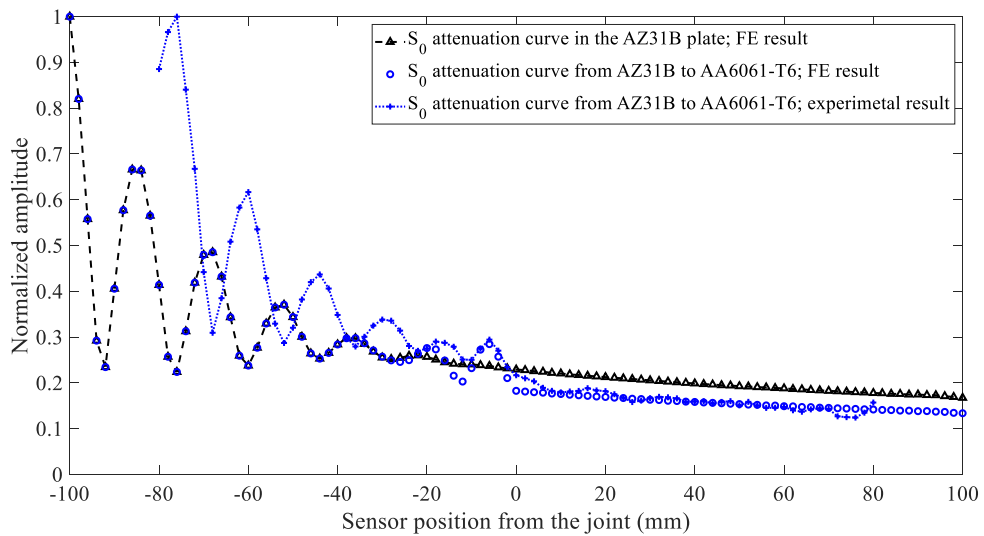


Figure 2.27. S_0 -mode attenuation curves in both the AZ31B plate (FE result; $\hat{i} = 0^\circ$; 3rd peak) and the AA6061-T6/AZ31B plate (FE and experimental results; backward direction; $\hat{i} = 0^\circ$; 3rd peak).

2.5.5 Transmission and Reflection Coefficients

The transmission and reflection coefficients of the wave modes were determined through a direct comparison of the amplitudes of the transmitted and reflected fields with the transmissions of the wave in the incidence medium (single-material propagation). Equations (2.16) and (2.17) were respectively used to compute the transmission and reflection coefficients of both the A_0 and S_0 modes. The SH_0 mode is a conversion from the S_0 mode, therefore, the transmission and reflection coefficients of the S_0 - SH_0 mode were determined using equations (2.18) and (2.19), respectively.

$$T_{(S_0 \text{ or } A_0)}^{\hat{i}} = \frac{A_{tr}^{\hat{i}}(S_0 \text{ or } A_0)}{A_{tr-s}(S_0 \text{ or } A_0)} \quad (2.16)$$

$$R_{(S_0 \text{ or } A_0)}^{\hat{i}} = \frac{A_{refl}^{\hat{i}}(S_0 \text{ or } A_0)}{A_{tr-s}(S_0 \text{ or } A_0)} \quad (2.17)$$

$$T_{(S_0-SH_0)}^{\hat{i}} = \frac{A_{tr}^{\hat{i}}(S_0-SH_0)}{A_{tr-s}(S_0)} \quad (2.18)$$

$$R_{(S_0-SH_0)}^{\hat{i}} = \frac{A_{refl}^{\hat{i}}(S_0-SH_0)}{A_{tr-s}(S_0)} \quad (2.19)$$

where:

- $T_{(\tilde{m})}^{\hat{i}}$: transmission coefficient of mode “ \tilde{m} ” at an incidence angle \hat{i} ;
- $R_{(\tilde{m})}^{\hat{i}}$: reflection coefficient of mode “ \tilde{m} ” at an incidence angle \hat{i} ;
- $A_{tr}^{\hat{i}}(\tilde{m})$: amplitude of the transmitted mode “ \tilde{m} ” after traveling a distance r

from material X to material Y; incident wave propagating from material X to material Y at an angle of incidence \hat{i} ;

- $A_{refl}^i(\tilde{m})$: amplitude of the reflected mode “ \tilde{m} ” after traveling a distance r in material X; incident wave propagating from material X to material Y at an angle of incidence \hat{i} ;
- $A_{tr-s}(\tilde{m})$: amplitude of the transmitted mode “ \tilde{m} ” after traveling a distance r in a single material X.

Amplitudes of the single-material propagations ($A_{tr-s}(\tilde{m})$ appearing in the denominators of equations (2.16) to (2.19)) can be taken at any incidence angle since there is no material interface. For the FE calculations, it was preferred to take them at the same incidence angle as that of the dissimilar-material propagation (in the numerators) to eliminate the numerical discrepancies that may result from the mesh errors due to wave propagations in different mesh shapes.

To minimize possible errors and variations in the experimental data, and to have only one reference, experimental single-material measurements ($A_{tr-s}(\tilde{m})$) were taken as an average combining all the tested incidence angles (as mentioned in Section 2.5.4). Furthermore, given that the data normalization relied on the 3rd peak of the signal, the calculations of the coefficients were based on the 3rd peak, whenever possible, for consistency.

Transmission and reflection coefficients can be calculated after the wave travels any distance r , as long as r is kept constant between the dissimilar-material and single-material propagations (same r for the numerator and the denominator). For example, the FE transmission coefficient of the S_0 mode can be calculated using any of the attenuation curves presented in Figure 2.26(a),(b), or (c), by the division of the value of any blue point (propagation from AA6061-T6 to AZ31B) over the value of its

corresponding black point (AA6061-T6 single-material propagation) at the same sensor position. Calculations should be performed after the wave interacts with the material interface (sensor position > 0). Similarly, values from Figure 2.24(a), (b), or (c) can be used to calculate the experimental transmission coefficient of the S_0 mode. Since experimental data show some perturbation, the transmission coefficient was calculated using all possible data points of each peak, then the average value was considered. Experimental coefficients were calculated using all the possible peaks, and the peaks with minimal variations were considered. This process was also applied to calculate all the transmission and reflection coefficients of the studied modes.

Figure 2.28 and Figure 2.29 show the transmission and reflection coefficients of the symmetric (S_0 and S_0 - SH_0) and anti-symmetric (A_0) wave modes, respectively, for both the forward and the backward propagation directions.

The determination of all experimental coefficients was tedious due to the undesirable superpositions between the anticipated modes and other modes and/or boundary reflections. For this reason, some experimental data points are missing in Figure 2.29 (AA6061-T6 to AZ31B; A_0 reflection at $\hat{i} = 60^\circ$ and $\hat{i} = 80^\circ$). In addition, the experimental S_0 - SH_0 transmission coefficients are not available in Figure 2.28 because the transmission of this mode is extremely weak. The weak amplitude of the S_0 - SH_0 mode is also observed in the FE and PWA results (Figure 2.28). Further, the experimental results could not be determined for the backward direction because the single-material measurements from the AZ31B plate are not available.

The FE and PWA results are in good agreement. Some variations exist when comparing to the experimental results. The variation is within the acceptable range

taking into consideration the sources of errors associated with the PZT placement, material properties, weld condition, and the operational conditions during the testing.

The transmissions of the S_0 and A_0 modes remain approximately constant and unaffected by the change of the incidence angle until it becomes very steep ($\hat{i} \approx 78^\circ$), as can be seen in the experimental, FE, and PWA results. At the S_0 mode's critical angle, a sharp peak appears in the transmission before it drops back to zero. Material properties and excitation frequencies would cause a change in the critical angles of the modes and their interaction behavior; this means that the constant trait among most of the incidence-angle range may not be generalized for other types of materials and other excitation frequencies.

The values of the A_0 and S_0 transmission coefficients are above unity (≈ 1.2 for both modes) when the wave propagates from AA6061-T6 to AZ31B. This means that the amplitude of the propagating wave is amplified by about 20% when it passes from AA6061-T6 to AZ31B. On the other hand, the transmission coefficients of the LW modes are about 0.8 when the wave propagates in the opposite direction. Thus, the wave amplitude drops by about 20% when passing from AZ31B to AA6061-T6. This indicates that the wavefield is amplified when passing from a stiff medium to a softer medium, while it is attenuated when the wave's propagation direction is reversed. While energy is conserved, the energy of the wave mode propagating in a soft medium can oscillate the particles with higher amplitude than it can when propagating in a stiffer medium.

The reflection coefficients of the three wave modes (S_0 , A_0 , and S_0 - SH_0) are approximately equal for the forward and backward propagation directions, but they have opposite signs. The opposite signs mean that there is a 180° -phase difference

between the reflected modes among the two propagation directions. The similarity in the reflection coefficients, between the two propagation directions, vanishes in the vicinity of the critical angle where sudden sharp peaks appear in the forward direction. Considering the absolute values, the reflection of the A_0 mode has shown a gradual increase with the increase in the incidence angle, with values between 6 and 20% (Figure 2.29). The reflection of the S_0 mode decreases with the increase in the incidence angle until it reaches zero (at \hat{i} between 55.5° and 57.1°), after which it starts to increase. The reflected S_0 - SH_0 mode increases with the increase in the incidence angle from zero (at $\hat{i} = 0^\circ$) up to a certain angle ($\hat{i} \approx 46.5^\circ$), after which it starts to decrease, with values varying between 0 and 30%.

When an ultrasonic wave encounters a tough interface/medium, the phase of its reflection is expected to change [77]. This is observed in the results for the AZ31B to AA6061-T6 propagation and is only applicable to the shear modes (negative reflection coefficients for the A_0 and S_0 - SH_0 reflections). On the contrary, S_0 starts with a positive reflection coefficient (AZ31B to AA6061-T6), then it switches its phase at an incidence angle of around 57.2° , after crossing through the point of zero reflection. It was observed that the phase of the S_0 - SH_0 reflection in the FE results was shifted from that of experimental and PWA results, this phase-shift was ignored in the reported findings.

PWA has shown that the maximum S_0 - SH_0 conversion occurs around $\hat{i} \approx 45^\circ$, as was discussed in Section 2.2.4. FE simulations and experiments were not performed at $\hat{i} = 45^\circ$, however, this result is confirmed by the trend of the FE and experimental results. While the transmitted converted mode is extremely weak, a significant S_0 - SH_0 mode conversion appears as a reflection from the material interface, reaching values of above 20% of the incident wave amplitude.

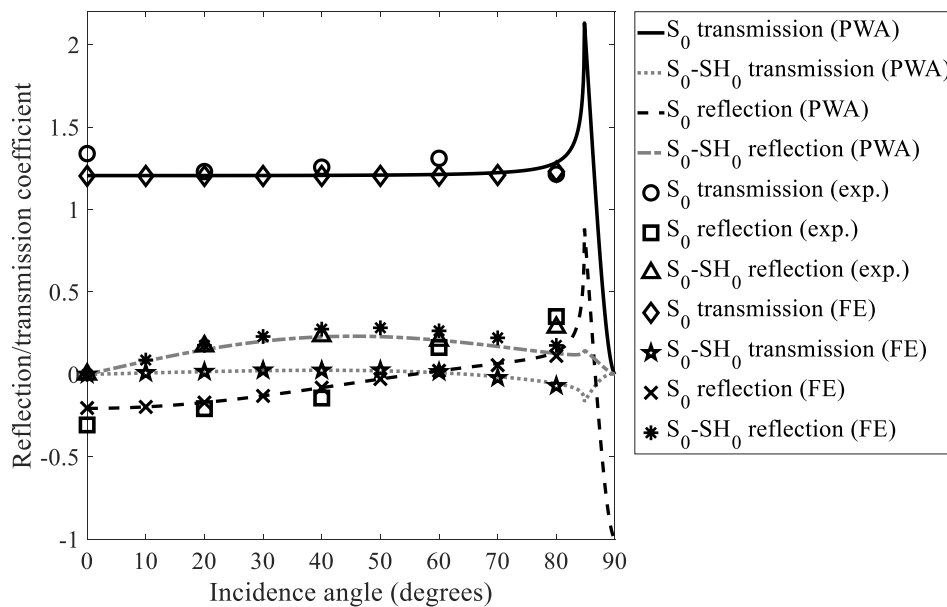
Capturing reflections with higher values than what was obtained in this study may indicate the existence of a flaw or damage within the welded AA6061-T6/AZ31B plate. This applies also when capturing transmissions of lower values than the ones that were determined for an intact joint using the same excitation frequency. However, obtaining the same values of reflection and transmission coefficients does not reflect the intact condition of the plate, unless proper sensor placement and plate coverage were insured. This can be achieved by performing sensor-network optimization [25, 78].

It can be noticed that the FE results of the transmitted S_0 mode and the experimental results of the S_0 and S_0 - SH_0 modes are a bit deviated from the PWA results at $\hat{i} = 80^\circ$. The problem at this steep angle is the possible superposition of multiple wave lobes reflecting or transmitting from the weld line due to the wave propagation near the weld. Such superpositions are difficult to separate or identify in the measured signals, which may be the reason for the recorded deviation. Additionally, evanescent modes possibly existing near the PZT or the weld line may also interfere with the studied propagating modes [69]. This is in addition to the fact that this incidence angle is close to the critical angles of both LW modes.

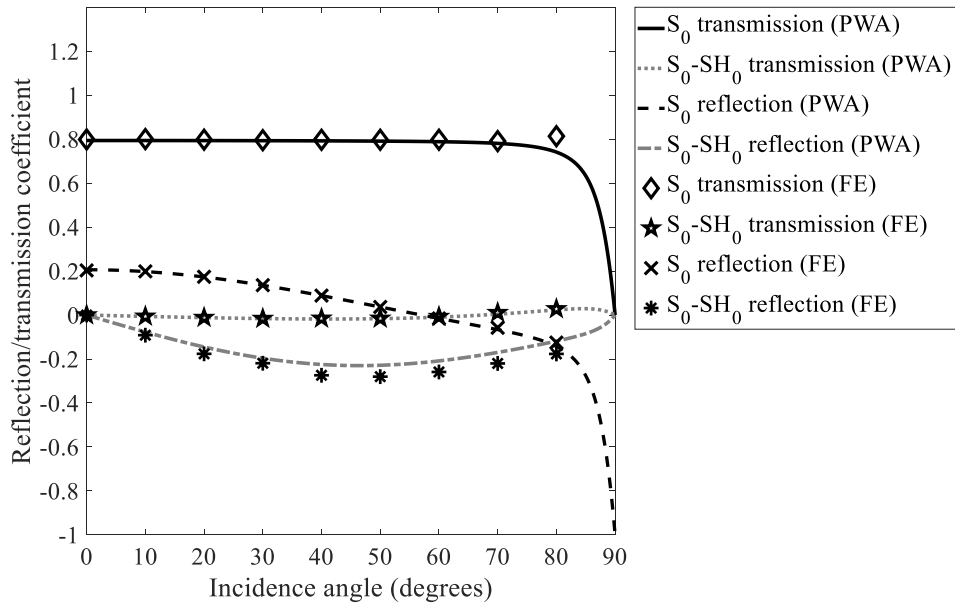
Based on the results presented in this section, mode reflections seem to be highly influenced by the excitation incidence angle. This fact should be taken into consideration by investigators before using wave reflections for NDE applications. Consequently, reflection-based sensor networks in structures containing an AA6061-T6/AZ31B dissimilar joint could be complex to design and may not be efficient enough. The incidence angles and the amount of reflection expected to emerge from the joint toward each sensor should be taken into consideration while designing or optimizing a sensor network. A stronger reflection means a higher potential of this reflection to carry

information about flaws lying between the actuator and the joint or within the joint itself.

On the other hand, Lamb-mode transmissions are almost constant up to a very steep incidence angle ($\hat{i} \approx 78^\circ$) in both the forward and backward propagation directions. This means that transmission-based NDE and sensor networks could be easier to design and use efficiently without considering the complexities of many incident-wave angles.



(a) AA6061-T6 to AZ31B



(b) AZ31B to AA6061-T6

Figure 2.28. Transmission and reflection coefficients of the studied symmetric modes.

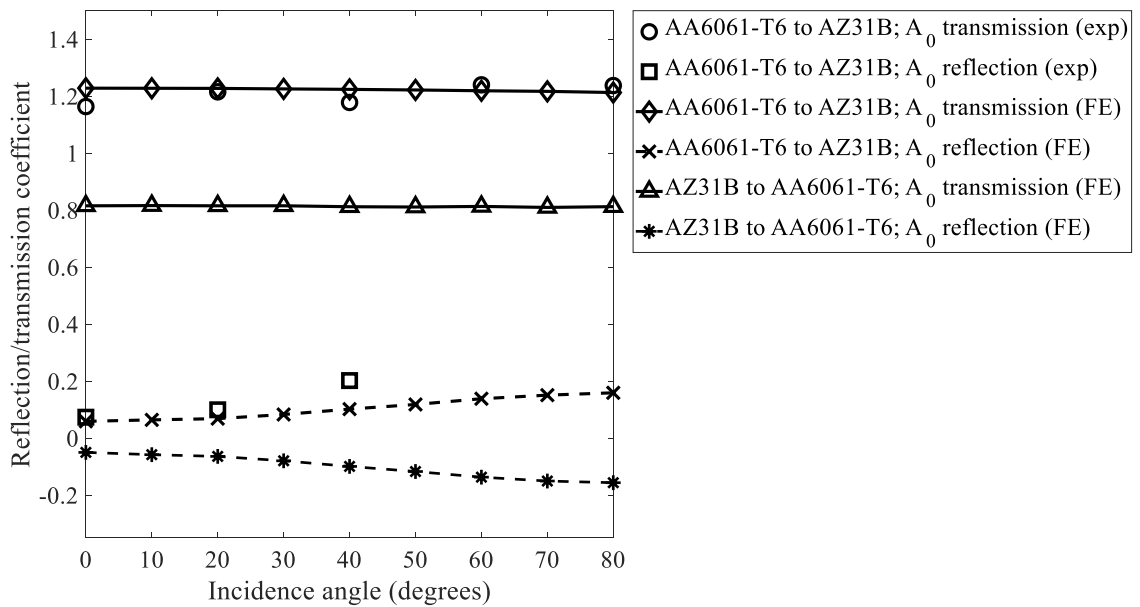


Figure 2.29. Transmission and reflection coefficients of the A_0 mode.

2.6 Summary

The propagation behavior of the fundamental Lamb-wave modes, upon the oblique interaction with dissimilar solid mediums, was numerically and experimentally investigated. An intact AA6061-T6/AZ31B joint and non-welded plate(s) were used for this purpose. A technique was developed to identify in-plane and out-of-plane guided-wave modes from the 3D-scanning-laser-vibrometer measurements and the 3D finite element simulations. Reflections from the material interface, as well as the converted S_0 - SH_0 mode's transmissions, were separated from other superpositions appearing in the measured wavefields. The transmission and reflection coefficients of the studied modes (S_0 , A_0 , and S_0 - SH_0) were assessed and analyzed. The existence of an S_0 - SH_0 mode conversion was verified when an obliquely-incident S_0 mode interacts with the material interface. The transmission of the converted S_0 - SH_0 mode was found to be extremely weak, while the amplitude of its reflection reaches values above 20% of the incident S_0 mode. Reflection amplitudes of the S_0 and A_0 Lamb-wave modes vary with the incidence angle and reach values up to around 20% of the incident waves. The transmission coefficients of the S_0 and A_0 modes are almost constant, with a variation of less than 5% until a very steep incidence angle ($\hat{i} \approx 78^\circ$). The transmission amplitudes of both modes increase by around 20% when the wave propagates from AA6061-T6 to AZ31B, while they drop by the same percentage in the inverse propagation direction.

The transmission and reflection coefficients of the symmetric modes were accurately predicted using plane-wave analytical solutions. It was confirmed that this approximation can provide good prediction, compared to finite element analysis and experimental investigations, over a range of frequency \times thickness values.

CHAPTER 3

A BAYESIAN DAMAGE IDENTIFICATION FRAMEWORK

3.1 Introduction

Many challenges still have to be addressed to guarantee a successful implementation and reliable application of SHM systems on real structures. Early damage identification is one of the main objectives that need to be met using a continuous SHM system. It includes early damage detection, localization, and assessment [26]. Achieving these three objectives with a minimal number of transducers is of high importance for the industrial community to move the developed technology from research into real-life applications.

The design of the sensor network is one of the main bottlenecks for the successful implementation of SHM systems [79]. Even in an optimized sensor network, to maximize the coverage, a relatively large number of transducers is still required. Tarhini et al. [80] and Ismail et al. [25, 78] have worked on the optimization of sensor networks using a mixed-integer nonlinear program and genetic algorithm, respectively. The networks were aiming for damage localization in plate-like structures using LWs excited and received by dual-functional PZT transducers. In [80], a plate of $400 \times 400 \text{ mm}^2$ surface area, required 14 PZTs to ensure a 95% coverage (of the area understudy). In [78], 14 PZTs were also needed to cover a plate of $500 \times 500 \text{ mm}^2$ with geometrical discontinuity (two circular holes). In [25], the coverage of a large metallic surface ($2740 \times 2385 \text{ mm}^2$), of an Airbus A330 cargo door, required 48 PZTs in the study's best-case scenario assuming a maximum effective actuator-sensor distance of 1.5 meters. Using a Bayesian damage localization approach, Cantero-Chinchilla et al. [81]

have developed various frameworks for sensor-network optimization based on the value-of-information [82] and a convex cost-benefit optimization technique [83]. In [82], 6 transducers (1 actuator and 5 sensors) were needed to ensure decent coverage of a damage area of $200 \times 400 \text{ mm}^2$, while in [83], 6 dual-functional PZTs were shown to be enough to cover a damage area more than five times larger. Based on those numbers, covering the whole structure of an aircraft or a wind turbine, as typical engineering structures, would demand the employment of a significant number of transducers. This leads to many challenges in the design and integration of the network, besides the additional weight and high cost.

Fakih et al. [12, 32, 84] have tackled the damage assessment problem based on several damage indices (DIs) extracted as metric comparisons between measurements from healthy and damaged structures. The extracted metrics proved to be useful for qualitative classification or comparison between several damage severities, assuming no other variables are affecting the measurements (e.g., measurements from different plates). However, an accurate or a quantitative assessment of the damage severity was not addressed.

The current study aims at the development of a novel technique to tackle the three damage identification objectives (detection, localization, and assessment) using a minimal number of transducers. A model-driven inverse problem methodology embedded within different computational intelligence algorithms, including Artificial Neural Network (ANN) and Approximate Bayesian Computation (ABC) [85], is employed.

Damage detection and assessment models found in literature such as time of flight [86], time-reversal [28], probabilistic damage imaging [87], and tomographic

mapping [88] rely on the physical properties of the propagating wave. Extracting the physical properties (wave speed, amplitude attenuation, etc.) requires a deep understanding of the physics and the medium that the wave is propagating in [30], which adds complexity to the implementation of such techniques. An increasing amount of artificial intelligence techniques in application to structural or mechanical engineering, including SHM, can be found in the literature [89]. The studies addressed in this area were categorized as model-driven and data-driven approaches [90, 91]. Model-driven approaches are based on models that can mimic physical data coming from real measurements to be used as benchmarks for damage detection. These models include analytical and numerical models, such as FE or semi-analytical FE models, that can reflect the physics of the actual structure. On the other hand, data-driven approaches use real measurements from a known health condition of the structure for comparison with newly collected data. Authors in [89] highlight the drawbacks of model-driven approaches due to the inefficient computational demand and the possible inaccuracies of simulation data when compared to experimental data. Sbarufatti et al. [92], have developed a model-based diagnostic framework for damage localization and assessment using LWs. LWs recorded by a 6-PZT sensor network, attached to an aluminum skin of 2-*mm* thickness, were simulated for 516 damage cases of different crack lengths and positions. Cross-correlation DI was calculated for each actuator-sensor path of the sensor network, based on the healthy-baseline simulation. The DIs were used as inputs for training supervised learning regressors based on ANNs to output damage position or length. Sensitivity to input changes was evaluated by testing the algorithm on simulated inputs with added uncertainties, and experimental validation with a good precision was introduced.

The current work addresses the drawbacks mentioned in [89] by training a LW surrogate model, based on previously performed FE simulations, to efficiently replace the FE model during online SHM. Both the physics of the propagating wave (FE model) and the data-driven approach were combined for surrogate modeling. The surrogate model can predict LW measurements at a certain sensing point in almost real-time, given the damage size and position. This has allowed for the application of Bayesian damage inference which would have been computationally infeasible if the computationally-expensive physical model was directly employed. Six damage parameters of size and position are precisely inferred using a minimal actuator-sensor configuration. In fact, the proposed surrogate modeling approach can cater to different sources of information for training like analytical, numerical, and experimental data, which would allow for a more informed model. The proposed damage identification approach has also shown robustness against measurement noise expected in experimental data.

Similar to the work by Sbarufatti et al. [92], most of the work found in literature uses DIs or features extracted from the waves as inputs for the ANN (or another machine-learning model), which in turn is used to predict the damage parameters [93-95]. On the contrary, the work in this dissertation will use ANN to produce LWs and not as a regressor of damage position and size. The inputs of the ANN will be the damage parameters (size and position), producing as output the predicted LW signal. Figure 3.1 shows a schematic illustrating the main steps of the proposed damage identification framework.

The proposed methodology is generic; i.e., can be applied to any structure. The approach has been validated using welded joints between dissimilar metals, ultimately

to detect and quantify defects that may exist at the weld line. The dissimilar-material joint represents an FSW between AA6061-T6 and AZ31B alloys. Wormhole damage within the weld is investigated for detection, localization, and assessment. The training of the ANN is carried out based on the output of the FE simulations for a large enough number of damage cases (changing 6 damage parameters of size and position). After training and validation, the ANN is adopted as a surrogate model that serves as a data feeder for the Bayesian damage-inference problem. Signals from simulation damage cases, that are not used for ANN training, are corrupted with noise then fed to the ABC damage-inference algorithm to test its performance. ABC by subset simulation (known as ABC-SubSim [96]) algorithm is used due to its efficiency and accuracy. The algorithm yields probability density functions (PDFs) of the inferred damage parameters. The PDFs show the relative degree of confidence in the possible damage scenarios, considering both measurement and modeling uncertainties.

The rest of the chapter is organized as follows. Section 3.2 introduces the FE model developed for generating sensor measurements of different damage cases. Section 3.3 presents the ANN-based surrogate modeling of the FE physical model. Section 3.4 introduces the application of ABC-SubSim to infer the damage parameters using single and multiple sensor measurements. Section 3.5 presents the inference results of selected test cases and assesses the prediction performance. Finally, conclusions are highlighted in Section 3.6.

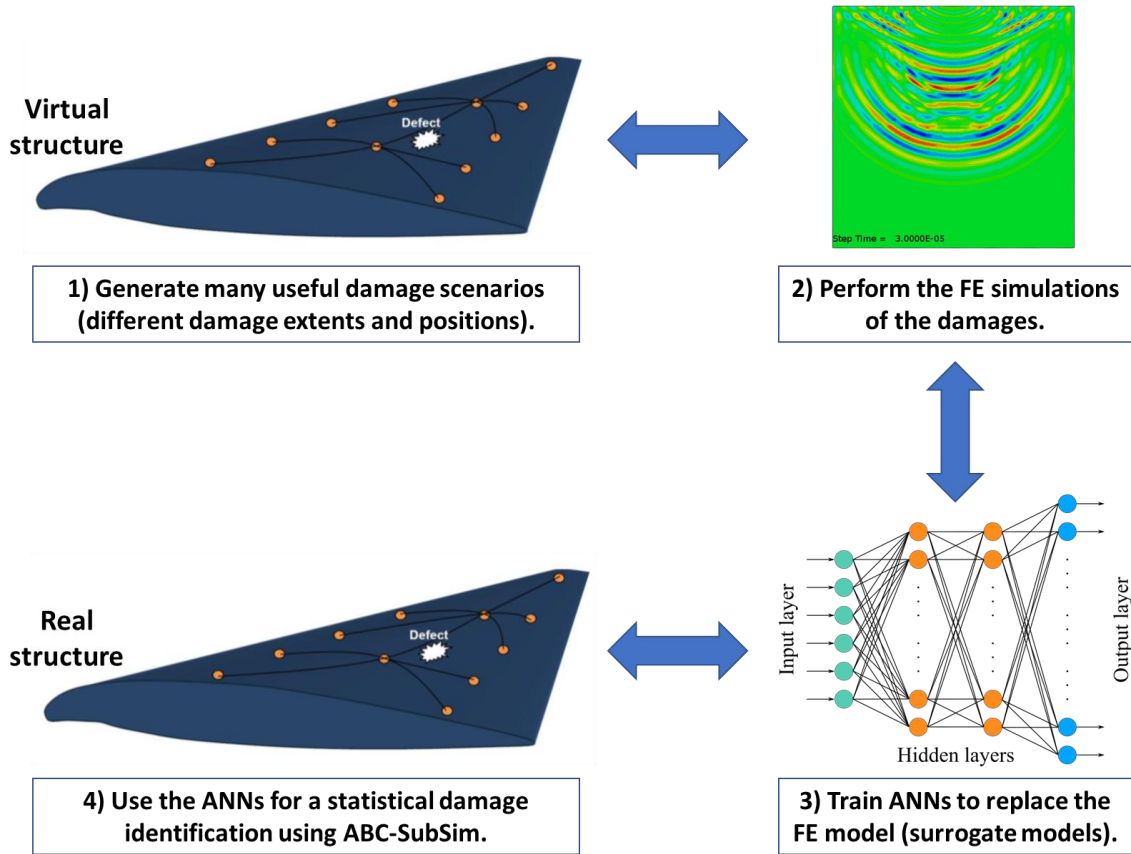


Figure 3.1. A schematic illustrating the main steps of the damage identification framework proposed in this chapter.

3.2 Finite Element Modeling

FEM is used as a forward model to obtain physical simulations of Lamb-wave propagation through a metallic plate, including a dissimilar-material butt-welded joint, under different damage scenarios. The FE simulations are performed to generate a dataset of various damage cases and their corresponding ultrasonic measurements. The dataset can then be used for training a surrogate model that can replace the forward FE model.

A dissimilar-material butt-welded joint is modeled using *Abaqus*[®]/*CAE* commercial software, where two AA6061-T6 and AZ31B plates, sized $250 \times 125 \times 3$

mm^3 , are joined together assuming a perfect joint. The two sub-plates thus form a welded plate of $250 \times 250 \times 3 \text{ mm}^3$ dimensions. The weld line lies along the X -direction as shown in Figure 3.2. Homogeneous isotropic linearly-elastic behavior is assumed for the constituent-metallic materials, whose physical and mechanical properties are listed in Table 2.1.

The geometry is meshed using linear hexahedral elements with reduced integration through the element type C3D8R. The weld region (corresponding to 5 mm before and after the interface) is meshed using an element size of $0.5 \times 0.5 \times 0.5 \text{ mm}^3$, which allows enough flexibility to represent a variety of damage extents and positions. The rest of the plate is meshed using elements of $1 \times 0.5 \times 0.5 \text{ mm}^3$ size. This mesh configuration ensures the availability of more than ten elemental-nodes/wavelength in the in-plane dimensions, based on the used excitation frequency, as recommended in the literature for LW FE simulation [27, 36, 97-99]. Moreover, enhanced hourglass control is employed to avoid extreme element deformation upon using reduced integration elements. For the boundary conditions, the edges coinciding with the X -direction on the bottom surface of the plate are simply supported, whilst the lower-left corner is fixed to prevent the model from movement, as labeled on Figure 3.2.

Abaqus[®]/*Explicit* solver is used to perform the wave simulations of 150 *microseconds* (μs) each, with a maximum time step of $5 \times 10^{-8} \text{ s}$. A five-cycle Hann-windowed sinusoidal wave of 300-*kHz* central frequency (chosen as a typical frequency) is excited through the plate by feeding radial in-plane point forces to the nodes representing a circular PZT actuator [12, 39]. The actuator, of 10-*mm* diameter, is placed at 90-*mm* center-distance from the weld line in the AA6061-T6 sub-plate, with its center located at the YZ -plane. A surface node, 80 *mm* on the other side of the

weld line (in the AZ31B sub-plate), is used as a sensing point (referred to as S1). The in-plane displacements in the direction perpendicular to the weld line (U_2 , along the Y -axis) and the out-of-plane displacements (U_3 , along the Z -axis) were recorded for S1 at a sampling rate of 20 MHz. In real-life applications, measurements along multiple directions, from the same sensing point, can be taken using a 3D SLV, similar to what was done in Chapter 2.

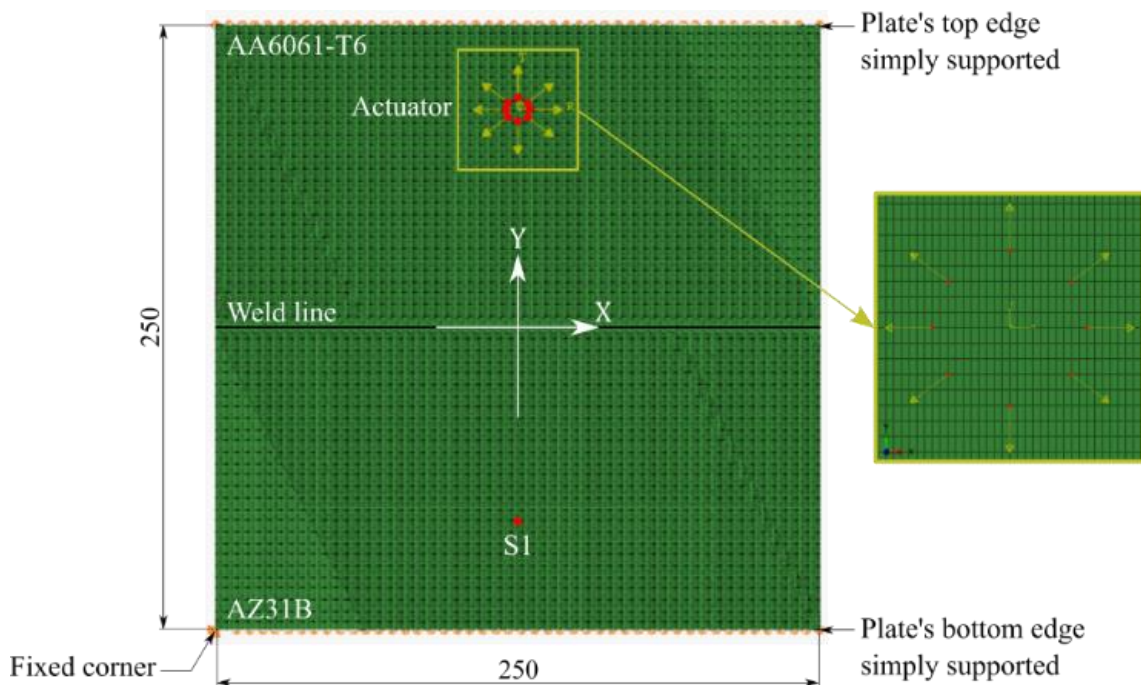


Figure 3.2. A view of the FE model showing the actuator model (inset) and the sensing point S1 (in red) on the other side of the weld line. Dimensions are expressed in *mm*.

As a typical damage type in FSW joints, wormhole damage of rectangular-cuboid shape is assumed to exist within the weld region. Simulations were performed for a set of damage cases of variable damage sizes and positions of the wormhole. Six damage parameters were used to mathematically describe the damage extent and

position, namely, length (L), width (W), and thickness (th), and x -, y -, and z -positions, respectively. A damage example is illustrated in Figure 3.3 indicating all the damage parameters. Note that the x -, y -, and z -positions were considered as the coordinates of the center of the damage with respect to the center of the plate. The damage was added to the model by deleting the damaged elements from the mesh using the *Abaqus*[®] *INPUT* file, before submitting the modified file for simulation. The automation required for modeling all the 10,800 damage cases, running their corresponding simulations, and extracting the results was performed using *MATLAB*[®]. The extraction of the results was carried out with the help of the *Abaqus2Matlab MATLAB*[®] software package [100].

For ANN training purposes, waves were excited from the AA6061-T6 to the AZ31B sub-plates using a variety of damage parameters, in addition to the intact state of the plate. The ranges of damage parameters were carefully chosen to ensure that the resulting simulated damage cases are a good representative of all possible damage scenarios. Table 3.1 lists the ranges of variation of the damage parameters along with their variation increments. Restricted by the model's geometrical constraints, 10,800 possible damage cases were finally generated.

Table 3.1. Ranges of the damage parameters used for the simulated damage cases. The third row shows the incremental step per damage parameter.

Damage parameter	L	W	th	x	y	z
Minimum value (mm)	25	1	0.5	-100	-1.25	-1.25
Increment (mm)	25	1	0.5	25	0.25	0.25
Maximum value (mm)	200	3	2.5	100	1.25	1.25

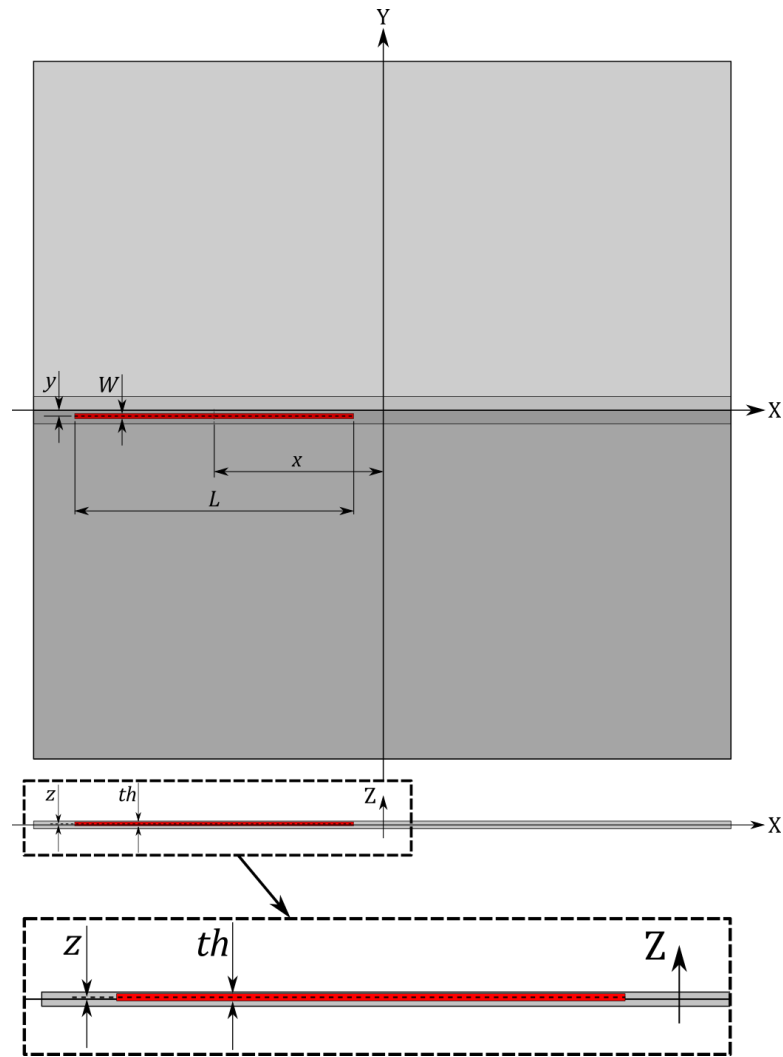
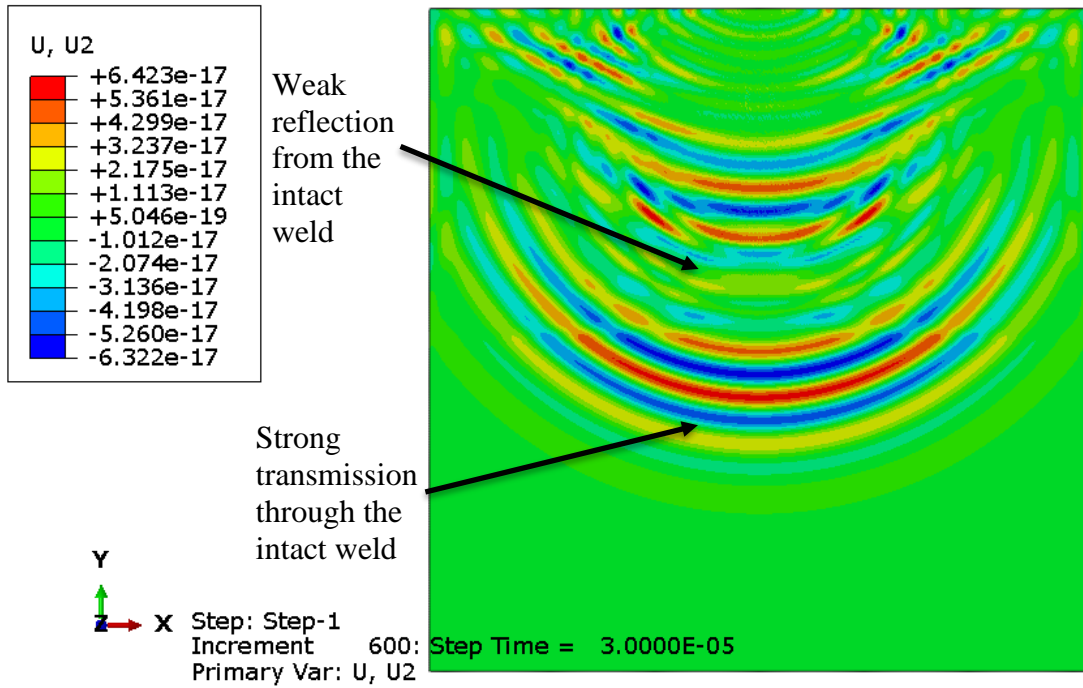


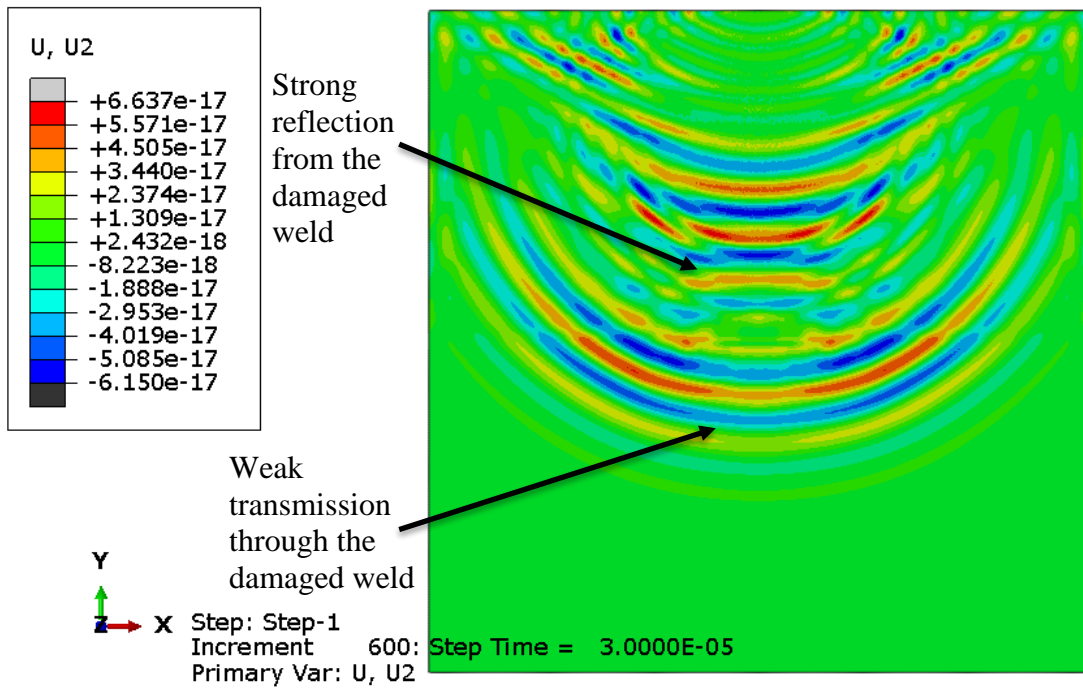
Figure 3.3. An illustration showing the welded plate containing a damage example (in red) and the six damage parameters. Position parameters are measured with respect to the center of the damage.

Figure 3.4(a) and (b) respectively display the U_2 displacements of the surface nodes of the whole FE model at time ($t = 30 \mu s$), for the intact weld and a sample of a weld including damage (D1: $L = 50 \text{ mm}$, $W = 2 \text{ mm}$, $th = 1.5 \text{ mm}$, $x = 0 \text{ mm}$, $y = 0 \text{ mm}$, and $z = 0.25 \text{ mm}$). A stronger wave reflection, bouncing back from the

weld region, can be observed in the case of damage existence, accompanied by a weaker transmission of the wave through the weld (marked on the figures).



(a) U_2 displacements (in meters) for the intact welded plate at $t = 30 \mu s$



(b) U_2 displacements (in meters) for a sample damage case D1 at $t = 30 \mu s$

Figure 3.4. FE U_2 displacements for the intact weld and a sample damage case D1; D1: $L = 50$, $W = 2$, $th = 1.5$, $x = 0$, $y = 0$, and $z = 0.25$.

3.3 ANN-Based Lamb-Wave Surrogate Modeling

In this section, an ANN-based Lamb-wave surrogate model is proposed as an approximated fast-computing forward model replacing the FE model. The surrogate modeling process is composed of several steps including data preprocessing, balancing, reduction, and splitting, in addition to the ANN design, training, validation, then testing. These steps will be explained in the following subsections.

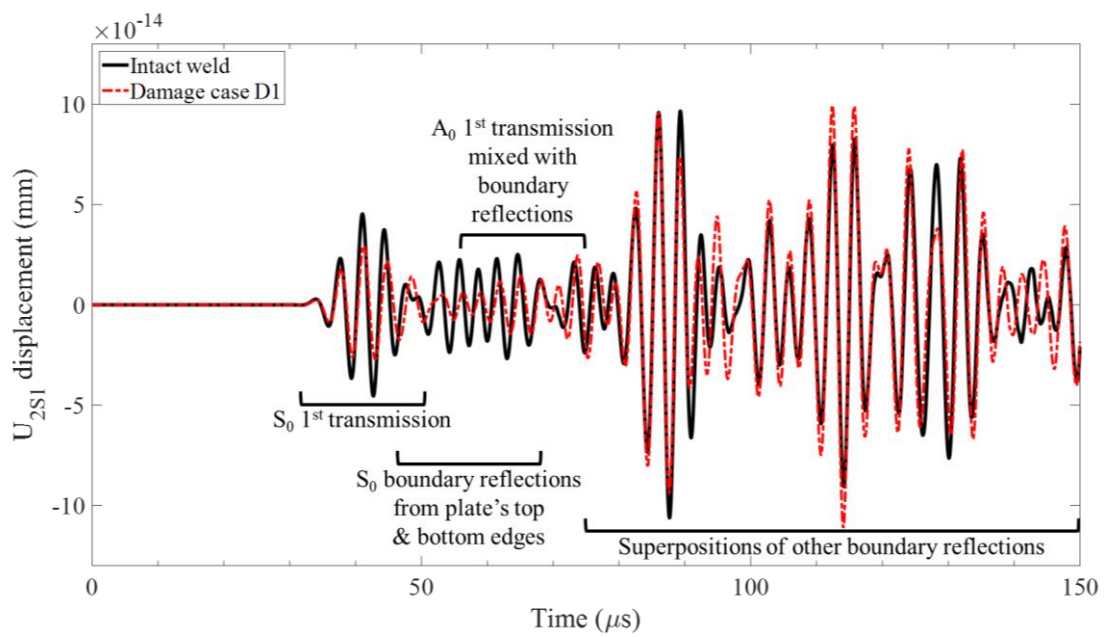
3.3.1 Data Preparation

3.3.1.1 Exploiting the Entire Ultrasonic Signal

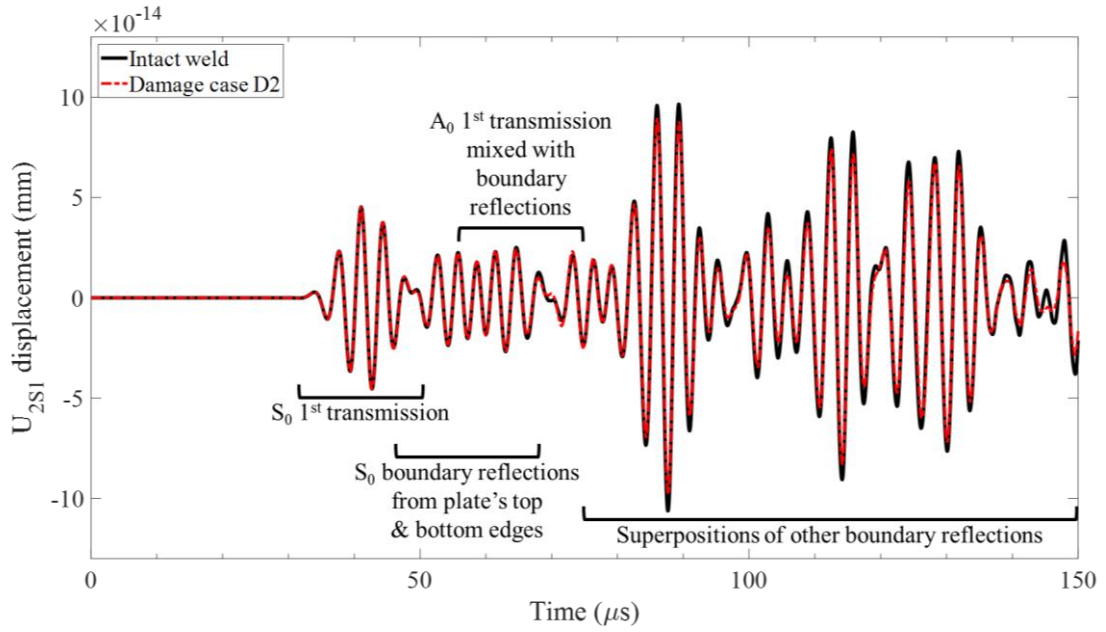
Figure 3.5(a) shows the simulation results of the U_2 displacements measured at S1 (U_{2S1}), for both the intact weld and the sample damage case D1. Amplitude variations and changes in the signal's shape are evident between the healthy and damaged case. The wave-packs corresponding to the first transmissions of the waves' S_0 and A_0 modes are marked on the figure. They correspond to the waves' S_0 and A_0 modes transmitted directly from the actuator to the sensing point. Mode identification was explained earlier in Section 2.2.2 (Chapter 2) of this dissertation, where a similar model and actuator-sensor configuration are used in the current study. Since the S_0 mode is considerably faster than the A_0 mode (Table 2.2), A_0 's first transmission is mixed with some S_0 boundary reflections, as indicated in the figure. The other wave-packs correspond to waves measured by the sensor after bouncing from the plate's boundaries, the so-called boundary reflections. The first transmission of the S_0 mode shows a significant amplitude drop (attenuation) due to the existence of the damage within the signal's direct path between the actuator and S1 (sensing path). The boundary reflections were also affected by the presence of the damage.

Similarly, Figure 3.5(b) shows the U_{2S1} measurement comparing the intact weld to another damage case (D2), of the same size as D1, but located on the left side of the weld (D2: $L = 50 \text{ mm}$, $W = 2 \text{ mm}$, $th = 1.5 \text{ mm}$, $x = -75 \text{ mm}$, $y = 0 \text{ mm}$, and $z = 0.25 \text{ mm}$). It is observed that the first transmission was not affected by the damage, unlike what was seen in the case of D1. This is due to the shift of the damage location from the line of sight. However, it is evident from Figure 3.5(b) that the boundary reflections were affected by the existence of the damage D2. Hence, it is essential to

consider the entire signal (including both the direct transmissions and boundary reflections) in the current study. For further emphasis, Figure 3.16(a) will later illustrate two damage cases where the damage does not exist within the coverage of the sensing path, however, it can still be perceived by the sensor when considering the wave's boundary reflections.



(a) Intact weld versus D1



(b) Intact weld versus D2

Figure 3.5. Raw signals of U_{2S1} for the intact weld and two sample damage cases. Damage D1 lies within the coverage of the sensing path, while damage D2 lies outside the coverage of the sensing path;

D1: $L = 50$, $W = 2$, $th = 1.5$, $x = 0$, $y = 0$, and $z = 0.25$;

D2: $L = 50$, $W = 2$, $th = 1.5$, $x = -75$, $y = 0$, and $z = 0.25$;

all parameters are in mm .

3.3.1.2 Data Preprocessing

A total of 10,801 damage scenarios were simulated using the FE model (10,800 damage cases plus one healthy weld), where both the U_2 and U_3 displacement measurements were recorded at the sensing point S1 (U_{2S1} and U_{3S1}). Hence, two ANNs will be trained for the prediction of U_{2S1} and U_{3S1} , separately.

To minimize the computational burden, data preprocessing was performed for all the available FE-wave simulations before being used as training or testing units.

Data reduction was carried out by three different means: signal cutting, signal down-sampling, and sample reduction, where the latter is explained in Section 3.3.2. The first

30- μ s signal-segment was cut out from all the signals since it does not carry any useful information, as can be seen in Figure 3.5. Further, all the signals were down-sampled from 20-MHz to 3-MHz sampling rate. After preprocessing, the length of each signal was reduced from 2,999 to 361 data points. Lowering the number of data samples in the signal lowers the size of the ANN's output layer in the same manner and, thus, allows for a less complex ANN architecture. This would not only reduce the training and testing computational cost of the ANN, but would also lead to a much faster surrogate model.

3.3.2 ANN Design and Performance

3.3.2.1 Training and Testing Datasets

The concept of overfitting is when the trained model learns the very details of the training data in such a way that it negatively affects the performance of the model on new data. When over-fitted, the trained model will fit too well to the training data that it would even learn the noise, errors, and outliers which are possibly available in the training dataset [101]. Such an over-fitted model would not fit for newly presented data, thus giving wrong or inaccurate predictions. This problem is called a generalization problem of the trained model. Generalization problems can also happen if the training dataset (i) is not large enough or not carefully chosen to represent the whole population of known and unknown samples, or (ii) is unbalanced in a way that makes the model learn about a part of the population more than it learns about other parts (so-called biased data). For instance, if one is training a model to differentiate between images of dogs and cats, he/she should provide the model with a balanced training set containing images of both dogs and cats. If the training data contains 90% images of dogs and only

10% images of cats, it will be expected from the model to overfit to dogs while not learning well the features of cats. At the same time, the model should also be provided with enough images to represent all kinds of dogs and all kinds of cats. If the model is given many images of the same kind of cats while not as many of the other kinds, it may overfit to this kind of cats while possibly missing the right classification of the other kinds. All such imbalance or bias in the training dataset would prevent the model from generalization when testing it over new data samples.

In the current study, the training data come from FE simulations, which cancels the possibility of noisy or outlier data within the training set. Further, the geometry of the monitored structure (the welded region of the plate in this case) makes the universe of all possible damage scenarios finite and well-bounded. This makes it easy for the user to define a well-balanced and well-distributed training dataset that can be a good representative of the whole population of possible damages. These facts allowed the training of the ANNs down to extremely-low performance errors, without the concern of having generalization problems. Figure 3.6 displays an illustration of the rationale behind this concept.

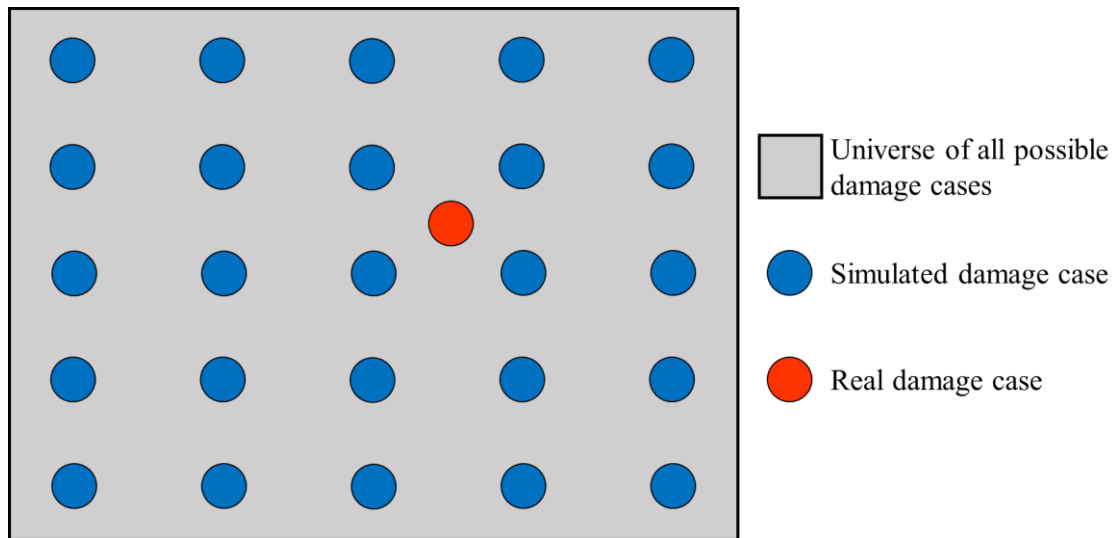


Figure 3.6. An illustration showing a well-balanced and well-distributed training dataset which should be convenient for training down to extremely-low performance errors, without generalization concerns when seeing a real damage case.

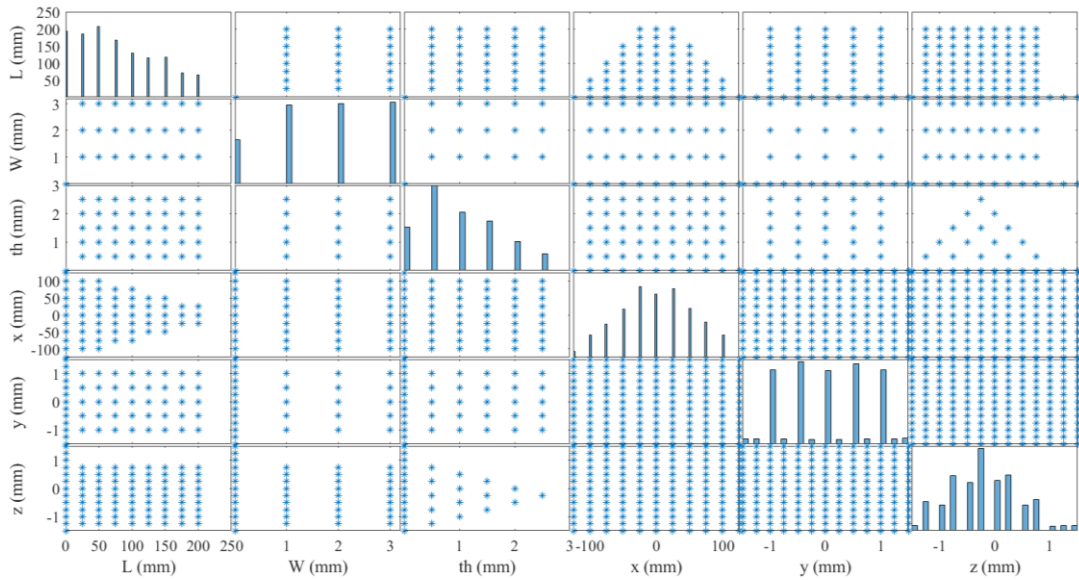
As mentioned earlier, 10,801 observations were collected, for each of the two ANNs. Out of these, 594 damage cases were chosen in a well-distributed manner to test the effectiveness of the approach over different ranges of damage sizes and positions. Thus, 10,207 cases were kept for training, including one healthy-weld case. To balance the training dataset and improve the results for small damages, the healthy case was repeated 1,859 times with different virtual damage positions (according to Table 3.2), thus increasing the total amount of observations in the training dataset to 12,065 cases for each of the two ANNs. Since selecting a random dataset from a large pool would keep a good data balance and distribution, the training dataset was reduced to half through a random sample reduction process. Finally, the training and testing datasets included 6,032 and 594 samples, respectively, for each of the two ANNs.

Figure 3.7(a) and (b) show scatter plots of the damage parameters of the training and testing data, respectively. The training dataset is well-balanced and well-

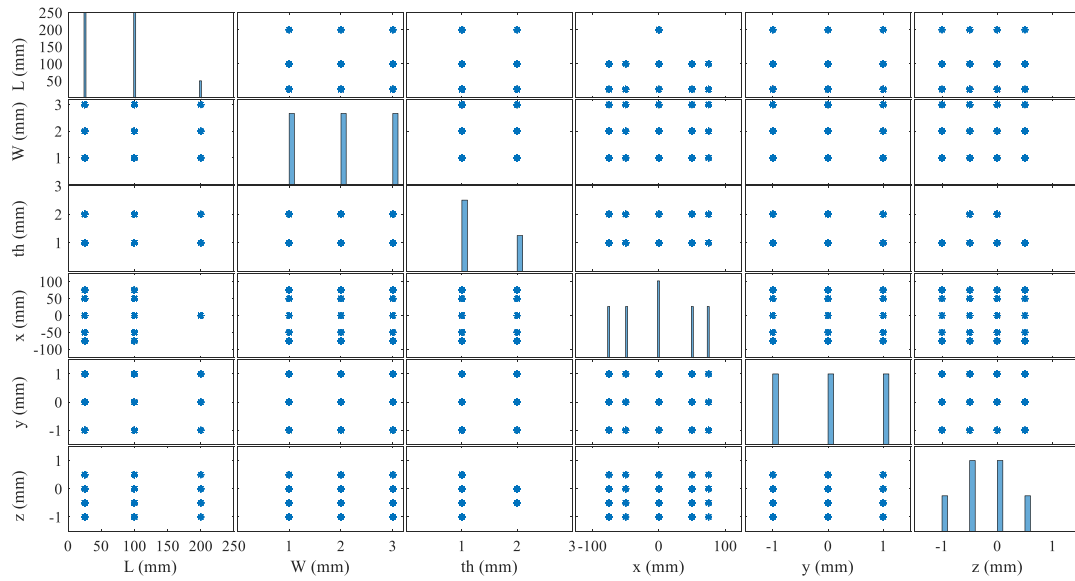
distributed over the universe of all possible damage cases, thus avoiding overfitting and generalization problems when training. The testing dataset is a good representative of all possible damage scenarios, which would provide a full picture of the methodology's overall performance.

Table 3.2. Range of virtual damage positions of the healthy signals added to the training dataset (for data balance). 1,859 healthy signals with different virtual damage positions were finally added.

Damage parameter	L	W	th	x	y	z
Minimum value (mm)				-125	-1.5	-1.5
Increment (mm)	0	0	0	25	0.25	0.25
Maximum value (mm)				125	1.5	1.5



(a) 6,032-sample training dataset (after sample reduction)



(b) 594-sample testing dataset

Figure 3.7. Scatter plots of the damage parameters of the training and testing datasets, chosen from the FE simulations.

3.3.2.2 ANN Architecture and Training

The inputs (predictors) of each ANN are the six damage parameters of the wormhole damage lying within the weld, namely L , W , th , x , y , and z , while the outputs are a set of 361 values representing the data points of the predicted LW signal received at the sensing point S1. After a trial and error process, an ANN architecture of two 200-neuron hidden layers plus a 361-neuron output layer was adopted, as shown in Figure 3.8.

The training dataset was split using the typical ANN design procedure into a training set and a validation set. To ensure good data splitting and better model generalization, *k-fold cross-validation* of ten folds (10-fold cross-validation) [102] was applied. *Scaled conjugate gradient backpropagation function* [103] was used for

training the model, and the performance of the ANN, while training, was evaluated using the *mean square error* (MSE) function. To prevent overfitting, the *maximum validation fails* ($maxFails = 1000$) early stopping criterion was used. The other stopping criteria were relaxed so that the training would not stop except when reaching the *maximum validation fails*. These include the maximum number of training epochs ($epochs = 500,000$), the best performance over the training data ($goal = 10^{-6}$), and the *minimum performance gradient* ($minGrad = 10^{-7}$).

Besides being used for testing during the ANN-training process, the testing signals can be visually checked to be in good agreement with the signals predicted by the trained ANN models. A sample of the ANN predictions for two of the testing damage cases is shown in Figure 3.9(a) and (b), as compared to the signal obtained using FE simulation (U_{3S1} measurement). The two damage cases were randomly chosen to be, respectively, as follows (D3: $L = 25\text{ mm}$, $W = 1\text{ mm}$, $th = 1\text{ mm}$, $x = -75\text{ mm}$, $y = -1\text{ mm}$, and $z = -1\text{ mm}$; and D4: $L = 100\text{ mm}$, $W = 3\text{ mm}$, $th = 1\text{ mm}$, $x = 50\text{ mm}$, $y = 1\text{ mm}$, and $z = 0\text{ mm}$). The signals predicted by the ANN are very close to the real signals calculated using FEM. The signals predicted by the ANN match well with the simulated signals calculated using FE analysis.

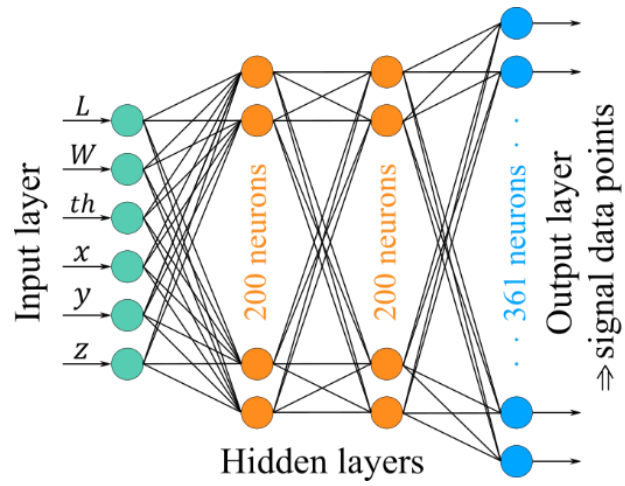
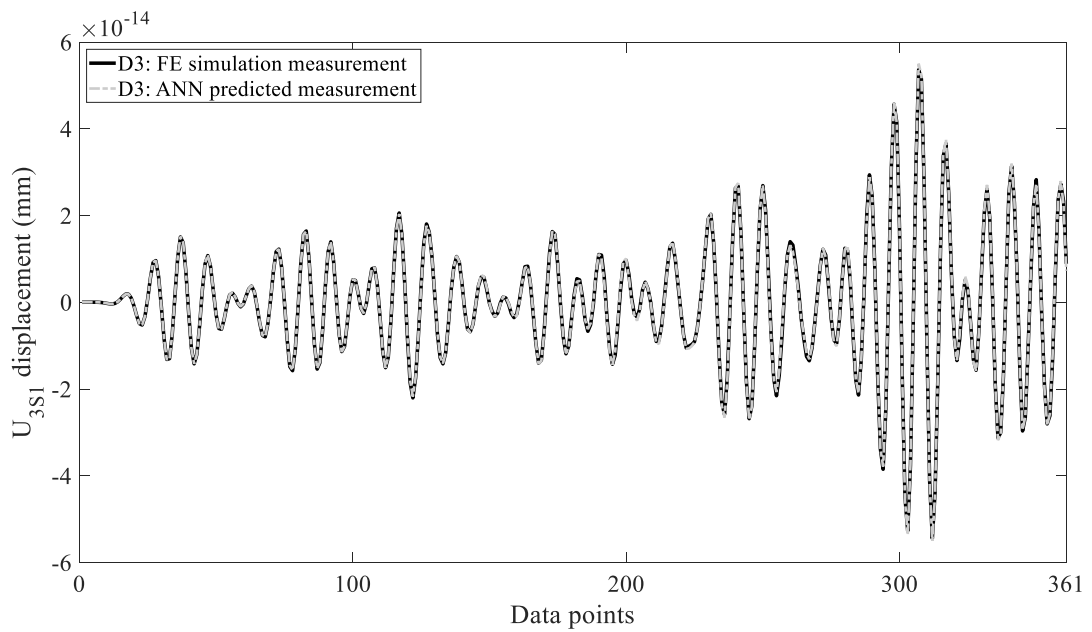
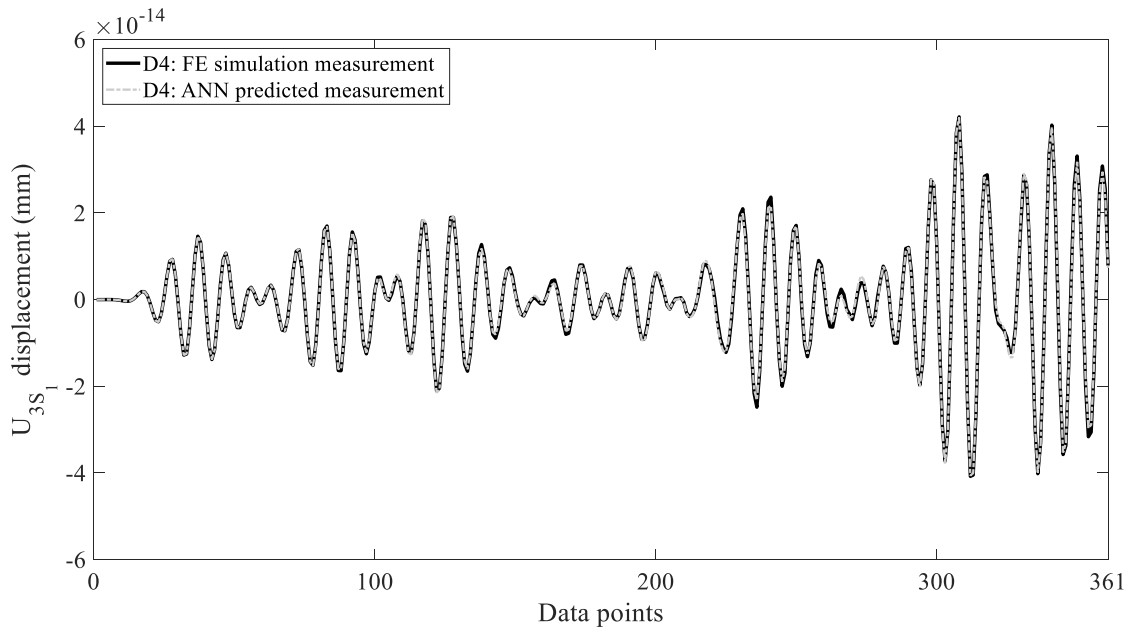


Figure 3.8. The architecture of the used ANNs for Lamb-wave surrogate modeling, determined using a trial and error process.



(a) D3



(b) D4

Figure 3.9. Two sample results of the ANN prediction of LW sensor measurement, when given specific damage parameters, compared to the signals obtained using FE simulation; D3: $L = 25, W = 1, th = 1, x = -75, y = -1,$ and $z = -1$; D4: $L = 100, W = 3, th = 1, x = 50, y = 1,$ and $z = 0$; all parameters are in mm .

3.4 Damage Inference by Approximate Bayesian Computation

Approximate Bayesian Computation is an efficient methodology for solving Bayesian inverse problems [96]. It is practically useful when the likelihood function of the model is unknown or difficult to compute. To apply ABC inference over a sensor measurement, a large set of ultrasonic signals, of known damage parameters, should be compared in a probabilistic manner to the reference signal measured from the real structure. The trained ANNs will serve as the forward models for LW prediction based on the input damage parameters. This makes possible the generation of a huge dataset of signals in a short period of time, rendering the ABC inference algorithm computationally applicable and suitable for onboard and/or online applications.

In this work, Approximate Bayesian Computation by Subset Simulation (ABC-SubSim) [96] is used to infer six damage parameters (size and position) from ultrasonic signals measured by specific sensor(s). To confer the reader with a minimal background about the inference methodology, the standard ABC algorithm is first introduced under a unified notation, before explaining the more efficient ABC-SubSim variant applied in this work.

3.4.1 Standard ABC for Damage Inference using One Sensor Measurement

Figure 3.10 shows a flowchart that explains how a standard ABC algorithm can be applied to the current damage identification problem when using one sensor measurement. The algorithm compares a randomly-generated ultrasonic wave (v) against the output (u) of the model (real structure), for which the inference of model parameters (damage parameters in this case) is needed. A suitable comparison distance metric (ρ) is chosen, and a threshold of acceptance or rejection is set using a tolerance parameter (ϵ). The algorithm then stochastically changes the values of the unknown parameters (θ_r) until the distance ρ between the model's output (u) and the random signal (v) lies within the set threshold ($\rho \leq \epsilon$). This random sample (θ_r) is then called a matching sample. This process is repeated until the desired number of matching samples (N) is attained. Finally, the set of all parameters passing this threshold condition (Θ_r), are selected to represent a sample approximation of the PDFs of the real model parameters, named as *approximated posterior*. The ranges that were used for the random generation of the six damage parameters are listed in Table 3.3. Problem geometric constraints are respected during the random parameter-generation process.

The number of generated samples (N) is identified by the user. A higher number of samples would provide a better quality of the *approximated posterior*. However, this is associated with higher computational demand. The quality of the *approximated posterior* also depends on a suitable selection of the distance metric (ρ) and the tolerance parameter (ϵ). The distance metric can be any kind of evaluation of the difference between the real sensor measurement (u) and that predicted by the ANN surrogate model (v) based on the randomly-generated damage parameters (θ_r). The tolerance parameter (ϵ) accounts for how close the two signals are, through the chosen distance metric. The choice of ϵ is a matter of the amount of computational effort that the user wishes to expend, with a possible guiding principle [96]. For a sufficiently small value ($\epsilon \rightarrow 0$), $v \rightarrow u$, hence all accepted samples come from the closest approximation to the required *posterior*. This desirable fact is at the expense of a high computational effort (usually prohibitive) to get $v = u$ using the forward model, i.e., using the ANN surrogate model in this case. On the contrary, as $\epsilon \rightarrow \infty$, all accepted observations come from the *prior* (random samples). Therefore, the choice of ϵ reflects a trade-off between computability and accuracy.

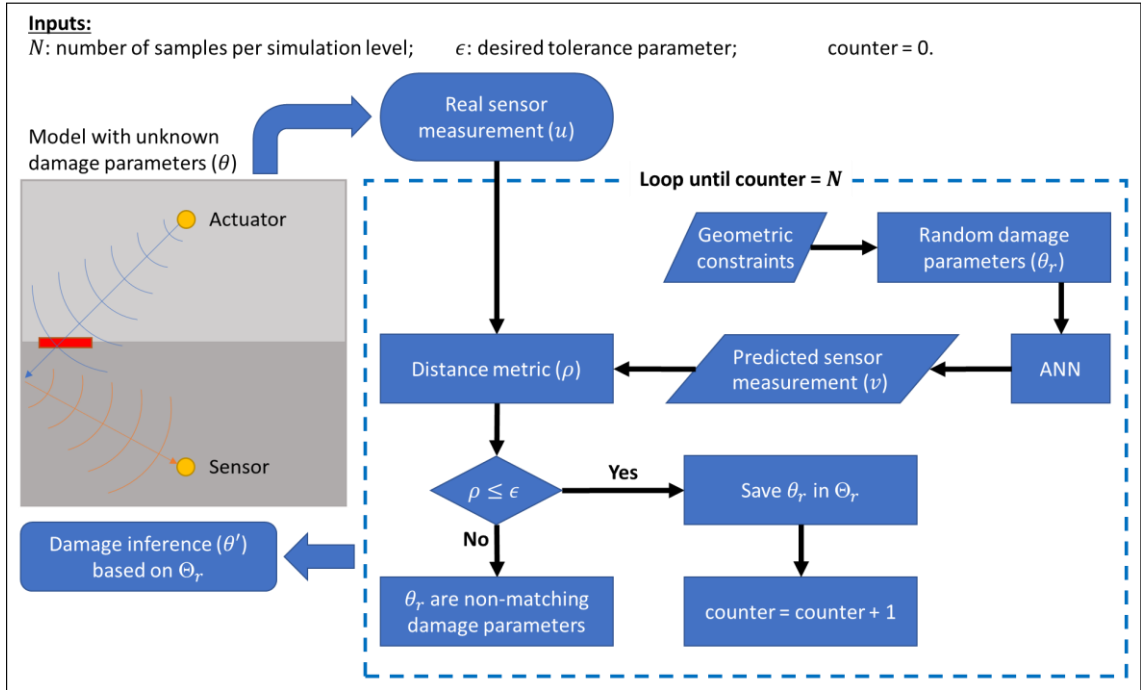


Figure 3.10. A flowchart explaining ABC damage inference from one sensor measurement using an ANN Lamb-wave surrogate model.

Table 3.3. Range of definition of the damage parameters when randomly generating damage cases (θ_r) for the application of ABC or ABC-SubSim.

Damage parameter	L	W	th	x	y	z
Minimum value (mm)	0	0	0	-125	-1.5	-1.5
Maximum value (mm)	250	3.2	3	125	1.5	1.5

3.4.2 ABC-SubSim for Damage Inference using One Sensor Measurement

ABC-SubSim merges the ABC principle with the technique of *Subset Simulation* [104-106] to achieve computational efficiency in a sequential way. It was proposed by Chiachío et al. [96] as a combination between the ABC algorithm and a highly-efficient rare-event sampler that draws conditional samples from a nested sequence of sub-domains. Figure 3.11 provides a simplified flowchart explaining the

implementation of ABC-SubSim for LW-based damage inference using one sensor measurement. The algorithm is implemented such that a maximum number of simulation levels (m) is allowed in case the specified final tolerance parameter (ϵ_f) is too small.

The algorithm starts by generating N samples of random damage parameters that satisfy the problem's geometric conditions (*prior*). Each random sample is denoted by θ_r , and the set of all random samples is denoted by Θ_r . The ANN LW surrogate model is used to generate N predicted sensor measurements from Θ_r . Each predicted sensor measurement is denoted by v , and the whole set of predicted measurements is denoted by V . The distance ρ between each of the predicted sensor measurements and the real sensor measurement (u) is calculated, giving a set (P) of N distances. Θ_r is then sorted according to the obtained distances, and an amount of Np_0 samples of the lowest ρ values are chosen out of the N available samples, where p_0 is a user-defined conditional-probability value. The chosen samples are used as seeds from which new $N(1 - p_0)$ samples closer to u are generated. This finalizes one simulation level, where new N samples, closer to u , are available for the next simulation level. The tolerance parameter (ϵ), attained at the current simulation level, is calculated as the average between the Np_0^{th} and the $(Np_0 + 1)^{th}$ distance. If the stopping criterion ($\epsilon \leq \epsilon_f$) is satisfied, the algorithm stops, otherwise, this process is repeated up to m simulation levels, where m is fixed after a trial and error process.

For sample generation, the chosen Np_0 samples are used as seeds for Np_0 Markov chains of length $1/p_0$ each, where the new $(1/p_0 - 1)$ samples in each chain are generated by the modified Metropolis algorithm (MMA) proposed in [104]. This process is explained in equation (3.1).

$$\theta_r(i, p) = \theta_r(i - 1, p) + STD_{prop}(j - 1, p) \times rand \quad (3.1)$$

where:

- i : is the index of the sample within the Markov chain, ranging from 1 to $1/p_0$;
- p : is the index of the generated damage parameter, ranging from 1 to the number of inferred parameters (6 damage parameters in this case);
- j : is the index of the current simulation level, ranging from 1 to m ;
- STD_{prop} : is the proposed standard deviation within which a new sample is generated around the parent sample;
- $rand$: is a standard normally-distributed random number; $rand \in [0, 1]$.

Each one of the seeds is used as a “parent” from which $(1/p_0 - 1)$ “children” samples are generated sequentially. The predicted sensor measurement (v) of each newly-generated child ($\theta_r(i)$) is tested against the real sensor measurement (u) utilizing the distance metric. If the distance between v and u is less than or equal to the current tolerance parameter ($\rho \leq \epsilon$), the child is accepted, otherwise, the child is replaced by its previous parent sample ($\theta_r(i - 1)$). For this process, the choice of STD_{prop} is recommended to be such that the acceptance rate (R_{acc}) of the newly-generated samples is within a range of 20% to 40% of N [107]. This choice is problem-dependent and may need the use of different STD_{prop} values at each simulation level, based on the range and convergence of each damage parameter. This process depends on the experience and engineering common sense of the user and may include some trial and error. Another alternative is to adaptively choose STD_{prop} [96, 108].

This sample generation process shows the strength that *Subset Simulation* adds to ABC, given that such a small probability (Np_0) is converted into a sequence of larger

conditional probabilities. A new generation of samples is bred out of the best samples from the previous generation, where accepting new samples depends on their evaluation based on the proposed distance metric (ρ). Repeating this process over several simulation levels leads to the convergence into a rich *approximated posterior*, while attaining a low enough tolerance parameter (ϵ).

The choice of the conditional probability p_0 has a significant influence on the number of intermediate simulation levels required by the algorithm. The higher p_0 is, the greater is the number of simulation levels needed to reach the specified tolerance ϵ_f . This necessarily increases the computational cost of the algorithm. Conversely, the smaller p_0 is, the lower is the quality of the *approximated posterior*. The choice of p_0 , therefore, requires a trade-off between computational efficiency and the accuracy of the algorithm, in terms of the quality of the ABC *posterior* approximation. It is recommended in the literature [96, 104, 107] to use a value in the range of $0.1 \leq p_0 \leq 0.3$. The values of ABC-SubSim control parameters that were used in this study are listed in Section 3.4.3.

The well-known *cosine* distance was chosen as the distance metric for comparison between the real (u) and predicted (v) ultrasonic signals. The metric was used in absolute value to have a range of $0 \leq \rho \leq 1$, as shown in equation (3.2).

$$\rho = \left| 1 - \frac{uv'}{\sqrt{(uu')(vv')}} \right| \quad (3.2)$$

where:

- u' and v' : are the transposes of the signals u and v , respectively, treated as vectors of data points.

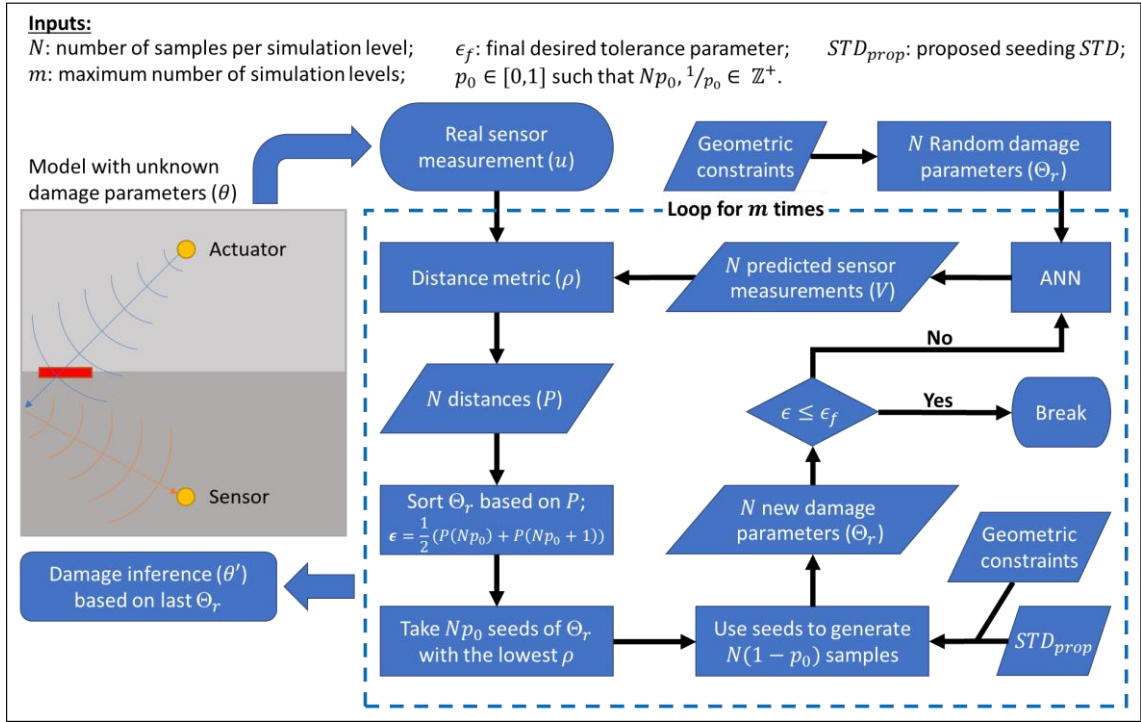


Figure 3.11. A flowchart explaining ABC-SubSim damage inference from one sensor measurement using an ANN Lamb-wave surrogate model.

3.4.3 Data Fusion: Applying ABC-SubSim to Multiple Sensor Measurements

To obtain an accurate and robust damage inference, more than one sensor measurement may be used. The application of ABC-SubSim using multiple sensor measurements requires the use of multiple LW surrogate models (i.e., trained ANNs), each for the prediction of one of the sensor measurements, as mentioned earlier in Section 3.3.1. Assuming the use of S sensor measurements, the same procedure shown in the flowchart of Figure 3.11 is used. However, S ANNs are employed to predict S sets of sensor measurements (V_1, V_2, \dots, V_S) , each composed of N predicted measurements of the same sensor, but corresponding to the N different random damage parameters (Θ_r) . The S sets (V_1, V_2, \dots, V_S) are then compared to the S real sensor

measurements (u_1, u_2, \dots, u_S) . To this end, each single sample of random damage parameters θ_r will have S distances corresponding to the S sensor measurements.

To proceed with the algorithm, data fusion of the S sensors is proposed at this stage, where the S distances are all merged into one distance metric. The combination of the distances is performed as a simple multiplication, accounting for a logical AND operator, according to equation (3.3). After the metric combination, each θ_r will have a single corresponding distance metric $\rho = P(n)$, and the rest of the algorithm can then be continued similar to ABC-SubSim using a single sensor measurement (refer to Figure 3.11).

$$P(n) = \prod_{s=1}^S \rho_s(n) \quad (3.3)$$

where:

- n : is the index of the sample θ_r within the set Θ_r , ranging from 1 to N ;
- s : is the index of the corresponding sensor measurement, ranging from 1 to S .

The values of all the ABC-SubSim control parameters that were used in this study are listed in Table 3.4. The number of simulation levels (m) was limited up to 13, but was controlled by the acceptance rate of the newly generated samples. As mentioned earlier, an acceptance rate ($20\% \leq R_{acc} \leq 40\%$) is usually sought to have good breeding. Thus, all simulation levels with an $R_{acc} < 15\%$ were disregarded. Consequently, depending on the damage case and the used sensor measurement(s), m generally varied between 10 and 13 simulation levels.

Table 3.4. ABC-SubSim control parameters used in this study.

Control parameter	Value						
N	8000 samples/simulation level						
m	≤ 13 simulation levels						
ϵ_f	10^{-6S}						
p_o	0.25						
STD_{prop}	10	0.5	0.5	10	0.5	0.5	} mm
	10	0.4	0.4	10	0.4	0.4	
	5	0.3	0.3	5	0.3	0.3	
	5	0.2	0.2	5	0.2	0.2	
	3	0.1	0.1	3	0.1	0.1	
	3	0.05	0.05	3	0.05	0.05	
	2	0.05	0.05	2	0.05	0.05	
	2	0.05	0.05	2	0.05	0.05	
	1	0.05	0.05	1	0.05	0.05	
	1	0.05	0.05	1	0.05	0.05	
	1	0.05	0.05	1	0.05	0.05	
	1	0.05	0.05	1	0.05	0.05	

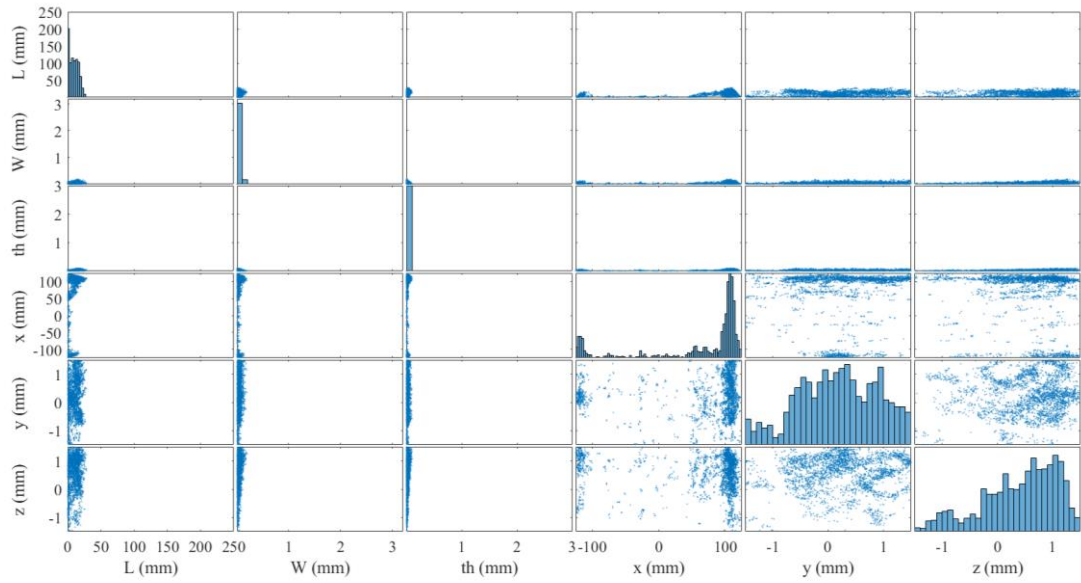
3.5 Results and Discussion

3.5.1 Damage Detection

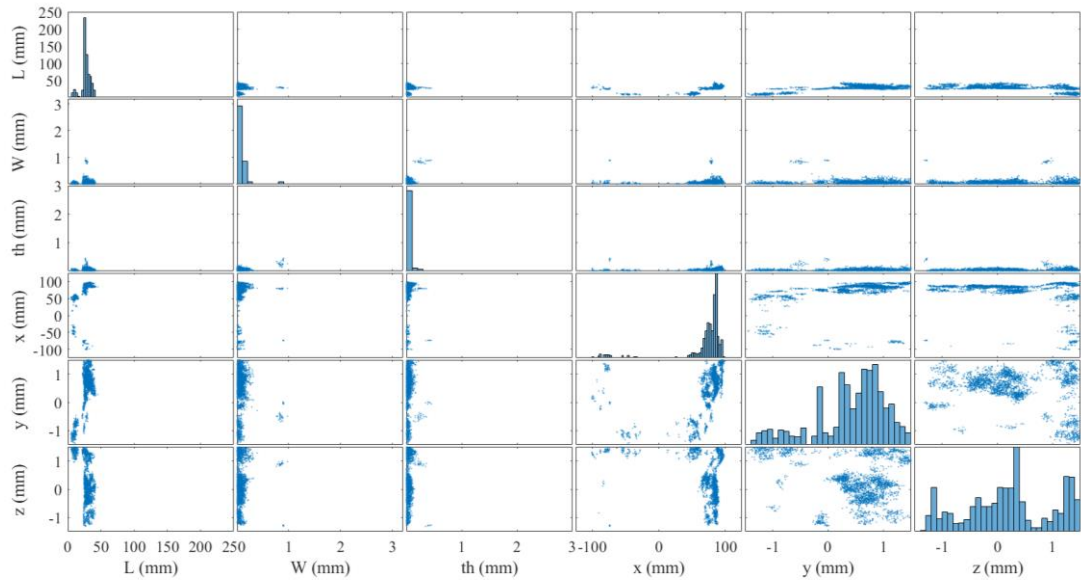
The inference results are visualized as scatter plots of the *approximated posterior* of the damage parameters (Θ_r) determined by ABC-SubSim. For example, Figure 3.12(a) shows the damage-inference results of the intact weld using U_{2S1} . Each scatter plot in the figure corresponds to two of the damage parameters plotted together. The plots on the diagonals are probability histograms representing the PDF of each of the damage parameters. While the size parameters of the damage are all successfully inferred to be null (1st three columns), the virtual position of the nonexistent damage can be anywhere as predicted in the scatter plots of the position parameters (the last three columns).

To ensure the healthy case can still be captured in the presence of noise, the intact signal was corrupted with random colored noise of a frequency up to 450 kHz. The maximum noise level (NL) is 3% of the healthy signal's maximum amplitude (check Section 3.5.5 for the effect of sensing-noise level). Figure 3.12(b) shows the inference results after adding the sensing noise to the tested healthy signal. Damage is inferred by calculating the *maximum a posteriori* (MAP) of each damage parameter using its obtained PDF. A damage-detection rule was set such that *all the three damage-size parameters (L , W , and th) should surpass their set thresholds (α , β , and γ , respectively) to indicate that a wormhole damage exists*. Since the targeted damage type is the wormhole welding defect (a relatively macro-sized damage type), the thresholds were chosen to be $\alpha = 1 \text{ mm}$, $\beta = 0.1 \text{ mm}$, and $\gamma = 0.1 \text{ mm}$. Size thresholds are problem-specific and should be chosen carefully based on the problem at hand and the targeted damage types and shapes.

MAP was calculated for the analyzed case (Figure 3.12(b)) to be $L = 25.2 \text{ mm}$, $W = 0.02 \text{ mm}$ ($< \beta$), and $th = 0.01 \text{ mm}$ ($< \gamma$). Even though the length parameter was not successfully inferred, it can still be concluded that there is no damage within the weld from the inference of the width (W) and thickness (th) damage parameters (second and third columns).



(a) Without sensing noise – $m = 10$ simulation levels, $R_{acc} = 22.1\%$.



(b) With sensing noise – $m = 11$ simulation levels, $R_{acc} = 22.1\%$.

Figure 3.12. ABC-SubSim damage-inference results of the intact weld using U_{2S1} : (a) without and (b) with adding sensing noise.

3.5.2 Damage Identification and Inference Evaluation

This section presents the results of the damage parameter inference in the weld joint taken as a case study. Since many testing damage cases are available (namely 594 cases), only 18 representative cases are chosen to be analyzed and discussed. The cases were chosen carefully to be representative of all the 594 testing damage cases. Table 3.5 lists the nominal damage parameters of the chosen damage cases of which the simulated ultrasound signals were produced. To reproduce a more realistic sensor measurement, the FE data of each testing damage case was contaminated with random colored noise, as was done with the intact signals.

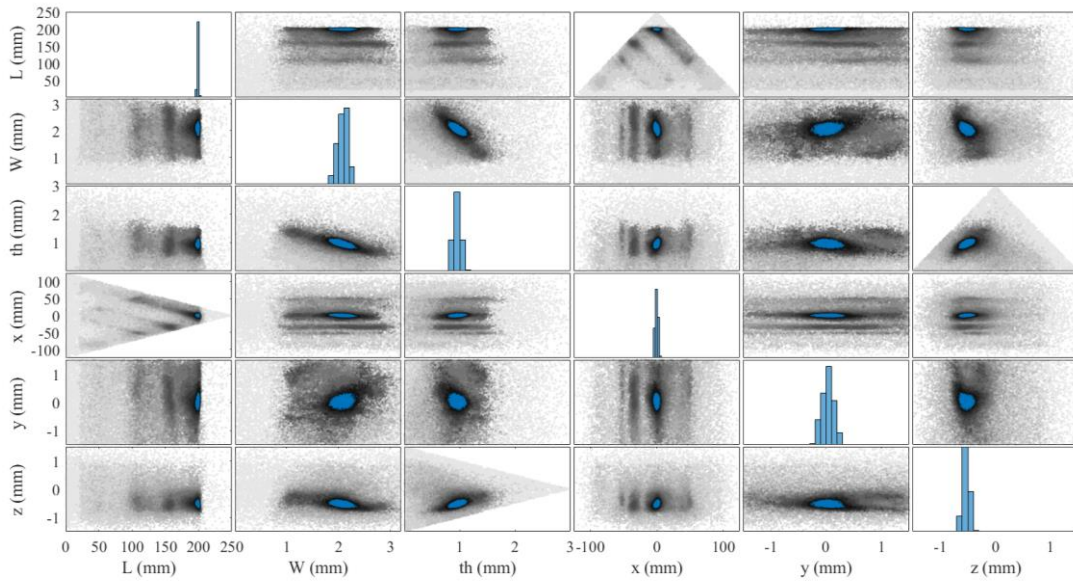
Figure 3.13 and Figure 3.14 show the ABC-SubSim damage-inference results of two test cases using U_{3S1} . Figure 3.13(a) shows the scatter plots of all the Θ_r samples starting from the *prior* at the first simulation level and until reaching the final *approximated posterior* at the final simulation level, which is marked in blue color. Samples of the intermediate simulation levels are drawn using increasing gray tones to show the strength in the algorithm's convergence towards the final damage inference. The empty and less dense regions in the *prior* reveal the geometric constraints that were imposed by the problem at hand.

Figure 3.13(b) displays only the final *approximated posterior* of the same damage case, along with the labels of the real damage parameters. The results show that the damage parameters are efficiently inferred using only one sensor measurement. The posterior PDF values are distributed in narrow regions, thus providing a good damage identification of the weld joint. However, this is not always the case when a smaller damage size is considered, as can be seen in Figure 3.14. When trying to capture small damage of 25-*mm* length, some scatter plots appear to be more spread over the damage-

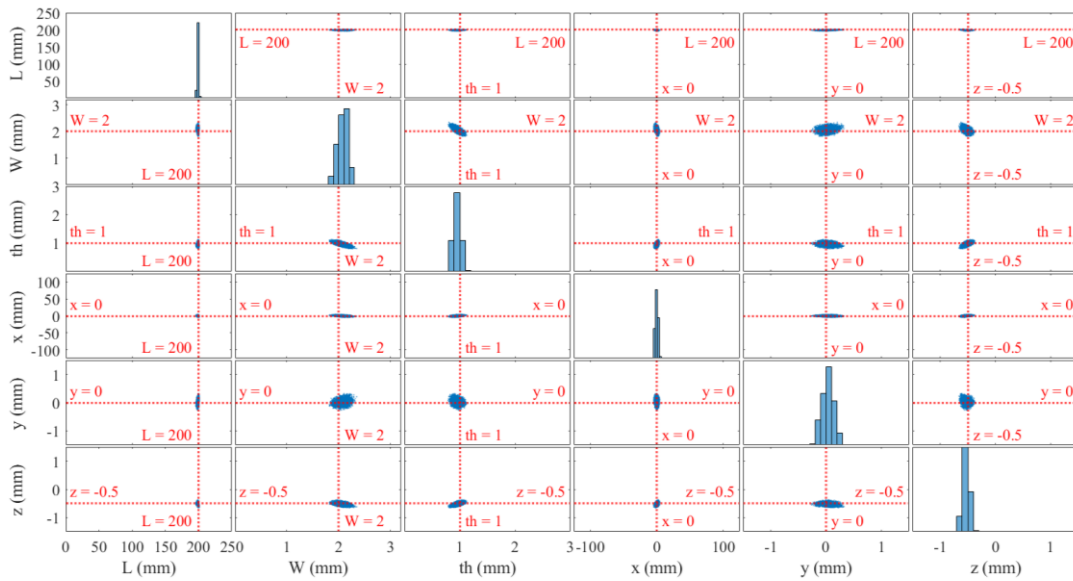
parameter ranges. Although the highest probabilities (seen on the diagonal plots) are close enough to the actual values for all the damage parameters, the spread in the scatter plots shows that the inference is subject to higher uncertainty. Hence, a quantitative approach is used to evaluate the damage-inference results and make them more comparable and physically meaningful.

Table 3.5. Damage parameters of the selected damage cases.

Test case #	L (mm)	W (mm)	th (mm)	x (mm)	y (mm)	z (mm)	θ (mm)
1	25	1	1	-75	-1	-1	[25, 1, 1, -75, -1, -1]
2	25	1	2	0	1	0	[25, 1, 2, 0, 1, 0]
3	25	2	1	-50	0	-0.5	[25, 2, 1, -50, 0, -0.5]
4	25	2	2	50	-1	-0.5	[25, 2, 2, 50, -1, -0.5]
5	25	3	1	0	0	0	[25, 3, 1, 0, 0, 0]
6	25	3	2	50	1	-0.5	[25, 3, 2, 50, 1, -0.5]
7	100	1	1	-75	-1	-1	[100, 1, 1, -75, -1, -1]
8	100	1	2	0	1	0	[100, 1, 2, 0, 1, 0]
9	100	2	1	-50	0	-0.5	[100, 2, 1, -50, 0, -0.5]
10	100	2	2	50	-1	-0.5	[100, 2, 2, 50, -1, -0.5]
11	100	3	1	0	0	0	[100, 3, 1, 0, 0, 0]
12	100	3	2	50	1	-0.5	[100, 3, 2, 50, 1, -0.5]
13	200	1	1	0	-1	-1	[200, 1, 1, 0, -1, -1]
14	200	1	2	0	1	0	[200, 1, 2, 0, 1, 0]
15	200	2	1	0	0	-0.5	[200, 2, 1, 0, 0, -0.5]
16	200	2	2	0	-1	-0.5	[200, 2, 2, 0, -1, -0.5]
17	200	3	1	0	0	0	[200, 3, 1, 0, 0, 0]
18	200	3	2	0	1	-0.5	[200, 3, 2, 0, 1, -0.5]



(a) All simulation levels superposed in the scatter plots (diagonal plots are excluded). Each scatter plot presents samples of Θ_r at different simulation levels, where the final posterior samples are marked in blue. To reveal the uncertainty reduction, the intermediate posterior samples are superposed in increasing gray tones. Light gray dots correspond to prior samples (initial random Θ_r at simulation level = 1).



(b) Final simulation level. The real damage parameters are marked and labeled in red color.

Figure 3.13. ABC-SubSim damage-inference results of test case 15 (refer to Table 3.5) using $U_{3S1} - m = 13$ simulation levels and $R_{acc} = 22.9\%$.

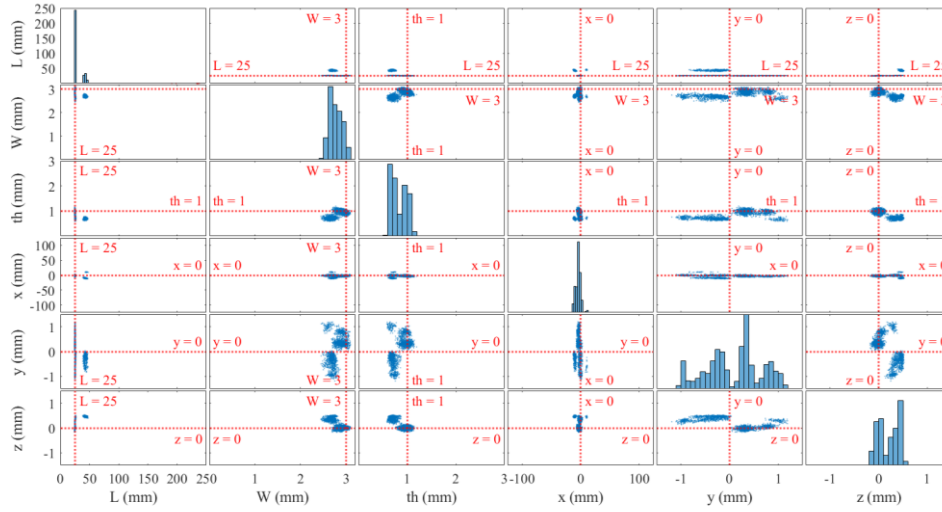


Figure 3.14. ABC-SubSim damage-inference results of test case 5 (refer to Table 3.5) using $U_{3S1} - m = 12$ simulation levels and $R_{acc} = 17.9\%$. The real damage parameters are marked and labeled in red color.

The prediction of the damage parameters was performed based on the MAP. The precision (Pr) of damage prediction was calculated using equation (3.4), taking an acceptance threshold value of 90%. A value of 90% means that the error in predicting the damage parameter is 10% of the damage parameter's range, imposed by the problem's geometrical constraints. The ranges that were used for the six damage parameters being predicted are listed in Table 3.3. Note that equation (3.4) gives an array of six precision values, each corresponding to one of the predicted damage parameters.

$$Pr (\%) = 100 \times \left[1 - \frac{|\theta - \theta'_{map}|}{\theta_{max} - \theta_{min}} \right] \quad (3.4)$$

where:

- θ : is the set of the real damage parameters; $\theta = [L, W, th, x, y, z]$ in mm ;

- θ'_{map} : is the set of predicted damage parameters based on MAP;

$\theta'_{map} = [L', W', th', x', y', z']$ in *mm*;

- θ_{max} and θ_{min} : are the set of maximum and minimum allowed values of the damage parameters, respectively, imposed by the geometrical constraints.

On the other hand, the uncertainty (ξ) in the damage inference is a measure of how unconfident the inference of each damage parameter is. This can be seen in the dispersion of the scatter plot of this specific parameter. If the scatter plot is narrow and definite (like those in Figure 3.13), then the inference is more confident, and the uncertainty is low. On the contrary, if the data are spread over a big scale of the damage parameter's range (e.g., y -position in Figure 3.14), then the inference of this parameter is uncertain, and the uncertainty is high. The uncertainty was calculated based on equation (3.5), and a threshold 15% of the damage parameter's range was adopted as the maximum acceptable value.

$$\xi (\%) = 100 \times \frac{2\theta_{\sigma}}{\theta_{max} - \theta_{min}} \quad (3.5)$$

where:

- θ_{σ} : is the standard deviation of the *approximated posterior* Θ_r .

3.5.3 ABC-SubSim based on One Sensor Measurement

Table 3.6 and Table 3.7 are summaries of the inference results of all the 18 chosen testing damage cases using U_{2S1} and U_{3S1} , respectively. Damage parameters that are inferred with a precision of less than 90% are marked in red color in the tables to indicate a lower precision. Uncertainties of values above 15% of the damage

parameter's range are also marked in red color, signifying higher uncertainty. Values in the tables written in **bold** are not to be considered, at this level, due to a symmetry problem, related to S1, which will be discussed later.

High uncertainty in the inference of at least one of the damage parameters is attained for 9 out of 18 damage cases when using the measurement U_{2S1} , and for 11 out of 18 damages cases when using the measurement U_{3S1} . Higher uncertainties and lower precision in the damage prediction are mostly associated with the 1st six damage cases, where the damage length is relatively small ($L = 25 \text{ mm}$). On the other hand, the damage cases of $L = 200 \text{ mm}$ (test cases 13 till 18) are perfectly inferred, with high precision and low uncertainties for both sensor measurements. Damage cases of $L = 100 \text{ mm}$ (test cases 7 till 12) are inferred with high precision as well, however, more uncertainties exist among their results.

Table 3.6. A summary of the ABC-SubSim inference results using U_{2S1} sensor measurement, for the selected damage cases.

Test case #	θ (mm)	θ'_{map} (mm)	Pr (%)	ξ (%)
1	[25, 1, 1, -75, -1, -1]	[25.31, 1.00, 1.40 , 77.40 , 0.28 , -0.32]	[99.88, 99.93, 86.52 , 39.04 , 57.45 , 77.36]	[15.43, 19.37, 18.27, 39.77 , 26.00 , 27.83]
2	[25, 1, 2, 0, 1, 0]	[25.68, 0.89, 1.78, 6.89, -0.87 , 0.17]	[99.73, 96.69, 92.57, 97.24, 37.78 , 94.37]	[9.95, 3.24, 9.07, 3.36, 12.97, 6.78]
3	[25, 2, 1, -50, 0, -0.5]	[25.42, 1.90, 0.92, -48.55 , -0.56 , -0.43]	[99.83, 96.97, 97.36, 99.42 , 81.49 , 97.73]	[4.13, 19.75 , 9.57, 32.07 , 21.13 , 23.63]
4	[25, 2, 2, 50, -1, -0.5]	[24.91, 1.79, 1.90, -50.17 , -1.03, -0.33]	[99.96, 93.46, 96.51, 59.93 , 99.10, 94.45]	[0.36, 26.90 , 10.20, 22.17 , 10.84, 11.71]
5	[25, 3, 1, 0, 0, 0]	[25.30, 3.00, 0.65 , -22.47, -0.01, 0.24]	[99.88, 99.95, 88.20 , 91.01, 99.57, 91.94]	[18.45, 2.79, 8.07, 13.56, 11.56, 9.41]
6	[25, 3, 2, 50, 1, -0.5]	[24.88, 2.56 , 2.00, -50.77 , 1.36 , -0.38]	[99.95, 86.22 , 99.90, 59.69 , 88.00 , 96.10]	[0.28, 6.29, 5.02, 8.88 , 19.04 , 5.45]
7	[100, 1, 1, -75, -1, -1]	[97.74, 0.89, 1.15, 76.37 , -0.78, -0.86]	[99.09, 96.61, 95.00, 39.45 , 92.72, 95.47]	[1.75, 11.33, 5.66, 35.67 , 8.20, 3.86]
8	[100, 1, 2, 0, 1, 0]	[100.53, 1.01, 1.98, -1.11, 1.01, 0.00]	[99.79, 99.58, 99.49, 99.56, 99.64, 99.84]	[2.87, 2.94, 3.71, 1.76, 7.59, 2.64]
9	[100, 2, 1, -50, 0, -0.5]	[100.35, 1.97, 0.99, 45.27 , -0.08, -0.52]	[99.86, 99.01, 99.75, 61.89 , 97.17, 99.33]	[17.61, 4.66, 6.46, 35.30 , 7.18, 6.82]
10	[100, 2, 2, 50, -1, -0.5]	[100.84, 2.00, 1.88, -49.75 , -0.98, -0.50]	[99.66, 100.0, 96.16, 60.10 , 99.37, 99.85]	[2.38, 18.18 , 6.98, 39.80 , 7.03, 3.79]
11	[100, 3, 1, 0, 0, 0]	[145.10, 2.99, 0.93, 25.01, 0.18, -0.04]	[81.96 , 99.65, 97.82, 90.00, 93.91, 98.61]	[15.50, 1.17, 5.67, 15.59 , 16.02 , 3.37]
12	[100, 3, 2, 50, 1, -0.5]	[100.67, 2.94, 2.05, -51.15 , 1.01, -0.45]	[99.73, 98.24, 98.47, 59.54 , 99.81, 98.28]	[2.87, 2.78, 6.79, 40.71 , 10.68, 3.68]
13	[200, 1, 1, 0, -1, -1]	[200.80, 0.93, 1.06, -2.15, -0.80, -0.95]	[99.68, 97.76, 97.97, 99.14, 93.25, 98.28]	[6.08, 14.98, 4.35, 4.33, 8.26, 3.26]
14	[200, 1, 2, 0, 1, 0]	[200.62, 0.97, 2.03, 1.61, 1.09, 0.01]	[99.75, 98.91, 98.96, 99.35, 97.01, 99.71]	[1.11, 3.89, 4.52, 4.56, 10.87, 2.97]
15	[200, 2, 1, 0, 0, -0.5]	[199.95, 2.03, 1.02, -2.27, -0.02, -0.51]	[99.98, 99.21, 99.46, 99.09, 99.34, 99.83]	[6.57, 3.34, 3.33, 5.12, 6.31, 2.29]
16	[200, 2, 2, 0, -1, -0.5]	[200.16, 2.01, 1.95, -2.46, -1.07, -0.50]	[99.94, 99.57, 98.26, 99.02, 97.66, 99.95]	[0.88, 20.94 , 5.39, 2.47, 5.69, 3.08]
17	[200, 3, 1, 0, 0, 0]	[195.37, 2.98, 1.08, -5.51, 0.02, 0.05]	[98.15, 99.46, 97.44, 97.80, 99.33, 98.41]	[11.95, 1.15, 5.65, 10.59, 12.21, 2.79]
18	[200, 3, 2, 0, 1, -0.5]	[178.95, 2.98, 1.99, -8.30, 0.84, -0.48]	[91.58, 99.50, 99.62, 96.68, 94.64, 99.37]	[8.81, 2.12, 6.73, 5.63, 9.63, 3.60]

Table 3.7. A summary of the ABC-SubSim inference results using U_{3S1} sensor measurement, for the selected damage cases.

Test case #	θ (mm)	θ'_{map} (mm)	Pr (%)	ξ (%)
1	[25, 1, 1, -75, -1, -1]	[24.45, 1.02, 0.99, -74.49 , -1.18, -0.98]	[99.78, 99.33, 99.62, 99.80 , 94.02, 99.35]	[0.49, 18.55 , 7.50, 44.42 , 26.56 , 4.98]
2	[25, 1, 2, 0, 1, 0]	[25.36, 1.02, 1.74, 0.87, -0.46 , -0.00]	[99.86, 99.52, 91.19, 99.65, 51.28 , 99.90]	[0.27, 17.19 , 7.60, 1.50, 14.85, 3.77]
3	[25, 2, 1, -50, 0, -0.5]	[24.47, 2.04, 0.96, -47.68 , 0.16, -0.46]	[99.79, 98.86, 98.75, 99.07 , 94.76, 98.74]	[0.35, 19.79 , 9.90, 34.16 , 27.77 , 6.95]
4	[25, 2, 2, 50, -1, -0.5]	[25.21, 2.32 , 2.11, -51.13 , -0.73, -0.38]	[99.92, 89.89 , 96.30, 59.55 , 90.94, 96.05]	[0.63, 25.69 , 10.76, 40.97 , 16.79 , 5.54]
5	[25, 3, 1, 0, 0, 0]	[25.11, 2.68, 0.69 , -3.34, 0.33 , 0.45]	[99.95, 90.13, 89.67 , 98.66, 88.92 , 85.15]	[5.92, 8.23, 10.10, 3.21, 37.63 , 13.98]
6	[25, 3, 2, 50, 1, -0.5]	[24.80, 1.58 , 1.82, -49.56 , 0.93, -0.48]	[99.92, 55.60 , 93.85, 60.18 , 97.56, 99.48]	[0.29, 43.67 , 12.26, 39.00 , 14.32, 7.25]
7	[100, 1, 1, -75, -1, -1]	[97.07, 1.12, 0.96, 75.90 , -1.05, -1.01]	[98.83, 96.13, 98.70, 39.64 , 98.46, 99.74]	[1.10, 34.18 , 6.42, 59.15 , 12.49, 4.29]
8	[100, 1, 2, 0, 1, 0]	[99.54, 1.00, 1.97, -2.29, 0.87, -0.00]	[99.82, 99.97, 98.85, 99.08, 95.75, 99.85]	[8.21, 2.19, 2.65, 4.72, 26.81 , 1.81]
9	[100, 2, 1, -50, 0, -0.5]	[100.78, 1.84, 1.06, 49.99 , 0.18, -0.40]	[99.69, 94.96, 97.93, 60.00 , 94.03, 96.51]	[1.36, 6.18, 5.06, 32.21 , 9.81, 4.08]
10	[100, 2, 2, 50, -1, -0.5]	[100.96, 2.08, 1.80, 49.78 , -0.80, -0.57]	[99.62, 97.39, 93.18, 99.91 , 93.41, 97.67]	[1.79, 25.61 , 9.31, 32.55 , 17.36 , 4.42]
11	[100, 3, 1, 0, 0, 0]	[93.45, 3.01, 1.06, 2.19, 0.15, -0.01]	[97.38, 99.74, 97.97, 99.12, 94.88, 99.77]	[8.11, 1.54, 4.68, 5.10, 11.49, 1.97]
12	[100, 3, 2, 50, 1, -0.5]	[102.81, 2.94, 1.95, 50.88 , 1.04, -0.49]	[98.87, 98.18, 98.44, 99.65 , 98.62, 99.76]	[2.74, 14.85, 7.41, 39.79 , 12.51, 3.91]
13	[200, 1, 1, 0, -1, -1]	[199.61, 1.20, 1.00, 2.11, -0.81, -0.97]	[99.85, 93.71, 99.95, 99.16, 93.65, 99.10]	[1.79, 16.44 , 3.85, 1.82, 9.21, 2.67]
14	[200, 1, 2, 0, 1, 0]	[199.71, 1.01, 1.96, 2.83, 1.23, 0.00]	[99.88, 99.72, 98.75, 98.87, 92.39, 99.97]	[8.04, 2.85, 3.15, 8.43, 38.17 , 1.92]
15	[200, 2, 1, 0, 0, -0.5]	[199.85, 2.12, 0.96, 0.82, 0.06, -0.54]	[99.94, 96.32, 98.58, 99.67, 98.07, 98.59]	[0.79, 6.07, 4.19, 1.58, 7.07, 3.64]
16	[200, 2, 2, 0, -1, -0.5]	[199.50, 2.38 , 1.89, -0.42, -0.92, -0.52]	[99.80, 88.23 , 96.39, 99.83, 97.47, 99.24]	[1.69, 14.09, 6.02, 1.60, 10.61, 2.82]
17	[200, 3, 1, 0, 0, 0]	[199.58, 3.01, 1.00, 0.08, 0.14, -0.02]	[99.83, 99.56, 99.99, 99.97, 95.38, 99.38]	[1.22, 1.80, 4.38, 2.76, 14.93, 2.49]
18	[200, 3, 2, 0, 1, -0.5]	[201.15, 3.00, 1.97, 3.68, 0.94, -0.50]	[99.54, 99.91, 98.85, 98.53, 98.06, 99.90]	[8.69, 9.69, 5.26, 8.75, 10.69, 2.72]

Figure 3.15 shows ABC-SubSim damage-inference results of test case 12 using U_{2S1} . While all damage parameters are perfectly inferred, two x -positions of opposite values are predicted. This is due to the symmetry associated with the sensing point S1, as both the actuator and S1 are located within the YZ -plane, the plane of symmetry of the plate. This is demonstrated in Figure 3.16(a) which illustrates an example of two identical damages, each having an opposite x -position with respect to the other. The two damages are symmetric with respect to the YZ -plane, where both the actuator and the sensor are located. Hence, assuming there is no noise or variation in the boundary conditions or any other factor affecting the measurements, the two damage cases yield the same LW measurements at the sensor. This fact should be taken into consideration

when trying to infer the damage parameters using measurements from a single sensor (S1).

To verify this concept, U_{2S1} simulation results of the damage case D2 were compared to those of the damage case having the same damage parameters but an opposite x -position; i.e., D2-sym: $L = 50 \text{ mm}$, $W = 2 \text{ mm}$, $th = 1.5 \text{ mm}$, $x = 75 \text{ mm}$, $y = 0 \text{ mm}$, and $z = 0.25 \text{ mm}$. The two signals overlap without any visible difference as can be seen in Figure 3.16(b).

It is evident, in Table 3.6 and Table 3.7, that either of the symmetric x -positions is successfully inferred in all of the test cases (values written in **bold**). The other symmetric values are also predicted but with a lower probability. This can be seen when visualizing the *approximated posterior* Θ_r , as was shown in Figure 3.15.

To avoid the symmetry of S1, two additional sensing points were used as shown in Figure 3.17. The coordinates of the two added sensing points, with respect to the coordinate-axis defined at the center of the plate, are S2(-100, -80) and S3(-100, 80), expressed in mm . Similar to S1, displacements in the U_2 and U_3 directions were recorded, and the same methodology was repeated for all the sensor measurements (U_{2S2} , U_{3S2} , U_{2S3} , and U_{3S3}), including preprocessing, data balancing, sample reduction, ANN training, and ABC-SubSim damage inference.

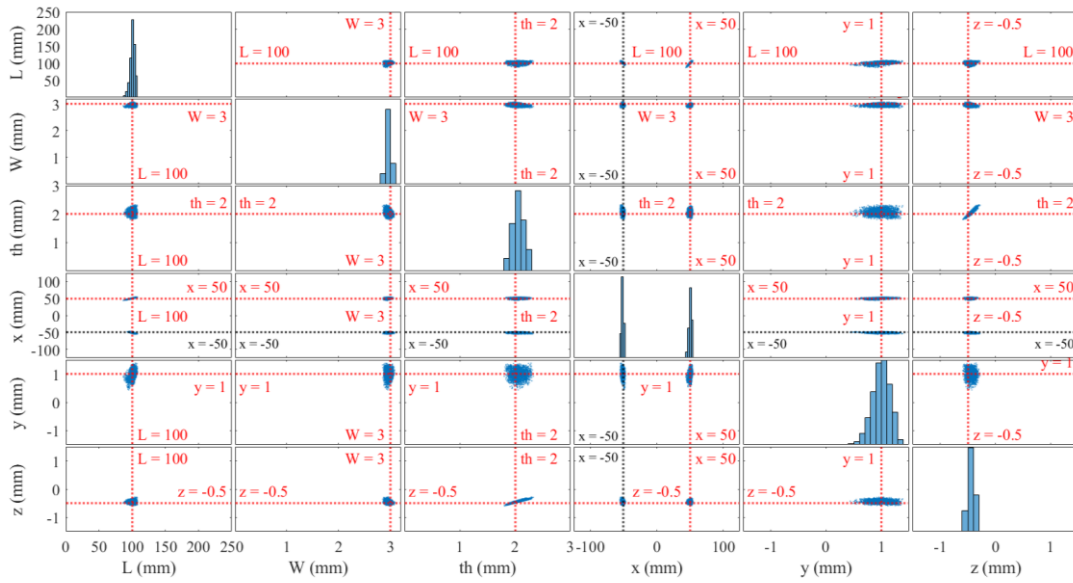
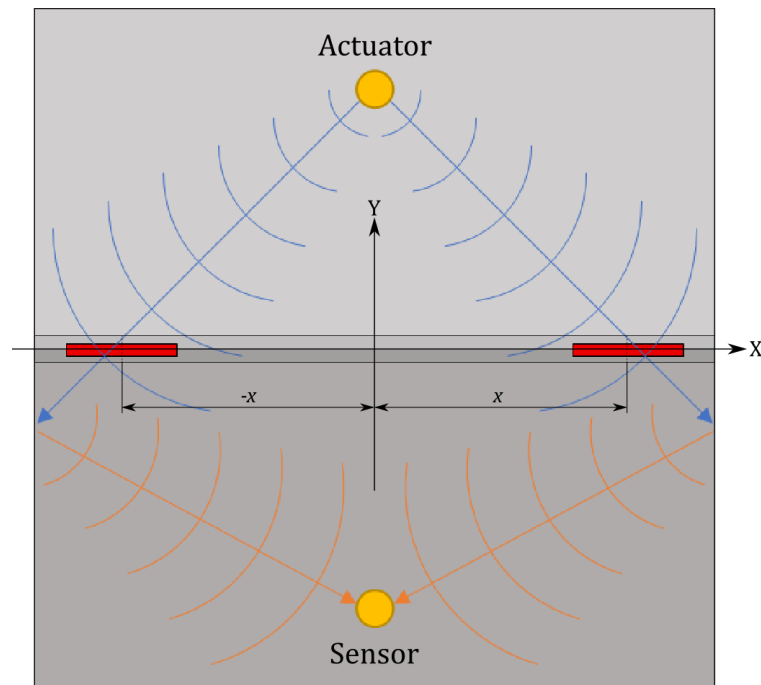
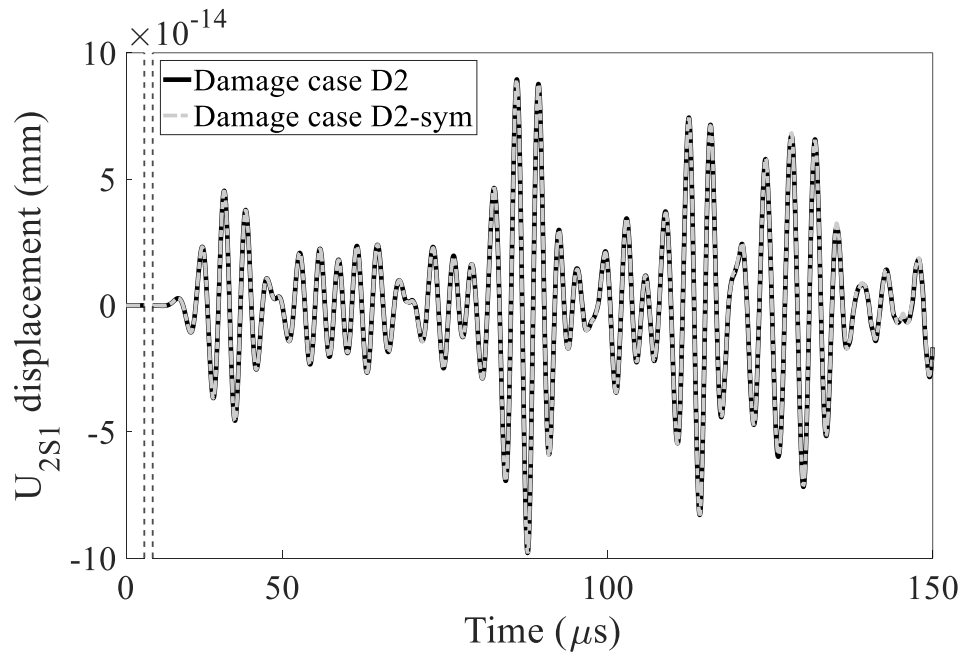


Figure 3.15. ABC-SubSim damage-inference results of test case 12 (refer to Table 3.5) using $U_{2S1} - m = 13$ simulation levels and $R_{acc} = 22.2\%$. The real damage parameters are marked and labeled in red color. The x -position, marked in black, is the symmetric value of the actual x -position.



(a)



(b)

**Figure 3.16. (a) An illustration demonstrating the need for using the whole signal, including the wave's boundary reflections, to perceive damages lying outside the coverage of the sensing path. The illustration also shows how two symmetric damage cases would yield the same LW measurement at a sensor located along the Y -axis. The damages are drawn in red color. (b) FE results of symmetric sample damage cases;
D2: $L = 50, W = 2, th = 1.5, x = -75, y = 0, \text{ and } z = 0.25$;
D2-sym: $L = 50, W = 2, th = 1.5, x = 75, y = 0, \text{ and } z = 0.25$;
all parameters are in mm .**

Figure 3.18 shows the boxplots summarizing ABC-SubSim damage-inference results for the whole testing dataset (594 cases) using U_{2S2} . Results of different damage lengths are separated to investigate the effect of the damage size on the accuracy of prediction. The boxplot of each damage parameter consists of a box bounded by the 25th and 75th percentiles (lower and upper quartiles) of the 594 inferences, with a central mark representing the median. Hence, the interquartile range (IQR) represented within the box signifies 50% of the plotted inference cases. The fences/whiskers extend from

the box edges up to a maximum length of $1.5 \times \text{IQR}$. Points lying outside this range are considered outliers and are plotted separately.

Considering the inference of the x -position, very narrow IQRs are observed showing high precision (above 98%) and low uncertainty (below 4%). Few outliers lie within regions of precision below 90% or uncertainty above 15%. This confirms the resolution of the symmetry problem when using a sensing point outside the plane of symmetry. Moving the actuator to a position outside the plane of symmetry would have also solved the problem.

Damage length (L) is accurately identified, as well, in all the testing dataset with few outlier cases (Figure 3.18(a-c)). Wider IQRs and more outliers are observed for the other damage parameters in the case of $L = 25 \text{ mm}$ (Figure 3.18(a)). The damage width (W) and y -positions are hardly differentiated between different cases, showing higher percentages within the unacceptable thresholds of precision ($<90\%$) and uncertainty ($>15\%$). Higher precisions and lower uncertainties are generally attained for $L = 100 \text{ mm}$ (Figure 3.18(b)), and very accurate predictions are achieved in the case of $L = 200 \text{ mm}$ (Figure 3.18(c)).

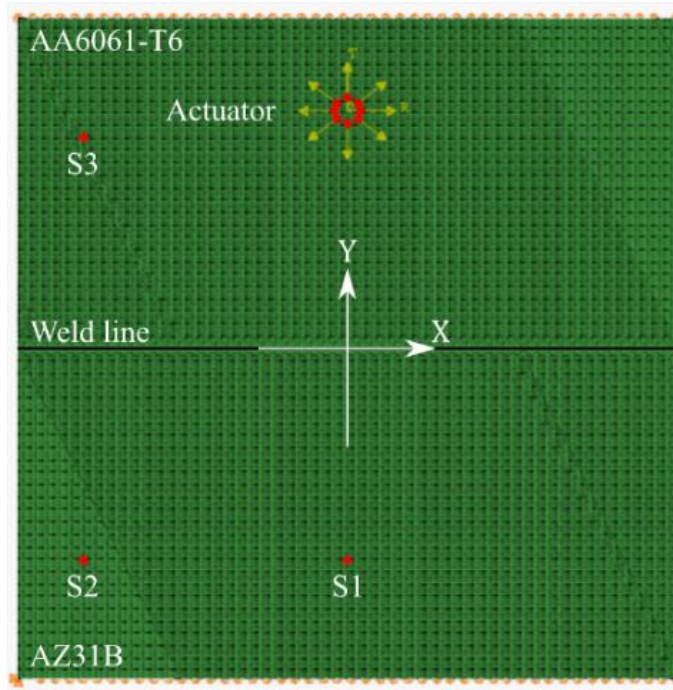
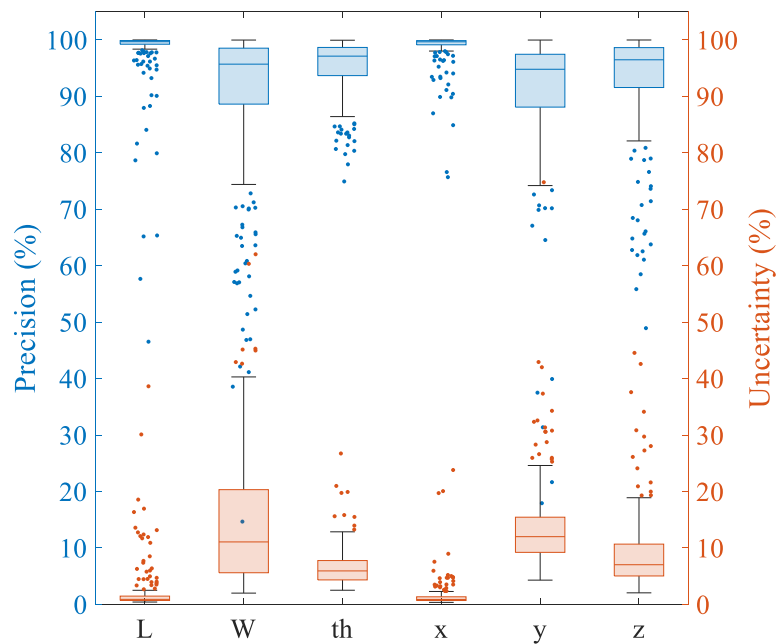
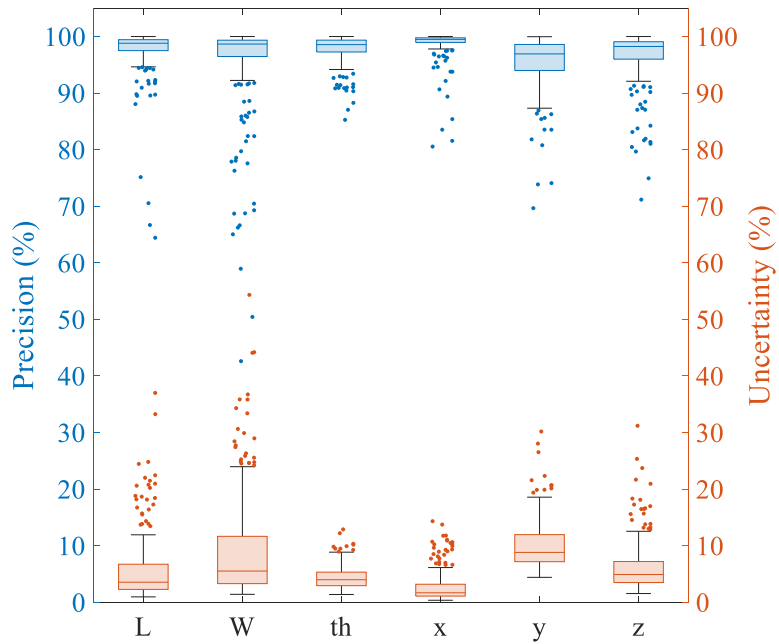


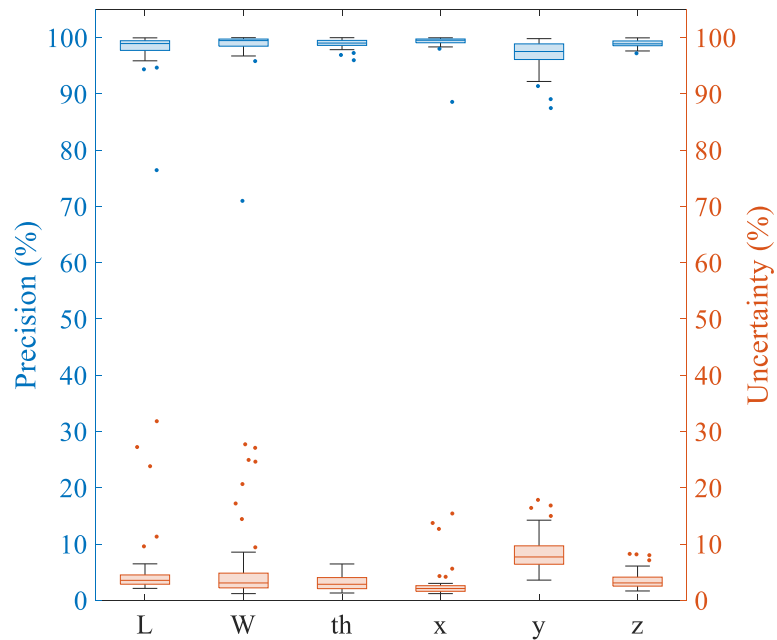
Figure 3.17. The FE model showing the two added sensing points S2 and S3 (in red).



(a) $L = 25 \text{ mm}$ (270 testing cases out of 594)



(b) $L = 100 \text{ mm}$ (270 testing cases out of 594)



(c) $L = 200 \text{ mm}$ (54 testing cases out of 594)

Figure 3.18. Boxplots summarizing the precision and uncertainty of ABC-SubSim damage inference for the whole testing dataset (594 cases) using U_{252} . Results of different damage lengths are shown separately.

3.5.4 ABC-SubSim based on Multiple Sensor Measurements

To overcome the shortages of using a single sensor measurement, data were fused based on two or more sensor measurements, eventually aiming to improve the robustness and accuracy of the inference results. ABC-SubSim results of only six test cases (cases 1 to 6 of $L = 25 \text{ mm}$ in Table 3.5) will be discussed as they showed the lowest precision and highest uncertainty when using a single sensor measurement (Table 3.6, Table 3.7, and Figure 3.18(a)).

Combinations of U_2 measurements from different sensing points were used together by employing the methodology explained in Section 3.4.3. Table 3.8 summarizes the inference results when using U_{2S1} and U_{2S2} together, while Table 3.9 summarizes those of fusing U_{2S2} with U_{2S3} . Finally, Table 3.10 summarizes the results of fusing U_2 measurements from all the three sensing points S1, S2, and S3. The results show that both damage length (L) and x -position are inferred with a precision higher than 99% for all the shown cases and sensor combinations. Very low uncertainties are also attained for both damage parameters. This proves the high potential of the methodology for accurately assessing these two important parameters defining the length of the wormhole and its position along the weld.

The best inference results are obtained when merging U_2 measurements from S2 and S3 (Table 3.9). Damage parameters are inferred with a precision of above 95% for more than 83% of the cases. The only inference with a precision below 91% is for the damage width (W) in test case 4, with an inference error $< 0.9 \text{ mm}$. Moreover, only two uncertainty values above 15% are recorded and are also for the damage width (W).

Combining U_2 measurements from S1 and S2 does not show a significant improvement over inference using one sensor measurement (Table 3.8), however, combining the measurements of the three sensors shows better results, as depicted in Table 3.10. Damage is inferred with high precision ($> 90\%$) for all the cases except two damage parameters (highlighted in red), with errors less than 0.6 mm. More than half of the other inference results are of precision above 99%, while being above 95% in most of the cases.

In both Table 3.8 and Table 3.10, high uncertainties are noticed at four different places for W and y -position, with two values exceeding 30%.

Table 3.8. A summary of the ABC-SubSim inference results using U_{2S1} and U_{2S2} sensor measurements, for the testing damage cases 1 to 6.

Test case #	θ (mm)	θ'_{map} (mm)	Pr (%)	ξ (%)
1	[25, 1, 1, -75, -1, -1]	[25.26, 1.74 , 1.10, -74.78, -0.89, -0.64]	[99.90, 76.97 , 96.56, 99.91, 96.49, 87.87]	[0.36, 17.57 , 7.43, 0.64, 16.63 , 11.11]
2	[25, 1, 2, 0, 1, 0]	[24.93, 0.96, 2.06, 1.26, 0.17 , 0.01]	[99.97, 98.62, 98.09, 99.49, 72.29 , 99.69]	[0.22, 5.86, 9.12, 2.02, 14.84, 5.94]
3	[25, 2, 1, -50, 0, -0.5]	[25.40, 2.06, 1.00, -50.15, -0.25, -0.58]	[99.84, 98.05, 99.97, 99.94, 91.82, 97.42]	[0.42, 9.59, 6.21, 0.93, 10.55, 9.71]
4	[25, 2, 2, 50, -1, -0.5]	[25.07, 2.45 , 1.85, 50.78, -0.86, -0.47]	[99.97, 86.05 , 95.08, 99.69, 95.28, 98.91]	[0.24, 33.85 , 9.09, 1.05, 9.73, 9.17]
5	[25, 3, 1, 0, 0, 0]	[25.33, 2.96, 0.96, 1.90, 1.31 , -0.01]	[99.87, 98.86, 98.83, 99.24, 56.43 , 99.61]	[5.55, 2.11, 8.21, 3.57, 40.63 , 5.42]
6	[25, 3, 2, 50, 1, -0.5]	[25.07, 2.82, 1.93, 48.42, 0.54 , -0.19]	[99.97, 94.48, 97.71, 99.37, 84.83 , 89.62]	[0.26, 9.18, 4.96, 0.97, 14.58, 8.95]

Table 3.9. A summary of the ABC-SubSim inference results using U_{2S2} and U_{2S3} sensor measurements, for the testing damage cases 1 to 6.

Test case #	θ (mm)	θ'_{map} (mm)	Pr (%)	ξ (%)
1	[25, 1, 1, -75, -1, -1]	[24.34, 0.97, 0.98, -75.74, -1.07, -0.94]	[99.74, 99.12, 99.48, 99.70, 97.63, 98.15]	[0.75, 19.77 , 6.30, 0.66, 7.50, 4.48]
2	[25, 1, 2, 0, 1, 0]	[25.11, 0.93, 2.10, -0.15, 0.75, -0.11]	[99.96, 97.86, 96.55, 99.94, 91.57, 96.30]	[1.18, 8.62, 10.04, 0.85, 9.86, 11.13]
3	[25, 2, 1, -50, 0, -0.5]	[25.19, 2.10, 0.99, -50.24, 0.00, -0.56]	[99.92, 96.81, 99.77, 99.90, 99.94, 98.15]	[0.48, 7.51, 4.89, 0.67, 7.14, 8.57]
4	[25, 2, 2, 50, -1, -0.5]	[26.80, 1.12 , 2.23, 51.07, -0.74, -0.32]	[99.28, 72.55 , 92.26, 99.57, 91.30, 94.06]	[0.72, 26.47 , 11.32, 0.78, 12.93, 6.10]
5	[25, 3, 1, 0, 0, 0]	[23.72, 3.02, 1.10, -0.22, 0.26, -0.09]	[99.49, 99.35, 96.61, 99.91, 91.42, 97.11]	[0.97, 3.25, 8.56, 0.82, 14.62, 5.97]
6	[25, 3, 2, 50, 1, -0.5]	[25.11, 2.90, 2.13, 48.61, 1.00, -0.37]	[99.96, 96.82, 95.53, 99.45, 100.0, 95.65]	[0.45, 10.95, 8.58, 0.91, 10.10, 7.13]

Table 3.10. A summary of the ABC-SubSim inference results using the three sensor measurements (U_{2S1} , U_{2S2} , and U_{2S3}), for the testing damage cases 1 to 6.

Test case #	θ (mm)	θ'_{map} (mm)	Pr (%)	ξ (%)
1	[25, 1, 1, -75, -1, -1]	[25.11, 1.15, 1.00, -74.83, -0.74, -0.93]	[99.96, 95.17, 99.84, 99.93, 91.41, 97.62]	[0.34, 22.89 , 6.72, 0.56, 11.31, 5.03]
2	[25, 1, 2, 0, 1, 0]	[25.18, 0.89, 1.85, 1.13, 0.44 , -0.01]	[99.93, 96.53, 95.12, 99.55, 81.21 , 99.54]	[0.30, 5.39, 6.07, 1.13, 15.27 , 6.48]
3	[25, 2, 1, -50, 0, -0.5]	[25.09, 1.96, 1.00, -50.16, 0.10, -0.39]	[99.96, 98.83, 99.92, 99.93, 96.77, 96.31]	[0.42, 7.37, 6.08, 0.79, 7.73, 8.23]
4	[25, 2, 2, 50, -1, -0.5]	[25.06, 2.01, 1.91, 49.74, -1.09, -0.48]	[99.98, 99.57, 97.11, 99.89, 97.00, 99.40]	[0.27, 31.07 , 10.38, 1.04, 6.69, 9.73]
5	[25, 3, 1, 0, 0, 0]	[25.60, 2.97, 1.08, 1.15, 0.16, -0.11]	[99.76, 99.08, 97.20, 99.54, 94.64, 96.48]	[0.56, 2.42, 10.08, 1.18, 30.07 , 7.25]
6	[25, 3, 2, 50, 1, -0.5]	[25.14, 2.53 , 1.95, 49.71, 0.96, -0.28]	[99.94, 85.18 , 98.32, 99.89, 98.53, 92.74]	[0.27, 11.63, 6.85, 0.81, 8.64, 7.97]

3.5.5 Effect of Sensing Noise

Noise of various levels was added to the testing data to investigate the effect of sensing noise on the proposed damage inference approach. As mentioned earlier, the NL is defined as the ratio of the noise's maximum amplitude to that of the healthy signal of the corresponding sensor measurement. While a 3% NL was used throughout the chapter, damage was inferred for the 18 chosen test cases using a NL of 0% (no sensing noise), 2%, 5%, and 10% using U_{2S2} sensor measurement. A random colored noise of a frequency up to 450 kHz was used, as this can be well-controlled in current experimental setups (using built-in software or physical low-pass filters). Table 3.11, Table 3.12, and Table 3.13 summarize the results of the testing damage cases of $L = 25$, 100, and 200 mm, respectively.

In most of the tested cases, inference precision is not affected by the addition of various levels of noise, showing evident robustness against sensing noise. Cases of big damage size ($L = 200$ mm; Table 3.13) show a negligible noise effect. On the other hand, cases of small and middle-sized damage ($L \leq 100$ mm; Table 3.11 and Table 3.12) are more affected, where the inference precision of few additional parameters has dropped below 90% for NLs of 5 and 10%. A maximum precision reduction of around

41% was recorded for one case. It was noticed that cases with higher uncertainty before adding noise are more susceptible to changes after adding noise. Due to the random nature of noise, it may occasionally lead sometimes to a better inference.

The same NLs were also tested against the healthy weld signal using the same sensor measurement (U_{2S2}) and using U_{2S1} . Table 3.14 shows the inferred damage sizes for various sensing noise levels. For a sensing noise up to 5% NL, the inferred damage sizes do not pass the damage detection rule; i.e., at least one of the three damage-size parameters ($[L, W, th]$; highlighted in green in Table 3.14) does not exceed its set threshold ($[1, 0.1, 0.1] \text{ mm}$). When adding a noise of 10% NL to the healthy U_{2S2} sensor measurement, a false positive is inferred. From a practical point of view, a NL reaching 10% of the signal's maximum amplitude is considered non-realistic, especially with the availability of advanced experimental setups and sophisticated data acquisition technologies.

Hence, the healthy state of the weld is proved to be successfully inferred even with the existence of realistic high levels of sensing noise. The obtained results demonstrate that the approach proposed in this paper shows good immunity against sensing noise, which is similar to what was concluded in the literature using data-driven models [109].

Table 3.11. A summary of the ABC-SubSim inference results using U_{2S2} sensor measurement with variable sensing-noise levels, for the selected damage cases of $L = 25$ mm.

Noise level = 0%				
Test case #	θ (mm)	θ'_{map} (mm)	Pr (%)	ξ (%)
1	[25, 1, 1, -75, -1, -1]	[24.45, 1.62 , 0.98, -74.61, -0.78, -0.91]	[99.78, 80.59 , 99.38, 99.84, 92.58, 96.84]	[0.67, 15.15 , 4.70, 0.51, 9.14, 5.74]
2	[25, 1, 2, 0, 1, 0]	[25.57, 1.02, 1.95, -0.88, 1.20, 0.13]	[99.77, 99.53, 98.42, 99.65, 93.32, 95.70]	[1.00, 5.49, 5.77, 0.75, 12.31, 13.87]
3	[25, 2, 1, -50, 0, -0.5]	[25.05, 2.03, 1.05, -49.78, -0.06, -0.47]	[99.98, 99.03, 98.44, 99.91, 98.10, 98.92]	[0.50, 6.40, 4.45, 0.72, 7.87, 6.63]
4	[25, 2, 2, 50, -1, -0.5]	[25.79, 1.99, 2.26, 52.44, -1.06, -0.34]	[99.68, 99.57, 91.27, 99.02, 97.88, 94.59]	[0.77, 15.93 , 7.22, 0.84, 16.16 , 3.67]
5	[25, 3, 1, 0, 0, 0]	[24.57, 3.04, 1.56 , -0.13, -0.03, 0.06]	[99.83, 98.68, 81.27 , 99.95, 98.96, 97.92]	[1.25, 3.58, 21.80 , 1.27, 33.54 , 6.83]
6	[25, 3, 2, 50, 1, -0.5]	[25.42, 2.67 , 1.90, 50.88, 0.48 , -0.33]	[99.83, 89.76 , 96.70, 99.65, 82.55 , 94.44]	[1.25, 12.66, 7.67, 1.12, 22.95 , 9.37]
Noise level = 2%				
Test case #	θ (mm)	θ'_{map} (mm)	Pr (%)	ξ (%)
1	[25, 1, 1, -75, -1, -1]	[24.29, 1.65 , 0.98, -74.65, -0.93, -0.87]	[99.72, 79.55 , 99.27, 99.86, 97.57, 95.74]	[0.73, 16.10 , 5.37, 0.60, 12.05, 6.03]
2	[25, 1, 2, 0, 1, 0]	[26.18, 1.01, 1.95, -0.52, 1.09, -0.23]	[99.53, 99.82, 98.49, 99.79, 97.15, 92.32]	[0.85, 4.95, 6.01, 0.65, 8.61, 11.50]
3	[25, 2, 1, -50, 0, -0.5]	[25.33, 2.01, 1.00, -49.71, -0.13, -0.46]	[99.87, 99.78, 99.97, 99.88, 95.57, 98.51]	[0.54, 5.49, 4.30, 0.67, 10.97, 6.32]
4	[25, 2, 2, 50, -1, -0.5]	[24.84, 2.12, 2.10, 53.00, -1.08, -0.38]	[99.94, 96.20, 96.53, 98.80, 97.43, 95.90]	[0.85, 20.09 , 5.82, 0.88, 11.17, 3.63]
5	[25, 3, 1, 0, 0, 0]	[23.92, 3.03, 1.35 , -1.15, 0.16, -0.07]	[99.57, 98.98, 88.31 , 99.54, 94.71, 97.81]	[1.36, 3.62, 20.94 , 1.35, 37.67 , 7.42]
6	[25, 3, 2, 50, 1, -0.5]	[25.53, 2.75, 1.92, 50.72, 0.43 , -0.25]	[99.79, 92.15, 97.23, 99.71, 81.04 , 91.81]	[0.76, 7.72, 4.92, 0.93, 15.23 , 7.83]
Noise level = 3%				
Test case #	θ (mm)	θ'_{map} (mm)	Pr (%)	ξ (%)
1	[25, 1, 1, -75, -1, -1]	[24.20, 1.46 , 1.02, -74.90, -0.96, -0.88]	[99.68, 85.61 , 99.45, 99.96, 98.54, 95.97]	[0.64, 20.23 , 4.61, 0.50, 9.13, 5.61]
2	[25, 1, 2, 0, 1, 0]	[26.72, 1.01, 1.93, -0.70, 1.25, -0.30]	[99.31, 99.57, 97.82, 99.72, 91.75, 90.04]	[1.05, 7.09, 6.31, 0.84, 13.05, 14.34]
3	[25, 2, 1, -50, 0, -0.5]	[25.34, 2.01, 1.03, -49.85, -0.05, -0.41]	[99.86, 99.73, 99.11, 99.94, 98.50, 96.94]	[0.49, 4.61, 3.67, 0.66, 8.58, 5.42]
4	[25, 2, 2, 50, -1, -0.5]	[25.95, 1.96, 2.16, 52.79, -1.01, -0.35]	[99.62, 98.68, 94.63, 98.88, 99.68, 95.07]	[0.82, 17.61 , 7.46, 0.74, 13.71, 3.99]
5	[25, 3, 1, 0, 0, 0]	[24.41, 3.03, 1.41 , -1.17, -0.03, -0.04]	[99.77, 98.91, 86.20 , 99.53, 99.16, 98.73]	[0.77, 3.26, 13.08, 0.89, 10.97, 5.89]
6	[25, 3, 2, 50, 1, -0.5]	[25.45, 2.54 , 1.90, 52.04, 0.17 , -0.37]	[99.82, 85.68 , 96.59, 99.18, 72.43 , 95.68]	[1.51, 10.49, 8.74, 1.02, 27.04 , 12.35]
Noise level = 5%				
Test case #	θ (mm)	θ'_{map} (mm)	Pr (%)	ξ (%)
1	[25, 1, 1, -75, -1, -1]	[24.98, 1.85 , 1.04, -74.93, -0.65, -0.92]	[99.99, 73.56 , 98.68, 99.97, 88.34 , 97.45]	[0.62, 20.14 , 3.86, 0.49, 10.23, 4.40]
2	[25, 1, 2, 0, 1, 0]	[26.32, 1.15, 1.96, -0.80, 1.02, -0.34]	[99.47, 95.40, 98.55, 99.68, 99.17, 88.66]	[0.72, 7.03, 6.41, 0.62, 9.00, 8.50]
3	[25, 2, 1, -50, 0, -0.5]	[25.34, 2.14, 0.97, -49.46, -0.13, -0.61]	[99.86, 95.62, 99.06, 99.78, 95.54, 96.40]	[0.71, 7.88, 6.22, 0.85, 7.30, 6.40]
4	[25, 2, 2, 50, -1, -0.5]	[26.11, 1.92, 2.16, 52.96, -1.04, -0.32]	[99.56, 97.36, 94.53, 98.81, 98.65, 93.89]	[0.83, 23.20 , 8.72, 0.80, 16.14 , 4.83]
5	[25, 3, 1, 0, 0, 0]	[26.62, 3.05, 2.20 , 11.58, 1.22 , -0.19]	[99.35, 98.43, 60.12 , 95.37, 59.44 , 93.63]	[1.46, 27.08 , 43.99 , 5.06, 31.95 , 8.96]
6	[25, 3, 2, 50, 1, -0.5]	[24.97, 2.66 , 1.84, 53.88, 0.43 , -0.48]	[99.99, 89.45 , 94.58, 98.45, 80.99 , 99.41]	[2.55, 13.61, 14.27, 1.56, 38.15 , 11.15]
Noise level = 10%				
Test case #	θ (mm)	θ'_{map} (mm)	Pr (%)	ξ (%)
1	[25, 1, 1, -75, -1, -1]	[25.19, 2.05 , 1.09, -74.72, -0.40, -0.87]	[99.92, 67.30 , 96.99, 99.89, 80.02 , 95.71]	[0.59, 15.14 , 3.35, 0.47, 12.19, 4.26]
2	[25, 1, 2, 0, 1, 0]	[28.08, 1.05, 2.14, -1.29, 0.64 , -0.20]	[98.77, 98.29, 95.49, 99.48, 87.87 , 93.37]	[0.79, 5.64, 5.48, 0.62, 7.71, 6.24]
3	[25, 2, 1, -50, 0, -0.5]	[24.76, 1.98, 1.03, -49.27, 0.20, -0.34]	[99.90, 99.34, 98.96, 99.71, 93.37, 94.54]	[0.57, 6.40, 5.30, 0.75, 12.16, 7.72]
4	[25, 2, 2, 50, -1, -0.5]	[24.50, 1.97, 2.09, 51.23, -0.89, -0.41]	[99.80, 99.20, 96.98, 99.51, 96.40, 97.04]	[0.84, 32.88 , 7.98, 2.05, 17.46 , 4.90]
5	[25, 3, 1, 0, 0, 0]	[23.37, 3.05, 1.04, -1.58, 1.27 , -0.09]	[99.35, 98.40, 98.60, 99.37, 57.58 , 96.92]	[1.89, 2.74, 14.22, 1.57, 31.39 , 5.74]
6	[25, 3, 2, 50, 1, -0.5]	[26.09, 2.82, 2.11, 52.73, 0.77, -0.17]	[99.56, 94.52, 96.34, 98.91, 92.31, 89.05]	[0.72, 7.31, 5.69, 0.99, 13.01, 7.56]

Table 3.12. A summary of the ABC-SubSim inference results using U_{2S2} sensor measurement with variable sensing-noise levels, for the selected damage cases of $L = 100$ mm.

Noise level = 0%				
Test case #	θ (mm)	θ'_{map} (mm)	Pr (%)	ξ (%)
7	[100, 1, 1, -75, -1, -1]	[101.50, 1.27, 0.98, -73.05, -0.84, -0.99]	[99.40, 91.66, 99.28, 99.22, 94.79, 99.77]	[4.22, 12.50, 4.92, 2.09, 9.28, 3.59]
8	[100, 1, 2, 0, 1, 0]	[103.23, 0.98, 1.93, 1.04, 1.03, -0.01]	[98.71, 99.27, 97.67, 99.58, 98.84, 99.62]	[4.39, 3.47, 3.58, 2.37, 7.04, 4.57]
9	[100, 2, 1, -50, 0, -0.5]	[111.47, 1.98, 1.01, -49.14, -0.04, -0.53]	[95.41, 99.39, 99.60, 99.66, 98.79, 99.10]	[9.03, 3.52, 2.46, 4.26, 4.69, 4.21]
10	[100, 2, 2, 50, -1, -0.5]	[101.44, 2.18, 1.92, 51.32, -1.04, -0.45]	[99.42, 94.48, 97.43, 99.47, 98.77, 98.45]	[1.73, 33.54 , 10.32, 0.71, 18.86 , 6.02]
11	[100, 3, 1, 0, 0, 0]	[50.71 , 3.00, 1.01, -24.90, -0.06, -0.01]	[80.28 , 99.88, 99.79, 90.04, 97.89, 99.51]	[23.77 , 1.78, 4.13, 11.41, 12.36, 3.61]
12	[100, 3, 2, 50, 1, -0.5]	[101.38, 1.43 , 2.04, 50.50, 1.23, -0.45]	[99.45, 50.84 , 98.69, 99.80, 92.31, 98.21]	[1.73, 31.42 , 14.30, 1.22, 8.62, 9.10]
Noise level = 2%				
Test case #	θ (mm)	θ'_{map} (mm)	Pr (%)	ξ (%)
7	[100, 1, 1, -75, -1, -1]	[97.65, 1.44 , 1.00, -74.15, -0.86, -0.98]	[99.06, 86.17 , 100.0, 99.66, 95.34, 99.26]	[4.88, 15.68 , 4.32, 2.41, 8.04, 3.11]
8	[100, 1, 2, 0, 1, 0]	[105.83, 0.99, 1.95, 3.13, 0.99, -0.00]	[97.67, 99.79, 98.38, 98.75, 99.56, 99.97]	[5.01, 3.68, 3.98, 2.55, 7.84, 4.96]
9	[100, 2, 1, -50, 0, -0.5]	[119.68, 1.99, 0.98, -42.92, -0.06, -0.54]	[92.13, 99.81, 99.36, 97.17, 97.96, 98.69]	[9.62, 3.55, 2.27, 4.40, 4.62, 4.00]
10	[100, 2, 2, 50, -1, -0.5]	[101.11, 0.88 , 1.98, 51.66, -1.10, -0.44]	[99.56, 65.13 , 99.49, 99.34, 96.79, 98.05]	[2.17, 41.54 , 11.81, 0.96, 20.91 , 7.94]
11	[100, 3, 1, 0, 0, 0]	[85.43, 2.99, 0.98, -9.82, -0.14, -0.04]	[94.17, 99.80, 99.41, 96.07, 95.35, 98.80]	[19.96 , 1.82, 5.09, 10.07, 14.20, 4.24]
12	[100, 3, 2, 50, 1, -0.5]	[100.46, 1.36 , 2.01, 50.87, 1.22, -0.47]	[99.82, 48.61 , 99.58, 99.65, 92.55, 99.07]	[1.43, 29.38 , 12.78, 1.11, 7.05, 8.39]
Noise level = 3%				
Test case #	θ (mm)	θ'_{map} (mm)	Pr (%)	ξ (%)
7	[100, 1, 1, -75, -1, -1]	[97.62, 1.12, 1.04, -75.11, -0.86, -0.95]	[99.05, 96.24, 98.79, 99.95, 95.44, 98.36]	[5.05, 11.03, 4.17, 2.49, 9.28, 3.07]
8	[100, 1, 2, 0, 1, 0]	[107.41, 0.99, 1.96, 3.26, 0.97, 0.05]	[97.04, 99.65, 98.61, 98.70, 99.12, 98.42]	[4.32, 3.18, 3.44, 2.18, 7.16, 4.36]
9	[100, 2, 1, -50, 0, -0.5]	[110.27, 2.01, 0.99, -47.19, -0.10, -0.54]	[95.89, 99.78, 99.56, 98.88, 96.75, 98.72]	[9.59, 3.75, 2.47, 4.70, 4.59, 4.19]
10	[100, 2, 2, 50, -1, -0.5]	[102.99, 0.92 , 1.98, 52.28, -1.03, -0.44]	[98.80, 66.21 , 99.35, 99.09, 98.87, 97.87]	[1.85, 43.85 , 9.24, 0.76, 12.45, 6.03]
11	[100, 3, 1, 0, 0, 0]	[97.96, 3.00, 0.96, -1.86, 0.12, -0.01]	[99.18, 99.89, 98.65, 99.26, 95.88, 99.53]	[14.82, 1.68, 4.87, 7.49, 13.22, 3.96]
12	[100, 3, 2, 50, 1, -0.5]	[100.91, 1.88 , 1.82, 51.56, 1.26, -0.57]	[99.64, 64.87 , 94.14, 99.37, 91.20, 97.61]	[1.71, 27.48 , 10.88, 1.29, 8.12, 6.25]
Noise level = 5%				
Test case #	θ (mm)	θ'_{map} (mm)	Pr (%)	ξ (%)
7	[100, 1, 1, -75, -1, -1]	[104.45, 1.38 , 0.97, -72.28, -0.66, -1.00]	[98.22, 88.27 , 98.90, 98.91, 88.52 , 99.85]	[4.73, 14.51, 4.35, 2.31, 10.18, 3.21]
8	[100, 1, 2, 0, 1, 0]	[104.99, 0.99, 1.91, 4.44, 1.01, 0.07]	[98.00, 99.73, 96.99, 98.22, 99.83, 97.53]	[4.62, 3.43, 3.44, 2.27, 6.97, 4.34]
9	[100, 2, 1, -50, 0, -0.5]	[115.55, 2.02, 1.01, -45.46, -0.08, -0.51]	[93.78, 99.37, 99.68, 98.19, 97.37, 99.62]	[8.94, 3.80, 2.31, 4.16, 4.85, 3.97]
10	[100, 2, 2, 50, -1, -0.5]	[100.00, 0.99 , 2.29, 51.01, -0.99, -0.27]	[100.0, 68.35 , 90.36, 99.60, 99.60, 92.22]	[1.85, 32.79 , 10.60, 0.81, 21.73 , 6.02]
11	[100, 3, 1, 0, 0, 0]	[50.82 , 3.00, 1.00, -24.86, 0.03, -0.00]	[80.33 , 99.94, 99.89, 90.06, 98.88, 99.90]	[23.83 , 1.92, 4.78, 11.56, 16.54 , 3.72]
12	[100, 3, 2, 50, 1, -0.5]	[101.24, 1.61 , 1.98, 50.49, 1.26, -0.62]	[99.50, 56.70 , 99.41, 99.80, 91.21, 96.15]	[1.94, 34.32 , 12.61, 1.28, 8.08, 7.97]
Noise level = 10%				
Test case #	θ (mm)	θ'_{map} (mm)	Pr (%)	ξ (%)
7	[100, 1, 1, -75, -1, -1]	[106.43, 1.36 , 0.96, -70.89, -0.81, -0.99]	[97.43, 88.80 , 98.83, 98.36, 93.82, 99.79]	[8.40, 12.77, 4.02, 4.16, 9.99, 2.73]
8	[100, 1, 2, 0, 1, 0]	[105.64, 0.93, 1.92, 1.68, 0.96, -0.03]	[97.74, 97.88, 97.40, 99.33, 98.69, 98.93]	[4.40, 3.29, 3.59, 2.18, 6.69, 4.14]
9	[100, 2, 1, -50, 0, -0.5]	[152.04 , 2.08, 0.98, -26.61, -0.04, -0.58]	[79.18 , 97.62, 99.44, 90.65, 98.67, 97.25]	[18.18 , 3.84, 2.73, 8.50, 3.89, 4.61]
10	[100, 2, 2, 50, -1, -0.5]	[103.56, 1.77, 2.03, 50.76, -0.86, -0.43]	[98.58, 92.91, 99.15, 99.70, 95.30, 97.57]	[1.43, 16.77 , 5.98, 0.57, 10.23, 4.43]
11	[100, 3, 1, 0, 0, 0]	[81.49, 2.99, 1.01, -10.82, -0.29, 0.02]	[92.60, 99.73, 99.55, 95.67, 90.35, 99.32]	[17.48 , 2.16, 4.85, 8.76, 14.03, 3.71]
12	[100, 3, 2, 50, 1, -0.5]	[101.81, 2.03 , 1.62 , 52.31, 1.32 , -0.65]	[99.28, 69.62 , 87.22 , 99.07, 89.26 , 94.92]	[1.55, 25.33 , 7.96, 0.92, 8.15, 4.05]

Table 3.13. A summary of the ABC-SubSim inference results using U_{2S2} sensor measurement with variable sensing-noise levels, for the selected damage cases of $L = 200$ mm.

Noise level = 0%				
Test case #	θ (mm)	θ'_{map} (mm)	Pr (%)	ξ (%)
13	[200, 1, 1, 0, -1, -1]	[210.27, 0.99, 0.99, 3.14, -0.95, -0.98]	[95.89, 99.78, 99.69, 98.74, 98.42, 99.47]	[5.33, 21.08 , 3.40, 2.77, 6.68, 2.27]
14	[200, 1, 2, 0, 1, 0]	[200.37, 1.03, 1.97, 0.57, 0.89, 0.02]	[99.85, 99.17, 99.06, 99.77, 96.35, 99.39]	[2.89, 1.96, 2.34, 1.46, 5.89, 3.26]
15	[200, 2, 1, 0, 0, -0.5]	[199.39, 2.06, 1.01, -1.82, -0.04, -0.51]	[99.76, 98.06, 99.70, 99.27, 98.54, 99.58]	[3.43, 3.13, 1.87, 2.10, 3.88, 3.73]
16	[200, 2, 2, 0, -1, -0.5]	[199.76, 2.10, 1.95, 0.23, -1.04, -0.49]	[99.91, 96.89, 98.45, 99.91, 98.57, 99.51]	[2.31, 11.11, 5.45, 1.29, 6.44, 3.41]
17	[200, 3, 1, 0, 0, 0]	[203.21, 3.00, 1.02, -0.82, 0.07, -0.00]	[98.72, 99.93, 99.30, 99.67, 97.70, 99.97]	[9.18, 1.56, 6.13, 3.99, 18.05 , 4.49]
18	[200, 3, 2, 0, 1, -0.5]	[196.97, 3.00, 1.96, -0.22, 0.98, -0.47]	[98.79, 99.89, 98.62, 99.91, 99.32, 99.06]	[3.25, 3.15, 4.02, 1.58, 10.41, 2.80]
Noise level = 2%				
Test case #	θ (mm)	θ'_{map} (mm)	Pr (%)	ξ (%)
13	[200, 1, 1, 0, -1, -1]	[206.42, 1.49 , 0.99, 2.70, -0.91, -0.98]	[97.43, 84.76 , 99.55, 98.92, 96.84, 99.31]	[4.25, 18.77 , 3.70, 2.34, 6.99, 2.43]
14	[200, 1, 2, 0, 1, 0]	[204.45, 1.03, 1.97, 1.54, 0.94, -0.04]	[98.22, 98.92, 98.90, 99.38, 97.97, 98.80]	[3.07, 2.17, 2.47, 1.65, 6.13, 3.39]
15	[200, 2, 1, 0, 0, -0.5]	[201.11, 2.06, 1.01, -1.67, -0.08, -0.52]	[99.55, 98.10, 99.77, 99.33, 97.45, 99.41]	[3.62, 3.43, 2.05, 2.17, 4.52, 4.14]
16	[200, 2, 2, 0, -1, -0.5]	[196.11, 2.23, 1.97, 0.72, -1.04, -0.49]	[98.44, 92.72, 98.92, 99.71, 98.51, 99.64]	[2.69, 10.50, 5.19, 1.28, 6.01, 3.34]
17	[200, 3, 1, 0, 0, 0]	[203.14, 3.01, 1.09, 1.72, -0.18, 0.04]	[98.74, 99.66, 97.09, 99.31, 94.12, 98.70]	[11.75, 1.70, 5.94, 5.25, 17.80 , 4.92]
18	[200, 3, 2, 0, 1, -0.5]	[201.57, 3.00, 1.96, -0.12, 0.88, -0.46]	[99.37, 99.91, 98.69, 99.95, 96.09, 98.52]	[3.01, 3.15, 4.45, 1.65, 9.25, 2.91]
Noise level = 3%				
Test case #	θ (mm)	θ'_{map} (mm)	Pr (%)	ξ (%)
13	[200, 1, 1, 0, -1, -1]	[202.66, 0.94, 0.98, 2.52, -0.95, -0.96]	[98.94, 98.13, 99.19, 98.99, 98.32, 98.63]	[4.76, 23.22 , 4.07, 2.49, 6.35, 2.39]
14	[200, 1, 2, 0, 1, 0]	[200.52, 1.02, 1.96, 0.73, 0.91, 0.03]	[99.79, 99.24, 98.56, 99.71, 97.00, 98.94]	[3.53, 2.20, 2.69, 1.75, 7.31, 3.69]
15	[200, 2, 1, 0, 0, -0.5]	[197.60, 2.06, 1.01, -1.95, -0.08, -0.52]	[99.04, 97.98, 99.66, 99.22, 97.41, 99.25]	[3.33, 2.90, 1.74, 2.05, 3.70, 3.49]
16	[200, 2, 2, 0, -1, -0.5]	[198.36, 2.13, 2.00, 0.59, -1.05, -0.46]	[99.35, 95.97, 99.92, 99.77, 98.17, 98.52]	[2.08, 7.75, 5.01, 1.05, 5.48, 3.21]
17	[200, 3, 1, 0, 0, 0]	[194.19, 3.00, 1.02, -3.42, 0.24, 0.03]	[97.68, 99.96, 99.44, 98.63, 92.03, 99.11]	[10.16, 1.63, 5.75, 4.81, 20.26 , 4.75]
18	[200, 3, 2, 0, 1, -0.5]	[199.99, 2.97, 1.99, -0.12, 0.95, -0.44]	[100.0, 98.96, 99.55, 99.95, 98.45, 97.98]	[2.86, 3.08, 4.07, 1.47, 9.33, 2.60]
Noise level = 5%				
Test case #	θ (mm)	θ'_{map} (mm)	Pr (%)	ξ (%)
13	[200, 1, 1, 0, -1, -1]	[205.65, 1.61 , 0.98, 1.91, -0.94, -0.98]	[97.74, 81.07 , 99.29, 99.23, 97.84, 99.35]	[5.19, 21.68 , 3.71, 2.62, 7.38, 2.36]
14	[200, 1, 2, 0, 1, 0]	[202.18, 1.02, 1.98, 1.52, 0.85, 0.00]	[99.13, 99.42, 99.29, 99.39, 94.88, 99.88]	[2.76, 1.95, 2.34, 1.56, 5.90, 3.19]
15	[200, 2, 1, 0, 0, -0.5]	[200.78, 2.07, 1.00, -1.21, -0.07, -0.53]	[99.69, 97.85, 99.92, 99.51, 97.82, 98.85]	[3.06, 2.76, 1.72, 1.81, 3.29, 3.08]
16	[200, 2, 2, 0, -1, -0.5]	[198.88, 2.18, 2.01, -0.12, -1.03, -0.47]	[99.55, 94.44, 99.58, 99.95, 98.87, 99.09]	[2.19, 7.12, 4.61, 1.13, 5.68, 2.80]
17	[200, 3, 1, 0, 0, 0]	[194.67, 3.02, 1.02, -0.63, 0.12, 0.04]	[97.87, 99.51, 99.27, 99.75, 96.02, 98.57]	[10.25, 1.57, 5.53, 5.01, 19.15 , 4.46]
18	[200, 3, 2, 0, 1, -0.5]	[197.34, 2.98, 1.94, 0.12, 0.93, -0.46]	[98.94, 99.47, 98.10, 99.95, 97.82, 98.58]	[3.46, 3.24, 4.31, 1.77, 9.94, 3.06]
Noise level = 10%				
Test case #	θ (mm)	θ'_{map} (mm)	Pr (%)	ξ (%)
13	[200, 1, 1, 0, -1, -1]	[198.58, 2.07 , 0.92, -0.06, -0.99, -1.00]	[99.43, 66.67 , 97.36, 99.97, 99.75, 99.91]	[6.87, 32.13 , 4.06, 3.18, 5.81, 2.30]
14	[200, 1, 2, 0, 1, 0]	[202.96, 1.03, 1.98, 0.13, 0.90, -0.02]	[98.82, 99.16, 99.34, 99.95, 96.65, 99.48]	[3.23, 2.18, 2.82, 1.84, 7.72, 3.42]
15	[200, 2, 1, 0, 0, -0.5]	[193.30, 2.10, 0.99, -4.85, 0.03, -0.54]	[97.32, 96.96, 99.52, 98.06, 98.86, 98.66]	[5.11, 2.64, 1.79, 2.73, 3.36, 3.00]
16	[200, 2, 2, 0, -1, -0.5]	[198.35, 2.18, 2.00, -0.08, -1.04, -0.47]	[99.34, 94.30, 99.91, 99.97, 98.72, 98.83]	[1.86, 6.24, 4.10, 0.92, 5.26, 2.57]
17	[200, 3, 1, 0, 0, 0]	[195.92, 2.99, 1.01, 1.85, -0.10, 0.05]	[98.37, 99.80, 99.69, 99.26, 96.75, 98.49]	[9.67, 1.71, 6.05, 5.11, 22.02 , 4.47]
18	[200, 3, 2, 0, 1, -0.5]	[204.21, 2.98, 1.93, 1.54, 0.84, -0.48]	[98.32, 99.36, 97.80, 99.38, 94.60, 99.28]	[2.98, 3.06, 4.20, 1.73, 9.82, 2.47]

Table 3.14. A summary of the ABC-SubSim inference results using U_{2S1} and U_{2S2} sensor measurements with variable sensing-noise levels, for the healthy-weld case.

U_{2S1}				
Noise level (%)	θ (mm)	θ'_{map} (mm)	Damage detection thresholds (mm)	Detection result
0		[1.91, 0.01, 0.00]		No damage (healthy weld)
2		[18.92, 0.35, 0.04]		No damage (healthy weld)
3	[0, 0, 0]	[25.20, 0.02, 0.01]	[1, 0.1, 0.1]	No damage (healthy weld)
5		[11.22, 0.13, 0.03]		No damage (healthy weld)
10		[24.71, 1.62, 0.08]		No damage (healthy weld)
U_{2S2}				
Noise level (%)	θ (mm)	θ'_{map} (mm)	Damage detection thresholds (mm)	Detection result
0		[0.13, 0.01, 0.13]		No damage (healthy weld)
2		[0.10, 0.01, 0.11]		No damage (healthy weld)
3	[0, 0, 0]	[0.64, 0.22, 0.23]	[1, 0.1, 0.1]	No damage (healthy weld)
5		[0.90, 0.06, 0.47]		No damage (healthy weld)
10		[94.13, 2.21, 0.56]		Damage exists (false positive)

3.5.6 Discussion

The suggested approach performs a probabilistic damage identification instead of a deterministic identification; i.e., it gives a PDF for each of the damage parameters (size and position parameters), which provides a complete uncertainty quantification of these parameters. The lower the uncertainty, the greater our degree of belief about the damage parameters, as identified by ABC-SubSim.

The proposed methodology is proved capable of inferring the intact state of the monitored weld using a single sensor measurement, despite its noisy condition. Using a single sensor measurement corrupted with noise, damage of significant size is also inferred with high precision and low uncertainty, while damage of smaller size shows less certain results.

Two x -positions are inferred when using measurements from the central sensing point (S1), revealing a geometrical symmetry for both the actuator and the sensing point, which is expected. Nevertheless, the successful prediction of both the real

x and its symmetric value, by the developed algorithm, means that the ANN-based surrogate model has effectively learned this symmetry from the training data. This result is a validation of the ANN's performance and of the methodology's potential for detecting multiple possibilities of the available damage.

The symmetry problem is resolved upon using measurements from another sensing point lying outside the plate's plane of symmetry. Damage length (L) and x -position are precisely predicted even for small damage sizes, while for large damages, very accurate predictions are attained for all the damage parameters. This resolution in inferring a precise size and position of the damage, using only one single measurement, is considered an important achievement in the damage identification field. The symmetry of S1 is obvious in the problem under study; however, other non-trivial similarities of measurements from different damage cases may be faced in real-life situations. Hence, data fusion from multiple sensing points (at least two sensor measurements) is thought to be a necessity to avoid such issues and increase the reliability of the damage identification process.

After fusing multiple sensor measurements (U_{2S1} , U_{2S2} , and/or U_{2S3}) within the ABC-SubSim algorithm, higher precision and lower uncertainty are achieved for the cases of small damage size. More specifically, the best results are obtained when fusing data from S2 and S3.

It is noticed in all the presented inference results, that the width (W) and the y -position show higher uncertainties accompanied sometimes with less inference precision than all the other damage parameters. This is most obvious when looking at damages of small size ($L = 25 \text{ mm}$); i.e. for test cases 1 to 6 (Table 3.5). This may

mean an imperfect performance of the ANN surrogate model over the W and y parameters when $L = 25 \text{ mm}$.

If a better inference is desired in the case of small damages, an additional inference step may be added. This step is activated only if L is inferred to be below a certain threshold in the first inference step. This would include the training of additional ANNs using training data of small damage lengths only, to help the ANNs learn more how to differentiate the other damage parameters. Such an improvement can lead to more accurate inference results whenever the application necessitates. ABC-SubSim parameters may also be tuned, in this case, to make the first inference faster but probably less accurate.

In practice, the SHM system designer should be aware of types, shapes, and possible positions of damages, in the monitored structure, that should be considered and modeled in the finite element model for data generation. Thus, the architecture of the trained neural network should also be adapted to the new number of input variables (size, position, and probably orientation and shape parameters of the damage) and to the new signal length, as needed. More complex damage cases can be integrated by using multiple neural networks to cover different types of damage and sizes. The problem can be broken into a classification stage first, identifying the damage type using machine learning classifier(s), and then an identification stage, inferring the predefined damage parameters and using a specific surrogate model (based on the classified damage type).

When implementing the proposed framework, calibration/normalization of the sensor measurements is required to make the experimental data comparable to the numerical data in terms of amplitude. A deviation in the placement of the actuators and sensors is not expected to cause a major difference in the collected responses; neither

will highly impact the coverage of the sensor network [25]. Also, slight misplacement of the PZT wafers may lead to small variations in the signals which are of the level of noise, however, it was demonstrated that damage inference is robust to such disparity. Non-contact sensing and actuation methods (e.g., air-coupled or laser-based transducers) would provide a better control and data-normalization ability when applicable. The FE modeling should be modified based on the used actuation and sensing methods to produce signals that are well-matching with the experimental measurements.

The better the match is between the FE simulations and real experimental signals, the more robust is the inference when applied to real sensor measurements, with less yielded uncertainties. The differences in a signal that may arise due to noise or environmental changes (as temperature and pressure on an airplane structure) are expected to appear as small inference deviation rather than failure in prediction, which was demonstrated by adding different levels of sensing noise (Section 3.5.5). In addition, to account for environmental changes, they may be used as inputs to the FE model, and training data at variable conditions can be generated for the surrogate model. Those inputs should also be added to the inputs of the surrogate model, towards a better but more sophisticated condition-based damage identification.

Further, a prognostics-based decision-making SHM system is envisaged as desirable future work, where the structure's deterioration and remaining useful life are predicted to make informed decisions. A more intelligent system would also add self-adaptation algorithms to dynamically account for environmental changes and operational conditions, therefore increasing both the structure's integrity and efficiency.

Finally, time is a key factor when monitoring critical structures that, in case of failure, may endanger people's lives. This factor is more important when such structures are subject to highly variable loads (e.g., an operating passenger airplane) or may be exposed to abrupt changes (e.g., severe impact damage). A successful SHM system should be able to detect any damage at the moment it happens or even have the potential for capturing the deterioration in the structure's strength before damage occurs. The time elapsed to perform one FE simulation was, on average, around 4.75 minutes using an Intel® Core™ i7-8750H CPU (parallel *Abaqus*® simulation over 8 CPUs). However, the ANN takes around 8 *ms* to predict the signal using the same processor. This obvious advantage (more than 35,000 times faster) and the possibility to do the ANN prediction with minimal processing needs, both give the surrogate modeling its importance for applying a probabilistic damage-inference methodology in a real SHM system. On the other hand, the computational time needed to perform a damage inference considerably varies when using different numbers of sensor measurements. The time needed to apply the ABC-SubSim algorithm using 1, 2, 3, and 4 sensor measurements was respectively around 10, 24, 36, and 60 minutes using the same processor. Therefore, a trade-off between time and the advantages of adding more sensor measurements to the damage inference process should be considered.

The advantage of performing the damage inference through an ABC algorithm and using a surrogate model is that they do not require heavy computations, and thus a small lightweight processor can be used. The ultimate goal of the current study is to have smart sensors, that include microprocessors, or to have small processors aboard the monitored system which can infer damage in real-time.

3.6 Summary

This chapter proposed a novel framework for damage detection, localization, and assessment using ultrasonic measurements. The framework allows for full identification, in size and position, of damage within a dissimilar-material joint using only one ultrasonic actuator and one sensor measurement.

Surrogate models, based on Artificial Neural Networks (ANNs), were trained using finite element simulations to predict Lamb-wave sensor measurements when given specific damage. The ANNs were then employed to perform a probabilistic damage inference on simulated data corrupted with noise using Approximate Bayesian Computation, thus, providing *posterior* PDFs of six damage parameters (length, width, thickness, and x -, y -, and z -positions).

The potential of the algorithm for detecting multiple damage scenarios that may lead to the same sensor measurement was proved. This made it advisable to fuse information from at least two sensor measurements to guarantee a more reliable damage identification. Upon data fusion of multiple sensor measurements, the length and x -position of the damage were inferred with a precision higher than 99% in all the test cases. The inference of the other four damage parameters (width, thickness, and y and z -positions) was attained with an error of less than 0.9 mm , in the worst-case scenario. Damage parameters were inferred with a precision of above 95% for more than 83% of the cases when using a combination of two sensor measurements (U_2 from S2 and S3).

The developed framework is computationally inexpensive, thus rendering the methodology suitable for online/onboard monitoring applications. The high resolution attained, inferring an accurate size and position of the damage by employing only one or

two sensor measurements, is considered a major advancement in the structural assessment field.

CHAPTER 4

ASSESSMENT OF INTERMETALLIC COMPOUNDS WITHIN DISSIMILAR JOINTS USING LAMB-WAVE NONLINEARITY

4.1 Introduction

One of the major challenges in dissimilar welding processes is the formation of intermetallic compounds (IMCs) at the level of the joint [110, 111]. The availability of such compounds, appearing at the microstructural level, is associated with brittleness and weakness in the weld [112]. Various welding techniques, including diffusion, friction, electron beam, and laser welding, have led to joints weaker than both base materials, due to the development of IMCs across the joint [113, 114]. Though explosive welding could avoid the formation of intermetallics at low loads [115], however, it leads to poor corrosion resistance [116]. The lower heat input in friction stir welding, which is also controllable through the welding parameters, made FSW a promising alternative for producing reliable dissimilar joints [17, 117, 118]. In 2010, Fazel-Najafabadi et al. [119] studied the joining of pure titanium (CP-Ti) to 304 stainless steel in a lap joint by friction stir welding using different process parameters. The strongest achieved joint had a maximum failure load of 73% of that of pure titanium. Liao et al. [113] have also used friction stir welding to join a commercially pure titanium plate to a structural steel plate in a lap joint. The obtained microstructure at the interface of the joint was intensively examined and the different phases and grain sizes were identified. The joint was found to be stronger than the base metals even with the existence of IMCs. This might be due to the distribution of small intermetallic particles and the formation of β titanium at the interface. Many other examples of

successful dissimilar friction stir welding are reported in literature [120-123]; however, the welding process parameters play a critical role in dictating the joint's quality and microstructural condition [117, 124, 125]. The problem of IMC formation is still present, especially when there is a major physical differences between the welded materials (e.g., melting intervals, thermal conductivity, and thermal expansion) or due to the low solubility of one material within the other (e.g., steel in aluminum) [111, 121]. Yamamoto et al. [125] have shown that the tensile strength of the dissimilar FSW joint decreases significantly with the increase in the IMC layer's thickness. It is therefore of great importance to be able to detect and quantitatively assess the amount of IMCs within the joint to evaluate/predict its strength.

Using the standard linear features of ultrasonic waves (e.g., amplitude attenuation, time-of-flight, transmission and reflection coefficients, and various distance metrics between time-domain signals) is usually restricted to detecting/assessing changes within a certain order of magnitude of the probing wave's wavelength [126, 127]. On the other hand, nonlinear ultrasonic features have demonstrated high sensitivity to micro changes in materials [128]. These features include sub-harmonics [129, 130], higher harmonics [131, 132], nonlinear resonance [133, 134], and nonlinear modulation [135, 136], among others. Fukuda et al. [137, 138] have used the second-harmonic and sub-harmonic features to detect plastic deformation in metallic rods. Two designs of double-layered piezoelectric transducers (DLPT) were proposed to enhance the receiver's sensitivity to the targeted harmonic components in the measured signals. The ratio between the amplitudes of the sub-harmonic and fundamental wave components was observed to increase with the increase in the plastic strain. Zhang et al. [139] have investigated the effect of nonlinear boundary conditions, of an aluminum

plate, on fatigue-crack detection using the sub-harmonic resonance of LWs. It was experimentally verified that the sub-harmonic component can be used to both detect the fatigue crack and differentiate it from nonlinear boundary conditions. Yang et al. [35] have performed a parametric study addressing the effects of fatigue-crack opening (due to loading) and the incidence angle of excitation on the second-harmonic generation (SHG) in LWs. Numerical and experimental results showed the significant importance of considering the loading conditions and excitation angles during fatigue-crack inspection using SHG. A similar study was also introduced in [140], addressing the effect of different fundamental LW excitations at low frequencies, and more physical insights were provided on the SHG due to contact nonlinearity at fatigue cracks. The same authors [41] have numerically studied the SHG due to the interaction of LWs with crack-induced debonding in an aluminum plate strengthened by fiber-reinforced polymer (FRP). Different damage scenarios were considered including cracks and debonding of different sizes. It was found that exciting using the S_0 or A_0 LW modes shows different sensitivities of the SHG to different kinds and sizes of damage. Cao et al. [141] have used both S_0 - S_0 and S_1 - S_2 synchronism of LWs in the low- and high-frequency ranges, respectively, to characterize pitting damage in an aluminum plate. After a theoretical insight of SHG due to pitting damage, a SAFE method was employed to perform a numerical investigation, and an experimental validation was also carried. A nonlinearity index was utilized for a successful damage imaging using a dense PZT sensor network. Belanger and Jahazi [142] have explored the evaluation of aluminum FSW lap joints using the S_0 LW mode. Welds were manufactured using different tool rotational speeds, and both linear and nonlinear (second-harmonic) LW-based examinations were performed. A strong correlation was found between the transmission

coefficient of the S_0 mode and the width of the friction-stir zone; however, no clear correlation could be established for the SHG.

There is no work found in the literature studying the effect of intermetallic compounds, formed in dissimilar welds, on guided waves. In this chapter, the assessment of IMCs, within dissimilar FSW, using LW nonlinearity is explored. The analysis is performed on simulated dissimilar FSW lap joints, between AA5052-H32 aluminum and ASTM 516-70 steel, containing intermetallic layers of variable thickness. Nonlinear FE modeling is utilized to account for the nonlinear-elastic characteristics of the materials. Micro-scaled intermetallic regions are imitated in 2D FE models with different scenarios (thickness and material properties). Symmetric Lamb waves are excited in the models, using PZT transducers, with a central excitation frequency of 1,785 *kHz* to meet the synchronism and zero-flux conditions of SHG. Afterward, the effects of IMCs on the nonlinear features of LWs, namely the relative acoustic nonlinearity parameter, are investigated.

Section 4.2 introduces a theoretical background about nonlinear ultrasound. Sources of nonlinearity and ways of evaluation and enhancement of the second-harmonic modes are presented. Section 4.3 describes the FE modeling process, based on the available specimens, including the preliminary single-material model and the dissimilar-FSW lap-joint model. Section 4.4 shows the signal processing methodology and discusses the results of the FE investigation. Finally, concluding remarks are presented in Section 4.5.

4.2 Theoretical Background

As an ultrasonic wave propagates through an elastic medium, it is distorted by the intrinsic nonlinearities within the medium itself and by nonlinearities that may arise from other disturbing features [87, 143]. This can lead to a set of various nonlinear components in the probing wave including those generated at fractional multiples (e.g., half) of the excitation/fundamental frequency, also known as sub-harmonics; at twice, thrice, or a higher multiple of the fundamental frequency, so-called higher-order harmonics or super-harmonics (first pointed out by L. Rayleigh in 1896 [144]); or at other mixed frequencies, induced by another excitation, to modulate the interrogating wave [87]. Closed cracks [145-148], voids [141], and even dislocations [149, 150] were all identified as potential sources of nonlinearities that can be detected or even assessed by different nonlinear features of ultrasonic waves. Due to their proven sensitivity to different microstructural changes and degradation in both composite and metallic structures, second-order harmonics of LWs, in particular, have attracted the attention of many researchers in the last few decades [151-155].

The acoustic nonlinearity parameter, designated as β , is a term used to express the nonlinearity of LWs and other ultrasonic waves. It can be derived from the nonlinear stress-strain relation of the medium [143, 156], and is stated as follows [156, 157]:

$$\beta = \frac{8}{k^2 r} \frac{A_2}{A_1^2} \cdot \delta \quad (4.1)$$

where:

- A_1 : is the amplitude of the fundamental probing wave mode;
- A_2 : is the amplitude of the second-harmonic wave mode paired to the fundamental probing mode;
- k : is the fundamental wavenumber;

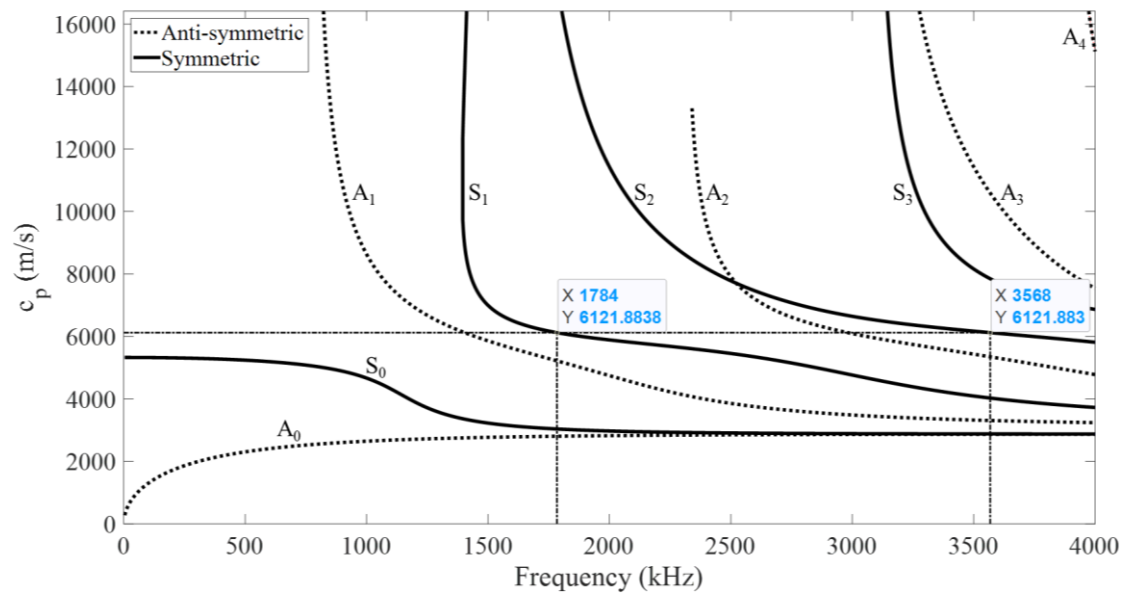
- r : is the wave's propagation distance;
- δ : is a scaling function for LWs, independent of the propagating medium's health condition [156].

To detect damage or microstructural changes, the variation in β is of one's interest, rather than its real value; thus, β is normalized, for a fixed wavenumber (k) and propagation distance (r), to give the so-called relative acoustic nonlinearity parameter (RANP), denoted by β' [143, 157]:

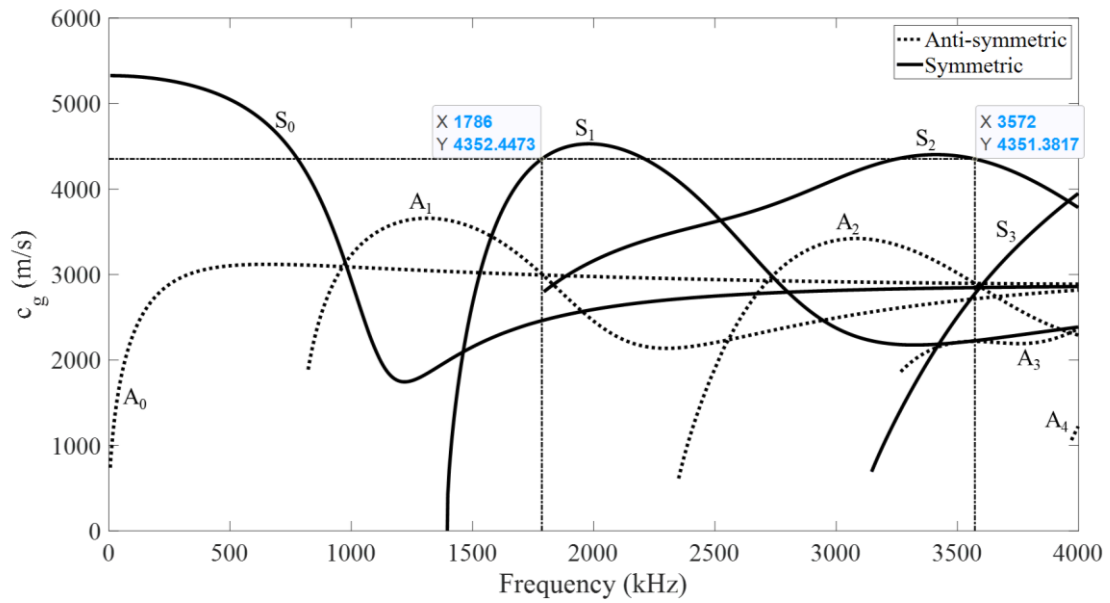
$$\beta' = \frac{A_2}{A_1^2} \quad (4.2)$$

Due to the weak amplitudes of the second-harmonic modes, it is desirable to excite LWs at specific frequencies to attain a cumulative second-harmonic generation with an acceptable signal-to-noise ratio (SNR). This is achieved if (1) the phase velocity of the fundamental wave mode at the excitation frequency is equal (or approximately equal) to the phase velocity of another mode at double the excitation frequency (synchronism condition; check Figure 4.1), (2) accompanied with non-zero power flux between the modes [152, 158]. The synchronism and non-zero power flux conditions lead to internal resonance between the two modes, where energy is effectively transferred from the fundamental mode to the second-harmonic mode during the wave propagation. This ensures the accumulation of this specific second-harmonic mode, while other double-frequency modes would rapidly vanish due to their amplitude attenuation over the propagation distance (explained in Chapter 2, Section 2.5.4) [157, 158]. The synchronism condition between the fundamental mode and its paired second-harmonic mode is usually accompanied by similar group velocities as well [30].

As an application on the 2-*mm* thick AA5052-H32 aluminum plate used in the current study, Figure 4.1 shows its theoretical phase- and group-velocity dispersion curves determined using *Wavescope* [70]. The two conditions of internal resonance are satisfied between the first-order and second-order symmetric modes (S_1 and S_2) at a fundamental excitation frequency of around $f_E = 1,785 \text{ kHz}$. It can be noticed from Figure 4.1(b) that S_1 and S_2 have, respectively, the highest group velocities at f_E and $2f_E$, which makes them easily distinguished from other propagating wave modes. This excitation frequency will therefore be used to ensure proper SHG within the upper sub-plate of the examined joints, as will be explained further in the subsequent sections.



(a) Phase velocities



(b) Group velocities

Figure 4.1. Dispersion curves of LW modes in a 2-mm thick AA5052-H32 aluminum plate.

4.3 Finite Element Modeling

4.3.1 Available Specimens

This study was inspired by the work by Ibrahim et al. [159], where the microstructural and mechanical properties of friction stir diffusion cladding (FSDC) samples were extensively examined. FSDC is a new cladding technique that is performed in a way similar to FSW lap welding, where the whole cladding surface is processed. Figure 4.2 shows photos of the top and cross-sectional views of a cut FSDC specimen including two cladding passes. Six specimens of one-pass FSDC joints (resembling FSW lap joints) between 2-mm AA5052-H32 aluminum and 7-mm ASTM 516-70 steel were received from the research group at the King Fahd University of Petroleum and Minerals (KFUPM) [159]. Their dimensions and varied FSDC process parameters are listed in Table 4.1. Figure 4.3 shows the top and side photos of one of

the six available samples, which all share the same geometrical shape. The diffusion zone, which defines the interface between the two materials, was characterized using energy dispersive spectroscopy (EDS) line-scan analysis, and the interface thickness was measured through the composition variation technique. Different process parameters have led to a variation in the interface thickness between the specimens, as shown in Figure 4.4 [159]. The interface thickness can be correlated to the amount of IMCs available within the weld region.

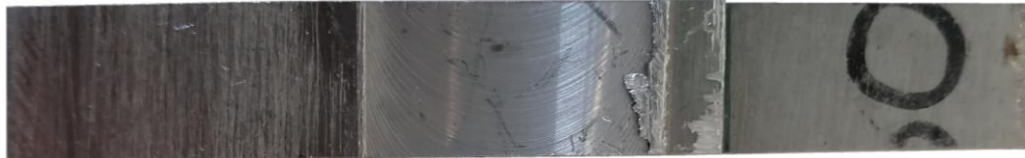
This work focuses on the numerical modeling of the problem, while an experimental investigation will be the subject of future work. Thus, a numerical FE model mimicking the available samples is used, while varying the thickness and composition of the interface layer based on the performed characterization [159].



Figure 4.2. Two photographs of the top and cross-sectional views of a cut FSDC specimen with two cladding passes [159].

Table 4.1. Geometry and variable welding parameters of the available FSDC specimens.

Name	Number of available specimens	Length (mm)	Width (mm)	Tool's rotational speed (RPM)	Tool's feed speed (m/s)
A50	2	80	12-12.5	1000	50
A100	1	80	11	1000	100
B100	1	80	19	500	100
B150	2	80	12.3-15	500	150



(a) Top view



(b) Side view

Figure 4.3. Top and side photos of one of the available FSDC samples.

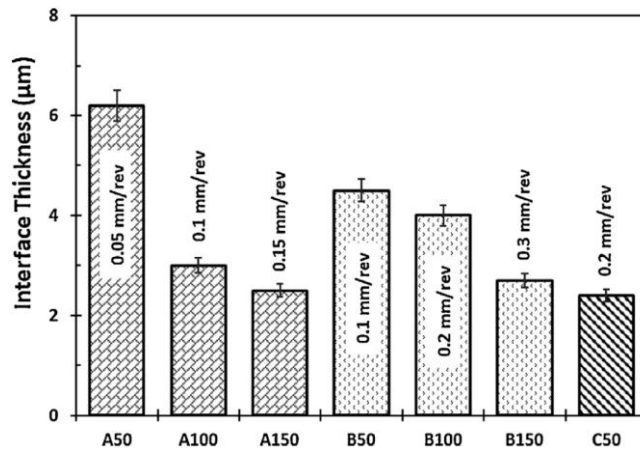


Figure 4.4. The interface-layer thickness (in μm) of different specimens [159].

4.3.2 Single-Material Model

To have a better insight into the SHG and accumulation in the upper plate of the FSW lap joint, the nonlinear behavior of the wave was examined in a single-material model before modeling the complete welded specimens.

A 2D plane-strain model of an AA5052-H32 plate of 2-*mm* thickness and 300-*mm* length was built in *COMSOL*[®] *Multiphysics* (Figure 4.5) using Murnaghan nonlinear-elastic material model [160, 161]. The used material properties, including Lamé second-order elastic (SoE) constants [159] and Murnaghan third-order elastic (ToE) constants [162], are listed in Table 4.2. The model's width was set to be 12 *mm* based on the width of the available specimens (Table 4.1). Two PZT actuators (of 7-*mm* length and 0.5-*mm* thickness) were placed on the opposite surfaces of the same edge of the plate and were modeled based on a solid-mechanics/electrostatics multiphysics solver. The two PZTs (PZT-5H) were excited simultaneously using the same input signals to selectively excite the symmetric LW modes and suppress/weaken the anti-symmetric modes [163]. The 15.5-cycle Hann-windowed sinusoidal excitation signals, of 1,785-*kHz* central frequency and 240-*V* peak-to-peak voltage, were fed into the outer (symmetric) poles of the PZT wafers.

A free quadrilateral mesh was used with a maximum element size of 0.125 *mm*, allowing around 10 elements per wavelength of the second-harmonic S_2 mode. The plate was made long enough to prevent reflections, from the plate's far side, from interfering with the propagating wave modes; where the total simulation time was set to be $t = 65 \mu s$ based on the highest group velocities of the excited modes (propagating distance $r = c_g \times t = 4352.64 \text{ m/s} \times 65 \times 10^{-6} \text{ s} \approx 0.283 \text{ m} = 283 \text{ mm} < 300 \text{ mm}$). Waves were received (as in-plane displacements (U_1) along the plate's length), at a

sampling rate of 100 MHz, from a set of 15 sensing points uniformly distributed on the upper surface of the plate. The sensing points were placed at 10-mm spacing along a distance of 50 to 190 mm from the plate's left edge. The plate's bottom right corner was fixed to prevent model movement.

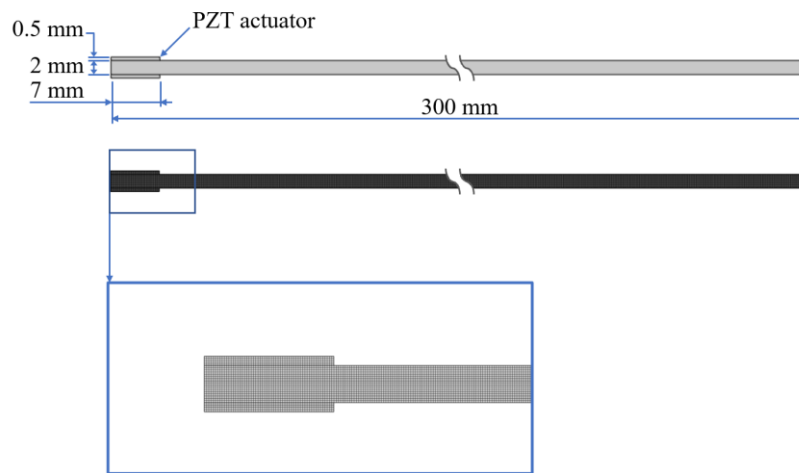


Figure 4.5. Geometry and mesh of the single-material (AA5052-H32) 2D plane-strain FE model.

Table 4.2. Physical and mechanical properties of the used sub-plate materials.

Material	Density (kg/m^3)	Lamé parameters (GPa)		Murnaghan ToE constants (GPa)		
		λ	μ	l	m	n
AA5052-H32	2680	51.3	26.43	-252.2	-325	-351.2
ASTM 516-70	7800	107.05	77.52	-248	-623	-714

4.3.3 Dissimilar Lap-Weld Model with Variable IMCs

Similar to the single-material model, a 2D plane-strain model was built using *COMSOL*[®] *Multiphysics* for the AA5052-H32/ASTM 516-70 lap weld. An AA5052-H32 plate of 2-*mm* thickness and 56-*mm* length was placed on top of an ASTM 516-70 plate of 7-*mm* thickness and 55-*mm* length, assuming a perfect joint, as can be seen in Figure 4.6. Murnaghan's nonlinear-elastic material model was used to model both the aluminum and steel sub-plates [160, 161]. The material properties assigned to the steel sub-plate, including Lamé constants [159] and Murnaghan ToE constants [164], are listed in Table 4.2. The model's width was also set to be 12 *mm* based on the width of the available specimens (Table 4.1). The same actuator-PZT configuration and excitation was used on the left edge of the aluminum plate. Intermetallic regions were mimicked in the FE model by varying the material properties of several interface sub-layers (each of 2- μm thickness and 21.5-*mm* length) within the welded region between the two materials. Figure 4.6 includes insets of zoomed-in portions of the weld region showing the used interface sub-layers. Six different scenarios of IMC existence were built in six different models, namely, a model with no IMCs and five other models including 2-, 4-, 6-, 8-, and 10- μm IMC layers. A free quadrilateral mesh was used with a maximum element size of about 0.135 *mm* in the aluminum sub-plate, to guarantee a minimum of 9 elements per wavelength of the S_2 mode (propagating in the upper sub-plate). Rectangular elements, of $0.002 \times 0.02 \text{ mm}^2$ size, were used to ensure proper meshing of the micro-sized interface sub-layers. This has generated a very fine mesh within the weld region, with element sizes in the order of a few μm (Figure 4.6). The mesh size was relaxed, after around 3.5 *mm* below the weld interface, up to a maximum element size of about 1.35 *mm* at the bottom edge of the steel sub-plate. The total

simulation time was set to be $t = 50 \mu s$, and U_1 displacements were measured, at a sampling rate of 100 MHz, from a set of 24 sensing points uniformly distributed on the upper surfaces of both sub-plates. The sensing points were placed at 3-mm inter-distance along a range of 9 to 78 mm from the model's left edge. The model's bottom right corner was fixed to prevent its movement.

Due to the ambiguity about the exact composition and material properties of the interface layers, and since the nonlinear-elastic properties of IMCs can hardly be obtained, the interface layers were modeled as homogeneous isotropic linear-elastic materials. The EDS characterization of interface layers, presented in Figure 4.7 [159], shows that the composition fraction of steel versus aluminum (and vice-versa) varies in a relatively linear manner within the interface layer, showing a smooth transformation from steel to aluminum composition. Therefore, the IMC layer was divided into multiple sub-layers, each of $2\text{-}\mu m$ thickness, and the material properties of the sub-layers were assumed through linear interpolation between those of aluminum and steel. Table 4.3 shows an example of the case of a $6\text{-}\mu m$ interface layer, where three sub-layers were assigned different material properties (linearly interpolated between the properties of aluminum and steel). This was applied to all the five models including variable-thickness (2 to 10 μm) IMC layers.

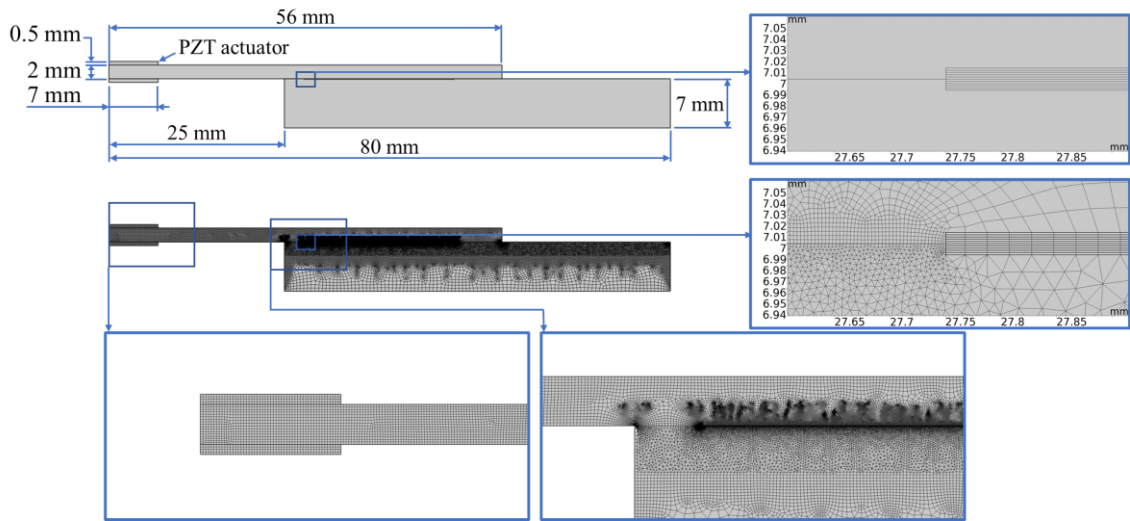


Figure 4.6. Geometry and mesh of the AA5052-H32/ASTM 516-70 lap-weld 2D plane-strain FE model.

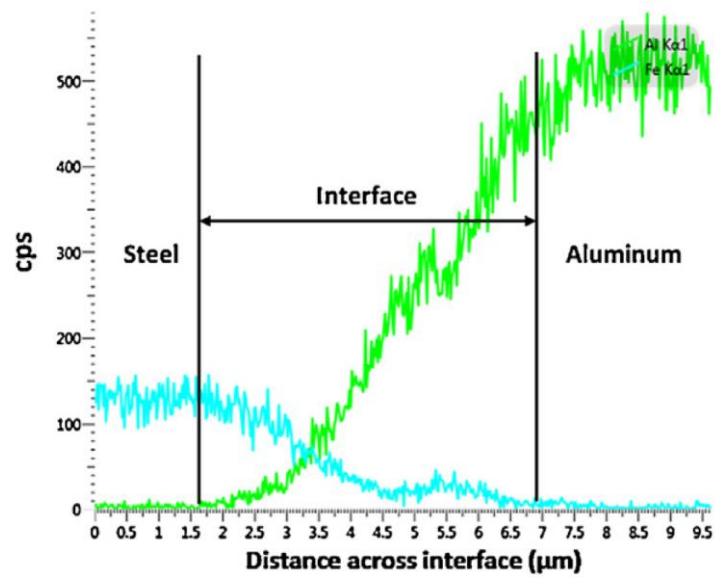


Figure 4.7. EDS line scan analyzing the interface layer of a selected A50 sample [159].

Table 4.3. Physical and mechanical properties of the 6- μm IMC layer, divided into three sub-layers whose properties were determined via linear interpolation between the material properties of AA5052-H32 and ASTM 516-70.

Material	Density (D) in kg/m^3	Young's modulus (E) in GPa	Poisson's ratio (ν)
AA5052-H32	2680	70.3	0.33
IMC sub-layer 1	3960	102.73	0.32
IMC sub-layer 2	5240	135.15	0.31
IMC sub-layer 3	6520	167.58	0.30
ASTM 516-70	7800	200	0.29

4.4 Results and Discussion

4.4.1 Time-Domain Mode Identification

Figure 4.8 shows the two time-domain signals measured in the single-material model at sensor positions of 50 and 160 mm from the plate's left edge. The signals show a gradual separation between two main propagating modes of different speeds, where their group velocities were calculated to be around 3,191.2 m/s and 2,782.7 m/s . The maximum peaks of the apparent wave packets were used for group-velocity calculations (marked on Figure 4.8), where the two modes were not yet separated at 50 mm . Both calculated group velocities do not match with the theoretical group velocity of the S_1 - S_2 mode-pair at f_E ($c_g \approx 4,350 \text{ m/s}$; Figure 4.1(b)). Based on Figure 4.1(b), the velocity of the slower mode ($c_g = 2,782.7 \text{ m/s}$) is close to that of the S_0 mode ($c_g \approx 2,460 \text{ m/s}$). However, the high-velocity mode ($c_g = 3,191.2 \text{ m/s}$) may correspond to the A_0 or A_1 modes ($c_g \approx 3,000 \text{ m/s}$) which could be still be excited at 1,785 kHz , even though a symmetric excitation was employed in the FE model [163].

On the other hand, a faster but extremely weak mode is detected at the beginning of each signal. Due to the low amplitudes of the mode, some peaks vanished after propagating for some distance, which led to difficulty in accurately identifying its peaks. The group velocity was calculated, using the time-of-arrival of the fourth appearing peaks (marked on Figure 4.8), to be about $3,811.5 \text{ m/s}$, which is closer to that of the S_1 - S_2 mode-pair than to any other mode indicated in the dispersion curves (Figure 4.1(b)). This suggests that the S_1 - S_2 mode-pair is weakly appearing in the measured waves while being partially or totally covered by other stronger propagating modes; thus, it can hardly be identified in the time-domain signals.

Similarly, Figure 4.9 shows the two time-domain signals measured in the dissimilar lap-weld model at sensor positions of 9 and 24 mm from the model's left edge. Both measurements are taken before the steel plate begins. Larger signal amplitudes are evident in the measurement at 24 mm , which is caused by the superposition with different reflections after the wave interacts with the steel plate. The fourth peak of each of the signals (marked on the figure) was used for calculating the group velocity of the fastest appearing mode. A value of $3,926.7 \text{ m/s}$ was obtained which is relatively close to the group velocity of the S_1 - S_2 mode-pair in the aluminum sub-plate. Complex shapes are observed in the measured signals, including superpositions with multiple possible reflections and converted modes.

The measured signals are analyzed in both the frequency and time-frequency domains in the subsequent sections.

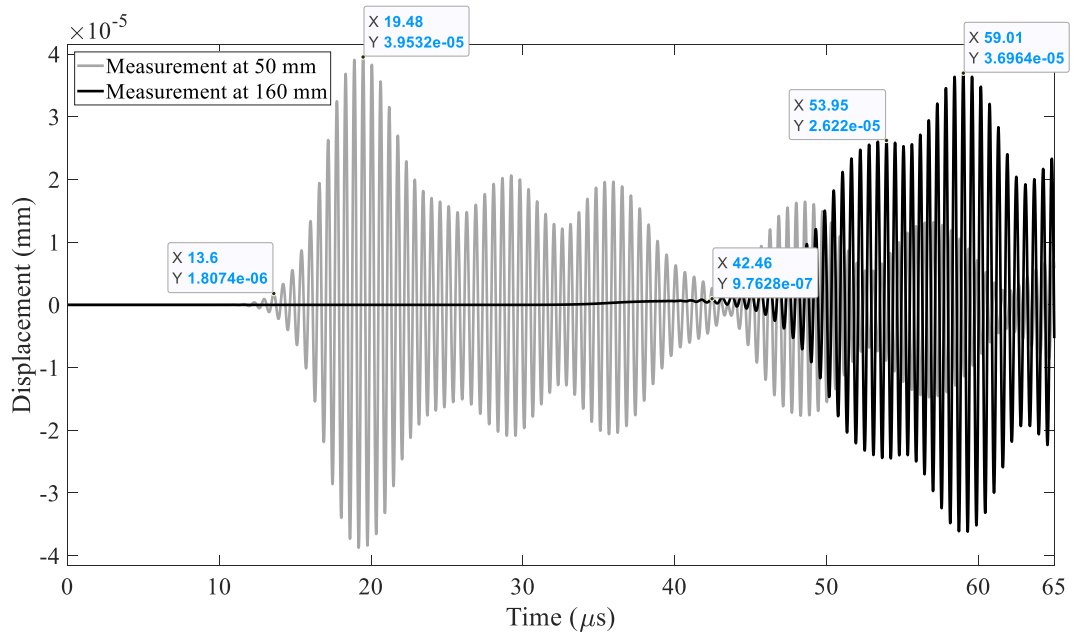


Figure 4.8. Time-domain signals from the single-material AA5052-H32 model, measured at sensor positions = 50 and 160 mm.

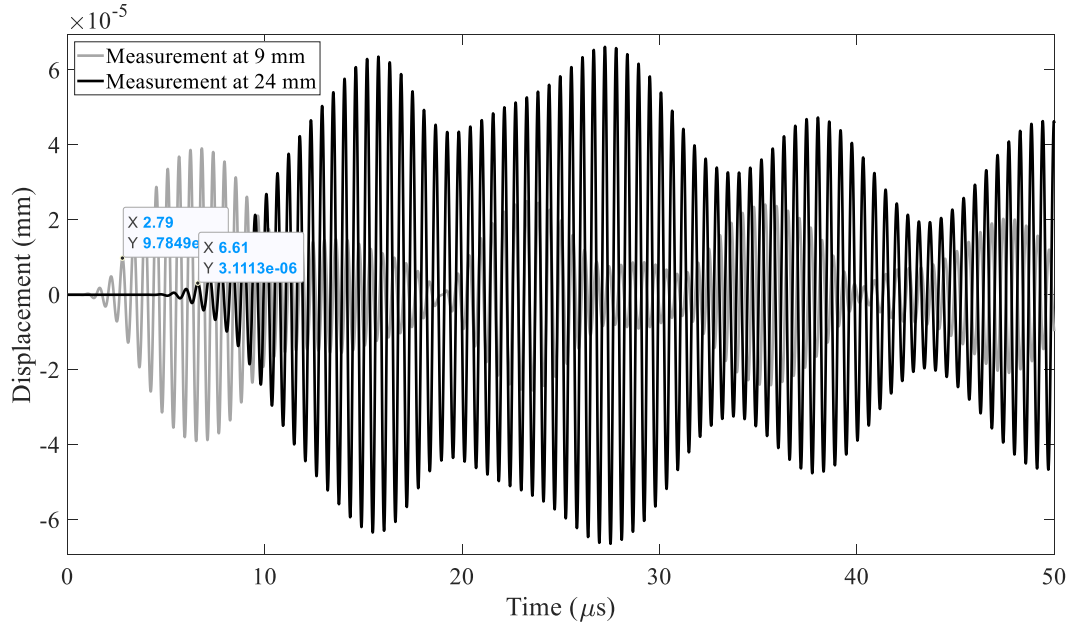


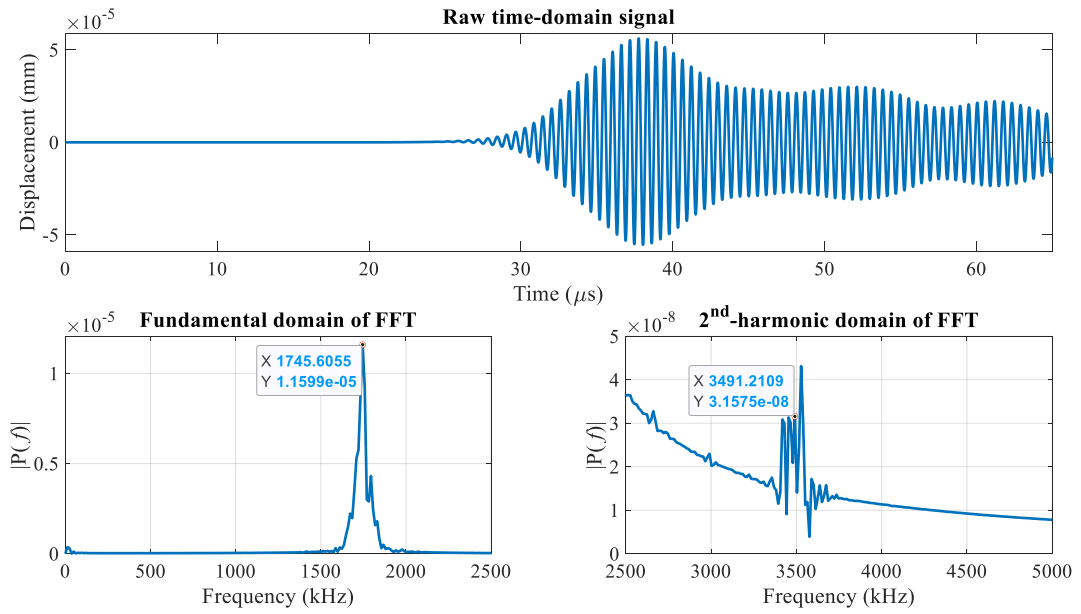
Figure 4.9. Time-domain signals from the dissimilar lap-weld model with no IMCs, measured at sensor positions = 9 and 24 mm.

4.4.2 Spectral and Nonlinearity Analysis

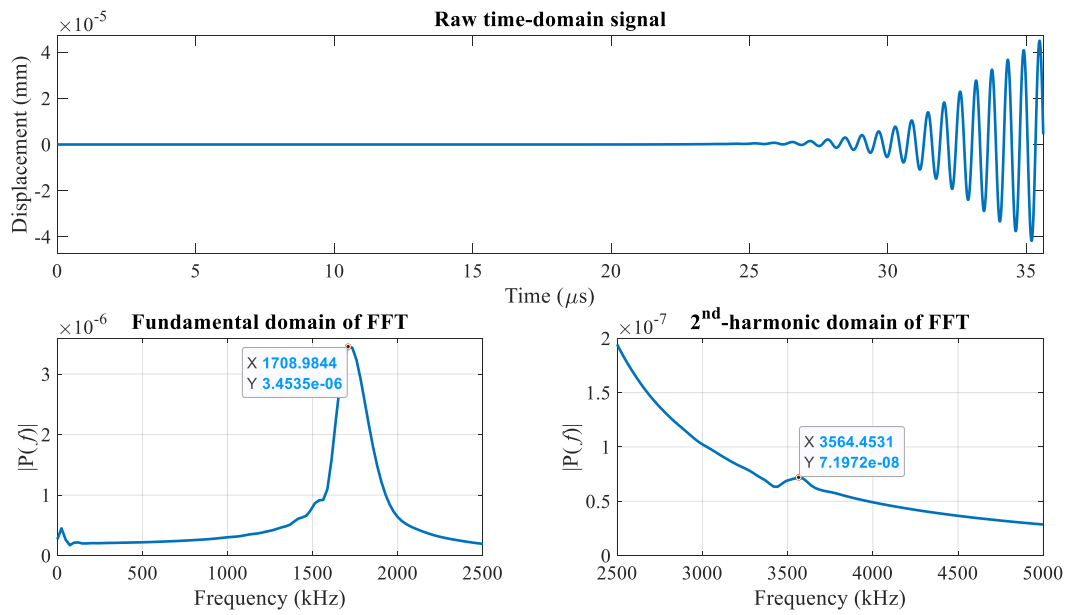
4.4.2.1 Fast Fourier Transform

The measured time-domain signals were transformed to the frequency domain using the fast Fourier transform (FFT) to investigate their frequency content and analyze the second-harmonic generation. Figure 4.10(a) shows a sample measurement, from the single-material model at sensor position = 100 mm, with its obtained frequency content. Due to the big difference between the amplitudes of the fundamental and second-harmonic frequencies, the FFT plot was divided into two plots showing the f_E and $2f_E$ domains separately. The fundamental frequency captured by FFT ($f_{n(FFT)}$; marked on its corresponding FFT plot) is in the vicinity of f_E (1,785 kHz) but not exactly equal to it. The second-harmonic component is evident in the wave, showing multiple peaks around $2f_{n(FFT)}$, where the nearest peak is marked. FFT was also performed for the first 20 and 30 cycles of the signal, and the results are shown in Figure 4.10(b) and (c), respectively. It can be observed that the SHG is building up with the length of the signal until having multiple noisy peaks when using the complete signal. This means that the SHG is being superposed from different double-frequency modes and not only from the internal resonance of the S_1 - S_2 mode-pair (available within the first 20 cycles); however, this may affect the linear shape of SHG accumulation. This is discussed further in Section 4.4.2.3. On the other hand, Figure 4.11 shows a sample measurement, from the dissimilar lap-weld model with not IMCs at sensor position = 54 mm, with its obtained frequency content. Similar observations can be made as those from the single-material model.

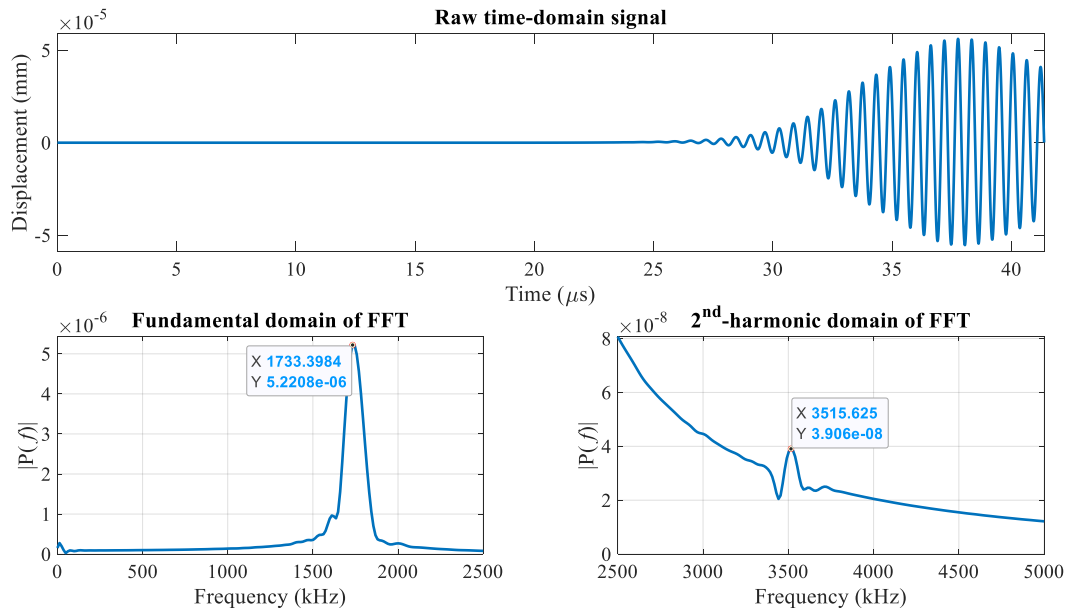
The amplitudes corresponding to $f_{n(FFT)}$ and $2f_{n(FFT)}$, obtained from the FFT analysis, will be later used to calculate the relative acoustic nonlinearity parameter.



(a) Complete signal

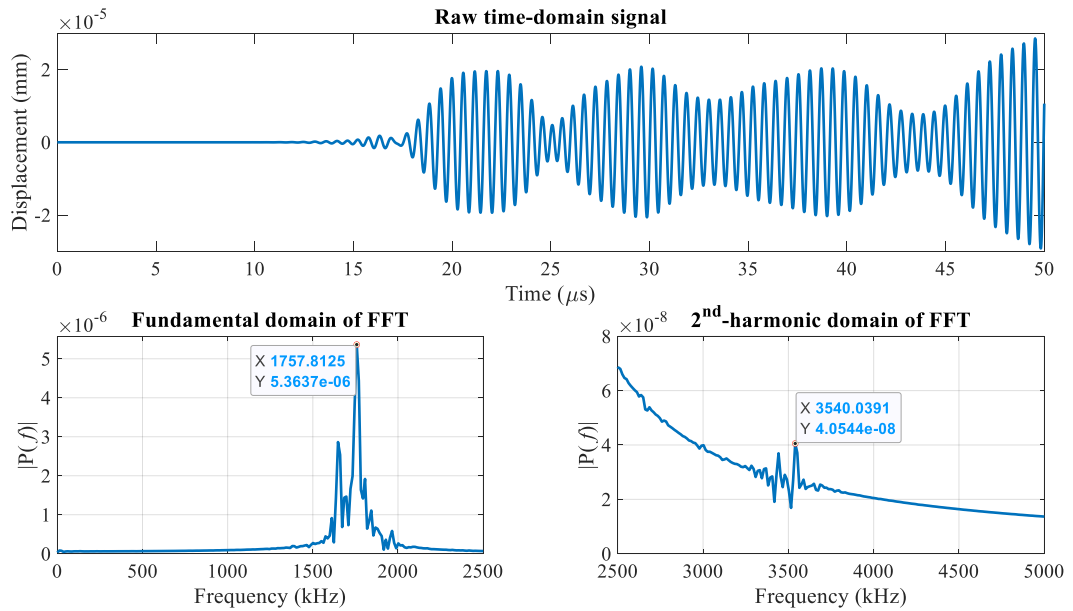


(b) First 20 cycles of the signal

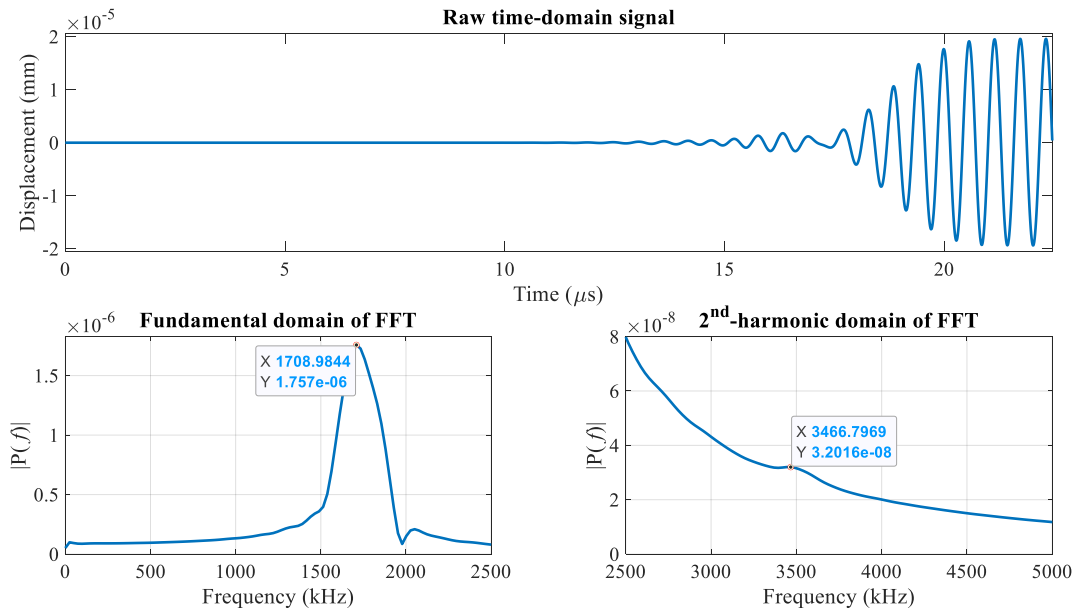


(c) First 30 cycles of the signal

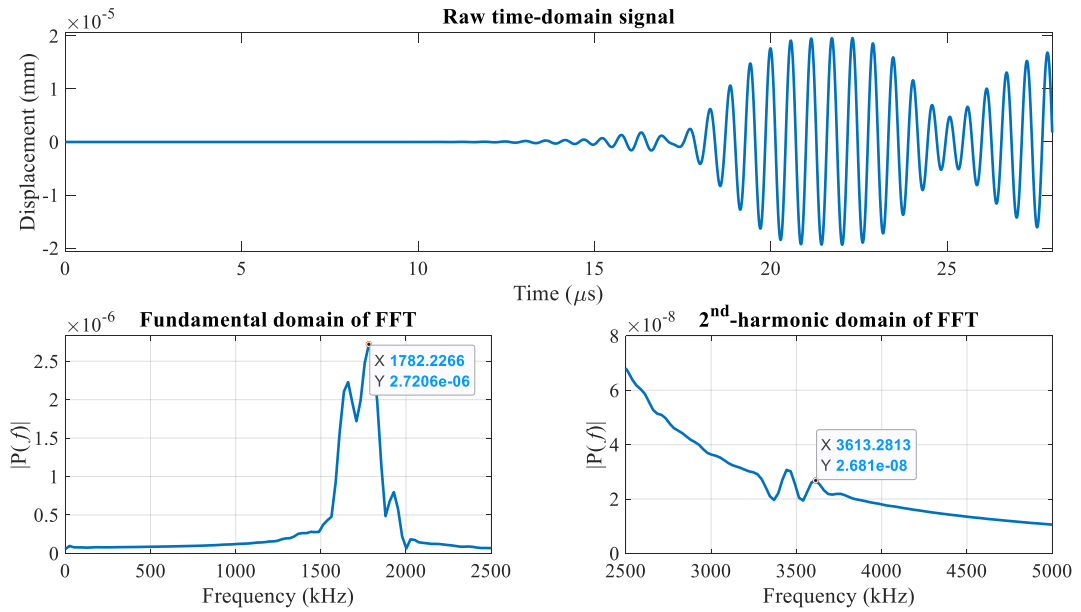
Figure 4.10. A sample raw signal and its FFT, measured at sensor position = 100 mm in the single-material AA5052-H32 model.



(a) Complete signal



(b) First 20 cycles of the signal



(c) First 30 cycles of the signal

Figure 4.11. A sample raw signal and its FFT, measured at sensor position = 54 mm in the dissimilar lap-weld model with no IMCs.

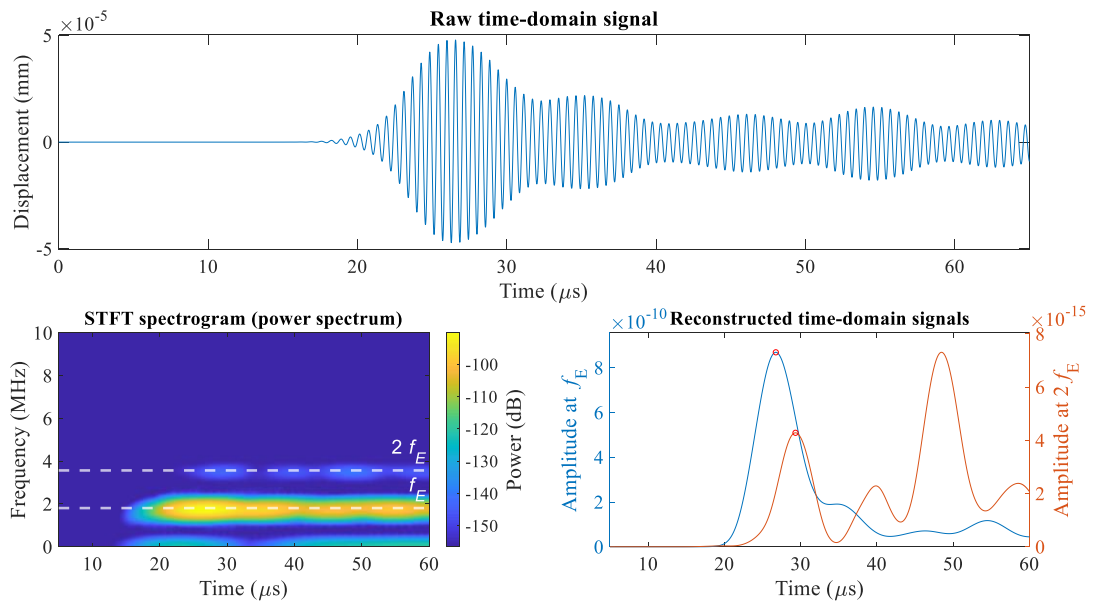
4.4.2.2 Short-Time Fourier Transform

In parallel to the FFT analysis, a more comprehensive examination of the signals' time-frequency content is presented in the next section. The spectrograms of the waves measured in both FE models were determined using the short-time Fourier transform (STFT) to analyze the signals in the time-frequency domain.

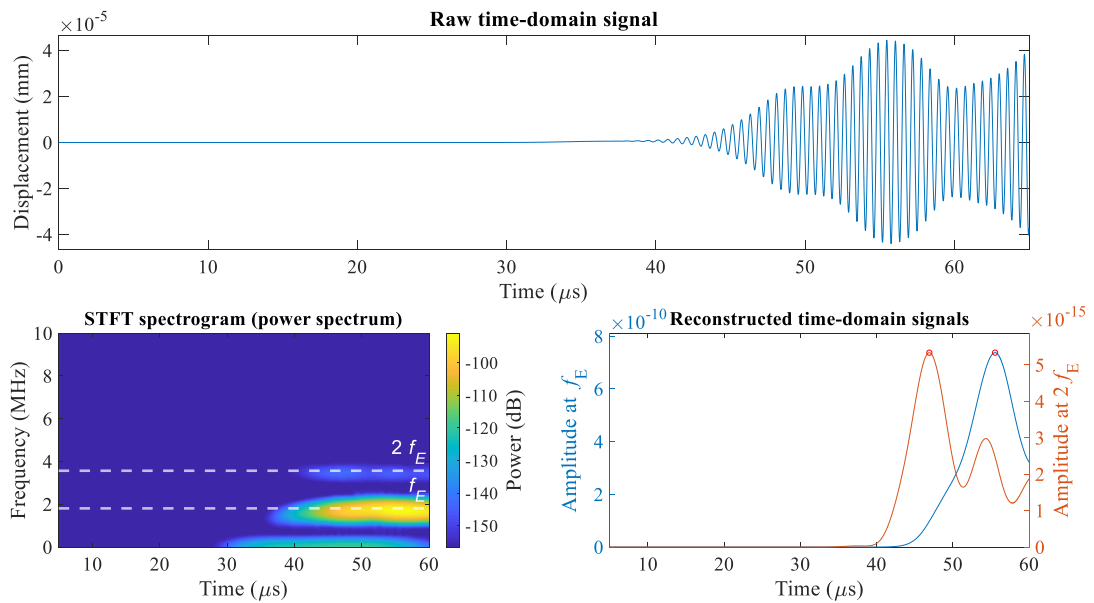
As an example, Figure 4.12(a) shows a sample raw time-domain signal, measured at sensor position = 70 mm from the single-material model, along with its STFT spectrograms. The second-harmonic components are obvious in the spectrogram, but with much weaker amplitudes than the fundamental components. The time-domain signals corresponding to both frequency components (f_E and $2f_E$) were extracted from the spectrogram (along the marked white dashed lines) and plotted on the right within the same figure. Based on the internal-resonance conditions, the generated second-harmonic mode should have the same velocity as that of the fundamental mode; however, a time shift is observed between the 1st peaks of both modes in Figure 4.12(a) (peaks marked using red circles). Figure 4.12(b) shows the STFT spectrogram and reconstructed time-domain signals for the wave measured from the same model at sensor position = 150 mm. Based on the 1st peak's arrival time of the fundamental and second-harmonic modes at 70 and 150 mm (Figure 4.12(a) and (b), respectively), the group velocities were calculated to be, respectively, 2,779.7 and 4,550.6 m/s. This confirms that the S_1 mode is dominated by other stronger fundamental-frequency modes in the propagating wave. However, the 1st peak of the second-harmonic wave is identified to be corresponding to the S_2 mode which is the only mode having such a high group velocity at $2f_E$ (Figure 4.1(b)).

Similarly, Figure 4.13(a) and (b) show the raw time-domain signals, measured respectively at 9 and 54 *mm* in the dissimilar lap-weld model, with their STFT spectrograms and reconstructed waves at f_E and $2f_E$. The group velocities of the fundamental and second-harmonic modes in the aluminum sub-plate (sensor position = 9 to 54 *mm*) were calculated, based on the 1st peaks in the reconstructed signals, to be 2,962.2 and 2,502 *m/s*, respectively (average values from all sensing positions). A faster but weak second-harmonic peak is observed at some sensing positions while it vanishes at others (an example is shown in Figure 4.13(c) at sensor position = 15 *mm*). Its group velocity was calculated to be around 3,114.2 *m/s*. The three velocity values show that the 1st appearing peaks, in the reconstructed signals, do not correspond to the S₁-S₂ mode-pair. This confirms that there exist other double-frequency modes that are contributing to the SHG in the propagating wave.

The amplitudes of the 1st peaks in the reconstructed time-domain signals, determined by STFT (exemplified by those marked on Figure 4.12 and Figure 4.13), were used to calculate β' according to equation (4.2).

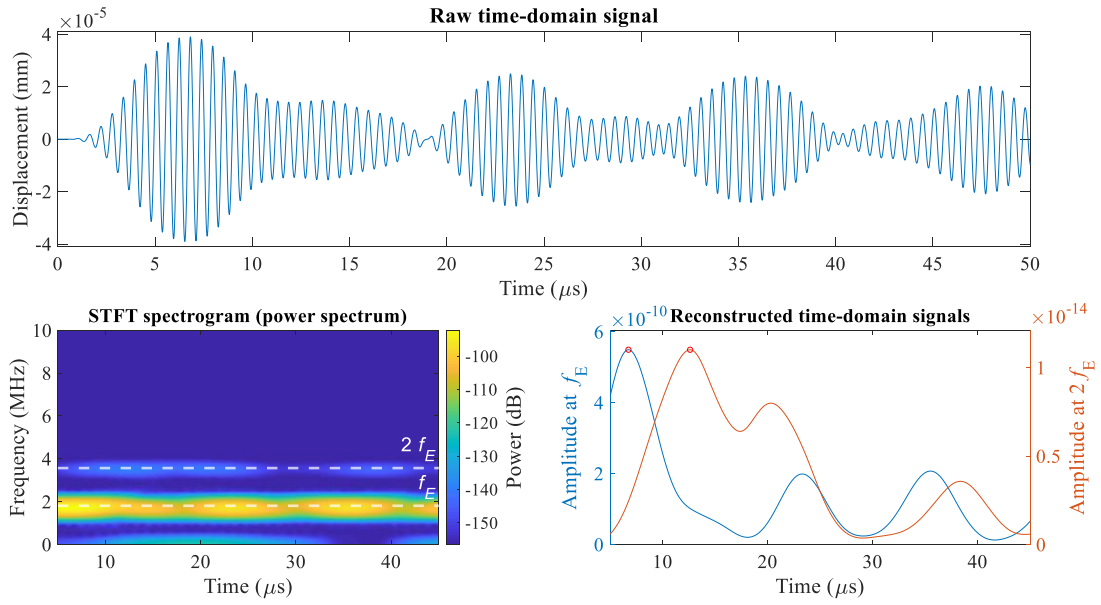


(a) Sensor position = 70 mm

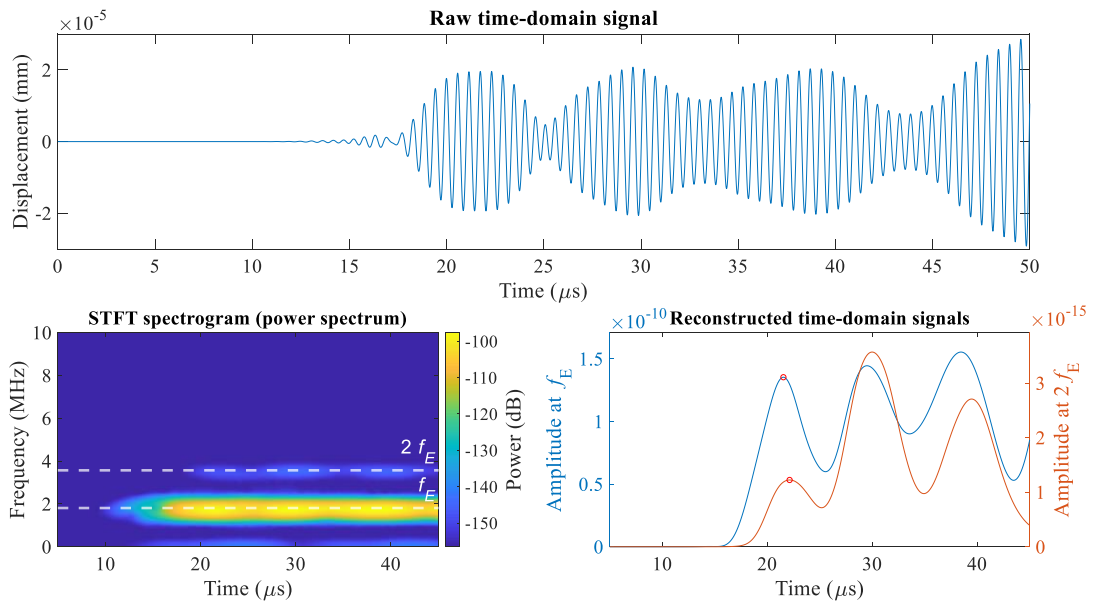


(a) Sensor position = 150 mm

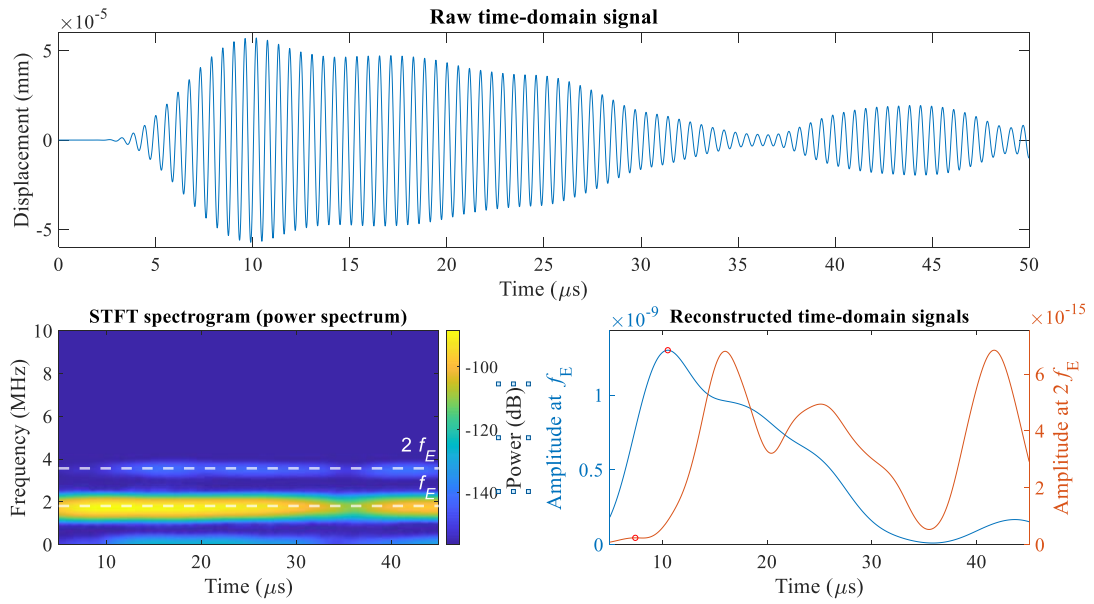
Figure 4.12. Sample raw signals, their STFT spectrograms, and their reconstructed time-domain signals at the fundamental (1,785 kHz) and second-harmonic (3,570 kHz) frequencies – measured at different sensor positions in the single-material AA5052-H32 model.



(a) Sensor position = 9 mm



(b) Sensor position = 54 mm



(c) Sensor position = 15 mm

Figure 4.13. Sample raw signals, their STFT spectrograms, and their reconstructed time-domain signals at the fundamental (1,785 kHz) and second-harmonic (3,570 kHz) frequencies – measured at different sensor positions in the dissimilar lap-weld model with no IMCs.

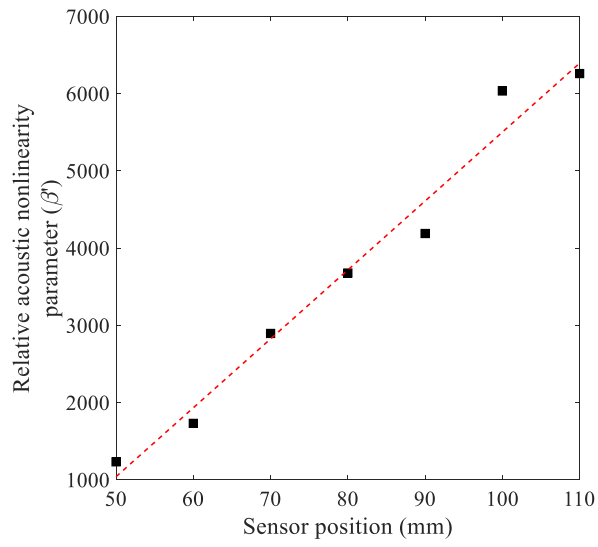
4.4.2.3 Cumulative Second-Harmonic Generation

RANP, or β' , was plotted versus the sensor positions to visualize the cumulative SHG over the propagation distance in the two models. Figure 4.14 and Figure 4.15 show the plots for the single-material and dissimilar lap-weld models, respectively, when using both FFT and STFT.

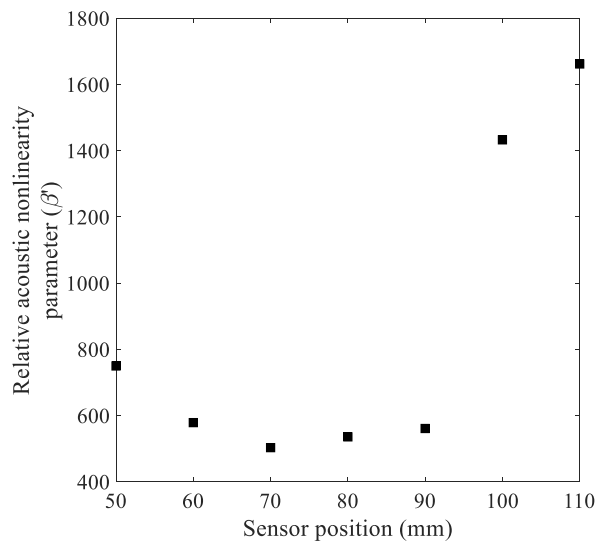
Considering the single-material model, linear growth of β' over the propagation distance was obtained only when using FFT over the first 20 cycles of the measured waves (Figure 4.14(a)). This verifies that the S_1 - S_2 mode-pair was successfully excited and is contained within the first 20 cycles of the signals. On the other hand, using more wave cycles to calculate FFT leads to the disturbance of this linear trend in the accumulation of the SHG (Figure 4.14(b) and (c)). This reconfirms

that other double-frequency modes also exist within the signals, which adds to the SHG of the S_1 - S_2 mode-pair and randomly changes its trend. β' , determined using STFT, was plotted versus the sensor positions at which the peaks of both the fundamental and second-harmonic modes were clearly identified (i.e., sensor position = 60 to 170 mm; Figure 4.14(d)). A trend comparable to that determined from FFT of the complete signal is observed. Even though the S_2 mode was successfully identified as the 1st peak in the reconstructed time-domain signal at $2f_E$, its amplitude was divided by that of the 1st appearing fundamental mode (according to equation (4.2)). However, this mode is not the S_1 mode, as was explained in section 4.4.2.2; thus, a linear accumulation of β' was not attained.

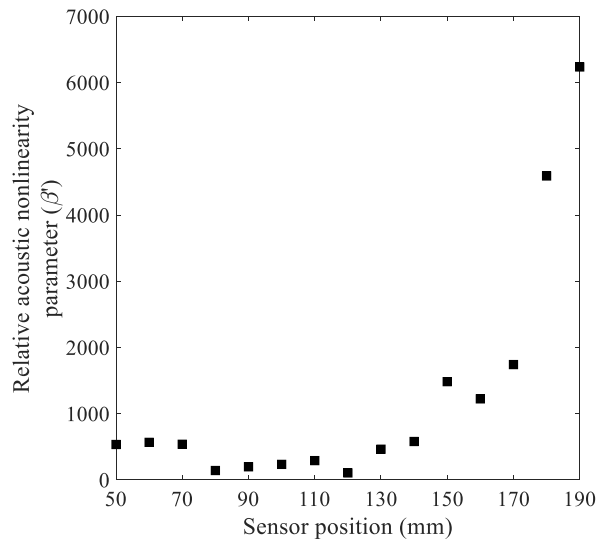
Regarding the dissimilar lap-weld model, three regions can be differentiated when using FFT over the first 20 wave cycles (Figure 4.15(a)). β' increases in a relatively linear manner from 9 to 24 mm (just before the beginning of the steel plate), after which the linear SHG accumulation is interrupted due to the wave's interaction with the steel plate. A sharp variation is then noticed beyond 54 mm after the end of the aluminum plate, where the waves were measured on the surface of the steel plate. However, this trend is not observed when using the complete signal for computing the FFT or STFT (Figure 4.15(b) and (c)), where random variations of β' versus the sensing position are attained. In addition to the reasons mentioned for the single-material plate, the absence of a clear trend for β' in the welded model can be attributed to its complex geometry and small size, which cause wave interactions with various features and interference with reflections from multiple boundaries.



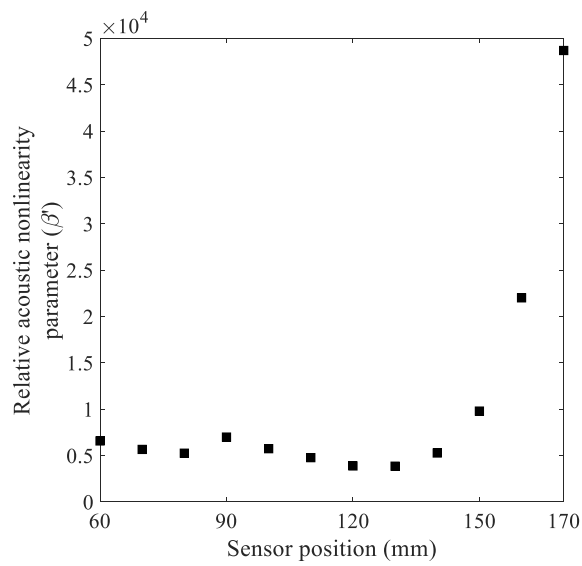
(a) Based on FFT using the first 20 cycles of the signal (50 to 110 mm)



(b) Based on FFT using the first 30 cycles of the signal (50 to 110 mm)

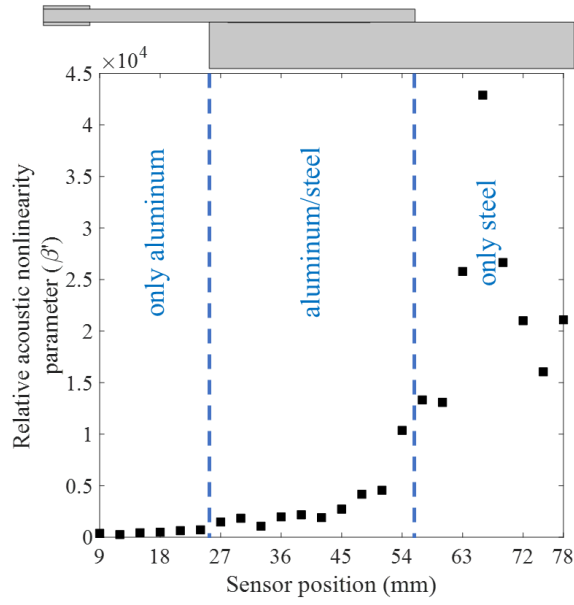


(c) Based on FFT using the complete signal (50 to 190 mm)

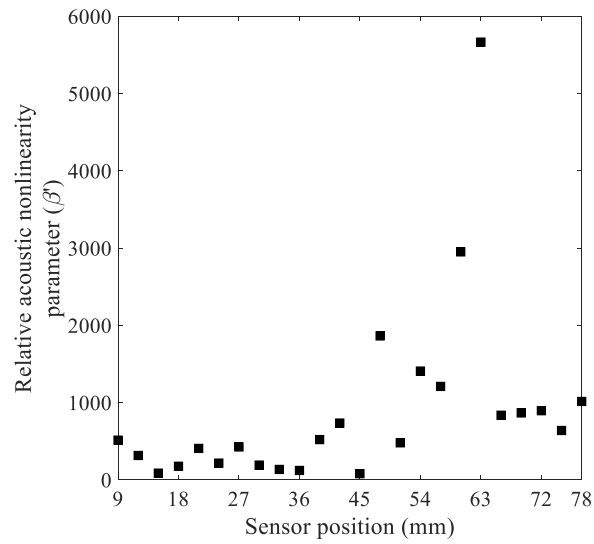


(d) Based on STFT using the complete signal (60 to 170 mm)

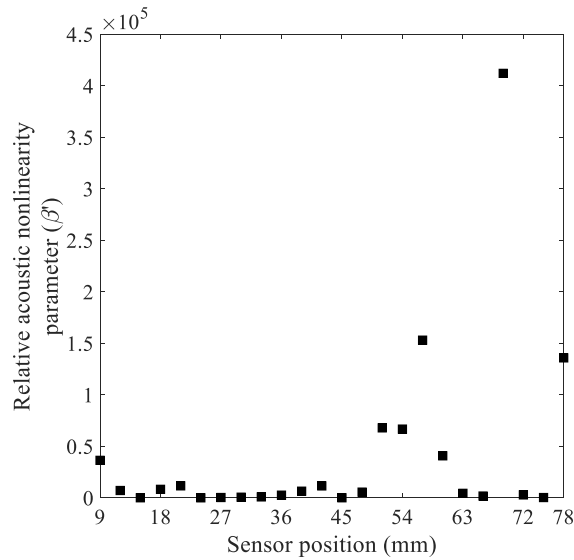
Figure 4.14. β' versus the sensor positions in the single-material model.



(a) Based on FFT using the first 20 cycles of the signal



(b) Based on FFT using the complete signal



(c) Based on STFT using the complete signal

Figure 4.15. β' versus the sensor positions in the dissimilar lap-weld model with no IMCs.

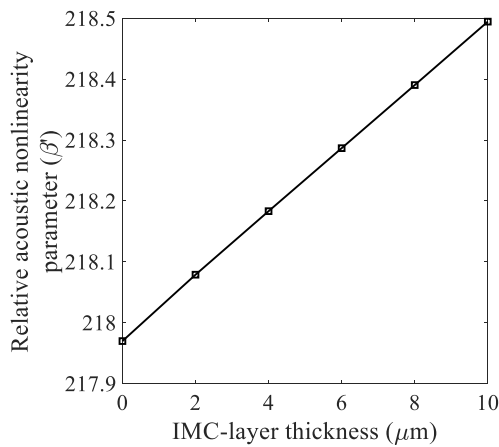
4.4.3 Assessment of Intermetallic Compounds

Measurements were taken at chosen sensing positions from the six dissimilar lap-weld models with variable IMC-layer thickness (ranging from zero to $10 \mu m$ with a step of $2 \mu m$). RANP, or β' , was then calculated using, both FFT (complete signal) and STFT, for all the models at each sensing position. The plots showing β' variation versus the IMC-layer thickness are presented in Figure 4.16, for four sensing positions, namely, $24 mm$ (just before the lap joint), $54 mm$ (last point on the aluminum sub-plate), $57 mm$ (first point on the steel sub-plate), and $75 mm$ (just before the end of the steel sub-plate).

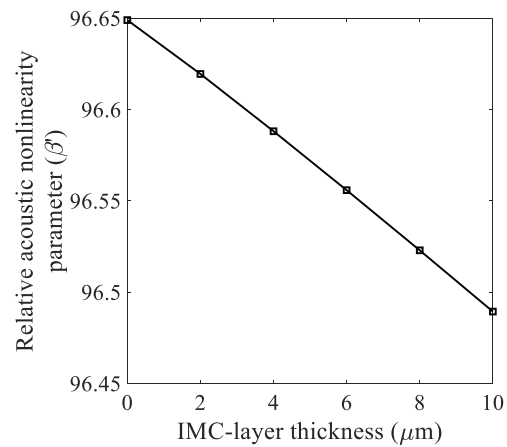
Regardless of the different possible sources of the second-harmonic generation in the measured waves (whether including the S_1 - S_2 mode-pair or not), the SHG could detect the very minimal variations in the thickness of the intermetallic compounds within the welded joint. A linear correlation is evident between β' and the thickness of

the IMC layer, irrespective of the sensing position or the used signal processing approach. Further, considering different peaks for β' calculation from the STFT second-harmonic component did not affect the linear variation of β' , as long as the same peak is being used for all the IMC-varied models. This linear trend is a very important trait that confirms the possibility of a quantitative assessment of such microstructural features, within dissimilar welded joints, using Lamb waves.

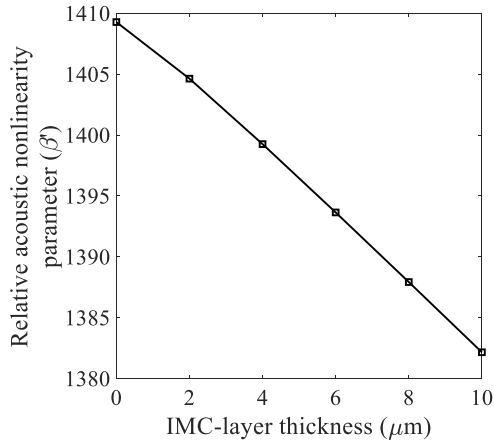
On the other hand, no clear understanding could be established of the reason behind the decreasing or increasing monotone of β' versus IMC-layer thickness. Such understanding is desirable when a quantitative assessment of IMCs is to be implemented.



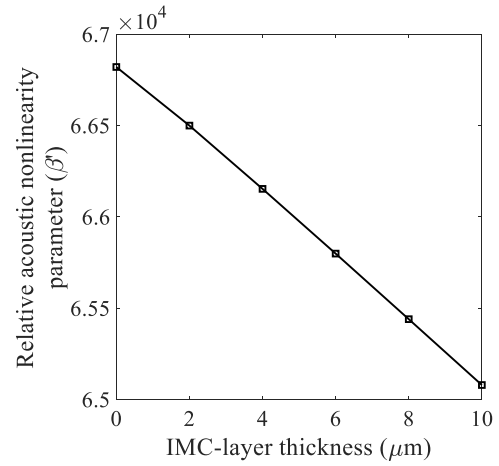
(a) Based on FFT (complete signal)
sensor position = 24 mm
(just before the joint)



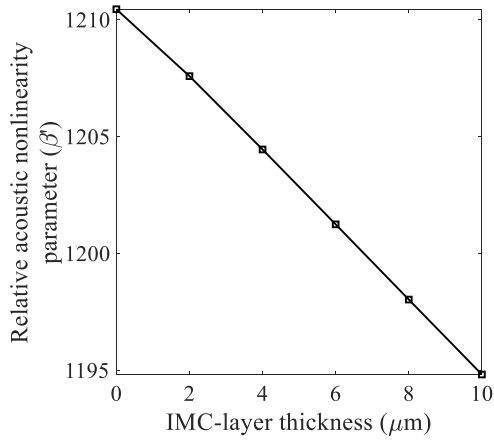
(b) Based on STFT
sensor position = 24 mm
(just before the joint)



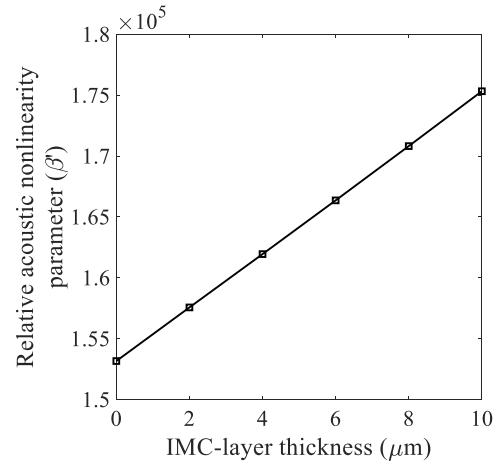
(c) Based on FFT (complete signal)
sensor position = 54 mm
(last point on the aluminum sub-plate)



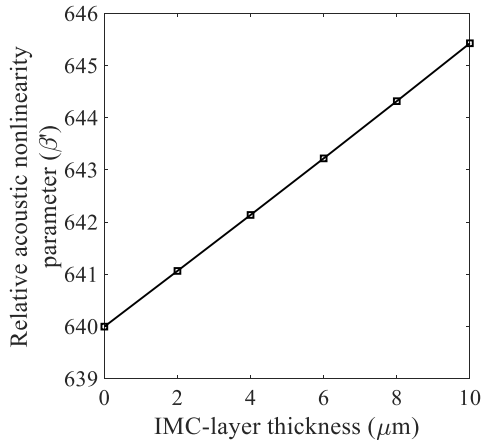
(d) Based on STFT
sensor position = 54 mm
(last point on the aluminum sub-plate)



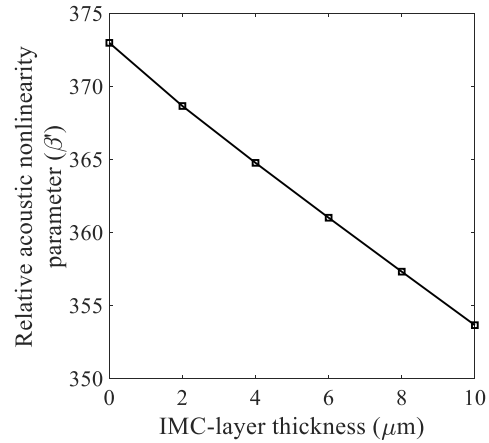
(e) Based on FFT (complete signal)
sensor position = 57 mm
(first point on the steel sub-plate)



(f) Based on STFT
sensor position = 57 mm
(first point on the steel sub-plate)



(g) Based on FFT (complete signal)
sensor position = 75 mm
(just before the end of the steel sub-plate)



(h) Based on STFT
sensor position = 75 mm
(just before the end of the steel sub-plate)

Figure 4.16. The linear trend between β' and the IMC-layer thickness – shown for four different sensor positions on the aluminum and steel sub-plates, based on both FFT (left) and STFT (right).

4.5 Summary

This chapter investigated the potential of Lamb-wave nonlinear features, namely the second-harmonic generation, for the quantitative assessment of micro-scaled intermetallic compounds within the interface region of a dissimilar welded joint. Two finite element models were built (a single-material AA5052-H32 plate and an intact AA5052-H32/ASTM 516-70 lap-weld), and Murnaghan's nonlinear-elastic properties were assigned to the materials. Symmetric Lamb waves were selectively excited within the model, based on the internal-resonance conditions of the S_1 - S_2 mode-pair. Waves were measured at different sensing positions and were extensively analyzed in the time, frequency, and time-frequency domains. The relative acoustic nonlinearity parameter (β') was calculated based on multiple signal processing approaches including the fast and short-time Fourier transforms. The cumulative second-harmonic generation was

then interpreted in regards to the propagating modes. Intermetallic compounds, of thickness varying between 2 and 10 μm , were modeled within the interface layer of the dissimilar lap-joint, based on already available specimens. The variation of β' , upon the introduction of the IMC layers (of various thickness and material properties) into the lap-weld interface, was then scrutinized. It was demonstrated that the nonlinearity parameter varies linearly with the increase of the IMC-layer thickness, where 2- μm variations were easily distinguished. This proves the capability of nonlinear Lamb-wave features, and specifically the second-harmonic generation, of the quantitative evaluation of micro-scaled damage or microstructural variations within dissimilar welded joints. Further, physical insights into the second-harmonic generation phenomenon in dissimilar lap-welded joints, as well as in single-material plates, were gained.

CHAPTER 5

CONCLUSIONS AND RECOMMENDATIONS

5.1 Introduction

Using different materials in specific locations of structures is an advantageous strategy to optimize designs, from both mechanical and economical perspectives, by fully exploiting the materials' native properties (e.g., mechanical, thermal, physical, and chemical). This imposes the joining of dissimilar materials and necessitates the establishment of powerful SHM techniques to monitor structures including dissimilar joints.

The presented work provided a better understanding of Lamb-wave interaction with intact dissimilar-material friction stir welding based on analytical, finite-element, and experimental investigations. In addition, an efficient methodology for detecting and accurately identifying buried weld defects, in size and position, was proposed. The sensitivity of nonlinear LW features to microstructural variations within the dissimilar-material interface was also confirmed, and their potential for the quantitative assessment of micro-scaled intermetallic compounds was demonstrated.

This chapter reiterates the concluding remarks of the conducted research and discusses the achieved contributions. Finally, recommendations are provided, based on the obtained results, and future work improvements are proposed.

5.2 Concluding Remarks

The introductory chapter of this dissertation justified the need for dissimilar-material joining and listed the advantages of using friction stir welding over other

conventional welding techniques. FSW was briefly introduced, and its potential defects were presented, which included possible buried or invisible defects that may compromise structural safety and risk people's lives. The importance of LW-based inspection techniques as compared to traditional nondestructive evaluation methods was discussed, and the significant advantage of using LWs for SHM of structures containing dissimilar FSW was highlighted. This explained the motivation of the work presented in this dissertation

LW-based assessment of FSW between dissimilar materials requires a prior understanding of the wave's interaction with the material interface. Upon propagation through a material discontinuity, a LW may encounter reflection, refraction, and/or mode conversion. Background knowledge about the fundamental guided-wave modes and their possible interactions with a dissimilar-material joint was presented, after which a numerical and experimental study was conducted to calculate their transmission and reflection coefficients. Different signal processing methods were developed to extract the existing wave modes (S_0 , A_0 , and converted S_0 - SH_0) from 3D measurements along their propagation directions, and to separate the reflection and transmission wavefields from other wave superpositions. Results showed that the symmetric S_0 mode is partially converted into the fundamental shear-horizontal (SH_0) GW mode when obliquely interacting with the material interface. While the reflection of the S_0 - SH_0 mode from the joint was found to be well-pronounced (reaching amplitudes above 20% of the incident S_0), its transmission to the other material is extremely weak. The transmissions of the S_0 and A_0 modes were found to be almost constant except for very steep incidence angles ($> 78^\circ$). The transmission amplitudes of both modes increase by around 20% when the wave propagates from AA6061-T6 to AZ31B, while they drop by

the same percentage in the inverse propagation direction. On the other hand, the reflection coefficients of the propagating modes varied with the angle of incidence, with values up to 35%. Despite the peaks appearing at the critical angle, the absolute values of the reflection coefficients of each of the modes have shown similar trends between the forward (AA6061-T6 to AZ31B) and the backward (AZ31B to AA6061-T6) propagation directions. The total reflection of the excited wave, from the material interface, was not observed in any condition. Further, an analytical solution, based on plane-wave approximation, was shown to be accurate for predicting the behavior of the in-plane modes (S_0 and S_0 - SH_0 modes) over a range of low frequency \times thickness values.

Furthermore, a new framework for damage identification using ultrasonic measurements was developed. Wormhole damage within a dissimilar-material joint could be fully identified, in size and position, using only one ultrasonic actuator and one/two sensors. Finite-element simulations were performed, on a model of the monitored structure, to simulate the measured LWs from a pre-allocated sensor network. The simulation data were then used to train several artificial neural networks. Each ANN served as a surrogate model that can predict a sensor measurement upon a given damage within the monitored structure. Finally, the surrogate models were employed to perform a statistical damage inference, using the ABC-SubSim algorithm, on simulated sensor measurements corrupted with noise. The inference outputs were the *posterior* PDFs of six damage parameters (length, width, thickness, and x -, y -, and z -positions), which also provided the level of uncertainty in the prediction. Different sensing-noise levels were tested, showing high robustness of the proposed method against noise; accurate damage inference persisted, and healthy welds could still be differentiated from the damaged ones. It was proved that the algorithm can detect

multiple damage scenarios that may produce the same sensor measurement. Thus, it was advised to fuse data from at least two sensors to guarantee reliable and accurate results. A successful data fusion method was applied leading to accuracies higher than 99%, for all the tested cases, when inferring the damage length and x -position. The other four damage parameters (width, thickness, and y and z -positions) were predicted with a maximum error of 0.9 mm . A combination of only two sensor measurements has led to an inference precision of above 95% for more than 83% of the performed predictions. This high resolution in predicting the 3D dimensions and coordinates of damage, using only one or two sensor measurements, is considered a major improvement in the field of condition assessment. Another important feature of the developed methodology is being computationally inexpensive, which makes it convenient for online/onboard monitoring applications.

In addition, the sensitivity of LW nonlinear features, namely the second-harmonic generation, to micro-scaled intermetallic compounds in dissimilar joints was examined. Nonlinear-elastic FE simulations were performed for an aluminum plate and a dissimilar aluminum/steel FSW lap joint. Symmetric LWs were selectively excited, obeying the S_1 - S_2 internal resonance conditions, and multiple measurements were taken. The measured signals were interpreted in the time, frequency, and time-frequency domains, and SHG was extensively analyzed. The relative acoustic nonlinearity parameter was determined using both the fast and short-time Fourier transforms, and its cumulative generation over the propagation distance was scrutinized. Intermetallic regions were then introduced into the interface of the dissimilar lap weld, and the interaction of LWs with different scenarios of their existence was investigated. The thickness of the introduced intermetallic layers varied between zero and 10 μm with a

step of $2 \mu m$, and the nonlinearity parameter was compared over various sensing locations within the model. RANP showed high sensitivity to this minimal variation and revealed a linear correlation with the IMC-layer thickness. This important outcome confirms the capability of such nonlinear LW features in detecting microstructural changes, and proves the potential of LWs for a quantitative evaluation of IMCs in dissimilar welds. Physical insights about the SHG in single-material plates and dissimilar lap-welded joints were also gained.

5.3 Recommendations for Future Work

A framework for experimental and 3D-FE transmission/reflection coefficient determination was proposed, and an accurate approximation methodology for the in-plane modes was validated. This is thought to be of importance to the NDE and SHM community, while further studies may consider implementing these calculations within sensor-network optimization problems for structures containing dissimilar-material joints. When designing sensor networks, actuator-sensor paths across a dissimilar joint should not be considered as straight lines; however, sensing-path deviations should be considered based on the excitation incidence angles (with respect to the joint) and the transmission angles (calculated based on the involved material properties).

While the amplitudes of reflected guided-wave modes showed high dependence on the incidence angle of excitation, constant transmissions of the S_0 and A_0 modes were obtained up to very steep angles. This is an important feature that should be investigated for combinations of materials other than the one used in this study (AA6061-T6/AZ31B). Plane-wave approximation can be easily employed for this purpose when the S_0 mode is to be used. PWA has also shown that the transmission of

the S_0 mode is constant over a wide frequency range. Therefore, it would be recommended to use transmission-based inspections across dissimilar joints or, otherwise, beware of the expected reflection coefficients according to the incidence angle of excitation. On the other hand, it would be very useful if a handy solution, similar to PWA, could be found for a fast prediction of the transmission and reflection coefficients of the A_0 mode across intact dissimilar joints.

The proposed Bayesian damage inference methodology is very promising based on the achieved results, but it opened the door for new questions and research ideas. As a successful and accurate diagnostics framework, it forms a first step towards lifetime predictions and prognostics to plan maintenance and optimize inspections, which would also necessitate the development of a damage evolution model. The advantage of performing the damage inference using an ABC algorithm is that it doesn't require heavy computations, and thus a small processor of lighter weight can be used. The ultimate goal, of the current study, is to have smart sensors that include microprocessors or to have small processors onboard that can infer damage in a real-time manner. For application on large structures, the structure can be subdivided into smaller regions which can be modeled more easily for simulations. The level of accuracy needed (based on the criticality of each subdivision and its susceptibility to damage) would then dictate how accurate should be the modeling and how much data is needed for the ANN training. Common transducers can be used between different regions to optimize the number of used transducers for the whole structure. Engineering common sense and previous experience of possible damage occurrences and/or the most vulnerable regions would help in optimizing the process, in terms of time and computational demands.

A further improvement may include adding nonlinear ultrasound features as additional outputs of the ANN to provide the capability of assessing extremely small damage and detect damage in its early stage. Future work may also include the consideration of variable environmental and operational conditions within the surrogate modeling process; different surrogate models may be used for different conditions, or such conditions would be added as additional inputs of the trained ANNs (e.g., temperature and pressure). Hence, the ANN would predict different LW signals, for the same damage case, based on the operational and environmental conditions. Towards the application on real structures, the enrichment of the training data by experimental/real data is also worth investigation. Calibration/normalization methods that would allow for the fusion or comparison of data from both sources (FE simulations and real measurements) should be explored. Further, several developments within the implementation of the damage-identification algorithm may be explored (e.g., automatic hyper-parameter tuning, distance metric improvement, and other means of data fusion between multiple sensors, metrics, and/or LW features).

On the other hand, more analysis can be put into the big amount of available simulation results that were used for training and testing the surrogate models. The sensitivity of different LW modes to various damage parameters and sizes may be examined. Such an understanding is very critical for choosing frequencies and both excitation and sensing technologies in SHM applications. Moreover, damage imaging algorithms may be developed by making use of the available simulation data.

Concerning the assessment of IMCs, an experimental investigation, using the already available specimens, may be the subject of future work. Proper LW excitation and sensing techniques should be explored to ensure minimal variations while testing on

different samples (e.g., using noncontact transducers). An appropriate normalization technique should be also employed to account for possible variations that may still arise. The effect of geometrical differences between the specimens on different nonlinear LW features should be studied, and a practical methodology for the application of such a sensitive method among multiple specimens should be investigated. Information from multiple nonlinear LW features may be fused to make more accurate and reliable assessments. Further, the reason behind the increase or decrease in RANP versus IMC-layer thickness, depending on the sensing location, needs to be understood. Tackling all these challenges would eventually lead to the establishment of a robust algorithm for intermetallic-region detection and assessment within FSW joints, towards a predictive model of the joint strength.

To sum up, the work presented in this dissertation provides better knowledge and potent techniques that can serve as tools for SHM systems of structures containing joints between dissimilar materials. The application of such research outcomes in complete and comprehensive strategies, on real SHM systems, remains the ultimate goal. The goal aiming to improve the safety margins and extend the life span of our assets, and most sacredly, to secure people's lives.

APPENDIX

LIST OF PUBLICATIONS

Peer-Reviewed Journal Papers

1. **M.A. Fakh**, M. Chiachío, J. Chiachío, and S. Mustapha, “Damage Identification in Welded Structures using Bayesian Inference and Lamb-Wave Surrogate Models based on Artificial Neural Networks”, *Journal of Mechanical Systems and Signal Processing*. (Accepted with minor reviews)
2. **M.A. Fakh**, S. Mustapha, M.S. Harb, and C.T. Ng, “Understanding the Interaction of the Fundamental Lamb-Wave Modes with Material Discontinuity – Finite Element Analysis and Experimental Validation”, *Structural Health Monitoring*, 2021.
3. **M.A. Fakh**, S. Mustapha, and A. Abdul-Aziz, “Robust localization and classification of barely visible indentations in composite structures by fusion of ultrasonic damage indices”, *Journal of Nondestructive Evaluation, Diagnostics and Prognostics of Engineering Systems*, 2(3), 2019.
4. Z. Ismail, S. Mustapha, **M.A. Fakh**, and H. Tarhini, “Sensor placement optimization on complex and large metallic and composite structures”, *Structural Health Monitoring*, 19(1), pp. 262-280, 2020.
5. H. Tarhini, R. El Itani, **M.A. Fakh**, and S. Mustapha, “Optimization of piezoelectric wafer placement for structural health monitoring applications”, *Journal of Intelligent Material Systems and Structures*, 29(1), pp. 3758-3773, 2018.
6. J. Tarraf, S. Mustapha, **M.A. Fakh**, M.S. Harb, H. Wang, G. Ayoub, and R. Hamade, “Application of ultrasonic waves towards the inspection of similar and dissimilar friction stir welded joints”, *Journal of Materials Processing Technology*, 255, pp. 570-583, 2018.
7. **M.A. Fakh**, S. Mustapha, J. Tarraf, G. Ayoub, and R. Hamade, “Detection and assessment of flaws in friction stir welded joints using ultrasonic guided waves: experimental and finite element analysis”, *Journal of Mechanical Systems and Signal Processing*, 101, pp. 516-534, 2018.
8. **M.A. Fakh**, S. Mustapha, M. Makki Alamdari, and L. Ye, “Symbolic dynamics time series analysis for assessment of barely visible indentation damage in composite sandwich structures based on guided waves”, *Journal of Composite Materials*, 51(29), pp. 4129-4143, 2017.

International-Conference Papers

9. **M.A. Fakh**, M. Chiachío Ruano, J. Chiachío Ruano, and S. Mustapha, “Bayesian damage inference using a Lamb-wave artificial-neural-network model”, in *The 27th International Conference on Composite/Nano Engineering ICCE*, Granada, Spain, 2019.
10. **M.A. Fakh**, S. Mustapha, and M.S. Harb, “The interaction of the fundamental symmetric and antisymmetric Lamb wave modes with material discontinuity – a 3D finite element analysis”, in *The 7th Asia-Pacific Workshop for Structural Health Monitoring APWSHM*, Hong Kong SAR, China, 2018.
11. Z. Ismail, **M.A. Fakh**, S. Mustapha, and H. Tarhini, “The application of Genetic Algorithm for sensor placement of PZT wafers towards the application in structural health monitoring”, in *The 12th European Conference on Non-Destructive Testing ECNDT*, Gothenburg, Sweden, 2018.
12. R. Hamade, **M.A. Fakh**, M.S. Harb, and S. Mustapha, “Quality assessment of friction stir welded joints – using the fundamental anti-symmetric Lamb wave mode”, in *The 10th International Conference on Processing & Manufacturing of Advanced Materials THERMEC*, Paris, France. *Materials Science Forum*, 941, pp. 2429-2434. Trans Tech Publications Ltd., 2018.
13. **M.A. Fakh**, J. Tarraf, S. Mustapha, M.S. Harb, H. Wang, G. Ayoub, and R. Hamade, “Characterization of Lamb waves propagation behavior in friction stir welded joints of dissimilar materials”, in *The 11th International Workshop on Structural Health Monitoring IWSHM*, Stanford, California, USA, 2017.
14. **M.A. Fakh**, S. Mustapha, J. Tarraf, G. Ayoub, and R. Hamade, “Detection and assessment of flaws in friction stir welded metallic plates”, in *Sensors and Smart Structures Technologies for Civil, Mechanical, and Aerospace Systems*, 10168, pp. 101682L. *International Society for Optics and Photonics*, 2017.

Local-Conference Papers

15. **M.A. Fakh**, “Detection and assessment of flaws in friction stir welded AZ31B magnesium plates using Lamb waves”, in *FEASAC 16th of the American University of Beirut (AUB)*, 2017.
16. **M.A. Fakh**, S. Mustapha, M. Makki Alamdari, and L. Ye, “The application of symbolic dynamics time series analysis for assessing barely visible indentation damage in composite sandwich structures using ultrasonic guided waves”, in *The 22nd Conference of the Lebanese Association for the Advancement of Science (LAAS)*, USEK, Lebanon, 2016.

BIBLIOGRAPHY

1. Li, Y., et al., *Friction self-piercing riveting of aluminum alloy AA6061-T6 to magnesium alloy AZ31B*. Journal of Manufacturing Science and Engineering, 2013. **135**(6): p. 061007.
2. Borrisutthekul, R., Y. Miyashita, and Y. Mutoh, *Dissimilar material laser welding between magnesium alloy AZ31B and aluminum alloy A5052-O*. Science and Technology of Advanced Materials, 2005. **6**(2): p. 199.
3. Liu, L., X. Liu, and S. Liu, *Microstructure of laser-TIG hybrid welds of dissimilar Mg alloy and Al alloy with Ce as interlayer*. Scripta materialia, 2006. **55**(4): p. 383-386.
4. Haghshenas, M. and A. Gerlich, *Joining of automotive sheet materials by friction-based welding methods: a review*. Engineering science and technology, an international journal, 2018. **21**(1): p. 130-148.
5. Liu, L., H. Wang, and G. Song, *Microstructure characteristics and mechanical properties of laser weld bonding of magnesium alloy to aluminum alloy*. Journal of materials science, 2007. **42**(2): p. 565-572.
6. Burford, D., C. Widener, and B. Tweedy. *Advances in friction stir welding for aerospace applications*. in *6th AIAA Aviation Technology, Integration and Operations Conference (ATIO)*. 2006.
7. Babu, A.S. and C. Devanathan, *An Overview of Friction Stir Welding*. Int. J. Res. Mech. Eng. Technol, 2013. **3**(2): p. 259-265.
8. Thomas, W.M., et al., *Friction stir butt welding*. 1991: GB.
9. Thomas, W.M., et al., *Improvements relating to friction welding*. 1991: US.
10. Muthukrishnan, M. and K. Marimuthu. *Some studies on mechanical properties of friction stir butt welded Al-6082-T6 plates*. in *Frontiers in Automobile and Mechanical Engineering (FAME)*, 2010. 2010. IEEE.
11. Zhao, Y.-h., et al., *The influence of pin geometry on bonding and mechanical properties in friction stir weld 2014 Al alloy*. Materials Letters, 2005. **59**(23): p. 2948-2952.
12. Fakih, M.A., et al., *Detection and assessment of flaws in friction stir welded joints using ultrasonic guided waves: experimental and finite element analysis*. Mechanical Systems and Signal Processing, 2018. **101**: p. 516-534.
13. Fakih, M.A.H., *Ultrasonic waves time series analysis for damage detection and assessment in composite and metallic structures*. Master's Thesis. 2016.
14. Gite, R.A., P.K. Loharkar, and R. Shimpi, *Friction stir welding parameters and application: A review*. Materials Today: Proceedings, 2019. **19**: p. 361-365.
15. Kumbhar, N. and K. Bhanumurthy, *Friction stir welding of Al 6061 alloy*. Asian J. Exp. Sci, 2008. **22**(2): p. 63-74.
16. Kumar, H.A. and V.V. Ramana, *An Overview of Friction Stir Welding (FSW): A New Perspective*. Research Inventy: International Journal of Engineering And Science, 2014. **4**(6): p. 01-04.
17. Mishra, R.S. and Z. Ma, *Friction stir welding and processing*. Materials Science and Engineering: R: Reports, 2005. **50**(1): p. 1-78.
18. Arbegast, W.J., *Friction Stir Joining: Characteristic Defects*. South Dakota School of Mines and Technology, 2003.

19. Lee, W.-B. and S.-B. Jung, *Void free friction stir weld zone of the dissimilar 6061 aluminum and copper joint by shifting the tool insertion location*. Materials Research Innovations, 2004. **8**(2): p. 93-96.
20. Ostachowicz, W., et al., *Guided Waves in Structures for SHM : The Time - domain Spectral Element Method*. Vol. 1. 2011, Hoboken: Wiley.
21. Scott, I. and C. Scala, *A review of non-destructive testing of composite materials*. NDT international, 1982. **15**(2): p. 75-86.
22. Gholizadeh, S., *A review of non-destructive testing methods of composite materials*. Procedia Structural Integrity, 2016. **1**: p. 50-57.
23. Harb, M. and F. Yuan, *Barely visible impact damage imaging using non-contact air-coupled transducer/laser Doppler vibrometer system*. Structural Health Monitoring, 2017. **16**(6): p. 663-673.
24. Harb, M.S. and F.-G. Yuan, *Air-Coupled Nondestructive Evaluation Dissected*. Journal of Nondestructive Evaluation, 2018. **37**(3): p. 50.
25. Ismail, Z., et al., *Sensor placement optimization on complex and large metallic and composite structures*. Structural Health Monitoring, 2020. **19**(1): p. 262-280.
26. Su, Z. and L. Ye, *Identification of damage using Lamb waves: from fundamentals to applications*. Vol. 48. 2009: Springer Science & Business Media.
27. Mustapha, S. and L. Ye, *Leaky and non-leaky behaviours of guided waves in CF/EP sandwich structures*. Wave Motion, 2014. **51**(6): p. 905-918.
28. Mustapha, S. and L. Ye, *Propagation behaviour of guided waves in tapered sandwich structures and debonding identification using time reversal*. Wave Motion, 2015. **57**: p. 154-170.
29. Yeung, C. and C.T. Ng, *Time-domain spectral finite element method for analysis of torsional guided waves scattering and mode conversion by cracks in pipes*. Mechanical Systems and Signal Processing, 2019. **128**: p. 305-317.
30. Rose, J.L., *Ultrasonic guided waves in solid media*. 2014: Cambridge university press.
31. Su, Z., L. Ye, and Y. Lu, *Guided Lamb waves for identification of damage in composite structures: A review*. Journal of sound and vibration, 2006. **295**(3-5): p. 753-780.
32. Fakhri, M.A., S. Mustapha, and A. Abdul-Aziz, *Robust Localization and Classification of Barely Visible Indentations in Composite Structures by Fusion of Ultrasonic Damage Indices*. Journal of Nondestructive Evaluation, Diagnostics and Prognostics of Engineering Systems, 2019. **2**(3).
33. Hamade, R., et al. *Quality Assessment of Friction Stir Welded Joints—Using the Fundamental Anti-Symmetric Lamb Wave Mode*. in *Materials Science Forum*. 2018. Trans Tech Publ.
34. Staszewski, W., B. Lee, and R. Traynor, *Fatigue crack detection in metallic structures with Lamb waves and 3D laser vibrometry*. Measurement Science and Technology, 2007. **18**(3): p. 727.
35. Yang, Y., C.-T. Ng, and A. Kotousov, *Influence of crack opening and incident wave angle on second harmonic generation of Lamb waves*. Smart Materials and Structures, 2018. **27**(5): p. 055013.
36. Pan, N., et al., *A quantitative identification approach for delamination in laminated composite beams using digital damage fingerprints (DDFs)*. Composite structures, 2006. **75**(1-4): p. 559-570.

37. Pudipeddi, G.T., C.-T. Ng, and A. Kotousov, *Mode Conversion and Scattering of Lamb Waves at Delaminations in Composite Laminates*. Journal of Aerospace Engineering, 2019. **32**(5): p. 04019067.
38. Malinowski, P., et al. *Damage detection method for composites based on laser vibrometer*. in *5th International Symposium on NDT in Aerospace, Singapore*. 2013.
39. Mustapha, S., et al., *Evaluation of barely visible indentation damage (BVID) in CF/EP sandwich composites using guided wave signals*. Mechanical Systems and Signal Processing, 2016. **76**: p. 497-517.
40. Mustapha, S., et al., *Debonding detection in composite sandwich structures based on guided waves*. AIAA journal, 2012. **50**(8): p. 1697-1706.
41. Yang, Y., C.-T. Ng, and A. Kotousov, *Second harmonic generation of guided wave at crack-induced debonding in FRP-strengthened metallic plates*. International Journal of Structural Stability and Dynamics, 2019. **19**(01): p. 1940006.
42. Ostachowicz, W., et al., *Damage localisation in plate-like structures based on PZT sensors*. Mechanical Systems and Signal Processing, 2009. **23**(6): p. 1805-1829.
43. Aryan, P., et al., *A baseline-free and non-contact method for detection and imaging of structural damage using 3D laser vibrometry*. Structural Control and Health Monitoring, 2017. **24**(4): p. e1894.
44. Harb, M.S. and F.-G. Yuan, *Damage imaging using non-contact air-coupled transducer/laser Doppler vibrometer system*. Structural Health Monitoring, 2016. **15**(2): p. 193-203.
45. Rathod, V. and D.R. Mahapatra, *Ultrasonic Lamb wave based monitoring of corrosion type of damage in plate using a circular array of piezoelectric transducers*. NDT & E International, 2011. **44**(7): p. 628-636.
46. Santos, J. and M. Santos, *Lamb waves technique applied to the characterization of defects in friction stir welding of aluminum plates: comparison with X-ray and ultrasonic C-scan*. Journal of Testing and Evaluation, 2010. **38**(5): p. 1-6.
47. Delrue, S., et al., *Applying a nonlinear, pitch-catch, ultrasonic technique for the detection of kissing bonds in friction stir welds*. Ultrasonics, 2016. **68**: p. 71-79.
48. Tabatabaeipour, M., et al., *Non-destructive ultrasonic examination of root defects in friction stir welded butt-joints*. NDT & E International, 2016. **80**: p. 23-34.
49. Fakhri, M.A., et al. *Detection and assessment of flaws in friction stir welded metallic plates*. in *Sensors and Smart Structures Technologies for Civil, Mechanical, and Aerospace Systems 2017*. 2017. International Society for Optics and Photonics.
50. Fakhri, M.A., et al. *Characterization of Lamb Waves Propagation Behavior in Friction Stir Welded Joints of Dissimilar Materials*. in *Structural Health Monitoring 2017*. 2017.
51. Tarraf, J., et al., *Application of ultrasonic waves towards the inspection of similar and dissimilar friction stir welded joints*. Journal of Materials Processing Technology, 2018. **255**: p. 570-583.
52. Wilcox, P.D., et al., *Scattering of plane guided waves obliquely incident on a straight feature with uniform cross-section*. The Journal of the Acoustical Society of America, 2010. **128**(5): p. 2715-2725.

53. Sondhauss, C., *XIV. On the refraction of sound*. The London, Edinburgh, and Dublin Philosophical Magazine and Journal of Science, 1853. **5**(30): p. 73-77.
54. Knott, C.G., *III. Reflexion and refraction of elastic waves, with seismological applications*. The London, Edinburgh, and Dublin Philosophical Magazine and Journal of Science, 1899. **48**(290): p. 64-97.
55. Zoeppritz, K., *On the reflection and propagation of seismic waves*. Gottinger Nachrichten, 1919. **1**(5): p. 66-84.
56. Blut, H., *Contribution to the theory of reflection and refraction of elastic waves from layers of discontinuity*. Zeitschrift für Geophysik, 1932. **8**(3): p. 130-144.
57. McCamy, K., R.P. Meyer, and T.J. Smith, *Generally applicable solutions of Zoeppritz'amplitude equations*. Bulletin of the Seismological Society of America, 1962. **52**(4): p. 923-955.
58. Ergin, K., *Energy ratio of the seismic waves reflected and refracted at a rock-water boundary*. Bulletin of the Seismological Society of America, 1952. **42**(4): p. 349-372.
59. Mayer, W., *Energy partition of ultrasonic waves at flat boundaries*. Ultrasonics, 1965. **3**(2): p. 62-68.
60. Cheeke, J.D.N., *Fundamentals and applications of ultrasonic waves*. 2016: CRC press.
61. Gregory, R.D. and I. Gladwell, *The reflection of a symmetric Rayleigh-Lamb wave at the fixed or free edge of a plate*. Journal of Elasticity, 1983. **13**(2): p. 185-206.
62. Scandrett, C. and N. Vasudevan, *The propagation of time harmonic Rayleigh–Lamb waves in a bimaterial plate*. The Journal of the Acoustical Society of America, 1991. **89**(4): p. 1606-1614.
63. Gunawan, A. and S. Hirose, *Reflection of obliquely incident guided waves by an edge of a plate*. Materials transactions, 2007. **48**(6): p. 1236-1243.
64. Santhanam, S. and R. Demirli, *Reflection of Lamb waves obliquely incident on the free edge of a plate*. Ultrasonics, 2013. **53**(1): p. 271-282.
65. Shen, Y. and V. Giurgiutiu. *WFR-2D: an analytical model for PWAS-generated 2D ultrasonic guided wave propagation*. in *Health Monitoring of Structural and Biological Systems 2014*. 2014. International Society for Optics and Photonics.
66. Poddar, B. and V. Giurgiutiu, *Scattering of Lamb waves from a discontinuity: An improved analytical approach*. Wave Motion, 2016. **65**: p. 79-91.
67. Haider, M.F., et al., *Analytical and experimental investigation of the interaction of Lamb waves in a stiffened aluminum plate with a horizontal crack at the root of the stiffener*. Journal of Sound and Vibration, 2018. **431**: p. 212-225.
68. Lamb, H., *On waves in an elastic plate*. Proceedings of the Royal Society of London. Series A, Containing papers of a mathematical and physical character, 1917. **93**(648): p. 114-128.
69. Giurgiutiu, V., *Structural health monitoring: with piezoelectric wafer active sensors*. 2007: Elsevier.
70. Laboratory for Active Materials and Smart Structures (LAMSS), *Wavescope 2.5: Dispersion curves, group velocities, and tuning for metallic structures*. 2010, University of South Carolina. MATLAB-based software. Retrieved from <http://www.me.sc.edu/Research/lamss/html/software.html>
71. Su, Z., et al., *Assessment of delamination in composite beams using shear horizontal (SH) wave mode*. Composites science and technology, 2007. **67**(2): p. 244-251.

72. Callister, W.D. and D.G. Rethwisch, *Materials science and engineering*. Vol. 5. 2011: John Wiley & Sons NY.
73. Krautkramer, J. and H. Krautkramer, *Ultrasonic testing of materials*. Vol. 4th edition. 1990, New York: Springer-Verlag Berlin Heidelberg.
74. Cook, R. and J. Avrashi, *Error estimation and adaptive meshing for vibration problems*. Computers & structures, 1992. **44**(3): p. 619-626.
75. Moser, F., L.J. Jacobs, and J. Qu, *Modeling elastic wave propagation in waveguides with the finite element method*. Ndt & E International, 1999. **32**(4): p. 225-234.
76. Wilcox, P., M. Lowe, and P. Cawley, *Mode and transducer selection for long range Lamb wave inspection*. Journal of intelligent material systems and structures, 2001. **12**(8): p. 553-565.
77. Azhari, H., *Basics of biomedical ultrasound for engineers*. 2010: John Wiley & Sons.
78. Ismail, Z., et al. *The application of genetic algorithm for sensor placement of PZT wafer towards the application in structural health monitoring*. in *12th European conference on non-destructive testing (ENCNT)*, Gothenberg. 2018.
79. Ostachowicz, W., R. Soman, and P. Malinowski, *Optimization of sensor placement for structural health monitoring: A review*. Structural Health Monitoring, 2019. **18**(3): p. 963-988.
80. Tarhini, H., et al., *Optimization of piezoelectric wafer placement for structural health-monitoring applications*. Journal of Intelligent Material Systems and Structures, 2018. **29**(19): p. 3758-3773.
81. Cantero-Chinchilla, S., et al., *A robust Bayesian methodology for damage localization in plate-like structures using ultrasonic guided-waves*. Mechanical Systems and Signal Processing, 2019. **122**: p. 192-205.
82. Cantero-Chinchilla, S., et al., *Optimal sensor configuration for ultrasonic guided-wave inspection based on value of information*. Mechanical Systems and Signal Processing, 2020. **135**: p. 106377.
83. Cantero-Chinchilla, S., et al., *Optimal sensor and actuator placement for structural health monitoring via an efficient convex cost-benefit optimization*. Mechanical Systems and Signal Processing, 2020. **144**: p. 106901.
84. Fakhri, M.A., et al., *Symbolic dynamics time series analysis for assessment of barely visible indentation damage in composite sandwich structures based on guided waves*. Journal of Composite Materials, 2017. **51**(29): p. 4129-4143.
85. Marin, J.-M., et al., *Approximate Bayesian computational methods*. Statistics and Computing, 2012. **22**(6): p. 1167-1180.
86. Tua, P., S. Quek, and Q. Wang, *Detection of cracks in plates using piezo-actuated Lamb waves*. Smart Materials and Structures, 2004. **13**(4): p. 643.
87. Hong, M., et al., *Locating fatigue damage using temporal signal features of nonlinear Lamb waves*. Mechanical Systems and Signal Processing, 2015. **60**: p. 182-197.
88. Leonard, K.R., E.V. Malyarenko, and M.K. Hinders, *Ultrasonic Lamb wave tomography*. Inverse problems, 2002. **18**(6): p. 1795.
89. Salehi, H. and R. Burgueno, *Emerging artificial intelligence methods in structural engineering*. Engineering structures, 2018. **171**: p. 170-189.

90. Khoa, N.L., et al., *Robust dimensionality reduction and damage detection approaches in structural health monitoring*. Structural Health Monitoring, 2014. **13**(4): p. 406-417.
91. Smarsly, K., K. Dragos, and J. Wiggenbrock. *Machine learning techniques for structural health monitoring*. in *Proceedings of the 8th European Workshop on Structural Health Monitoring (EWSHM 2016), Bilbao, Spain*. 2016.
92. Sbarufatti, C., G. Manson, and K. Worden, *A numerically-enhanced machine learning approach to damage diagnosis using a Lamb wave sensing network*. Journal of Sound and Vibration, 2014. **333**(19): p. 4499-4525.
93. Su, Z. and L. Ye, *Lamb wave propagation-based damage identification for quasi-isotropic CF/EP composite laminates using artificial neural algorithm: Part I-methodology and database development*. Journal of intelligent material systems and structures, 2005. **16**(2): p. 97-111.
94. Su, Z. and L. Ye, *Lamb Wave Propagation-based Damage Identification for Quasi-isotropic CF/EP Composite Laminates Using Artificial Neural Algorithm: Part II-Implementation and Validation*. Journal of Intelligent Material Systems and Structures, 2005. **16**(2): p. 113-125.
95. Lu, Y., et al., *Artificial neural network (ANN)-based crack identification in aluminum plates with Lamb wave signals*. Journal of Intelligent Material Systems and Structures, 2009. **20**(1): p. 39-49.
96. Chiachio, M., et al., *Approximate Bayesian computation by subset simulation*. SIAM Journal on Scientific Computing, 2014. **36**(3): p. A1339-A1358.
97. Alleyne, D.N. and P. Cawley. *A 2-dimensional Fourier transform method for the quantitative measurement of Lamb modes*. in *IEEE Symposium on Ultrasonics*. 1990. IEEE.
98. Alleyne, D. and P. Cawley, *A two-dimensional Fourier transform method for the measurement of propagating multimode signals*. The Journal of the Acoustical Society of America, 1991. **89**(3): p. 1159-1168.
99. Song, F., G. Huang, and K. Hudson, *Guided wave propagation in honeycomb sandwich structures using a piezoelectric actuator/sensor system*. Smart Materials and Structures, 2009. **18**(12): p. 125007.
100. Papazafeiropoulos, G., M. Muñoz-Calvente, and E. Martínez-Pañeda, *Abaqus2Matlab: a suitable tool for finite element post-processing*. Advances in Engineering Software, 2017. **105**: p. 9-16.
101. Brownlee, J., *Master Machine Learning Algorithms: discover how they work and implement them from scratch*. 2016: Machine Learning Mastery.
102. Kohavi, R. *A study of cross-validation and bootstrap for accuracy estimation and model selection*. in *Ijcai*. 1995. Montreal, Canada.
103. Møller, M.F., *A scaled conjugate gradient algorithm for fast supervised learning*. Neural networks, 1993. **6**(4): p. 525-533.
104. Au, S.-K. and J.L. Beck, *Estimation of small failure probabilities in high dimensions by subset simulation*. Probabilistic engineering mechanics, 2001. **16**(4): p. 263-277.
105. Au, S.K. and J. Beck, *Subset simulation and its application to seismic risk based on dynamic analysis*. Journal of Engineering Mechanics, 2003. **129**(8): p. 901-917.
106. Au, S.K., J. Ching, and J. Beck, *Application of subset simulation methods to reliability benchmark problems*. Structural safety, 2007. **29**(3): p. 183-193.

107. Zuev, K.M., et al., *Bayesian post-processor and other enhancements of Subset Simulation for estimating failure probabilities in high dimensions*. Computers & structures, 2012. **92**: p. 283-296.
108. Vakilzadeh, M.K., et al., *Approximate Bayesian Computation by Subset Simulation using hierarchical state-space models*. Mechanical Systems and Signal Processing, 2017. **84**: p. 2-20.
109. Mustapha, S., et al., *Estimation of crowd flow and load on pedestrian bridges using machine learning with sensor fusion*. Automation in Construction, 2020. **112**: p. 103092.
110. Albannai, A.I., *Review The Common Defects In Friction Stir Welding*. International Journal of Scientific & Technology Research, 2020. **9**(11): p. 318-329.
111. Hussein, S.A. and A. Hadzley, *Characteristics of aluminum-to-steel joint made by friction stir welding: A review*. Materials Today Communications, 2015. **5**: p. 32-49.
112. Klag, O., et al., *Microstructural and thermodynamic investigations on friction stir welded Mg/Al-joints*. International Journal of Materials Research, 2014. **105**(2): p. 145-155.
113. Liao, J., et al., *Microstructure at friction stir lap joint interface of pure titanium and steel*. Materials letters, 2010. **64**(21): p. 2317-2320.
114. Gao, Y., T. Tsumura, and K. Nakata, *Dissimilar welding of titanium alloys to steels*. Transactions of JWRI, 2012. **41**(2): p. 7-12.
115. Mousavi, S.A. and P.F. Sartangi, *Experimental investigation of explosive welding of cp-titanium/AISI 304 stainless steel*. Materials & Design, 2009. **30**(3): p. 459-468.
116. Mudali, U.K., et al., *Corrosion and microstructural aspects of dissimilar joints of titanium and type 304L stainless steel*. Journal of Nuclear Materials, 2003. **321**(1): p. 40-48.
117. Dorbane, A., et al., *Mechanical, microstructural and fracture properties of dissimilar welds produced by friction stir welding of AZ31B and Al6061*. Materials Science and Engineering: A, 2016. **651**: p. 720-733.
118. Shi, H., et al., *Intermetallic compounds in the banded structure and their effect on mechanical properties of Al/Mg dissimilar friction stir welding joints*. Journal of Materials Science & Technology, 2017. **33**(4): p. 359-366.
119. Fazel-Najafabadi, M., S. Kashani-Bozorg, and A. Zarei-Hanzaki, *Joining of CP-Ti to 304 stainless steel using friction stir welding technique*. Materials & Design, 2010. **31**(10): p. 4800-4807.
120. Chen, T. and W.-B. Lin, *Optimal FSW process parameters for interface and welded zone toughness of dissimilar aluminium–steel joint*. Science and Technology of Welding and Joining, 2010. **15**(4): p. 279-285.
121. Coelho, R.S., et al., *Microstructure and Mechanical Properties of an AA6181-T4 Aluminium Alloy to HC340LA High Strength Steel Friction Stir Overlap Weld*. Advanced Engineering Materials, 2008. **10**(10): p. 961-972.
122. Liu, P., et al., *Microstructure and XRD analysis of FSW joints for copper T2/aluminium 5A06 dissimilar materials*. Materials letters, 2008. **62**(25): p. 4106-4108.
123. Barekatin, H., M. Kazeminezhad, and A. Kokabi, *Microstructure and mechanical properties in dissimilar butt friction stir welding of severely plastic*

- deformed aluminum AA 1050 and commercially pure copper sheets*. Journal of Materials Science & Technology, 2014. **30**(8): p. 826-834.
124. Imaizumi, S., *Welding Aluminium to Dissimilar Metals (III) Solid State Bonding*. Journal of Light Metal & Construction, 1984. **22**: p. 408-419.
 125. Yamamoto, N., et al., *Effect of intermetallic compound layer on tensile strength of dissimilar friction-stir weld of a high strength Mg alloy and Al alloy*. Materials transactions, 2009. **50**(12): p. 2833-2838.
 126. Alleyne, D.N. and P. Cawley, *The interaction of Lamb waves with defects*. IEEE transactions on ultrasonics, ferroelectrics, and frequency control, 1992. **39**(3): p. 381-397.
 127. Gresil, M. and V. Giurgiutiu, *Time-domain hybrid global-local concept for guided-wave propagation with piezoelectric wafer active sensor*. Journal of Intelligent Material systems and structures, 2013. **24**(15): p. 1897-1911.
 128. Jhang, K.-Y., *Nonlinear ultrasonic techniques for nondestructive assessment of micro damage in material: a review*. International journal of precision engineering and manufacturing, 2009. **10**(1): p. 123-135.
 129. Solodov, I., et al., *Nonlinear self-modulation and subharmonic acoustic spectroscopy for damage detection and location*. Applied physics letters, 2004. **84**(26): p. 5386-5388.
 130. Ohara, Y., et al., *Imaging of closed cracks using nonlinear response of elastic waves at subharmonic frequency*. Applied physics letters, 2007. **90**(1): p. 011902.
 131. Hikata, A., F. Sewell Jr, and C. Elbaum, *Generation of ultrasonic second and third harmonics due to dislocations. II*. Physical Review, 1966. **151**(2): p. 442.
 132. Hikata, A. and C. Elbaum, *Generation of ultrasonic second and third harmonics due to dislocations. I*. Physical Review, 1966. **144**(2): p. 469.
 133. Liu, X., et al., *Localization of material defects using nonlinear resonant ultrasound spectroscopy under asymmetric boundary conditions*. Physics Procedia, 2010. **3**(1): p. 55-61.
 134. Van Den Abeele, K.E., et al., *Micro-damage diagnostics using nonlinear elastic wave spectroscopy (NEWS)*. Ndt & E International, 2001. **34**(4): p. 239-248.
 135. Li, N., et al., *Quantitative evaluation of micro-cracks using nonlinear ultrasonic modulation method*. Ndt & E International, 2016. **79**: p. 63-72.
 136. Lim, H.J., et al., *Noncontact fatigue crack visualization using nonlinear ultrasonic modulation*. Ndt & E International, 2015. **73**: p. 8-14.
 137. Fukuda, M., M. Nishihira, and K. Imano, *Real time detection of second-harmonic components generated from plastic-deformed metal rod using double-layered piezoelectric transducer*. Japanese Journal of Applied Physics, 2007. **46**(7S): p. 4529.
 138. Fukuda, M., M. Nishihira, and K. Imano, *Novel detection system using double-layered piezoelectric transducer in same polarization direction for sub-harmonic components generated from plastic-deformed metal rod*. Japanese Journal of Applied Physics, 2008. **47**(5S): p. 3899.
 139. Zhang, M., et al., *Damage detection of fatigue cracks under nonlinear boundary condition using subharmonic resonance*. Ultrasonics, 2017. **77**: p. 152-159.
 140. Yang, Y., et al., *Second harmonic generation at fatigue cracks by low-frequency Lamb waves: Experimental and numerical studies*. Mechanical Systems and Signal Processing, 2018. **99**: p. 760-773.

141. Cao, W., et al., *Nonlinear ultrasonic evaluation of disorderedly clustered pitting damage using an in situ sensor network*. Structural Health Monitoring, 2020. **19**(6): p. 1989-2006.
142. Belanger, P. and M. Jahazi. *Friction stir welded lap joint inspection using ultrasonic guided waves*. in *AIP Conference Proceedings*. 2019. AIP Publishing LLC.
143. Su, Z., et al., *Acousto-ultrasonics-based fatigue damage characterization: Linear versus nonlinear signal features*. Mechanical Systems and Signal Processing, 2014. **45**(1): p. 225-239.
144. Rayleigh, J.W.S.B., *The theory of sound*. Vol. 2. 1896: Macmillan.
145. Len, K.S., et al., *Experimental observation of the influence of contact nonlinearity on the reflection of bulk acoustic waves and the propagation of surface acoustic waves*. Soviet physics. Acoustics, 1991. **37**(6): p. 610-612.
146. Na, J.K., J.H. Cantrell, and W.T. Yost, *Linear and nonlinear ultrasonic properties of fatigued 410CB stainless steel*, in *Review of progress in quantitative nondestructive evaluation*. 1996, Springer. p. 1347-1352.
147. Solodov, I.Y., N. Krohn, and G. Busse, *CAN: an example of nonclassical acoustic nonlinearity in solids*. Ultrasonics, 2002. **40**(1-8): p. 621-625.
148. Cantrell, J.H., *Dependence of microelastic-plastic nonlinearity of martensitic stainless steel on fatigue damage accumulation*. Journal of applied physics, 2006. **100**(6): p. 063508.
149. Hikata, A., B. Chick, and C. Elbaum, *Effect of dislocations on finite amplitude ultrasonic waves in aluminum*. Applied Physics Letters, 1963. **3**(11): p. 195-197.
150. Cantrell, J.H. and W.T. Yost, *Acoustic harmonic generation from fatigue-induced dislocation dipoles*. Philosophical magazine A, 1994. **69**(2): p. 315-326.
151. Bermes, C., et al., *Experimental characterization of material nonlinearity using Lamb waves*. Applied physics letters, 2007. **90**(2): p. 021901.
152. Müller, M.F., et al., *Characteristics of second harmonic generation of Lamb waves in nonlinear elastic plates*. The Journal of the Acoustical Society of America, 2010. **127**(4): p. 2141-2152.
153. Xiang, Y., et al., *Cumulative second-harmonic analysis of ultrasonic Lamb waves for ageing behavior study of modified-HP austenite steel*. Ultrasonics, 2011. **51**(8): p. 974-981.
154. Li, W., Y. Cho, and J.D. Achenbach, *Detection of thermal fatigue in composites by second harmonic Lamb waves*. Smart Materials and Structures, 2012. **21**(8): p. 085019.
155. Sun, X., et al., *Simulations on monitoring and evaluation of plasticity-driven material damage based on second harmonic of S0 mode Lamb waves in metallic plates*. Materials, 2017. **10**(7): p. 827.
156. Xiang, Y., et al., *Experimental study of thermal degradation in ferritic Cr-Ni alloy steel plates using nonlinear Lamb waves*. Ndt & E International, 2011. **44**(8): p. 768-774.
157. Su, Z. and M. Hong, *Nonlinear ultrasonics for health monitoring of aerospace structures using active sparse sensor networks*, in *Structural Health Monitoring (SHM) in Aerospace Structures*. 2016, Elsevier. p. 353-392.
158. Deng, M., *Analysis of second-harmonic generation of Lamb modes using a modal analysis approach*. Journal of applied physics, 2003. **94**(6): p. 4152-4159.

159. Ibrahim, A.B., et al., *Effect of process parameters on microstructural and mechanical properties of friction stir diffusion cladded ASTM A516-70 steel using 5052 Al alloy*. Journal of Manufacturing Processes, 2018. **34**: p. 451-462.
160. Metya, A.K., S. Tarafder, and K. Balasubramaniam, *Nonlinear Lamb wave mixing for assessing localized deformation during creep*. NDT & E International, 2018. **98**: p. 89-94.
161. Zuo, P., Y. Zhou, and Z. Fan, *Numerical and experimental investigation of nonlinear ultrasonic Lamb waves at low frequency*. Applied Physics Letters, 2016. **109**(2): p. 021902.
162. Stobbe, D.M., *Acoustoelasticity in 7075-T651 Aluminum and Dependence of Third Order Elastic Constants on Fatigue Damage*. 2005, Georgia Institute of Technology.
163. Su, Z. and L. Ye, *Selective generation of Lamb wave modes and their propagation characteristics in defective composite laminates*. Proceedings of the Institution of Mechanical Engineers, Part L: Journal of Materials: Design and Applications, 2004. **218**(2): p. 95-110.
164. Egle, D. and D. Bray, *Measurement of acoustoelastic and third-order elastic constants for rail steel*. The journal of the Acoustical Society of America, 1976. **60**(3): p. 741-744.

